Shocks, Jets, and Emerging Nebulae: Direct Detection and Characterization of Extragalactic Radio Transients in the VLA Sky Survey

Thesis by
Dillon Zhejun Dong

In Partial Fulfillment of the Requirements for the
Degree of
Doctor of Philosophy

CALIFORNIA INSTITUTE OF TECHNOLOGY
Pasadena, California

2023
Defended December 16, 2022

Dillon Zhejun Dong
ORCID: 0000-0001-9584-2531

For my mom and dad, Liping Yang and Allan Yuan-Yuan Dong

Thank you for always supporting me and encouraging me to dive deeply into my interests, no matter how seemingly useless or obscure. Whether you knew it or not, you taught me the value of creativity, being silly, and doing what I love.

For my grandmas, Yi Wen Sun and Qiu Qu

Thank you for coming all the way to America to take care of me when I was little. You walked me to school every day and knew all of my favorite foods. My life was made so much richer by your love.

Never saw what we could unravel
In traveling light
Nor how the trip debrides–
Like a stack of slides!
All we saw was that Time is taller than Space is wide.

– *Waltz of the 101st Lightborne* by Joanna Newsom

Horatio: O day and night, but this is wondrous strange!

Hamlet: And therefore as a stranger give it welcome.
There are more things in heaven and earth, Horatio,
Than are dreamt of in your philosophy.

Hamlet, Act I, Scene V

ACKNOWLEDGEMENTS

This thesis would not have been possible without the kind, thoughtful, and multi-faceted support that I've been so lucky to receive from so many people throughout the years. Many little interactions, conversations, and pieces of imparted wisdom have collectively shaped and inspired the way that I interact with the world today. For all of those influences, I am extremely grateful. Though there are far more people who have shaped my life than I can reasonably thank in a single acknowledgements section, I would like to highlight a few who been particularly influential in my science and in my journey through grad school.

First and foremost, I'd like to thank my advisor Gregg Hallinan, who believed in me from the start even though I had to google what a transient was and watch a PBS documentary on gamma ray bursts before we started working together. Thank you for all of our side-by-side adventures in rooting through this new parameter space and sniffing out the most interesting transients. You've shown me firsthand what it means to be scientifically creative, and for that, I'll always be grateful.

I'd also like to thank all of the other members of my thesis committee, past and present. Thanks to Vikram Ravi, Sterl Phinney, Jim Fuller, Katerina Chatziioannou, Mansi Kasliwal, and Evan Kirby for reading my work, attending my candidacy and thesis defense (in some cases with very little notice), and for your thoughtful feedback. Many of you have gone out of your way to provide me mentorship, bits of wisdom, research opportunities, and very useful pieces of knowledge from your specialties over the years. I'm thankful for each and every one of those interactions.

In addition to my committee, I've had the privilege of working with and learning from many fantastic advisors and mentors over the years. Thanks in particular to:

- Eric Murphy and Rob Kennicutt, who taught me how to be fastidious in doing research (along with most of what I know about galaxies). Though I've nominally switched fields, the skills and knowledge I gained from working with them are deeply influential in my research today (including in all the work done for this thesis).
- Emmanuel Momjian, who spent weeks teaching me the ins and outs of how to process VLA data. Many of my skills as a radio astronomer trace back directly to what I learned from him.

- Tom Moore, who taught a large plurality of all the physics classes I've ever taken, and went out of his way to teach a general relativity seminar on an off-semester even though I was the only student. The plurality was because I often signed up for whatever he was teaching regardless of what it was. I do not regret doing so in the slightest.

- Phil Choi, who taught my first astronomy class – the one that convinced me I wanted to to study astronomy in the first place. Even though I was terrible at aligning lasers for his adaptive optics system, he helped me find a job doing radio astronomy, something that I ended up being slightly better at. Thanks Phil, for being a fantastic mentor and for going out of your way to keep up with me throughout the years.

- Richard Shapiro, who taught me to always look for the *story* in a physics problem (a practice that heavily influences my research today), and who helped me find my first research job (in a UCSF bioinformatics lab as a high school senior).

- Bruce Cohen, who showed me that math is actually creative and fun, and who went out of his way one summer to meet with me once a week in a coffee shop and teach me python out of the goodness of his heart. Needless to say, I use that skill all the time today.

- Scott Dickerman, who convinced me – lastingly – that my favorite subject was physics (a tall task given how many things I was interested in), and whose classroom was a bona-fide refuge for awkward nerdy teens like myself.

I'd also like to extend my deep gratitude to the VLASS team, without whom my thesis would have no data. Thanks in particular to Steve Myers who taught me how to image (and otherwise work with) VLASS data and who has steadfastly attended nearly all of our VLASS research meetings despite having to call in from Socorro.

Thank you to the members of the Caltech Radio Astronomy group, particularly those who I've had the chance to collaborate with directly. You are all joys to work with. Thanks in particular to Jean Somalwar who was an instrumental collaborator on my final thesis paper, and who is a veritable fountain of good ideas. I'm very much looking forward to continuing our collaborations in the future. Thanks again to Vikram Ravi who never fails to provide insightful and detailed paper comments – the kind you wish you had thought of yourself months before! Thanks to Carlos

Ayala for being such an excellent mentee. It has been so much fun watching you grow as a researcher throughout the years – I can't wait to see what you do next! Thanks to Casey Law for always being available to chat and for continually reminding me to zoom out and look at the bigger picture. Thanks also to Casey, Yuping Huang, and Ivey Davis for being excellent co-mentors for Carlos and for sharing your expertise (particularly on the physics of stellar flares). Thanks so much to Jessie Miller for being great to work with, and for our conversations that have taught me so much about the way I think.

Finally, I'd like to thank my friends (both in the department and outside), who have been such an important part of my life during my time in grad school.

Thanks in particular to Peter and Sabrina for always being there for me, and for all you've taught me about myself as a person.

Thanks to Kathryn, Yuping, Matthew, Emma, Sarah, Devin, Chris, Ivey, Sam, Ryan, Katherine, Jean, Jess, Emily, Dee, Katelyn, Viraj, Jake, Denise, Rachel, Kishalay, Yuhan, Kaustav, Pranav, Evan, Max, Yashvi, Shreya, Nikita, Nitika, Cameron, Eloise, and Ruben for all the time we spent hanging out in your offices and homes, and for all the adventures we embarked on, at home, around the city, in gyms, and in the mountains.

Each and every one of you has made my life richer, and I am so grateful for all the time we've spent together.

ABSTRACT

For most of their lives, massive stars and supermassive black holes evolve steadily, changing only gradually on human timescales. But on occasion, these cosmic engines erupt, lighting up their surroundings like flashes in the dark. Under the right conditions, the eruptions can manifest as slow radio transients, rising and fading on timescales of weeks to decades. By finding these transients and observing their evolution, we can study otherwise inaccessible aspects of the engines' lives, and piece together their influence on their surroundings.

Until recently, most of our knowledge of slow radio transients came from follow-up observations of explosions first discovered as optical and high-energy transients. This avenue of discovery, while illuminating, provides an indelibly incomplete picture of the radio transient landscape. Moreover, each successful follow-up detection typically comes at the cost of many unsuccessful attempts (measured in both telescope and human time).

My thesis helps address these issues by finding and characterizing transients directly in radio surveys. By applying novel transient detection techniques to data from the Very Large Array Sky Survey (VLASS), I produced the first uniformly selected sample of radio transients associated with local universe galaxies. The 64 transients in my sample have roughly doubled the total number of directly detected slow radio transients in the literature. This sample has enabled the first volume-limited characterization of the demographics of extragalactic slow radio transients. It has also facilitated the discovery of two previously unseen transient types: the merger of a compact object with a massive star and a decades-old emerging pulsar wind nebula.

These early results used only ~15% of the currently available data from VLASS and focused only on extragalactic transients at low redshift. By applying the same techniques to the full survey, I have found ~2000 new transients, increasing the number of known slow radio transients (detected by any means) by a further order of magnitude. With this new sample, my collaborators and I are beginning to shift the study of slow radio transients from the domain of single-object deep-dives to the domain of statistical samples.

PUBLISHED CONTENT AND CONTRIBUTIONS

Dong, Dillon and Gregg Hallinan (June 2022). "A Flat-Spectrum Radio Transient at 122 Mpc consistent with an Emerging Pulsar Wind Nebula". In: *arXiv e-prints*, arXiv:2206.11911, arXiv:2206.11911. arXiv: 2206.11911 [astro-ph.HE].
D.Z.D. discovered the transient, helped identify it as a promising target for followup, proposed for, observed, reduced, and analyzed the radio and optical data, and wrote the manuscript.

Dong, D. Z. et al. (Sept. 2021). "A transient radio source consistent with a merger-triggered core collapse supernova". In: *Science* 373.6559, pp. 1125–1129. DOI: 10.1126/science.abg6037. arXiv: 2109.01752 [astro-ph.HE].
D.Z.D. helped design the transient search strategy, discovered the transient, helped identify it as a promising target for followup, proposed for, observed, reduced, and analyzed the radio and optical data, helped analyze the X-ray data, and led the writing of the manuscript.

TABLE OF CONTENTS

LIST OF ILLUSTRATIONS

LIST OF TABLES

Chapter 1

INTRODUCTION

1.1 The ever-changing universe

Throughout human history, astronomers have told stories about the night sky informed by the tools we've had at hand. The earliest available tools were our eyes and our imaginative brains. With just these, ancient astronomers could see the first hints that the universe is *dynamic*, ever changing in time. Some of the variations they saw were dramatic one-off events. The supernova of 1054 was recorded by astronomers across the world (most famously as a "guest star" in the ancient Chinese encyclopedia *Wengxian Tongkao*). Others were cyclical. In ~1200 B.C., ancient Egyptian scribes recorded a pattern of "lucky" days on a 2.85-day cycle, consistent with the period of the eclipsing binary Algol. Writings in the Cairo Calendar of Lucky and Unlucky Days suggest that they interpreted these eclipses as the death and rebirth of Horus, god of kingship and the sky (Jetsu and Porceddu, 2015).

As astronomers created more involved tools, our stories evolved. In the past ~century, multi-wavelength telescopes and astrophysical theory have led us toward deeper insights (with more predictive power) into the nature of the dynamic universe. In radio astronomy, observations of Algol showed that the same close binary orbit responsible for the "lucky" eclipses creates a strong surface magnetic field, which leads to frequent bright radio flares (Hughes and Woodsworth, 1972). Likewise, the year after Jocelyn Bell-Burnell discovered the first pulsar, Staelin and Reifenstein (1968) reported another pulsar associated with the remnant of supernova 1054: the Crab Nebula. Since then, decades of work have been done on both the pulsar itself and its relativistic wind, which creates the energetic particles that fill the nebula (Goldreich and Julian, 1969). Despite these decades of work, many mysteries still remain, including the origin of the hard energy distribution of particles in the nebula (Sironi and Spitkovsky, 2011; Bühler and R. Blandford, 2014). Many other mysteries remain about a wide range of dynamic astrophysical phenomena, including ones that have only been discovered in the past few years.

New tools can accelerate the process of learning about the dynamic universe in several ways, which are well illustrated by the history of supernova detection. One

of the simplest ways is by increasing the number of events detected. While ancient astronomers had to wait centuries in between naked-eye supernova detections, routine monitoring of nearby galaxies with foot- and meter- class telescopes at the Mt. Wilson and Palomar Observatories by Zwicky, Baade, and collaborators increased the supernova detection rate to a few per year by the 1930s (M. Stritzinger and Moriya, 2018). The routine detection of supernovae in other galaxies led directly to the realization that supernovae are in a luminosity class of their own (distinct from classical novae). Astrophysical arguments then showed that to produce such a high luminosity, these supernovae must be caused by the explosions of stars (Baade and Zwicky, 1934). Another qualitative shift in our understanding of supernovae came from the addition of orthogonal information in the form of spectroscopic follow-up observations. The distinction between hydrogen-poor (type I) and hydrogen-rich (type II) supernovae (Minkowski, 1941) turned out to be a crucial first step in identifying the stellar types responsible for the explosions.

Astrophysical fields are deeply interconnected, and as a result, supernova classification led to profound insights outside of the realm of stars. A sub-class of Type I supernovae (Type Ia's, produced by the explosions of white dwarfs) turned out to be standardizable candles, with intrinsic luminosities that can be measured simply by the duration of their lightcurves, thus providing luminosity distances to their host galaxies (Rust, 1974; Pskovskii, 1977). Using the newly statistically significant sample of Type Ia's at moderate redshifts detected by CCD-based sky surveys in the 1990s, Riess et al. (1998) and Perlmutter et al. (1999) showed that the expansion of the universe is accelerating, thus confirming the existence of dark energy (Guth, 1981) and establishing the ΛCDM cosmological paradigm.

Since that groundbreaking discovery, the rate of supernova detection has increased by yet another order of magnitude. One of the more recent developments that has come out of this latest expansion in sample size has been a proliferation of new transient types. Recent examples include fast blue optical transients, kilonovae, calcium-rich gap transients, superluminous supernovae, tidal disruption events, and many more. The Palomar Transient Factory (PTF) and its successor the Zwicky Transient Facility (ZTF) have been key contributors in this regard. ZTF in particular has driven most of the growth in the field in the past few years. As of December 2022, it has discovered 6600 spectroscopically confirmed supernovae in its $\sim$5 years since first light. Each year, ZTF discovers more supernovae than were discovered

from the start of humanity to the year 1990. The detection rates of other transient classes have increased by similar margins. Near-future facilities, particularly the Rubin Observatory Legacy Survey of Space and Time (LSST), are set to increase that rate by yet another order of magnitude.

Given all the built-up machinery in modern time-domain astronomy, a natural question might be: is there room to uncover truly new stories about the dynamic sky, particularly with an effort on the scale of a single PhD thesis? If so, where? To the first question, I'd say yes, definitely. There are always new stories to tell if you dig in the right directions. To the second question, I'd ask two questions of my own. Where are the new tools that can increase the number of events found in a manner orthogonal to what has already been done? How might those new events help to build bridges between fields?

Early on in grad school, I had the great fortune of being handed such a tool: fully processed images from the VLA Sky Survey (VLASS), a multi-epoch *radio* sky survey done (through the meticulous work of many staff at the National Radio Astronomy Observatory) at a scale and angular resolution that had never before been seen. This thesis has been my attempt to do justice to the bounty that I had been handed: to use VLASS to dig in directions mostly orthogonal to what had been done before, and to try and use what I dug up to build bridges between fields.

1.2 Slow radio transients: A new window into the dynamic sky

Much like the parable of the blind mice trying to picture an elephant with their localized sense of touch, each new tool that astronomers use provides a different but biased view of the dynamic universe as a whole. The VLA Sky Survey is no exception. The specific kind of transient that VLASS is most sensitive to is one that I will refer to in this thesis as a *slow radio transient*. The remainder of this section is aimed at providing some background on these transients. Much of the information summarized here is discussed in more detail in the papers presented in Chapters 2, 3, and 4.

What is a Slow Radio Transient?

In this thesis, I use the term *radio transient* to refer to a radio source detected in one observation (at the *detection epoch*) that is either known to be transient from association with a previously identified transient source, or is not detected in a previous

radio observation (at the *reference epoch*), though it should have been if it were non-varying. The label “slow" refers to the lengthy amount of time that these transients typically spend near peak luminosity (where they are most likely to be detected by a sky survey). Unlike fast radio bursts (FRBs) which last for milliseconds, slow radio transients often last for years (as is the case with ∼80% of the sources found in Chapter 2) if not decades (as will likely be the case for the pulsar wind nebula candidate VT 1137-0337, which is currently fading at a mere 5% per year; Chapter 4). The reason why my searches select for slow transients is the spacing between reference and detection epochs. FIRST and VLASS are separated by an average of ∼20 years, while the two epochs of VLASS are separated by ∼2–3 years depending on the region of sky. While in principle a FRB could occur during the 5-second effective integration of a VLASS observation, for every FRB that is detected in VLASS, there must be countless others that happened to occur in the years between epochs. While this does not preclude the detection of fast transients in VLASS, they would need to be extremely common to be found. On the other hand, a slowly fading transient is much more likely to still be detectable in the detection epoch, regardless of when after the reference epoch it became detectable. As it turns out, this selection bias is actually a useful and informative property, since it provides an expectation for the timescale of the transients detected. I expand on this notion in Chapter 2.

There is some subtlety to this observational definition of a radio transient, particularly when a transient is identified using only radio data. One issue is that when observed with a sufficiently sensitive telescope, every transient is produced by an object and located in an environment with *some* level of quiescent emission. This quiescent emission can cause a source to appear to be detected in the reference epoch even though it is actually transient. Optical and infrared transient astronomers are very familiar with this issue since the quiescent emission of galaxies, stars, galactic nuclei, etc. can be brighter than the transient emission itself. However, with the shallow depth of modern radio sky surveys and the general quietness of the radio sky, most transient classes will appear in locations with no detectable quiescent radio emission. A notable exception is flares occurring in already radio-loud AGN. I do not consider these transient types in the 200 Mpc sample, because the reference epoch I used (FIRST) is at a slightly different frequency (1.5 GHz) than the detection epoch (which is at 3 GHz), and in some cases (rare ones because the vast majority of GHz radio sources become fainter with increasing frequency), it can be difficult to disen-

tangle whether a detection in FIRST is due to a rising spectrum or true variability. This issue is discussed in more depth in Chapter 2. However, in the same-frequency VLASS vs VLASS search described in Chapter 5, this degeneracy between spectral index and variability is no longer an issue, thus opening the door to studying variable sources (many of which are transients that lie on top of quiescent emission).

Regardless of the presence or absence of quiescent emission, the region producing the time-variable component of any radio source is limited in size by causality if the variability is not due to scintillation. If it is due to scintillation, the emitting region is even smaller (Walker, 1998, also see below). For extragalactic transients, this limit is typically much smaller than what can be directly observed with Very Long Baseline Interferometry (VLBI). Given the small size and high luminosity for many of these transients, it is usually possible to argue that the emission is nonthermal in nature. This then points to synchrotron emission as the mechanism behind the transient radio emission.

The Ingredients of a Synchrotron Transient

Synchrotron emission is produced when electrons are accelerated to relativistic speeds and spiral in relatively strong magnetic fields (typically a fraction of a Gauss for the extragalactic transients that VLASS is most sensitive to). In order to produce these relativistic electrons in the numbers required for their emission to be detectable, there needs to be a powerful particle acceleration mechanism. In most cases, this mechanism is thought to be a shock, producing a power law energy distribution (typically $dN/dE \propto E^{-2}$ to E^{-3}) through the Fermi mechanism (Roger Blandford and Eichler, 1987). This explanation is particularly compelling in the context of radio emission from explosive transients, because shocks arise where there are large velocity differentials, and a very effective way to produce these differentials is to eject mass outwards at high speeds (e.g., with a jet or an outflow) toward a relatively stationary target (the surrounding gas).

Each synchrotron-emitting electron emits (on average) a certain amount of power dependent on its Lorentz factor γ and the magnetic field B in which it is spiraling (Rybicki and Lightman, 1986). Thus, one way to rapidly increase the luminosity of a synchrotron source (i.e., create a synchrotron *transient*) is to rapidly increase the number of emitting electrons. This happens when for instance a new shock is created. When a star explodes in a supernova, or is shredded apart by a black hole

and its pieces are sent flying outward, the outflow can suddenly collide with the surrounding gas. Where previously there was no shock, all of a sudden there is now a large number of relativistic particles being accelerated in a region where the ambient magnetic field is strongly amplified (also by the shock). Voilà, you have the makings of a synchrotron transient.

Here, I say the *makings* of a synchrotron transient because the production of new synchrotron photons does not guarantee that those photons will make it to your telescope on Earth. Even though radio synchrotron emission is impervious to the traditional obscurer of optical emission (dust), it suffers from propagation effects of its own. Radio synchrotron photons can be scattered and lensed by plasma in the Milky Way. This effect, known as scintillation, can magnify or demagnify a radio source, thus creating the appearance of variability where intrinsically there was none. Additionally, if there is a sufficiently dense (and relatively low-temperature) column of free electrons in between the synchrotron source and Earth, many of those photons will impart their energy to the electrons in a process known as free-free absorption. Finally, at sufficiently low frequencies, all synchrotron sources obscure *themselves*, in a process aptly named synchrotron self-absorption.

From one observational standpoint, scintillation is the most innocuous of the three effects. The timescale on which the effect occurs (seconds to hours depending on the type of scintillation) is very short compared to the duration of slow transients. Additionally, the magnitude of the induced variability is small at 3 GHz (typically of order 10s of percent at its strongest, far off the Galactic plane), so scintillation is much more likely to be observed as variability rather than transient behavior. Based on even limited information, it is often possible to make an argument strongly disfavoring scintillation as the source of a transient that you have observed. Conversely, the are sometimes very interesting things to learn where the source of the variability *is* scintillation. The modulation amplitude of scintillation is a strong function of the size of the radio emitting region. If the region is small in angular extent, the rays of light can be focused and defocused efficiently. But if the emitting region is large, the modulations from different parts of the region will on average cancel each other out, suppressing the effect. The angular scale on which this occurs is of order microarcseconds, far beyond the realm of what can be resolved by modern telescopes of any kind. The time of disappearance of the scintillation signal in the gamma ray burst GRB 980508 was used in Frail, Waxman, and Kulkarni (2000) as

a measure of the expansion rate of the radio emitting region. This provided direct evidence that the afterglow was produced by the shock of a relativisitic jet.

Free-free absorption is important when there is a high density of gas surrounding the transient. At the VLASS observing frequency of 3 GHz the ionized gas in the interstellar medium of all but the extreme star forming galaxies is insufficient to create substantial absorption. However, since the free-free optical depth scales as n_e^2, where n_e is the number density of free electrons, dense gas surrounding the site of a transient can be a significant source of obscuration. In some cases, this dense gas may be part of the very same structure that is being shocked to create the synchrotron transient (and may be photoionized by the shock itself). The association between the source of free-free absorption and the local conditions around the transient makes free-free absorption (or the lack thereof) yet another tool that can be used to diagnose the nature of the transient. This thesis contains a few examples of free-free absorption as a diagnostic tool. In Chapter 3, I argued that in the transient VT 1210+4956, the lack of free-free absorption in the radio spectrum coupled with the high density of gas being shocked suggested that the gas was distributed in an aspherical geometry. The radio emission was being produced by a shock in a dense equatorial region, while much of the line of sight between the emitting region and Earth is filled with relatively low-density and high temperature shock-heated gas. In Chapter 4, I argued that the transient VT 1137-0337 is a powerful pulsar wind nebula that only appeared as a transient after decades because the surrounding supernova ejecta had become diffuse enough to permit the synchrotron emission to escape from within.

Perhaps the best example of the duality between propagation-induced selection effects and informative diagnostic tools is synchrotron self-absorption. Because synchrotron self-absorption occurs within the emitting region itself, it is ubiquitous in slow radio transients. As discussed at length in the literature (e.g., Roger A. Chevalier, 1998; Granot and Re'em Sari, 2002; Barniol Duran, Ehud Nakar, and Piran, 2013; A. Y. Q. Ho, E. Sterl Phinney, et al., 2019; D. Z. Dong et al., 2021), the frequency and luminosity of the peak where self-absorption balances emission can be used to infer the size and magnetic field strength of the emitting region. With some additional assumptions, the energy in the shock, the shock velocity, and the density of the gas being shocked can also be constrained.

As described above, the same propagation effects that can make radio transients difficult to detect or identify are actually very informative diagnostic tools for the transients and the environments around them. Much of the information gained by analyzing these features cannot be learned from observations at other wavelengths. In this way, slow radio transients provide a new window into the dynamic universe. But to look through that window, it is necessary to find the transients first. In the literature, there are three main ways in which this has be done: targeted follow-up of transients found at other wavelengths, serendipitous follow-up of these transients in radio sky surveys, and direct detection in radio sky surveys.

Targeted and Serendipitous Follow-up

Prior to VLASS, the vast majority of slow radio transients were found through *targeted follow-up* observations of transients first discovered in optical or high-energy surveys. This approach has advantages in transient interpretability, sensitivity, and flexibility. Targets are often prioritized on the basis of an established classification scheme (such as TDEs, GRBs, and the various classes of SNe), or unusual features (such as the rapid optical rise of fast blue optical transients; FBOTs). These classifications and features are often associated with physical models which provide a ready-made framework for interpreting any potential radio detection. Targets of high scientific value identified via these frameworks can also be observed for long periods of time. Such sensitive observations have enabled a number of discoveries, including deep constraints on the circumstellar gas density of Type Ia SNe (and therefore limits on the presence of stellar-wind-emitting companion stars; Chomiuk et al., 2016) and the detection of a faint ($\sim 50\mu$Jy) radio counterpart to a Type I superluminous supernova by Eftekhari, E. Berger, B. Margalit, Blanchard, et al. (2019). If they are detected, targets can be monitored to track their lightcurve and spectral evolution. If they are not detected, high-value targets can be monitored to see if they appear at late times. Observations making use of this flexibility in cadence include the discovery of a large late-time bump in the radio lightcurve of the Ic-broadline (Ic-BL) supernova PTF 11qcj indicative of structure in the circumstellar medium (Palliyaguru et al., 2019) and the discovery of a rapid and delayed rise from a jet in the TDE AT 2018hyz (Yvette Cendes et al., 2022).

However, despite their advantages, targeted follow-up observations provide an incomplete picture of radio transients as a whole. One major issue is that targeted observations are difficult to scale up in a systematic way. As an example, there have

been $O(10^5)$ supernovae discovered to date (Guillochon et al., 2017), while only $\sim$ 300 supernovae have targeted radio follow-up observations with ~90 total detections (see the compilation in Bietenholz, Bartel, et al., 2021). This gap is likely to widen even further with upcoming facilities such as the Vera C. Rubin Observatory (Ivezić et al., 2019), which is expected to increase the optical supernova discovery rate by an order of magnitude while the total amount of follow-up time and the survey speed of follow-up instruments remains roughly fixed. Large gaps can also be found for other transient classes such as black hole flares.

The scarcity of follow-up resources (both in telescope time and human time) imposes a strong and difficult to quantify selection bias on our understanding of radio transients. Sources that are not a-priori expected to be luminous radio emitters (e.g., due to a lack of observational precedent, theoretical predictions, early diagnostic features, or a combination of the above) are unlikely to be targeted for follow-up in the first place. Even if a target is selected for follow-up, it may be observed too early or too late to catch the radio emission (see e.g., discussions in Kate D. Alexander et al., 2020; Bietenholz, Bartel, et al., 2021, about the delayed emission observed in TDEs and SNe). Though this can be addressed by monitoring, doing so is expensive, further magnifying the challenges of scale.

Likewise, follow-up observations with current facilities often do not (or cannot) reach the depth required to detect the associated radio emission. Since (even in the absence of noise due to calibration, dynamic range, or confusion) the signal-to-noise ratio (SNR) of a given radio observation scales with observing time $t_{\rm obs}$ as SNR $\propto t_{\rm obs}^2$, a 100$\times$ increase in sensitivity over a 5 second observation would require 14 hours on source. This effectively caps the possible improvement in SNR to ~2 orders of magnitude before the required $t_{\rm obs}$ becomes cost prohibitive. Meanwhile, most classes of radio transients span much more than 2 orders of magnitude in intrinsic luminosity, making the likelihood of a detection more a function of the difficult-to-predict intrinsic luminosity rather than the time spent observing. For instance, type Ic broadline (Ic-BL) supernovae span at least 4 orders of magnitude in their ~few GHz luminosity from $\lesssim 10^{27}$ erg s^{-1} Hz^{-1} in most cases (Corsi, A. Gal-Yam, et al., 2016) to $\sim 10^{31}$ erg s^{-1} Hz^{-1} for the small fraction that harbor particularly powerful relativistic jets (A. J. van der Horst et al., 2007). Sensitivity will continue to be a limiting factor for follow-up of transients found with Rubin, which will increase the transient rate primarily by detecting sources that are located

at larger distances. Finally, some radio transients and potentially entire transient classes are not detected at all in current optical and high-energy detection surveys. This can be due to incomplete coverage in the detection surveys or a fundamental lack of luminous multiwavelength signatures at early times.

Some but not all of these issues can be addressed through *serendipitous follow-up* in radio sky surveys. By default, a wide-field radio survey will observe the location of every known transient that previously exploded in the area observed. This provides a measurement or constraint on each transient's radio emission regardless of whether it is expected to be radio luminous or not. The measurements are provided at a random distribution of post-explosion delays, closely tracking the inverse of the transient discovery rate. Though the distribution is skewed towards short timescales, there is far more coverage of older transients than can typically be found in targeted follow-up observations, substantially increasing the sample of observations at very late times. The measurements and constraints obtained through serendipitous follow-up are typically much shallower than those obtained through targeted follow-up. For instance, a single VLASS epoch reaches a 1σ RMS noise of $\sim 140\mu$Jy/beam, which is $\sim$1 order of magnitude shallower than typical follow-up observations with the Jansky VLA. However, even at this sensitivity, quite a few transients can be found. Recently, Stroh et al. (2021) checked the locations of $\sim 70,000$ optical supernovae observed before Epoch 1 of VLASS (2017 - 2019) and found 19 with late-time radio counterparts. Of these, 10 were not present in the Bietenholz, Bartel, et al. (2021) compilation likely due to a lack of follow-up observations. Notably, their sample includes a 5-decade-old supernova (SN 1965G, located in NGC 4162 at a distance of $\sim$42 Mpc) which to this day maintains a luminosity of $\sim 10^{28}$ erg s^{-1} Hz^{-1}, two orders of magnitude more luminous and 1 to 2 orders of magnitude more long-lived than values expected from SNe found in follow-up (Bietenholz, Bartel, et al., 2021).

One group of transients missed by both targeted and serendipitous follow-up is those without detected or identified multiwavelength counterparts. Whether these transients are intrinsically radio-only or just appear to be so due to gaps in survey coverage and detection/identification pipelines, they are often drawn from classes that are selected *against* by methods used in well-established transient detection surveys. In many cases, they are distinct from well-established transient classes, which makes them promising candidates for extending our knowledge of transient

phenomena in new directions. One of the most effective ways to find these transients is by detecting them directly in radio sky surveys and identifying them with contextual clues.

Direct Detection of Transients in Radio Sky Surveys

Direct detection of radio transients works in the way described in my observational definition of radio transients above. There must be at least one detection epoch in which a transient is detected, and at least one reference epoch in which it is not (or at least where it is significantly different in brightness than in the detection epoch). Successful direct detection requires several ingredients. First, the reference and detection epochs must be reasonably well-matched in sensitivity, frequency, and spatial scales covered. No matter how many transients are present in the detection epoch, they cannot be identified as such if, due to mismatches in the above qualities, you cannot make a strong case that they should have been detected in the reference epoch. Next, since radio transients are relatively rare, both the detection and reference surveys must cover a large area on sky in order to maximize the chance of finding sources within the observed region. For scale, VLASS detects sources at a density of ~50-100 sources per square degree (depending on what you consider an appropriate threshold of significance), and only a fraction of a percent of these sources are transients. Finally, the separation between reference and detection epochs must be reasonably well-matched to the typical duration of the transients you are hoping to detect. Just as ~years to decades is not the appropriate separation for detection of FRBs, ~days or even months is too short of a separation for most extragalactic transients (see e.g., Pietka, Fender, and Keane, 2015, for priors on the variability timescale for radio transients). The problem here is again one of identification; you might observe any number of slow transients in a survey, but if the separation between the first and last epochs is too short, their variability will be indistinguishable from measurement uncertainties and scintillation.

Much of the history of direct radio transient detection has centered around improving the sensitivity and areal coverage of the radio surveys, while keeping epochs relatively well-matched and testing different separations between epochs. This history is illustrated in Figure 1.1 (reproduced from Lacy et al., 2020), which compiles three decades of efforts from 1994 to 2016. Over the course of these decades, there were a number of important technological developments that led to improvements in these measures. At the VLA specifically[1], the WIDAR correlator (installed in

[1]The text here is VLA-centric, but it is important to note that other hardware upgrades are

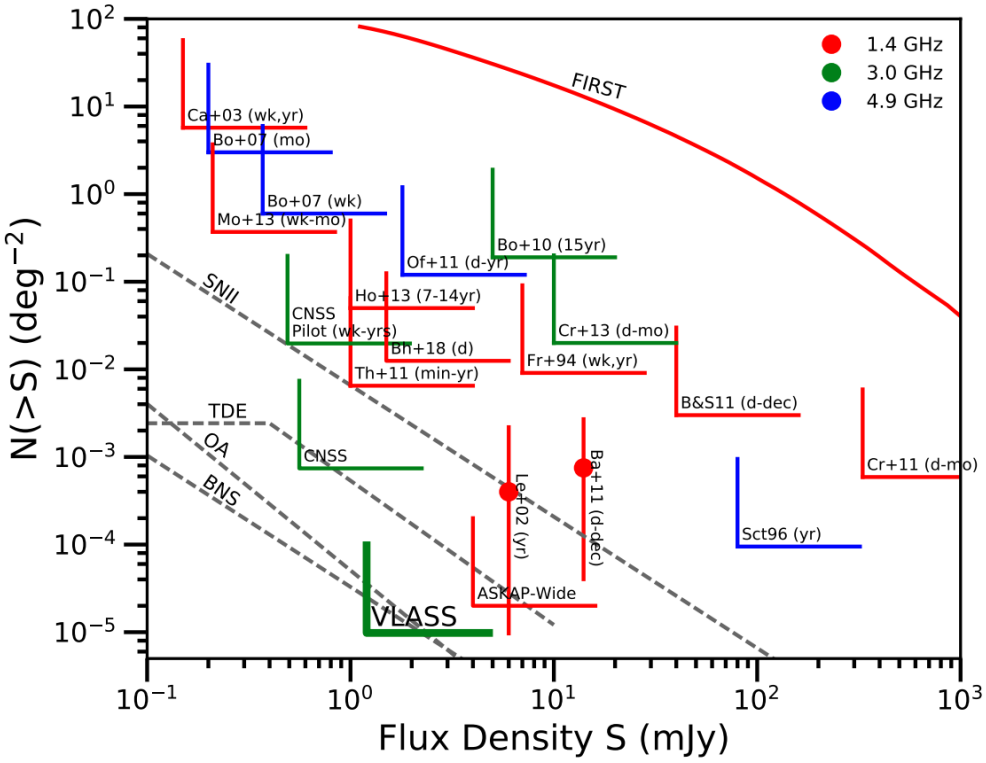

Figure 1.1: The sensitivity and inverse areal coverage of literature surveys used for radio transient detection. Reproduced from Figure 2 of the VLASS survey paper, Lacy et al. (2020).

2010) allowed for much larger instantaneous bandwidths to be observed than were previously possible. This dramatically improved the sensitivity of the instrument to continuum sources and thus reduced the time required to survey any particular area of sky. Another development was the commissioning of the on-the-fly (OTF) mapping observing mode at the VLA (Mooley, Myers, et al., 2019). This observational mode removed the overhead associated with physically re-pointing the VLA dishes and waiting for them to settle, in favor of taking continuous observations as the dishes are slewing and effectively repointing the array through the use of artificial electronic delays. OTF mapping is also used in VLASS, and is responsible for the effective 5-second-per-field integration time of the survey (which despite its short integration time can reach a reasonable sensitivity due to the WIDAR correlator and

continually being developed for radio interferometers around the world. One particularly impactful recent development is the installation of phased array feeds at the Australian Square Kilometer Array Pathfinder (ASKAP), which is undertaking a time-domain radio survey of its own (named VAST; T. Murphy, Shami Chatterjee, et al., 2013). We should expect to see more improvements along these lines in the near future.

other hardware updates).

A key argument for the use of OTF mapping in time-domain radio surveys comes from the tradeoff between surveying a wide field and taking deep observations. Most transient types are on average distributed isotropically, and uniformly in volume (aside for luminous Galactic transients which are concentrated in the Galactic plane). Under those assumptions, the number of transients found in a survey should scale with the volume probed: $N_{\rm trans} \propto V_{\rm survey} \propto A_{\rm survey} \times d_{\rm max}$, where $A_{\rm survey}$ is the total area covered by the survey and $d_{\rm max}$ is the maximum distance to which a transient can be detected and identified. The area covered by the survey can be increased simply by observing more fields, at a cost that is linear in observing time: $A_{\rm survey} \propto t_{\rm obs}$. This works up until the survey covers all 4π steradians of the sky. The maximum distance to which a transient can be *detected* can be increased by taking deeper images at a cost of $d_{\rm max} \propto t_{\rm obs}^{1/2}$. At larger distances, transient identification also typically becomes more challenging due to incompleteness in multi-wavelength catalogs used for cross matching. Altogether, it is far more efficient to increase $A_{\rm survey}$ instead of $d_{\rm max}$. This is the primary reason for using a technique like OTF mapping: for the same amount of observing time, your survey can detect far more transients by going wide instead of going deep. While OTF mapping cannot be used to go deep, it is one of the most efficient ways to go wide. As a shallow, all-sky survey, VLASS is optimized to do just that.

1.3 A quick summary of the VLA Sky Survey

VLASS is a survey of the entire northern sky accessible to the Jansky Very Large Array (everything north of declination -40°). It is split into 3 epochs (Epochs 1, 2, and 3), which are themselves split into two half-epochs (Epochs 1.1, 1.2, etc.). Epochs 1.1, 2.1, and 3.1 are repeated observations of the same 17,000 deg^2 and the same applies for 1.2, 2.2, and 3.2. At the time of writing this thesis, Epochs 1 and 2 have been fully observed, calibrated, and imaged, while Epoch 3.1 is scheduled to begin in January 2023.

Each half-epoch is timed according to the VLA's array reconfiguration schedule. Whenever the VLA switches into the second most extended configuration ("B configuration"), a half-epoch is observed. The array configuration results in a typical angular resolution (synthesized beam FWHM) of 2.5", and the time between repeated observations of the same field is ~2-3 years. VLASS is observed in an OTF

configuration where the effective integration time is 5 seconds per field, leading to a typical RMS noise of $\sim 140 \mu$Jy per beam in each epoch.

All VLASS observations are taken using the VLA's S band (2-4 GHz). S band data are recorded in 16 independently calibrated "spectral windows", which each span 128 MHz. Each spectral window contains 64 channels of width 2 MHz. All four Stokes products (I, Q, U, and V) are recorded, and will eventually be available in the fully processed "single epoch" images. At the moment, the available images are called "quicklook images" and are created in a manner that is computationally efficient but has not taken into account some of the finer details of radio image processing (such as w-projection). As a result, sources in the quicklook images have residual uncertainties of $\sim$10% in their fluxes and $\sim$0.5" in their positions after processing with my pipeline. Quicklook images are typically available a week or two after observation, and can be downloaded from `https://archive-new.nrao.edu/vlass/quicklook/`.

1.4 Outline of this thesis

In Chapter 2, I describe a search I ran for slow radio transients associated with galaxies within 200 Mpc that are present in VLASS but absent from the historical FIRST survey (Becker, R. L. White, and Helfand, 1995). In collaboration with fellow grad student Jean Somalwar, I used the resulting sample to characterize the demographics of extragalactic radio transients in the local universe. In exploring the individual transients within the 200 Mpc sample, my advisor Gregg Hallinan and I identified two of the transients as being observationally distinct from anything that had previously been identified. Chapters 3 and 4 discuss my in-depth exploration of these sources using multi-wavelength observations of the transients and their host environments, as well as order-of-magnitude theory. In both cases, I was able to argue that these two transients are not just peculiar; they're representatives of new transient classes (in one case, a merger between a compact object and a massive star, and in another, an emerging pulsar/magnetar wind nebula).

These results are what I have written up in the form of publications to date. However, I have also adapted the techniques I developed to identify transients in between VLASS epochs, as was the original intent in the survey design. That search has been a launch pad for new samples of flaring stars, tidal disruption events, AGN flares, Galactic transients, supernovae, and to-date unidentified hostless transients.

The analysis of these transients is currently being led by a number of people in the Caltech Radio Astronomy group, and I intend on publishing the catalog and leading some further analysis myself as a postdoc. In Chapter 5, I discuss the methods and initial results from this search. Finally, in Chapter 6, I look forward to what we can learn with results from 3 epochs of VLASS as well as next generation radio surveys such as the DSA 2000.

Chapter 2

A SYSTEMATIC SURVEY OF LUMINOUS, EXTRAGALACTIC RADIO TRANSIENTS IN THE $D_L < 200$ MPC UNIVERSE

To be submitted to the Astrophysical Journal *in two parts: one on the main survey, and one on CSM asymmetry in stellar explosions. D.Z.D. conducted the transient search, led the writing of the manuscript, and did much of the analysis. J.J.S. led the analysis of transient rates, host galaxy properties, and SMBH flares, and led the writing of the corresponding sections.*

Dillon Z. Dong[1], Jean J. Somalwar,[1], Gregg Hallinan[1], Yashvi Sharma[1], Carlos D. Ayala[1], Casey Law[1], Vikram Ravi[1], Andrew Hughes[2], Steven T. Myers[3]

[1] Division of Physics, Mathematics, and Astronomy, California Institute of Technology, Pasadena, California 91125, USA
[2] Department of Physics, University of Alberta, Edmonton AB T6G 2E1, Canada
[3] National Radio Astronomy Observatory, Socorro, NM 87801, USA

2.1 Abstract

We present a sample of 64 long-duration (∼years to decades) radio transients discovered in a systematic search for local-universe ($D_L < 200$ Mpc) extragalactic radio sources that appeared in the sky between the FIRST survey (1993-2011) and Epoch 1 of the VLA Sky Survey (2017-2019). In our sample, we find a sharp divide between off-nuclear transients (which have a $\sim 3\sigma$ excess of star-forming hosts relative to the overall prevalence of star-forming galaxies in SDSS) and nuclear transients (which have a $\sim 3\sigma$ deficit in star-forming hosts). Based on spectroscopy and imaging from optical sky surveys at the transient locations, we classify 31 transients as AGN flares, 3 as tidal disruption events, 29 as stellar explosions, and leave one unclassified. Due to the parameters of our search, our sample is likely dominated by powerful shocks that have been decelerated by dense circum-explosion environments. At their peak 3 GHz luminosity, these events should have characteristic radii of $O(0.1)$ pc, velocities of $O(10^3)$ km s^{-1}, and pre-shock densities of $O(10^5)$ cm^{-3}, though there is substantial room for variance within the sample. Plausible causes of the AGN flares include transient disk winds, frustrated sub-parsec jets, and other possibilities such as stellar explosions within the disks themselves. Flares with comparable radio luminosities and timescales should occur at a rate of ~ 1 transient per 100 years per

AGN. In our TDEs, we are likely seeing a population of lower-velocity outflows that produce long-lasting radio emission for up to ~a decade through interaction with the circumnuclear medium. Our results suggest that $\sim 1-30\%$ of TDEs eventually display such long-lived radio emission. The stellar explosions in our sample are likely dominated by supernovae interacting with asymmetric and dense circumstellar gas ejected by binary interaction in the ~decades to centuries before explosion. These terminal eruptions occur at a rate of up to $\sim 0.3\%$ of the core-collapse supernova rate.

2.2 Introduction

Extragalactic eruptions, such as stellar explosions and supermassive black hole (SMBH) accretion flares, can produce dramatic radio transients. These transients occur when large populations of charged particles are suddenly accelerated to relativistic speeds. In some cases, the particles are accelerated by shocks from newly launched jets traveling at large fractions of the speed of light. Such newborn jets have been observed from SMBHs in jetted tidal disruption events (TDEs) and active galactic nucleus (AGN) flares (e.g., Zauderer et al., 2011; Nyland, Dillon Z. Dong, et al., 2020; Yvette Cendes et al., 2022; Somalwar, Ravi, Dillon Z. Dong, et al., 2022), and during the birth of stellar mass compact objects in supernovae (SNe) and compact object mergers (e.g., Kulkarni, Frail, et al., 1998; G. Hallinan et al., 2017). In other cases, the accelerators are lower-velocity outflows that dissipate their energy by shocking dense circum-explosion gas. This has been seen in TDE outflows where the dense gas may be part of a complicated structure surrounding the black hole (e.g., M. M. Anderson et al., 2019; Kate D. Alexander et al., 2020; Somalwar, Ravi, D. Dong, et al., 2021) and SNe where the dense gas was likely ejected from the massive star in a period of intense pre-supernova mass loss (e.g., Margutti, Kamble, et al., 2017; Palliyaguru et al., 2019; D. Z. Dong et al., 2021). The full diversity of radio-transient-producing particle accelerators is just beginning to be uncovered.

The luminosity, evolution, and spectral features of a radio transient encode information about both the explosion and its immediate surroundings, much of which is inaccessible at shorter wavelengths. The most intrinsically luminous transients are produced by high-velocity shocks and/or high-density environments. At early times, this luminosity is often obscured by synchrotron self-absorption (SSA) or free-free absorption (FFA). In particular, a shock dominated by SSA can suddenly

become detectable once it expands to a sufficiently large radius, provided that it is still capable of accelerating a sufficient number of particles at that radius. This typically occurs when there is a dense reservoir of gas to shock at that radius. Likewise, a shock (or any other type of particle-acceleration region) dominated by FFA may suddenly appear if there is a rapid change in the external opacity. A decrease in free-free absorption may explain the appearance of radio emission in some supernovae surrounded by particularly compact and dense gas (e.g., Chandra, Roger A. Chevalier, N. Chugai, Fransson, et al., 2015) and has recently been seen in the emergence of an extremely radio-luminous nebula likely powered by an energetic neutron star within a shell of supernova ejecta (D. Dong and Gregg Hallinan, 2022). In both cases, there may be a delay of years or even decades before the radio emission becomes detectable.

To date, most radio transients with durations of ∼days to ∼decades have been found through targeted follow-up observations of transients first discovered in optical or high-energy surveys. Such follow-up has enabled a number of discoveries, including deep constraints on the circumstellar gas density of Type Ia SNe (and therefore limits on the presence of stellar-wind-emitting companion stars; Chomiuk et al., 2016) and the detection of a faint (∼50μJy) radio counterpart to a Type I superluminous supernova by Eftekhari, E. Berger, B. Margalit, Blanchard, et al. (2019), perhaps indicative of a central engine. Radio follow-up campaigns are, however, limited by available telescope time: it is not possible to follow-up every optically- or high-energy-selected event in the radio for years. Only targets that are perceived to have particularly high scientific value can have such extensive radio follow-up. The scarcity of follow-up resources (both in telescope time and human time) imposes a strong and difficult-to-quantify selection bias on our understanding of radio transients. Sources that are not a-priori expected to be luminous radio emitters (e.g., due to a lack of observational precedent, theoretical predictions, early diagnostic features, or a combination of the above) are unlikely to be targeted for follow-up in the first place. Even if a target is selected for follow-up, it may be observed too early or too late to catch the radio emission (see e.g., discussions in Kate D. Alexander et al., 2020; Bietenholz, Bartel, et al., 2021, about the delayed emission observed in TDEs and SNe).

Radio sky surveys provide a promising method of overcoming some of these difficulties. They can illuminate many transients that would not have been otherwise found,

such as those with no multiwavelength counterpart. Examples of transients that may be intrinsically radio-only include Galactic Center Radio Transients (GCRTs; Hyman, T. Joseph W. Lazio, Kassim, and Bartleson, 2002; Hyman, T. Joseph W. Lazio, Kassim, Ray, et al., 2005; Hyman, Wijnands, et al., 2009; Chiti et al., 2016; Wang et al., 2021), and Fast Radio Bursts (FRBs; see James M. Cordes and Shami Chatterjee, 2019, and references therein). Other examples that were not identified in detection surveys include VT 1210+4956, the radio afterglow of a compact object/massive star merger associated with a previously unidentified X-ray burst (D. Z. Dong et al., 2021), and VT 1137-0337, a luminous emerging radio nebula likely powered by a young neutron star where the associated supernova occurred a few decades ago (D. Dong and Gregg Hallinan, 2022). Radio transient surveys are also sensitive to those transients that were not classified by high-energy surveys as warranting follow-up. For example, Stroh et al. (2021) checked the locations of $\sim 70,000$ optical supernovae observed before Epoch 1 of VLASS (2017 - 2019) and found 19 with late-time radio counterparts. Of these, 10 were not present in the Bietenholz, Bartel, et al. (2021) compilation of supernovae with targeted follow-up.

The primary challenges faced by direct radio transient surveys are that they are typically not as sensitive as targeted follow-up and are subject to uncertainties in interpreting the transients because multiwavelength counterparts may not exist. These obstacles are orthogonal to those faced by targeted follow-up so, in spite of them, radio transient surveys will still probe a transient population complementary to that found through targeted follow-up. Moreover, these challenges are surmountable. The limited sensitivity will be overcome with future, more sensitive instruments. As seen with VT 1210+4956 and VT 1137-0337 among other examples, rich diagnostic information about radio transients can often be obtained through multi-wavelength follow-up observations even (and sometimes only) years after explosion.

In this paper, we present results from a direct search for radio transients in two surveys covering an overlapping area of ~ 10000 deg^2 and separated by $\sim$2 decades: the Faint Images of the Radio Sky at Twenty-Centimeters (FIRST; Becker, R. L. White, and Helfand, 1995) and Epoch 1 of the VLA Sky Survey (Lacy et al., 2020). In an effort to assemble a statistically significant sample while limiting selection biases, we restrict our search to sources associated with galaxies with a luminosity distance $d_L < 200$ Mpc. In Section 2.3, we discuss our transient selection procedure along with the sources of incompleteness, false positives, and selection biases,

which influence our final sample of 64 sources. We additionally provide validation for a subset of transients through association with archival transients and follow-up optical spectra. In Section 2.4, we present our scheme for assigning initial classifications to these transients using their host galaxy context. In Section 2.5, we compare those host galaxies with the overall population of $d_L < 200$ Mpc spectroscopic galaxies and identify some preliminary trends to be confirmed with larger future samples. In Section 2.6, we provide a joint fit for the volumetric rate and observed luminosity function of each class. In Section 4.7, we discuss the physical nature of transients in each sub class (stellar explosions, AGN flares, and TDEs). Finally, in Section 2.8, we summarize our results and discuss the implications for future radio transient searches.

Throughout this paper, we assume a flat ΛCDM cosmology where $H_0 = 69.6\,\mathrm{km\,s^{-1}\,Mpc^{-1}}$ such that our distance cutoff $D_L < 200$ Mpc corresponds to a redshift limit $z < 0.04487$ (Wright, 2006).

2.3 Sample Selection

The sample in this paper is from a new search of Epoch 1 of the VLA Sky Survey (VLASS; Lacy et al., 2020) for transients relative to the FIRST survey (Becker, R. L. White, and Helfand, 1995) associated with galaxies with luminosity distance $d_L < 200$ Mpc. Our search is very similar to an earlier version that we used to identify the transients VT 1210+4956 (D. Z. Dong et al., 2021) and VT 1137-0337 (D. Dong and Gregg Hallinan, 2022) and recovers both sources with high confidence. The main difference is that we have expanded our search to incorporate both halves of VLASS Epoch 1 and have substantially reduced our reliance on visual inspection in favor of automated filters.

Our new procedure can be briefly summarized as follows. We started with a source-extractor catalog of candidates found in the VLASS quicklook images. Using a combination of automated artifact filters and forced photometry, we removed the vast majority of image artifacts and faint FIRST sources. Then, to identify potential galaxy associations among the remaining transient candidates, we compared their locations against the fitted locations and light profiles of galaxies with spectroscopically confirmed luminosity distances $d_L < 200$ Mpc. Finally, we visually inspected radio and optical images of the remaining candidates and their locations to ensure that (1) they are bona-fide VLASS point sources with no discernible counterpart in

FIRST, and (2) show no indication of being background sources. This resulted in a sample of 64 likely extragalactic transients, which are shown in Figure 2.3 and listed in Table 2.2. In Section 2.3, we provide a detailed description of our new search. In Section 2.3, we provide quantitative estimates of our sample's incompleteness and false positive rates arising from observational selection biases. In Section 2.3, we discuss the physical selection biases arising from conducting a search at 3 GHz with epochs separated by ∼2 decades. We show how these biases can be used to set priors on the properties of the transients' emitting regions (which are generally confirmed in more detailed analysis of the stellar explosion sample; Section 2.7). Finally, a subset of the transients are confirmed by follow-up optical spectroscopy and/or association with archival transient counterparts. We discuss these counterparts in Section 2.3.

Transient Search Procedure

VLASS is a multi-epoch radio sky survey that is observing the entire sky accessible to the Jansky Very Large Array (VLA) (Dec ≥ -40°) 3 times over 8 years. VLASS Epoch 1 was observed in two half-epochs each covering ∼17,000 deg^2. The first half-epoch (Epoch 1.1) was observed from Sep 2017 to Feb 2018, and the second half-epoch (Epoch 1.2) was observed from Mar 2019 to Jul 2019. VLASS observations were taken in the VLA's B configuration with the 2 – 4 GHz S band receiver, leading to a typical angular resolution of ∼ 2". These observations used a recently commissioned mode of observing on the VLA called on-the-fly mapping (Mooley, Myers, et al., 2019), where the data are taken as the dishes are continually slewed. This mode of observing results in an effective integration time of ∼5 seconds per field, corresponding to a typical RMS noise of ∼140μJy. VLASS observations are calibrated and imaged by staff at the National Radio Astronomy Observatory, and initial quicklook images[1] are made publicly available for early science including transient searches. The latest versions of the quicklook images are corrected for systematic astrometric distortions induced by neglecting w-projection (M.Lacy; VLASS Memo 14). By cross matching these sources against sources with reliable astrometry from the Milliquas catalog (Flesch, 2021), we estimate that the median residual offset is ∼0.4 arcsec, with a scatter of ∼0.3 arcsec.

Our reference images come from the Faint Images of the Radio Sky at Twenty-

[1]VLASS quicklook images can be downloaded from `https://archive-new.nrao.edu/vlass/quicklook/` and viewed via a cutout server at `http://cutouts.cirada.ca/`.

cm (FIRST) survey (Becker, R. L. White, and Helfand, 1995). The FIRST field covers an estimated 10,575 deg^2 and is entirely contained within the area observed by VLASS Epoch 1. Roughly 80% of the FIRST observations are in the north Galactic cap, with right ascension (RA) between 8 to 17 hours and declination (Dec) between -10 and +65 degrees. These observations were taken between 1994 and 2005 with the pre-upgrade VLA (see R. A. Perley, Chandler, et al., 2011, for a description of the upgrade), using a pair of 21 MHz bandwidth spectral windows centered at 1365 and 1435 MHz. The remaining 20% of observations are in the southern Galactic cap, between RA = 21 to 4 hours, and Dec = -10 to +10 degrees. These observations were taken between 1995 and 2011, with a combination of the setup described above and a new setup with an early version of the upgraded VLA, using a pair of 128 MHz spectral windows centered at 1335 and 1730 MHz. In all cases, the integration times were chosen so that the RMS noise in the combined image of each field is $\sim$140μJy. All observations were taken in the VLA's B configuration, resulting in a typical resolution of $\sim$5.5". A list of sources brighter than 0.75 mJy in FIRST is publicly available through a catalog which has a typical astrometric uncertainty $< 0.5 - 1''$ (Richard L. White et al., 1997).

For this search, we used the Gordon, Boyce, Christopher P. O'Dea, Rudnick, Andernach, Vantyghem, Stefi A. Baum, Bui, and Dionyssiou (2020) and Gordon, Boyce, Christopher P. O'Dea, Rudnick, Andernach, Vantyghem, Stefi A. Baum, Bui, Dionyssiou, et al. (2021) catalog, which is compiled from the VLASS quicklook images using the source extractor `PyBDSF` (Mohan and Rafferty, 2015a). This catalog uses the default PyBDSF settings: `thresh_pix` = 5.0 and `thresh_isl` = 3.0 in the `process_image` task, which fits a set of Gaussian components to "islands" of pixels brighter than 3$\times$ the local noise σ which contain at least one pixel brighter than 5σ. It contains $\sim$3 million source components, which are a mixture of real sources and image artifacts. To remove duplicate sources, we applied their recommended setting *Duplicate_flag < 2*. However, as many of our previously identified transients (including ones confirmed by optical spectroscopy) would have been missed if we used their recommended artifact filters, we implemented our own filters described below.

The vast majority of VLASS image artifacts are drawn from two classes: sidelobes near bright sources from phase and amplitude calibration errors, and stripe artifacts (which are fainter sidelobes that extend in straight lines far from bright

sources). To remove the near sidelobes, we used a simple heuristic. We ran a forced photometry routine on the VLASS quicklook images at the location of each source candidate which measures the peak pixel within both a 2-arcsecond radius and a 30-arcsecond radius of the source location. Since sidelobes are always fainter than their parent sources (barring severe calibration errors that would be rejected by the VLASS quality assurance inspection), we remove all sources for which the 2 arcsecond peak is not also the 30-arcsecond peak. By visual inspection of ∼1000 image cutouts, we estimate that this method removes ∼100% of near sidelobes, while retaining ∼ 90% of real sources. To remove stripe artifacts, we use the *scikit-image* implementation of the probabilistic Hough transform (Kiryati, Eldar, and Bruckstein, 1991), which detects straight line features in input images. Using ∼3000 visually classified image cutouts, we tuned the parameters so that they provide a good compromise between removing stripes and retaining real sources in VLASS quicklook images. We estimate that our current implementation retains ∼90% of real sources while removing $\gtrsim$ 90% of stripe artifacts.

With a relatively clean catalog of VLASS sources, we then turned our attention to identifying transient candidates. We started by cross matching our VLASS catalog against the FIRST catalog using the *astropy* `match_coordinates_sky` function. We removed all sources separated by $>$ 1000 arcsec from the nearest cataloged FIRST source, since they are not within the area observed by FIRST. We also removed all sources separated by $<$ 2.5 arcsec (roughly half the size of the FIRST synthesized beam), since these sources are either the same as an already identified FIRST source, or would be blended with that source. At this stage, there are ∼300,000 sources that remain. To remove VLASS sources associated with faint or extended FIRST emission not identified in the catalog, we ran a forced photometry routine on the FIRST images at the location of each remaining VLASS source. Given that the FIRST pixel scale (1.8”) is larger than the quadrature sum of the FIRST and VLASS astrometric errors, we take the FIRST flux to be the value of single FIRST pixel nearest to the VLASS coordinate. Figure 2.1 shows the distribution of FIRST fluxes at the location of VLASS sources in comparison with FIRST fluxes measured in the same manner at 100,000 isotropic random positions in the field. We found that the random points have a roughly Gaussian flux distribution of $0^{+0.145}_{-0.145}$ mJy, while the VLASS source locations have a more complicated distribution incorporating both the random Gaussian and an extended distribution of fluxes tapering off at the catalog threshold (∼0.7 mJy). Random positions within

6" of a galaxy nucleus (drawn from the catalog described below) but separated by >2.5" from a cataloged FIRST source have a similar flux distribution: $0.03^{+0.18}_{-0.15}$ mJy. To exclude faint FIRST sources while retaining FIRST nondetections, we removed VLASS sources for which the corresponding FIRST flux is > 0.36 mJy, corresponding to the 99th percentile flux for random points and the 94th percentile of random points near galaxies. After this filter, we were left with a catalog of ~36,000 transient candidates with no clearly detected counterparts in FIRST.

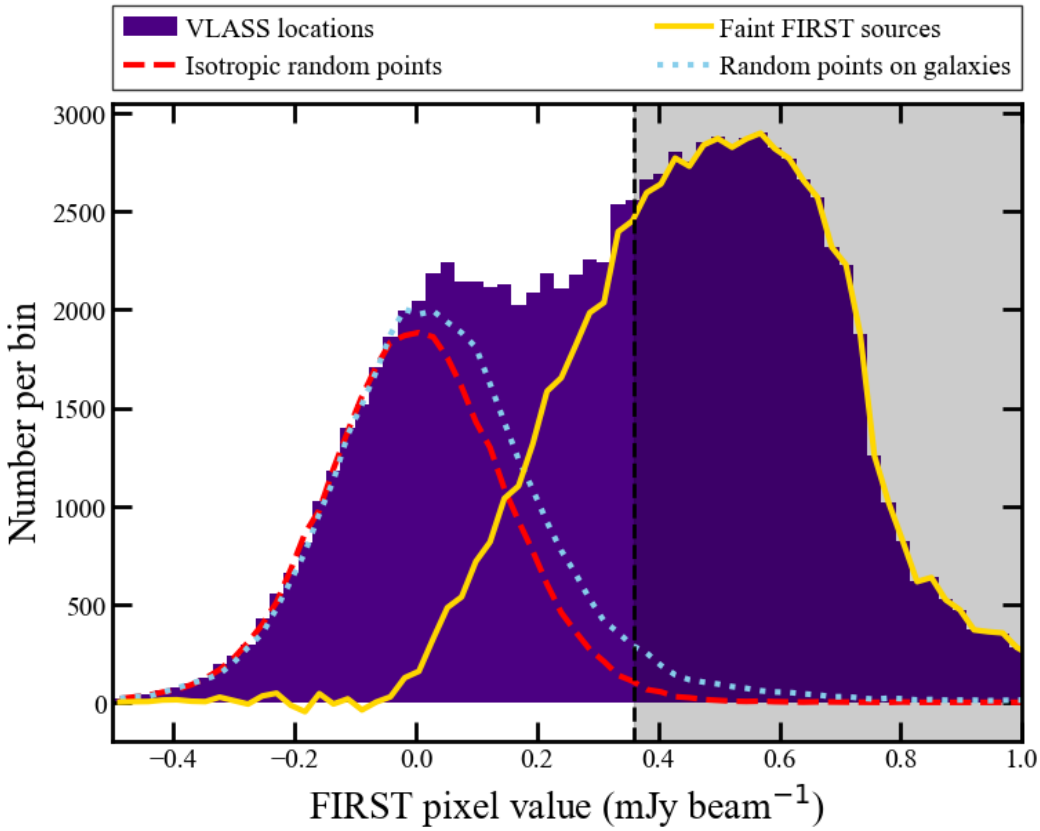

Figure 2.1: The distribution of FIRST fluxes at the location of VLASS sources that pass automated artifact filters (purple histogram) in comparison with FIRST fluxes at isotropic random points (dashed red line) and FIRST fluxes at isotropic random points separated by $\Delta\theta < 6''$ from a $D_L < 200$ Mpc galaxy (dotted blue line). The difference between the distributions (gold line) is primarily due to faint sources present in FIRST that fall below the 5σ FIRST catalog threshold. We remove all transient candidates with corresponding FIRST fluxes greater than 0.36 mJy (in the gray shaded region). This threshold corresponds to the 99th percentile for all isotropic random points, and the 94th percentile for those near galaxies.

Most of the remaining transient candidates are comprised of bona-fide transients,

highly variable sources, gigahertz peak spectrum (GPS) sources (typically AGN; e.g., C. P. O'Dea, S. A. Baum, and Stanghellini, 1991), and residual artifacts that are uncorrelated with the positions of local universe galaxies. However, a small subset are produced by objects (black holes, stellar explosions, etc.) residing in those galaxies, and should be co-located with the light produced by those galaxies. To identify this subset, we assembled a catalog of all galaxies with spectroscopic redshifts $z < 0.045$ in the Sloan Digital Sky Survey (SDSS) Data Release 17 (Abdurro'uf et al., 2022) and the NASA Extragalactic Database[2] (NED), corresponding to a luminosity distance of 200.6 Mpc with our adopted cosmological parameters (Wright, 2006). Using galaxy profile fits from the Dark Energy Camera Legacy Survey (DECaLS; Blum et al., 2016; Lang, 2020) and PanSTARRS Data Release 2 (Magnier et al., 2020), we approximated the 2D on-sky projection of each galaxy as an ellipse with semi- major and minor axis half-light radii a and b corresponding to an eccentricity $e = \sqrt{1 - (b/a)^2}$. The direction-dependent radius $r_{\rm half}(\phi)$ of such an ellipse is given by $r_{\rm half}(\phi) = b/\sqrt{1 - (e\cos\phi)^2}$, where ϕ is the angle measured counterclockwise from the semi-major axis in the direction of interest.

To test the transient candidates for galaxy association, we computed the angular offset $\Delta\theta$ between each candidate and the nuclei of the 5 nearest cataloged galaxies. To take into account galaxy shapes, and to place nearby galaxies with larger angular extents on a more equal footing with smaller, more distant galaxies, we normalized these 5 offsets by the corresponding galaxy's elliptical radius in the direction between the galaxy nucleus and transient candidate $r_{\rm half}(\phi)$. We took the galaxy with the smallest normalized elliptical offset $r_{\rm norm} = \min(\Delta\theta/r_{\rm half}(\phi))$ to be the one that is most likely to be associated. Figure 2.2 shows the distribution of $r_{\rm norm}$ for transient candidates that pass our automated filters, relative to a simulated distribution for isotropically-distributed random points in the FIRST field. For large values of $r_{\rm norm} \gtrsim 5$, the expected number per bin for random points matches the observed value to within ∼15 percent. This suggests that, as expected, the transient candidate catalog as a whole is consistent with being located at random positions relative to local universe galaxies. However, at $r_{\rm norm} < 2$, there is a factor of $\sim 3\times$ excess of transient candidates, which rises to 1-2 orders of magnitude at $r_{\rm norm} \lesssim 0.5$. This strong excess of candidates with low $r_{\rm norm}$ cannot be explained by chance alignment of foreground or background sources. Instead, they are best explained by sources

[2]The NASA/IPAC Extragalactic Database (NED) is funded by the National Aeronautics and Space Administration and operated by the California Institute of Technology.

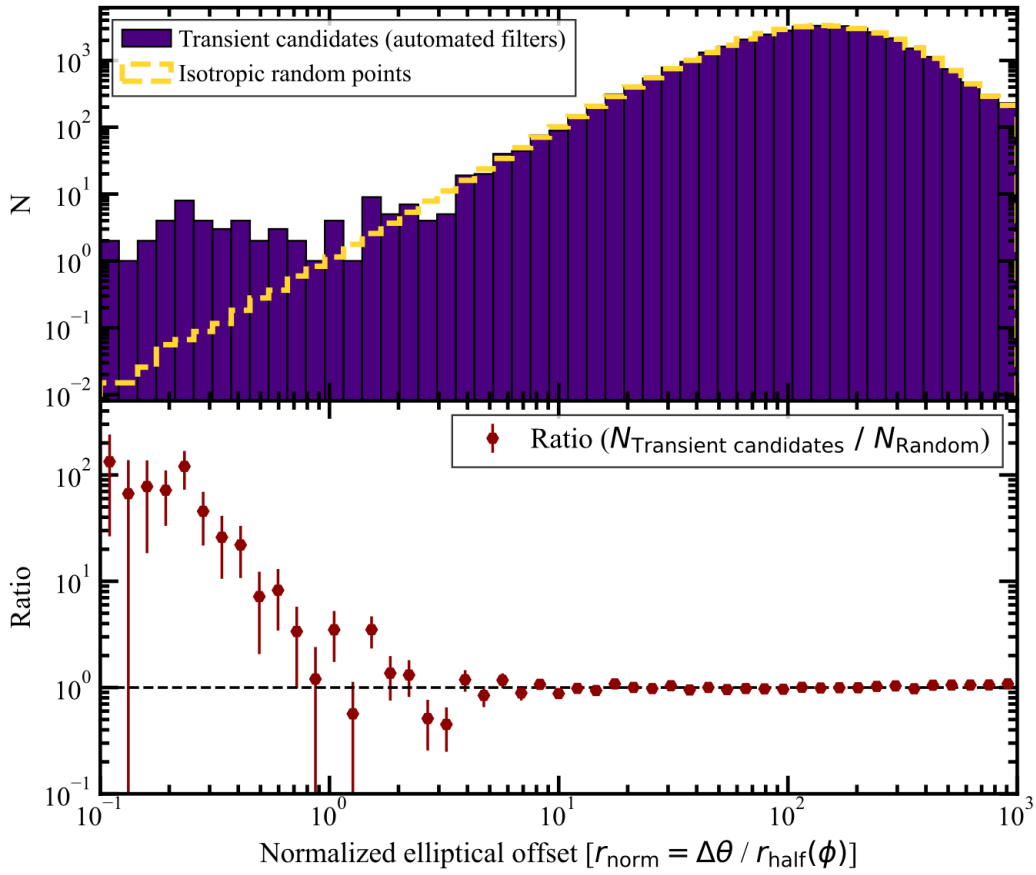

Figure 2.2: The offset distribution (purple histogram) of transient candidates (sources passing both automated artifact filters and the faint FIRST source cut) relative to $d_L < 200$ Mpc galaxies. The normalized elliptical offset $r_{\text{norm}} = \min(\Delta\theta/r_{\text{half}}(\phi))$ is defined in the text. The gold line shows the offset distribution for 17 million simulated random points in the FIRST field, weighted to match the size of the transient candidate catalog. The bottom panel shows the ratio of the transient candidates to the random points. The 50 bins are spaced logarithmically between $r_{\text{norm}} = 10^{-1}$ and $r_{\text{norm}} = 10^{3}$.

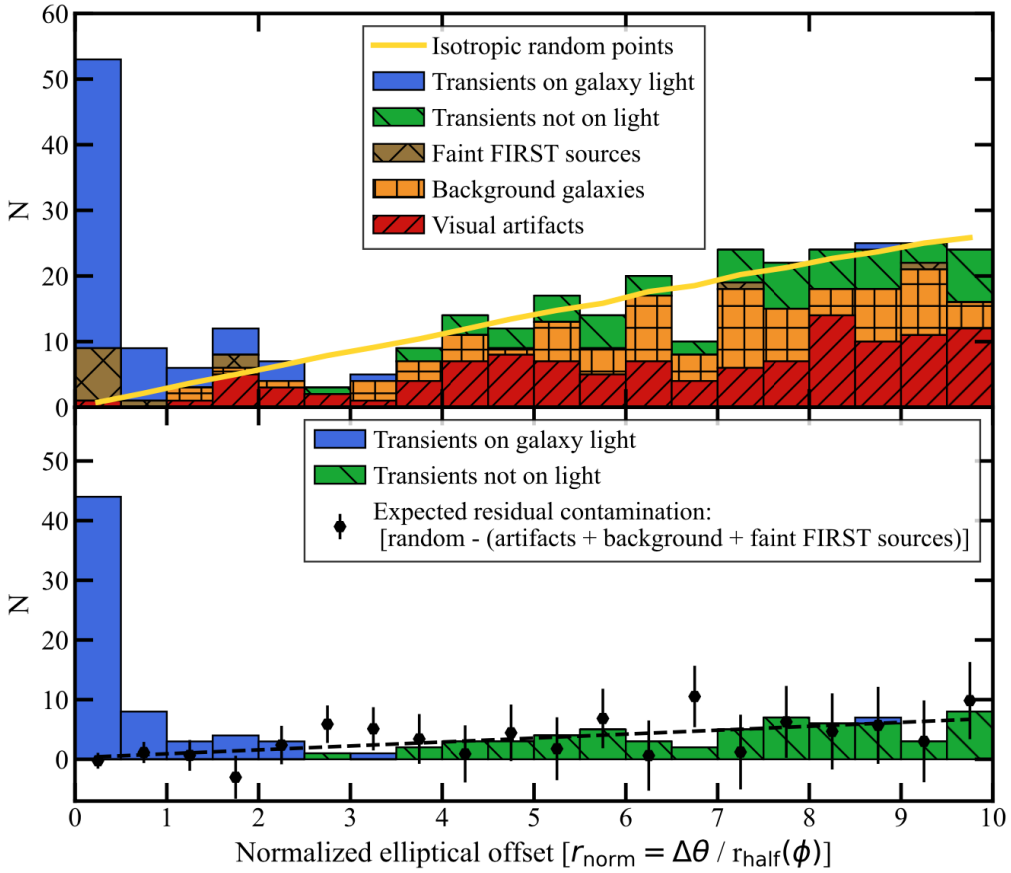

Figure 2.3: **Top:** A visual inspection based characterization of all transient candidates with a normalized elliptical half-light radius offset < 10 from the nearest $d_L < 200$ Mpc galaxy. Remaining artifacts are shown in red, transient candidates located on clumps of light ("background galaxies") distinct from their claimed hosts are shown in orange, and residual faint FIRST sources not falling under the above categories are shown in brown. Transients passing all our visual checks are shown in blue if they are co-located with their galaxy's light and green if not. The solid yellow line is similar to the one in Figure 2.2, showing the expected offset distribution for a set of isotropic random points of the same size as our transient candidate catalog. **Bottom:** Same as above except without the artifacts, background galaxies, and faint FIRST sources. The black points show the expected number of residual chance coincidences, estimated by subtracting the artifacts, background galaxies, and faint FIRST sources not astrometrically consistent with the host galaxy's nucleus from the expected chance coincidences. Errorbars assume Poisson uncertainties in each category. The dashed black line is a least squares fit to the black points.

associated with the galaxies themselves.

At this point, our automated procedures have reduced the search space from ∼3 million VLASS source candidates to a few hundred transient candidates with low $r_{\rm norm}$. These few hundred sources contain nearly all of VLASS vs FIRST transients associated with spectroscopically verified local universe galaxies (Section 2.3). With this downselection, it is straightforward to visually inspect each candidate in an effort to identify the bona-fide transients. We started by taking every candidate with $r_{\rm norm} < 10$ (n = 428), which is a conservative cut, well within the regime of random alignments (Figure 2.2). By visual inspection of the VLASS and FIRST images, we identified all of the remaining artifacts missed by our filters. We also identified and removed 7 clear instances of faint FIRST sources missed by our 0.36 mJy cut (due to rare systematic errors in the FIRST astrometry of ∼2 to 5"). We then used the DECaLS sky browser to identify which of the remaining sources are (a) coincident with the light of their candidate host galaxy, (b) nearby their candidate host but not coincident with the detected light, or (c) associated with an unassociated photometric object (typically red and faint), which we consider to be a likely background galaxy. Figure 2.3 shows the distribution of $r_{\rm norm}$ for each of these categories. We find that most of the expected chance coincidences (as modelled with the simulated random points) can be explained by a combination of artifacts and sources associated with background galaxies. The remaining expected chance alignments are mostly due to "hostless" transients not associated with the galaxy light (which may be from background objects fainter than the DECaLS detection thresholds of g ∼ 24.7, r ∼ 23.9, and z ∼ 23.0). Given this, we adopt a final selection criterion for our sample of $r_{\rm norm} < 2.5$ and a location coincident with the host galaxy's light. Our final sample contains 64 likely galaxy associated transients, summarized in Table 2.2.

Selection Effects

Our transient sample is subject to a number of selection effects which can cause some transients to be missed (false negatives) and some transients to be misidentified (false positives). Below, we list the primary selection effects and briefly discuss their influence on our sample, starting with the causes of false negatives.

1. The transient must be identifiable as a $\geq 5\sigma$ source with PyBDSF in the Epoch 1 VLASS quicklook images. In most cases, this amounts to (1) having

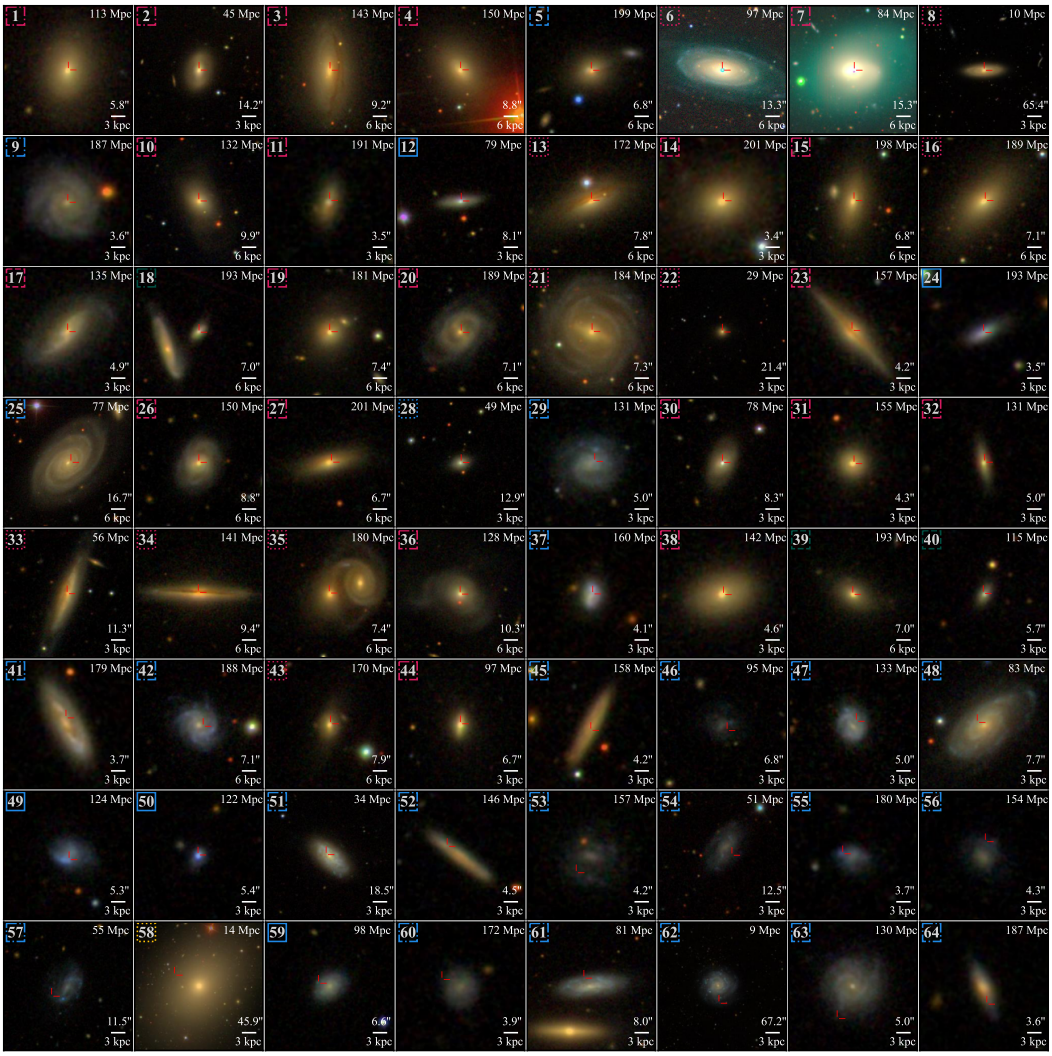

Figure 2.4: The host galaxies of our final transient sample in order of increasing normalized elliptical offset (r_{norm}). Each transient's ID number is given in the top left corner of its subplot, and its location is indicated by the red crosshairs. Each subplot's sidelength is fixed to a physical scale of either 30 or 60 kpc (indicated by a 3 or 6 kpc scale bar). The equivalent angular size in arcseconds is given above the scale bar. The luminosity distance to each galaxy is given in the top right corner. Image cutouts are taken from SDSS DR17, with the exception of IDs 6 and 7, which are not in the SDSS field and have cutouts taken from DeCALS DR9. The color of the box around the transient ID corresponds to its classification and its linestyle indicates our level of confidence in the classification. Blue boxes indicate stellar explosions, red boxes indicate AGN flares, green boxes indicate TDEs, and yellow boxes indicate unknown or ambiguous classifications. Solid boxes indicate "very high confidence" classifications confirmed with optical transient counterparts or other detailed analysis. Dash-dot boxes indicate "high confidence" classifications with low ambiguity according to our classification scheme (Section 2.4), dashed boxes indicate "medium confidence" classifications (typically from spectra with ambiguous BPT ratios), and dotted boxes indicate "low confidence" classifications made with low-quality or otherwise incomplete data.

a shape that can be reasonably described with a Gaussian (as should be the case for any point source barring severe calibration errors that would be rejected by the NRAO's quality assurance inspection), and (2) having a flux density $\gtrsim 0.7$ mJy at the time of observation. In some areas of the survey, the effective sensitivity is better (up to ~0.5 mJy) while in other areas, it can be substantially worse (particularly around bright sources). We will present a detailed sensitivity analysis in an upcoming paper (Dong et al., in prep), but in this paper, we assume a uniform sensitivity of 0.7 mJy.

2. It must pass our automated artifact filters. This requires that (1) the local noise is not dominated by a stripe passing through the position of the transient, and (2) the transient must be the brightest source within 30". We will present a more detailed analysis of the artifact filtering and its effects in Dong et al. in prep, but for now, we note that the combination of these two filters removes ~20% of total sources, and visual inspection of a random sampling of removed sources suggests that > 90% are artifacts. Based on this, we estimate that only a few percent of real sources are removed by this filtering. We do not expect that real sources that happen to be transient would be disproportionately affected.

3. The transient must have a corresponding single-pixel flux density in FIRST of < 0.36 mJy. This filter was designed to remove GPS sources and variable background AGN, since otherwise this population would dominate our sample. As shown in Figure 2.1, our chosen threshold should reject $\lesssim 6\%$ of transients if the transients are located in random positions on $d_L < 200$ Mpc galaxies. However, this may be an underestimate since our sample is primarily located on galaxy nuclei and off-nuclear HII regions (Figure 4.6), which can both have brighter quiescent radio emission than random locations in the galaxy.

   For off-nuclear HII regions, the anti-selection is likely to be rather weak, since throughout most of our searched volume, even the most luminous regions are unlikely to be detectable in FIRST. For scale, our FIRST flux threshold 0.36 mJy maps to a 1.4 GHz luminosity $L_\nu = 4\times10^{27}\left(\frac{d_L}{100\ \mathrm{Mpc}}\right)^2$ erg s^{-1} Hz^{-1}. This luminosity corresponds to a star formation rate of $\sim 1.8\left(\frac{d_L}{100\ \mathrm{Mpc}}\right)^2 M_\odot\ \mathrm{yr}^{-1}$ for pure free-free emission (which is expected on scales of individual HII re-

gions; Linden et al., 2020) and $\sim 0.25 \left(\frac{d_L}{100\ \mathrm{Mpc}}\right)^2 M_\odot\ \mathrm{yr}^{-1}$ for a mix of free-free and synchrotron emission (E. J. Murphy et al., 2011). By comparison, the most luminous giant star-forming complexes in the (Bradley et al., 2006) have Hα luminosities $\sim 10^{41}$ erg s^{-1}, corresponding to star formation rates of $\sim 0.05\ \mathrm{M}_\odot\ \mathrm{yr}^{-1}$. Altogether, only extremely luminous off-nuclear star-forming regions in nearby galaxies (at distances $\lesssim 30$ Mpc) should be excluded by our FIRST threshold. This region comprises $< 1\%$ of our searched volume.

The anti-selection should be much stronger for galaxy nuclei, where there may be low-level emission from an AGN on longer timescales than probed by our search, and where the synchrotron fraction from star formation is typically higher (so a lower star formation rate is required to produce the same radio luminosity; e.g., Tabatabaei et al., 2013; Linden et al., 2020). The scale of this selection effect can perhaps best be quantified by considering all variable sources, not just ones that are completely undetected in the reference epoch. However, the frequency mismatch between FIRST and VLASS makes it difficult to disentangle the intrinsic spectral index of the emission and the level of variability. We therefore defer analysis of this selection effect to a future paper on nuclear flares compared between VLASS epochs, and instead note that our search is likely underestimating the prevalence of nuclear flares in galaxies with intense nuclear star formation and previous epochs of AGN activity.

4. The transient must be located within 2.5 elliptical half-light radii of a galaxy with a spectroscopically confirmed redshift $z < 0.045$. Two types of bona-fide transients may be filtered out by this selection: (a) ones where the host galaxy do not have a redshift in NED or SDSS, and (b) ones with large offsets from the galaxy's nucleus.

   As an estimate of Selection (a)'s effects, Kulkarni, D. A. Perley, and Miller (2018) find that $\sim 65\%$ of type Ia supernova hosts with redshfits $z < 0.045$ have redshifts available in NED. This suggests that for the massive and/or rapidly star-forming galaxies traced by type Ia supernovae, our search is no more than $\sim$40% incomplete due to lack of host spectra.

   There is an additional selection against faint galaxies due to the targeting criteria of spectroscopic surveys. In particular, due to the SDSS legacy sample,

our search should not miss hosts with apparent r-band Petrosian magnitudes $r_p < 17.77$. One example of a galaxy barely making the completeness cut is the host of ID 56 (VT 1210+4956), a dwarf star-forming galaxy (stellar mass $\sim 10^{9.2} M_\odot$, star formation rate $\sim 0.4 M_\odot$ yr^{-1}) at luminosity $d_L = 154$ Mpc with $r_p = 17.75$. There is sporadic coverage for fainter galaxies due to other surveys (including other SDSS samples). One example is the host of ID 55 (another dwarf star-forming galaxy at $d_L = 180$ Mpc), which does not have a spectrum on its nucleus because its Petrosian magnitude $r_p = 18.15$ falls slightly below the SDSS targeting cut. This galaxy does, however, have an SDSS spectrum because of a bright blue knot at its edge which was targeted by the SDSS Baryonic Oscillation Spectroscopic Survey (BOSS; Dawson et al., 2013) due to being a possible quasar. This knot, which happens to also be the location of the radio transient, turned out to be a luminous HII region associated with the galaxy, adding the galaxy to our spectroscopic catalog and providing additional evidence for the ID 55's host galaxy association.

As a handle on Selection (b), Figure 2.3 shows that our elliptical offset filter selects heavily for sources co-located with the light of their corresponding galaxies. A similar circular half-light radius cut (i.e., not taking into account galaxy shapes) on the Fong and E. Berger (2013) sample would retain ~95% of optically selected core collapse supernovae, and slightly lower percentages of much rarer classes: ~75% of long gamma ray bursts (GRBs) and ~65% of short GRBs. While this comparison is not entirely straightforward (due in part to the much higher typical redshift of the SN and GRB sample), it does suggest that the vast majority of transients with host-offset distributions similar to known classes should be retained by our galaxy-association cut if they would have otherwise been detected. We note that there is an additional bias against offset sources in centrally concentrated galaxies, for which the half-light radius might underestimate the true extent of the galaxy.

5. Finally, the transient must pass our visual inspection, meaning that it is (1) not visually identified as an artifact, (2) not associated with a visually identifiable faint FIRST source missed by our cut, and (3) not associated with a clump of light that is visually distinct from the galaxy (i.e., likely to be a background galaxy or a different galaxy than the spectroscopically confirmed one).

Selection (1) is fairly innocuous; VLASS quicklook artifacts are reasonably

easy to identify by eye, and while some fainter sources may be mistaken for artifacts, this is not likely to lead to a large percentage of false negatives.

Selection (2) catches instances where, due to astrometry issues, the FIRST and VLASS positions are offset by enough (typically ∼1") to shift the peak of a faint FIRST source to a different pixel than the VLASS peak. These instances are also typically readily identifiable. There are some ambiguous cases where low-level extended emission from star formation can be seen. To avoid this, we have taken care to only remove cases where there is a distinct point source not surrounded by extended emission. We do not anticipate that this selection is a major source of false negatives.

Selection (3) is designed to directly remove transients associated with background galaxies, which are our main source of false positives. In most cases, these clumps of light are significantly redder than the nearby galaxy, suggesting that they are AGN at much higher redshift. In other cases, the source is located on a galaxy with no spectrum that could plausibly be within 200 Mpc. We remove these cases since we cannot verify their distance with publicly available data.

Altogether, we estimate that our sample contains $\gtrsim$ 50% of the ∼mJy, decade-timescale, extragalactic radio transients in the $z < 0.045$ FIRST footprint. The dominant cause of incompleteness in our search is limitations in using spectroscopic galaxy catalogs. Some specific classes of transients are disproportionately likely to be missed. These include: transients in areas with underlying AGN activity or extremely intense star formation, transients with large offsets from their host galaxies (particularly ones with strong central concentrations), and transients in very faint galaxies (including both field galaxies and satellites of larger galaxies). In Section 2.8, we will discuss ongoing and future efforts to address these sources of incompleteness.

Having estimated the prevalence and types of false negatives, we now discuss the likely sources of false positives: sources in our sample that pass our cuts but may not be true $d_L < 200$ Mpc transients. There are two ways for a source to be misidentified: (1) the source might be in the foreground or background and aligned coincidentally with its claimed host, or (2) the source might not be a bona-fide

transient.

1. We first estimate the number of coincidental galaxy alignments. Based on the simulated isotropic points, we expect that out of the 36,625 transient candidates that pass our automated filters, 17.9 ± 4.2 sources should pass our $r_{\rm norm} < 2.5$ cut by chance. As shown in Figure 2.3, visually identified artifacts can directly account for 10 of these, while 4 can be accounted for by optical background galaxies, and a further 3 can be accounted for by faint FIRST sources not already identified with a background galaxy. This leaves $0.9^{+4.2}_{-0.9}$ expected remaining chance alignments, corresponding to ∼0-8% of our sample.

2. We now estimate the prevalence of non-transients in our sample. There are two primary ways by which a source in our sample might not be a true transient: it might (a) be a low-SNR noise spike rather than a legitimate source (e.g., Frail, Kulkarni, E. O. Ofek, et al., 2012), (b) it might be a gigahertz-peak AGN (GPS source) where the rising spectrum between the 1.4 GHz FIRST frequency and the 3 GHz VLASS frequency is *entirely* responsible for the difference in flux between FIRST and VLASS.

   For scenario (a), random noise spikes should have positions that are uncorrelated with the locations of $d_L < 200$ Mpc galaxies and, as discussed above, we have already identified nearly all of the chance coincidences. If any remain in our sample, they should be faint ($\sim 5\sigma$), preferentially offset from their host galaxies, and not detected in VLASS Epoch 2. The four candidates that satisfy these conditions are IDs 52, 54, 59, 63. We cannot directly verify IDs 52, 54, and 63 with current data, but as discussed in Section 2.3, ID 59 is confirmed to be a supernova through follow-up optical spectroscopy. Altogether, scenario (a) likely accounts for $\lesssim 5\%$ of our sample, and all of this percentage counts toward the 0 - 8% estimated for chance alignments.

   For scenario (b), we start by noting that GPS sources can also be transient hosts. For instance, an AGN with some relic emission from a previous episode of activity (the GPS source) may undergo a new outburst (the transient). In that case, there is an associated transient and we have simply overestimated its luminosity by a factor of a few due to the GPS contribution. In some cases, the outburst may be enhanced by refractive scintillation. However as we will

discuss in Section 2.3, the magnified part of the emission would have to be on a physical scale of $\lesssim 10^{-2}$ pc. Shocks on that small of a scale are very likely due to a transient outflow (Section 2.7).

Given this, the scenarios that we would consider false positives are where the GPS source is in the background of the galaxy, or where the source is truly non-varying. With our chance coincidence constraints, we have already accounted for GPS sources in the background of our galaxies. The remaining GPS sources should be associated with the nuclei of the galaxies themselves. We expect that such GPS sources should be (1) astrometrically consistent with their host galaxies' nuclei, (2) have indications of AGN activity, and (3) have variability between VLASS Epoch 1 and Epoch 2 consistent with measurement error. In our sample, 5 sources (IDs 1, 2, 15, 27 and 44) fit these criteria, while 10 more (IDs 6, 8, 10, 13, 16, 23, 26, 27, 28, 34) have insufficient data or ambiguous AGN indicators. We note that even sources that fit all 3 criteria may be transients with durations much longer than the ∼2 year span between Epochs 1 and 2, particularly given that we are selecting for sources with variability on ∼decade timescales. We thus estimate that $\lesssim 15$ sources in our sample, or $\lesssim 23\%$ are non-transient GPS sources.

Priors Set by our Survey Parameters

Our final sample consists of sources in the 3 GHz luminosity range 10^{26} - 10^{30} erg s^{-1} Hz^{-1} that appeared in the ∼20 years between FIRST and VLASS Epoch 1. While that information alone is not enough to confidently diagnose the properties of any *individual* transient, our transient search is inherently more sensitive to certain transient-producing *physical conditions*. We can therefore use this information to make some order-of-magnitude generalizations about the population that we are selecting as a whole.

1. **Due to causality, all of our transients come from compact ($\lesssim$ 6 pc) regions.** Sources in our sample have brightened substantially (typically of order their own flux) on a timescale of ∼20 years. There are three ways by which this can happen, which all require a compact emitting region.

   (1a) If the source brightened due to some physical change in the emitting region itself (e.g., a star exploded and shocked its surroundings, or a black

hole launched an outflow that did the same), all parts of the brightening region are causally linked to the explosive event. In those cases (ignoring relativistic effects), the size of the region responsible for the transient emission must be smaller than a sphere of radius $c \times 20$ years ~ 6 pc.

(1b) If instead the source only appeared to brighten because of a nearby obscuring cloud moving away (as has been proposed for e.g., changing look AGN) or becoming optically thin (e.g., emerging pulsar wind nebulae), the changing part of the cloud is also limited by causality to be smaller than ∼6 pc. Because the distance between the obscuring cloud and the emitting region is much smaller than the distance between the cloud and Earth, geometry dictates that the cloud must be of order the size of the emitting region (or larger). In that case, the emitting region is still smaller than the ∼6 pc limit set by causality.

(1c) If the source brightened due to scintillation, the region whose size is limited by causality is a patch of the Milky Way's ISM, unrelated to the emitting region. Somewhat non-intuitively, this sets an *even more stringent* upper limit on the size of the emitting region. Refractive scintillation is suppressed when the source has an angular size larger than the size of the scattering disk. Over most of the sky, the disk size at 3 GHz is ∼a few microarcseconds (Walker, 2001), corresponding to $\sim 10^{-2}$ pc at our maximum searched distance of 200 Mpc. In the plane of the Galaxy, the disk size is larger due to the higher transition frequency, but due to that high frequency itself, the modulation index drops to ≈ 0. In that case, scintillation cannot explain the transients which returns us to cases (1a) and (1b) (Walker, 1998).

2. **The compactness likely requires that the radio emission is due to synchrotron emission.** The typical lower-limit brightness temperature set by the causality size constraint for transients in our sample is $\sim 10^6$ K. While this alone does not preclude free-free emission as an explanation for our transients, more detailed analysis (see e.g., Appendix A of D. Dong and Gregg Hallinan, 2022) shows that creating such an expanding nebula requires extreme (and potentially unphysical) temperatures, densities, and energies, such as a sphere of temperature 10^{10} K and density 10^7 cm^{-3} expanding outwards at 10,000 km/s for 20 years, requiring an energy of $\gtrsim 10^{55}$ erg. For the remainder of this section, we therefore make the self-consistent assumption that our transients

are produced by synchrotron emission.

3. **Our search is biased toward transients with longer detectable durations (up to ∼20 years) and spectral peaks ∼3 GHz.** Our two-epoch transient search essentially takes a snapshot of all the transients in the sky at a random point in their evolution. In order to detect a transient, we have to be lucky enough to observe it while it has a 3 GHz flux brighter than our detection limit. The probability of observing a transient while it is detectable is proportional to the time it spends above the detection limit. Thus, we are biased toward detecting longer duration transients. This effect starts to "saturate" at approximately the ∼20 year timespan between FIRST and VLASS. The longer the duration past that timespan, the more likely it is that the transient was already detectable in FIRST (and would thus be misidentified as a variable/GPS source and rejected by our search procedure).

   Synchrotron transients observed at radio frequencies have a spectral peak set by free-free or synchrotron self-absorption. This peak evolves with time, typically dropping to lower frequency as the emitting region expands (e.g., Roger A. Chevalier, 1998). As the peak frequency $\nu_p(t)$ drops toward 3 GHz, the 3 GHz lightcurve will start to sharply rise by a large factor $\approx \left(\frac{\nu_p(t)}{3\text{GHz}}\right)^{2.5}$ for a synchrotron self-absorption peak and even more for free-free absorption. As the peak frequency drops significantly below 3 GHz, the 3 GHz lightcurve will drop by a factor of $\approx \left(\frac{\nu_p(t)}{3\text{GHz}}\right)^{\alpha}$, where $\alpha \approx 1$ is the spectral index. There are some other effects that modulate the lightcurve (such as the degree to which new synchrotron electrons are being accelerated), but on balance, the steep declines on both sides of 3 GHz make it such that most transients will spend most of their detectable duration peaking around 3 GHz. Our search is therefore biased toward finding transients peaking at ∼3 GHz.

   With these biases, our transient search can be thought of as a filter that is most sensitive to transients of duration ∼20 years and peak frequency ∼3 GHz. To produce the observed sample, this filter is "convolved" with the intrinsic distribution of durations and peak frequencies of the transients present in the sky at the time of observation. Transients with peak luminosities $\lesssim 3 \times 10^{28}$ erg s^{-1} Hz^{-1} (the luminosity corresponding to our detection threshold at 200 Mpc), will tend to be located at larger distances (since there

is more volume at larger distances). These transients will tend to be detected at fluxes close to our detection threshold and will therefore experience the selection biases more heavily than more luminous transients, which have more leeway to be peaked at higher or lower frequencies and have faster rise/fade times before becoming undetectable. Confirming the peak frequencies and timescales requires observation and analysis of multi-epoch SEDs which is beyond the scope of this paper. However, given that most of our sample falls under the luminosity threshold where the selection effects become strong, we make the simplifying assumption that all of our transients are peaking at 3 GHz (within a factor of a few) and evolve on timescales of $\gtrsim$ a few years. The latter assumption is further justified by the slow evolution of our transients between VLASS Epoch 1 and Epoch 2 (Section 2.6, Figure 2.14).

4. **Transients in our sample with peaks caused by synchrotron self-absorption have characteristic radii $R \sim 10^{-2}$ pc, energies $U \gtrsim 10^{48}$ erg, velocities $v \sim 3000$ km s^{-1}, and pre-shock densities $n_e \gtrsim 10^5$ cm^{-3}.** With a measured luminosity and an assumed synchrotron self-absorption peak frequency $\sim$ 3 GHz, we can use standard synchrotron shock theory[3] to estimate the radius R of the emitting region and the magnetic field strength B in which the emitting electrons are spiraling up to some factors of order unity. From equations 13 and 14 in Roger A. Chevalier (1998) (see also expositions in e.g., A. Y. Q. Ho, E. Sterl Phinney, et al., 2019; D. Z. Dong et al., 2021; DeMarchi et al., 2022), the radius and magnetic field are given by $R \approx 4.2 \times 10^{16}\ L_{28}^{9/19}\ \nu_3^{-1}$ and $B \approx 0.16\ L_{28}^{-2/19}\ \nu_3$, where L_{28} is the peak luminosity in units of 10^{28} erg s^{-1} Hz^{-1} and ν_3 is the peak frequency in units of 3 GHz. The observed luminosity range and assumed peak frequencies of our transients therefore suggests that they come from far more compact regions than the upper limit set by causality. This further increases the brightness temperature requirement, consistent with our assumption of synchrotron emission.

   The energy in the magnetic field is $U_B = \frac{4}{3}\pi R^3 \frac{B^2}{8\pi} \approx 2.8 \times 10^{47}\ L_{28}^{23/19}\ \nu_3^{-1}$ erg. For the relatively slow moving synchrotron-producing shocks of supernovae, the total energy in the shock is typically assumed to be higher than U_B by

[3] Not all synchrotron transients are due to shocks (see e.g., D. Dong and Gregg Hallinan, 2022), but diffusive shock acceleration is the mechanism responsible for most luminous synchrotron sources, and without broadband radio SEDs, there is no a-priori reason to expect that our transients are different.

a factor of $(1/\epsilon_B)$ where $\epsilon_B \sim 0.1$ to 0.33. For the highly relativistic jets of gamma ray bursts (GRBs), ϵ_B has been measured to have a median value of 3 $\times 10^{-5}$, implying a vastly greater total energy (Kumar and B. Zhang, 2015).

Emitting regions that spend ~years at radii of $\sim 10^{16-17}$ cm are relatively slow-moving. These slow shock velocities suggest high pre-shock densities surrounding the transient. The characteristic velocity v for a shock that crosses the characteristic radius R in a time t is given by $v \approx 2700\, L_{28}^{9/19}\, \nu_3^{-1}\, t_5^{-1}$ km/s, where $t_5 = t/5$ years. The velocity of a shock is primarily set by the density of gas being shocked. The characteristic density implied by the above velocity is $n_e \sim 8.6 \times 10^5\, L_{28}^{-4/19}\, \nu_3^2\, v_{2.7}^{-2}$, where $v_{2.7}$ is the shock velocity in units of 2700 km/s and we have assumed $\epsilon_B = 0.1$. For synchrotron self-absorbed transients, a picture therefore emerges of slow, compact, and energetic shocks powered by interaction with dense circum-explosion gas.

5. **Transients in our sample with peaks due to free-free absorption may be larger in extent and faster moving than those dominated by synchrotron self-absorption. However, they are also likely to be surrounded by dense ionized gas $n_e \gtrsim 10^4$ cm^{-3}, much denser than typical conditions in the interstellar medium (ISM).** Spectral peaks of ~3 GHz can be caused by free-free absorption from ionized gas along the line of sight. For a uniform density absorbing medium, the free-free optical depth is given by $\tau_{ff} = 3.3 \times 10^{-8}\, \nu_3^{-2.1}\, T_4^{-2.1}\, (n_{csm}/\mathrm{cm}^{-3})^2\, (s_{csm}/\mathrm{pc})$, where n_{csm} is the electron density of the absorbing material along the line of sight, s_{csm} is its thickness, and T_4 is its temperature in units of 10^4K.

   Several conditions need to be satisfied in order for a transient's peak to be dominated by free-free absorption. First, the exterior absorbing medium needs to cover nearly the entire emitting region. An isolated filament (no matter how dense) will only cause a small dip in the overall flux of order the fraction of the emitting region that it covers. Next, it needs to be relatively low-temperature. Photo-ionized gas tends to come to an equilibrium temperature of roughly $\sim 10^4$ K (e.g., Osterbrock and Ferland, 2006). However, shock-ionized gas will be superheated to a temperature $T \sim 5.7 \times 10^8$ K $\left(v_{\mathrm{shock}}/5000\ \mathrm{km\ s^{-1}}\right)^2$, reducing τ_{ff} by a factor of $\sim 10^5$. For nearly all regions of appreciable size (with the possible exception of the interior of an AGN disk), having such a high

temperature will completely suppress free-free absorption at GHz frequencies.

Finally, the ionizing absorbing gas needs to be sufficiently dense and thick. In order for $\sim 10^4$ K gas to have $\tau_{ff} \sim 1$ at 3 GHz it needs to have a thickness of $s_{csm} \sim 1$ pc thick column and density $n_{csm} \sim 10^4$ cm^{-3} or some equivalent tradeoff. In Milky Way-like galaxies, the warm ionized phase of the ISM has a typical density of order ~ 1 cm^{-3}. Despite its thick column (up to the size of the galaxy), it contributes negligibly to free-free absorption at 3 GHz. Most star formation occurs in giant HII regions have densities of $\sim 10^2$ cm^{-3} and sizes of ~ 100 pc. This gets closer to being optically thick at $\tau_{ff} \sim 10^{-2}$, but is still not enough. Ultra-compact HII regions can have densities $\gtrsim 10^4$ cm^{-3}, but this density is typically restricted to a size $\lesssim 0.1$ pc (e.g., de la Fuente et al., 2020). Such regions might contribute slightly to free-free absorption, but would require a very compact shock similar to the ones described above for synchrotron self-absorption. Likewise, the densest supergiant winds or stars that have undergone late-stage eruptive mass loss can have similar density profiles, but would require a similarly compact shock (see e.g., figure 4 of D. Z. Dong et al., 2021). Finally, densities in some galaxy nuclei can exceed 10^4 cm^{-3} over sizes greater than 1 pc (citation) and a central AGN can produce enough hard UV and X-ray photons to keep this gas ionized. VLBI observations of GPS sources have shown that in some cases, even jets on the scale of 10s of parsecs can be obscured by free free absorption in this way (Kameno et al., 2003).

Altogether, our survey selects for sources that peak at ~ 3 GHz, regardless of the origin of that peak. For transients embedded in unusually dense, photoionized regions (extreme winds or eruptive mass loss for stellar explosions, and dense nuclei for SMBH flares), this peak can be due to free-free absorption. In the case of stellar explosions, the radii at which they can reasonably be obscured by free free absorption is not very different from the scale radius that would be implied by synchrotron self-absorption. In the case of the TDEs in quiescent nuclei, there may not be enough ionizing photons produced by accretion onto the SMBH to support free-free absorption on a large scale, though this requires further investigation. For AGN, however, it is plausible that a high free-free absorption peak frequency is hiding a low synchrotron self-absorption frequency. In that case, the radius of the emitting region may

be larger (up to the limit set by causality assuming transient emission). In that case, the velocity of the shock and its energy will be correspondingly higher, and the shocked density lower.

Altogether, these general considerations suggest that our search is optimized to find a population of explosions occurring in regions with gas densities far larger than typical ISM conditions. Those that have spectra dominated by synchrotron self-absorption are particularly slow-moving, as they are ploughing through that high-density gas. Those dominated by free free absorption have not yet broken through the gas. However, with the exception of AGN, they are likely still compact because otherwise it becomes difficult to account for the origin of the high-density exterior gas.

We emphasize that the picture painted above is only a prior, set by assuming that every transient detected is one that our transient "filter" is particularly sensitive to. In fact, some of the transients in our sample are likely produced by conditions very different from the ones described above. Our search is certainly sensitive to other types of transients (such as relativistic jets) particularly if they are extremely luminous. For instance, GRB 030329 would have remained above our detection threshold for $\gtrsim 1$ decade if located at a distance of 200 Mpc (A. J. van der Horst et al., 2007). However, unless such high-velocity transients are intrinsically far more common than slower shocks in high-density gas, we expect our sample to be dominated by the slower population.

Optical Spectroscopic Validation for a Subset of Off-Nuclear Transients

Some of the radio transients in our sample have spectroscopically-verified optical transient counterparts identified in archival catalogs and/or follow-up observations. These counterparts are useful in several ways: (1) they confirm that the radio transient is real, (2) their redshift confirms association with the host galaxy, and (3) their properties help diagnose the nature of the radio transient. Here we present a few of these associations from an initial search of archival catalogs and an initial set of follow-up observations. Due to incomplete and biased sampling in both archives and follow-up, the lack of an optical counterpart does not imply that one does not exist.

To identify archival transient counterparts, we cross matched our sample against

transients with arcsecond localizations in the Open Supernova Catalog (Guillochon et al., 2017) and the Transient Name Server. We found 3 matches, all to supernovae that exploded 5-8 years before detection in VLASS Epoch 1. ID 11 is associated with the type IIn supernova 2012ab (Bilinski et al., 2018; Stroh et al., 2021), ID 24 is associated with supernova PTF 11mpv (originally identified as a type II but also consistent with a Ic-broadline (Ic-BL)), and ID 49 is associated with the Ic-BL PTF 11qcj (Corsi, E. O. Ofek, et al., 2014; Palliyaguru et al., 2019; Stroh et al., 2021). Two of the three matches were previously identified in Stroh et al. (2021).

The PTF 11mpv spectrum taken 8 days after discovery was obtained by the PTF collaboration during their spectroscopic classification campaign with the Intermediate-dispersion Spectrograph and Imaging System (ISIS) on the 4.2m William Herschel Telescope (WHT) (Avishay Gal-Yam et al., 2011). Based on some similarities of this spectrum with Type IIb SN 2008ax (see Figure 2.5), it was initially classified as SN II. To confirm its classification, we re-analyzed the WHT spectrum using SuperNova IDentification spectral matching software (SNID; Blondin and Tonry, 2011) and found similar quality matches to both Type IIb and Type Ic-BL SNe (both stripped-envelope SN subtypes) which are shown in Fig 2.5. The broad feature dominating the far red-side is the Ca II NIR emission typical of stripped envelope SNe. Given the similar quality of fits, significant host contamination in the WHT spectrum and highly unconstrained phase of the SN ($\sim$ 100 days), we cannot reliably deduce whether PTF 11mpv was a SN IIb or a SN Ic-BL but we suspect it to be a stripped-envelope supernova.

For a subset of transients identified in an initial search of VLASS Epoch 1.1, we have obtained optical spectroscopy with the Low Resolution Imaging Spectrograph (LRIS; Oke et al., 1995) on Keck I. In our observations of IDs 56, 57, and 59 (all observed on April 13, 2018, roughly 5 to 7 months after first detection in VLASS), we used the the 560nm dichroic with the 400/8500 grating in the red-arm and the 400/3400 grism on the blue arm, resulting in a $\sim$7Å FWHM spectral resolution in both arms. In our observation of ID 25 (taken Jul 7, 2018), we used the 1200/7500 grating in the red-arm, resulting in a $\sim$2.4Å FWHM spectral resolution in that arm at the cost of a reduced wavelength coverage. In each observation, we used a blind offset star to acquire the location of the radio transient. We exposed for 1200s in the blue arm and 2×560s in the red-arm (to mitigate cosmic rays in the thicker red CCD), reaching a typical 3σ sensitivity of $\sim$23rd - 24th mag. One of the red-arm

observations of ID 58 due to a software malfunction, leading to a slightly lower sensitivity in that part of the spectrum.

Among our initial observations, we found spectrally resolved counterparts to ID 56, ID 57, and ID 59 at widths too large to explain by the velocity dispersion of HII regions. We did not detect a counterpart to ID 24 (PTF 11mpv). The LRIS spectra are shown in Figure 2.6. We will discuss the properties of these explosions further in Section 2.7.

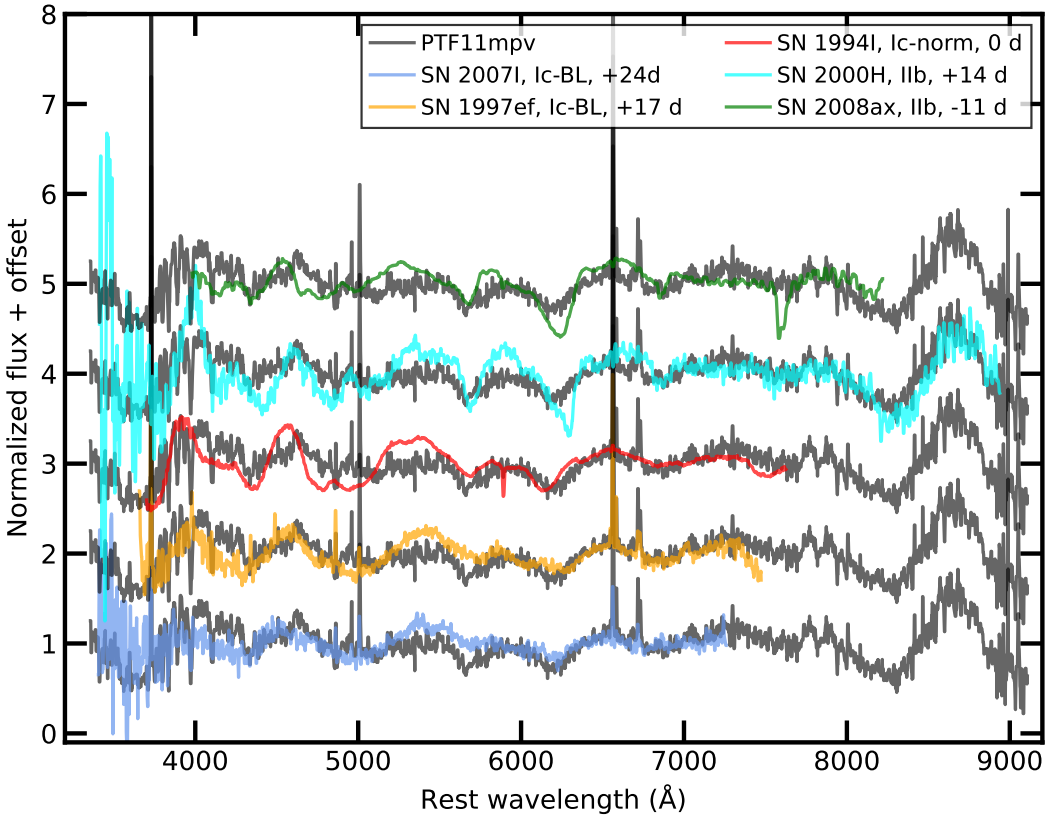

Figure 2.5: Comparisons between the spectrum of PTF 11mpv (gray) taken 8 days after first discovery and various standard supernovae used in automated supernova classifiers. From top to bottom, the supernovae are SN 2008ax (the type IIb SN originally used to classify PTF 11mpv as a type II), the IIb SN 2000H, the type Ic SN 1994L, and two Ic-BLs: SN 1997ef and SN 2007I.

2.4 Transient Classification Scheme

In this section, we begin a more in-depth investigation into the nature of our sample, starting with initial transient classifications. We adopt three broad classes for the transients: stellar explosion (SE), tidal disruption event (TDE), or active galactic

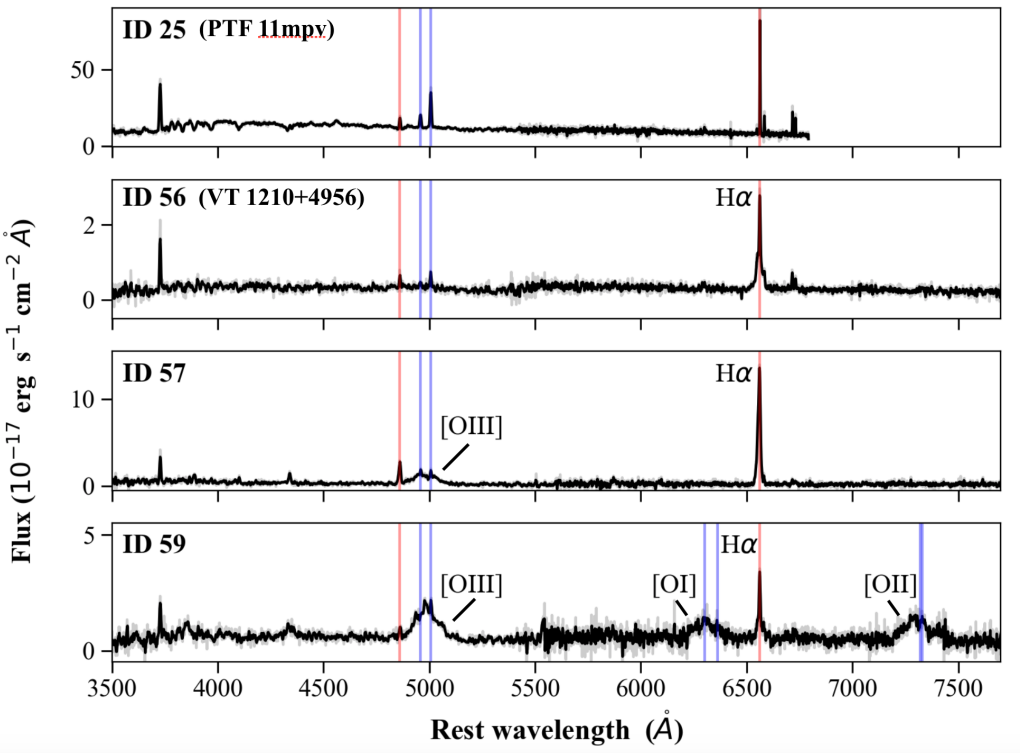

Figure 2.6: Nebular spectra of four stellar explosions in our sample taken with Keck/LRIS. Spectroscopically resolved lines are marked directly with labels in the subplots. The rest wavelengths of the hydrogen lines Hα and Hβ are indicated with red vertical lines, and the rest wavelengths of the oxygen lines [OIII] $\lambda\lambda$ 4959, 5007, [OI] $\lambda\lambda$ 6300, 6364, and [OII] $\lambda\lambda$ 7319, 7330 are indicated with blue vertical lines. The spectrum of ID 56 (VT 1210+4956) is reproduced from Figure 2 of D. Z. Dong et al. (2021).

nucleus (AGN) flare. These latter two categories can be combined into a broad category: supermassive black hole (SMBH) flares. These categories are based on host galaxy properties, which are the most widely available pieces of contextual information available. They are motivated by our knowledge of radio-transient producing classes from prior observations, but are left intentionally broad to encompass a range of physical phenomena.

In our scheme, stellar explosions include any events that are co-located with likely star-forming regions. Physically, this class likely encompasses a wide variety of supernovae as well as more unusual events. AGN flares encompass every source of transient radio emission in galaxy nuclei with evidence for AGN activity. This could include the launch of young jets, winds off of an accretion disk, stellar explosions

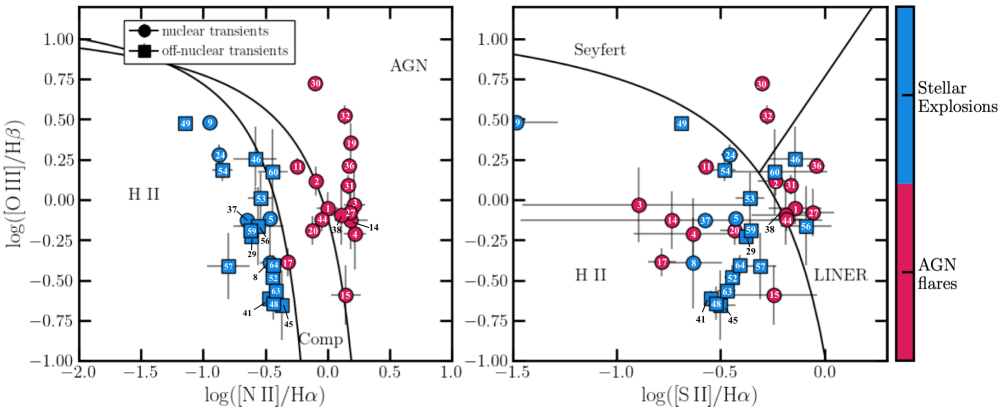

Figure 2.7: Baldwin, Phillips, and Terlevich (BPT) diagrams with our transient hosts (Baldwin, Phillips, and Terlevich, 1981a). The black lines on each panel demarcate different regions of the BPT diagram. In the *left* panel, the regions are an active galactic nucleus (AGN), composite, or H II region classification. In the *right* panel, the regions are H II, Seyfert, and low ionization nuclear emission region (LINER) galaxies. On both panels, we show the emission line ratios as measured by the SDSS collaboration for those transients with SDSS host spectra. We have noted the ID number for each transient on its corresponding marker. Note that quiescent sources and sources with no SDSS spectrum are not shown here. The final classifications of our galaxy are denoted by color. We also note whether a transient is in the nucleus of its host galaxy using the shape of the marker: circular points indicate nuclear transients, whereas square points indicate off-nuclear transients.

within an accretion disk, or tidal disruption events (TDEs) in AGN, among many alternatives. The TDE category contains all radio flares in the nuclei of galaxies with no evidence for AGN activity. Based on the energetic radio flares and lack of evidence for other sources of SMBH fueling, we expect these sources to be true TDEs.

To classify our sources, we use the following information:

- Nuclear or off-nuclear: we define a nuclear transient as a transient that is astrometrically consistent with the host galaxy nucleus, taking into account factors such as systematic errors in the VLASS astrometry and uncertain positions for host galaxy nuclei due to e.g., saturation in optical surveys. Any transient that is not astrometrically consistent with the nucleus is considered off-nuclear.

- AGN, star-forming, or quiescent galaxy: Where possible, we classify galax-

ies as AGN, star-forming, or quiescent using optical spectra. To isolate the emission lines, we subtract the galaxy continuum with the `ppxf` software (Cappellari and Emsellem, 2004). If after subtraction there are no detectable emission lines, we classify the galaxy as quiescent. Otherwise, we measure the fluxes in the Hα, Hβ, [NII], [OIII], and [SII] lines and plot them on two versions of the Baldwin, Phillips, and Terlevich (BPT; Baldwin, Phillips, and Terlevich, 1981b) diagrams (Figure 2.7). Galaxies that are most consistent with the AGN section of the [OIII]/Hβ vs [NII]/Hα diagram are classified as AGN while those that are most consistent with the HII section are classified as star-forming. In all cases, we checked the classifications by visual inspection. This resulted in one reclassification (the nuclear transient ID 17 from star-forming to AGN) due to the host galaxy's ambiguous BPT ratios and the likelihood of dilution of the nuclear emission with circumnuclear star formation in the 3" SDSS fiber.

Most of the spectra we considered were taken at the nuclei of the host galaxy. In cases where the subtracted spectra are consistent with AGN activity (either through broad lines or AGN-like BPT ratios), we classified the transient as an AGN flare. In cases where the BPT ratios were consistent with star formation, we classified the transient as a stellar explosion. If there is no evidence of emission lines (or the lines are only marginally detected), we classified the galaxy as quiescent and the transient as a TDE.

In rare cases, the available spectrum is off-nuclear and taken at the location of the transient. All of these spectra were consistent with star formation, and we classified the transients as stellar explosions. For the remaining off-nuclear transients, we compared the optical color at the location of the transient to those of confirmed star-forming regions. Regions with similar (blue) colors are assumed to be star-forming and we classify the transients as stellar explosions. The only off-nuclear transient not located in a star-forming region is ID 58, which is offset by $\sim 100''$ from its putative host (a giant elliptical galaxy with little evidence of active star formation). Due to the large angular offset, we suspect that this source may be a background source, though there is no direct evidence that this is the case. If it is associated, it may be an unusual event such as a luminous X-ray binary flare. We defer detailed analysis of this transient to future work.

The classification results are tabulated in Table 2.2 and illustrated in Figure 2.7, where we show BPT diagrams for the subset of our sample with SDSS spectra. We have adopted the SDSS DR16 emission line fluxes published in the `emissionLinesPort` catalog. Note that the flux ratios in Figure 2.7 are not those that we use in our classification scheme, as described in the second bullet point above. The blue-colored transients classified as SNe are star-forming galaxies on the BPT diagram and/or are off-nuclear. AGN flares are nuclear flares with evidence for AGN activity. Quiescent hosts are not shown here.

After performing this classification, we evaluate the quality of each classification. We first consider the quality of the galaxy type classification. If the optical spectrum is of poor quality, differentiating between galaxy classes becomes very challenging. We qualitatively assess the reliability of our galaxy type classification based on inspection of the optical spectra. We also consider galaxy orientation (edge-on or face-on). Off-nuclear transients may be projected into the nuclei of edge-on galaxies, whereas this is less probably with face-on galaxies. Hence, we use the b/a ratios for each galaxy along with by-eye inspection of each image to identify edge-on galaxies.

While we use this classification scheme to differentiate between transients in the rest of this work, there are a number of caveats. First and foremost, it is oversimplified. Each class contains many subclasses that may have very distinct physical mechanisms. Moreover, we expect contamination between the classes. For example, nuclear transients in star-forming galaxies could be either TDEs or SNe. Our quality assessment of each classification attempts to address this, but is unavoidably subjective. With our limited sample size, and the limited amount of multiwavelength data available for each object, a more complex scheme is not yet feasible. However, there are a number of ways to address these issues, which we will discuss in Section 2.8.

2.5 Host Galaxy Properties

With our radio transient sample and initial classifications in hand, we now compile evidence about the radio transient rate and luminosity function, and their correlation with the flare environment on kiloparsec scales. This latter point is determined by observations of the transient host galaxies; i.e., are there physical differences between the general galaxy population, the hosts of our sample and classified subsamples, and the hosts of transients selected at different wavelengths?

There is not much observational precedent for the types of host galaxy correlations we might expect. If radio-emitting supernovae more often occur when the exploding star was in a binary, the star formation history and stellar mass of a galaxy, which affect the environments that the stars form in and thus the stellar binary fraction, may correlate with the radio-emitting SNe rate. If AGN behave like X-ray binaries, we may expect new jets to be launched from the weakest AGN, which have puffy accretion disks that aid in jet collimation. To constrain possibilities such as these, in the rest of this section we perform a comprehensive study of the host galaxy properties of our radio transient sample.

Methodology

We evaluate the host galaxy properties of our transient sample using available catalogs from SDSS DR16. Hence, this section only concerns those transients with host spectra from the SDSS spectroscopic survey. Only considering such transients has the added benefit of allowing us to construct a reliable comparison sample: as we will discuss, we compare the host galaxy properties to a sample of SDSS spectroscopic galaxies within 200 Mpc. If we included transients with non-SDSS host spectra in this analysis, those galaxies could not necessarily be directly compared to the SDSS sample as they may not have passed the SDSS spectroscopic selection criteria. Moreover, as we rely on galaxy properties (e.g., emission line fluxes, stellar mass) as measured by the SDSS collaboration and we could not exactly replicate the SDSS analysis on the non-SDSS spectra, an attempt to compare the non-SDSS hosts to an SDSS sample would not be like-to-like. We also exclude the two sources with host offsets larger than 80 arcsec. These transients are a factor of $\gtrsim 100$ more likely to be background sources than the typical source in our sample because of the large area spanned by their host galaxies.

All emission line fluxes discussed hereafter were retrieved from the `emissionLinesPort` SDSS DR16 table (D. Thomas et al., 2013). They were measured using the Gas AND Absorption Line Fitting (GANDALF; Sarzi et al., 2006) code with stellar population fits from the penalised PiXel Fitting (pPXF; Cappellari and Emsellem, 2004) code and continuum stellar population models from C. Maraston and Strömbäck, 2011; Daniel Thomas, Claudia Maraston, and Johansson, 2011. We also adopt the Baldwin, Phillips, and Terlevich (BPT) classifications of the hosts from the `emissionLinesPort` table.

We retrieve galaxy stellar masses and star formation rates from the GALEX-SDSS-WISE legacy catalog (GSWLC) (Salim, Lee, et al., 2016; Salim, Médéric Boquien, and Lee, 2018). These galaxy properties are measured from spectral energy distribution fits to GALEX UV, SDSS optical, and WISE infrared fluxes using the Code Investigating GALaxy Emission (CIGALE) (M. Boquien, 2020). We refer the reader to Salim, Lee, et al., 2016; Salim, Médéric Boquien, and Lee, 2018 for details. We adopt the shallow version of the GSWLC, which covers 88% of SDSS and uses low-depth UV photometry, to maximize our comparison sample size. We do not see significant differences in our results if we use the medium or deep versions of the GSWLC.

We compare the host galaxy properties to a comparison SDSS sample consisting of every galaxy in the SDSS spectroscopic catalog with `zWarning`= 0 and $z < 0.045$. We retrieve the same galaxy measurements (emission line fluxes, stellar masses, etc.) using the same methods as for the transient host galaxy sample. We also compare the stellar explosion host properties to the Open Supernova Catalog (Guillochon et al., 2017), which contains all publicly available supernova candidates selected in any waveband. We only consider those supernova within 200 Mpc that have a classification and that are not classified as Type I or Type Ia supernova.

In the following section, we will show histograms of various galaxy properties of our sample. One of our goals is to test whether the galaxy properties of a comparison sample, like the SDSS spectroscopic galaxy sample within 200 Mpc, are consistent with our sample. We calculate the p-value that our sample is drawn from the comparison sample. Let there be $N_{\rm obs}$ objects in our sample. Let $N_{\rm comp}$ be the size of the comparison sample. If j indexes the comparison sample and $i \in [0, N_{\rm obs})$ indexes the objects in our sample, let $j_{i,1}, j_{i,2}, j_{i,3}, ...j_{i,N}$ for $N = 1000$ be randomly selected indices in the range $[0, N_{\rm comp})$. If we are considering a variable X with uncertainty σ, we calculate the test statistic

$$\mathrm{TS}_{\rm obs} = \sum_{i=0}^{N_{\rm obs}} \sum_{k=0}^{N} \left[-\frac{1}{2} \frac{(X_i - X_{j_{i,k}})^2}{\sigma_i^2 + \sigma_{j_{i,k}^2}} - \log \sqrt{2\,\pi\,(\sigma_i^2 + \sigma_{j_{i,k}}^2)} \right]. \tag{2.1}$$

Next, we select another set of random indices $j'_{i,1}, j'_{i,2}, j'_{i,3}, ...j'_{i,N'}$ for $i \in [0, N_{\rm obs})$ and $N' = 1000$. We use the $'$ notation here to differentiate between these random

indices and those identified above. We calculate an array of test statistics, indexed by $l \in [0, N')$:

$$\mathrm{TS}_l = \sum_{i=0}^{N_{\mathrm{obs}}} \sum_{k=0}^{N} \left[-\frac{1}{2} \frac{(X_{j'_{i,l}} - X_{j_{i,k}})^2}{\sigma^2_{j'_{i,l}} + \sigma^2_{j_{i,k}}} - \log \sqrt{2\pi(\sigma^2_{j'_{i,l}} + \sigma^2_{j_{i,k}})} \right]. \tag{2.2}$$

The p-value that the distribution of X for our sample is consistent with that for the comparison sample is then the fraction of $\mathrm{TS}_l \in [0, N')$ where $\mathrm{TS}_l < \mathrm{TS}_{\mathrm{obs}}$.

Results

First, we consider the radio transient host stellar mass distributions. In Figure 2.8, we show the stellar mass distributions for our sample compared to the SDSS galaxies. The full sample distribution (top left) is slightly biased toward high masses ($M_* \gtrsim 10^{10}\,M_\odot$) with $p = 0.04$. This high mass bias is driven by the AGN-hosted transients (top right), which are significantly skewed to $M_* \gtrsim 10^{10}\,M_\odot$ with $p = 0.01$. If we restrict the comparison sample to just those BPT AGN in the SDSS sample (grey histogram), we find a more consistent stellar mass distribution with $p = 0.27$.

Stellar explosions largely follow the SDSS mass distribution ($p = 0.59$). As shown, they are also consistent with the stellar mass distribution of SNe in the Open SN catalog ($p = 0.72$), suggesting that there is no significant difference between the masses of radio-selected stellar explosions versus those selected in other bands. The TDE candidate masses are consistent with those of the SDSS galaxies ($p = 0.9$). We will discuss the LERG histogram and our motivation for including it in Section 4.7.

In Figure 2.9, we show the specific star-formation (sSFR) rate distributions for the transient sample, in the same format as Figure 2.8. Note that the star-formation distributions are biased: we use star formation to select stellar explosion candidates. As expected, we see that AGN flares tend to lie at lower sSFRs, whereas stellar explosions are biased toward high sSFRs. Neither of these trends have significant p-values. Notably, The stellar explosion transients are not at very high sSFRs relative to the general SDSS population; most of the sSFRs are near the peak of the SDSS distribution. Still, the sSFRs of the stellar explosions transient hosts do not extend to as low sSFRs as the general SDSS population, as expected given that we select stellar explosions on SFR. The TDEs tend to lie near the peak of the SDSS SFR

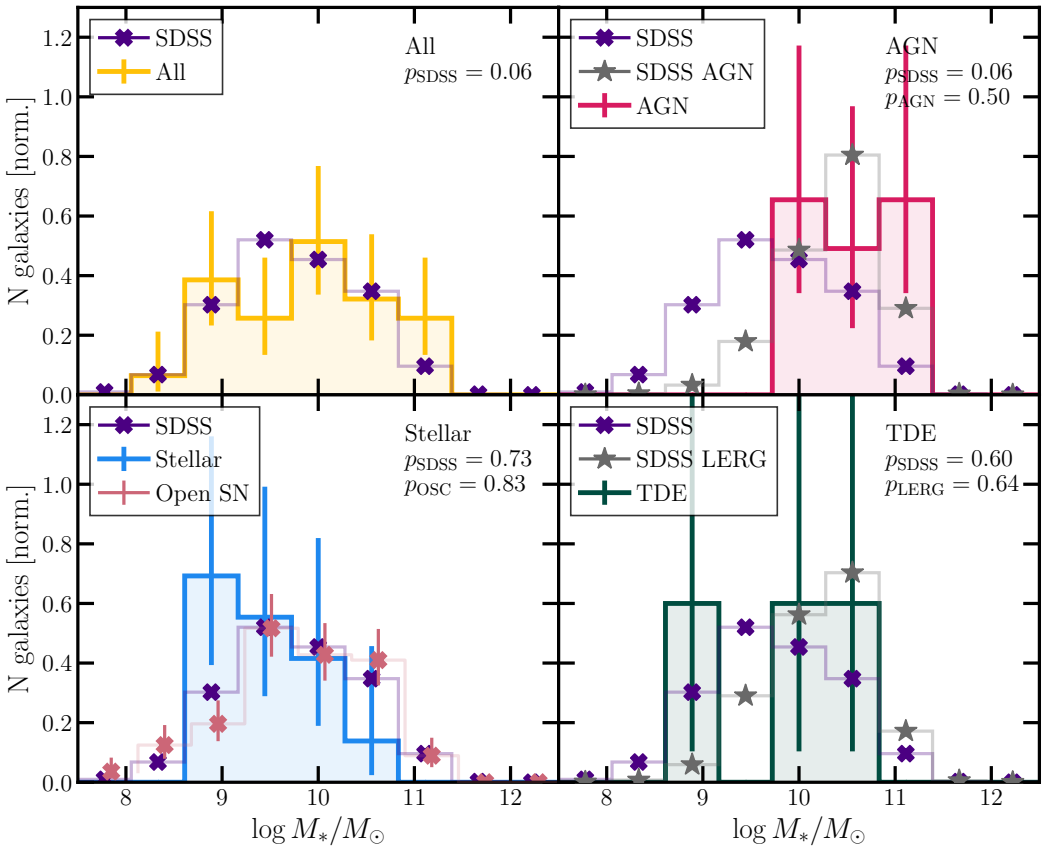

Figure 2.8: Stellar mass distributions for our transient sample and subsamples, compared to all galaxies in the SDSS spectroscopic survey within 200 Mpc with available SED fits in the GSWLC. In all panels, the SDSS stellar mass distribution is shown as a purple histogram. Errors are not shown for this histogram, but are very small given the large size of the SDSS spectroscopic catalog. Our transient samples are shown as shaded, colored histograms. The *top left* panel shows all transients with SED fits in the GSWLC, the *top right* panel all those classified as AGN or AGN/TDE, the *bottom left* panel all those classified as SN, SN/AGN, or SN/TDE, and the *bottom right* panel all those classified as TDE. AGN tend to lie at higher stellar masses than the SDSS population, and cause the entire transient stellar mas distribution to be biased high. The stellar explosion and TDE samples are consistent with the SDSS stellar mass distribution within uncertainties. The stellar explosion panel (*bottom left* also shows the stellar mass distribution for those SN in the Open Supernovae Catalog (Guillochon et al., 2017) within 200 Mpc with SED fit information in the GSWLC. The stellar mass distribution of our observed stellar explosion transients are consistent with the objects in the open SN catalog.

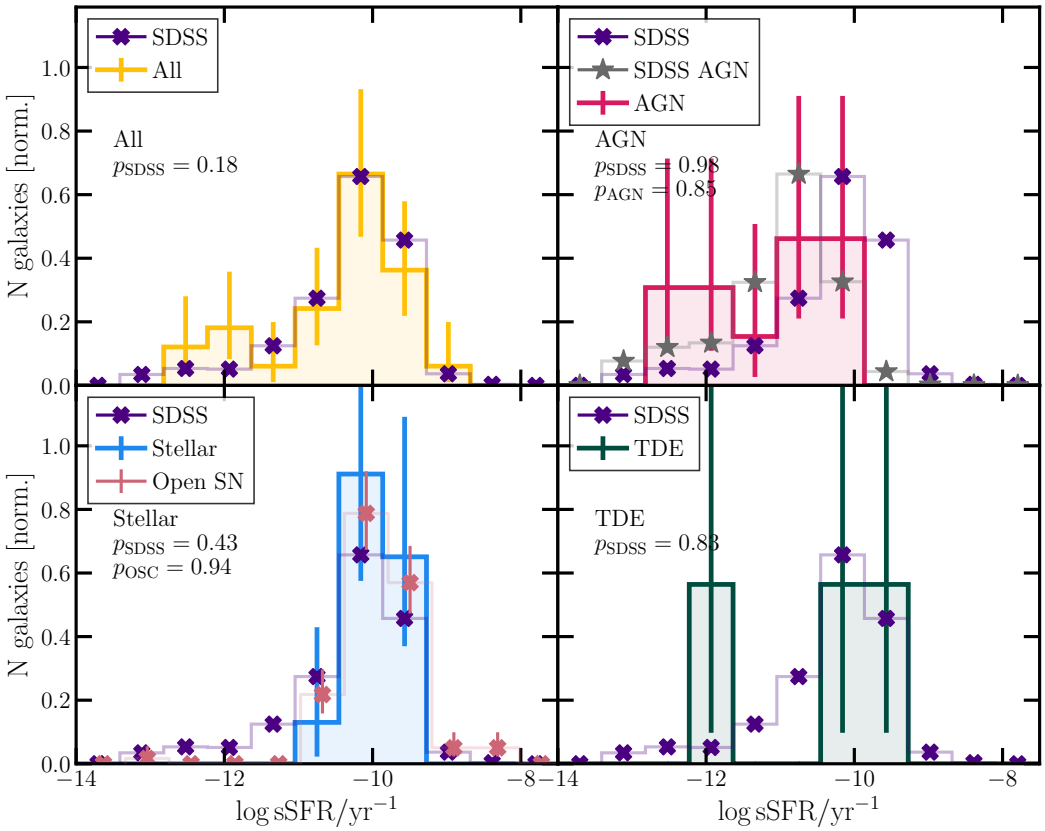

Figure 2.9: Specific star formation rate (sSFR) distributions for our transient sample and subsamples compared the the SDSS spectroscopic survey, in the same format as Figure 2.8. The overall transient sSFR distribution is consistent with that of the SDSS spectroscopic sample. The AGN sSFR is biased toward low sSFR relative to SDSS, and the stellar explosions are biased toward high sSFR. These trends are as expected given that we classify our sources based, in part, on sSFR. The stellar explosions are consistent with objects in the open SN catalog. The TDE candidates lie near the median SDSS sSFR, but there are too few TDE candidates to determine whether this is significant.

distribution, which may be expected if they are not biased toward high or low sSFRs. The total transient population traces the SDSS sSFR distribution well ($p = 0.75$).

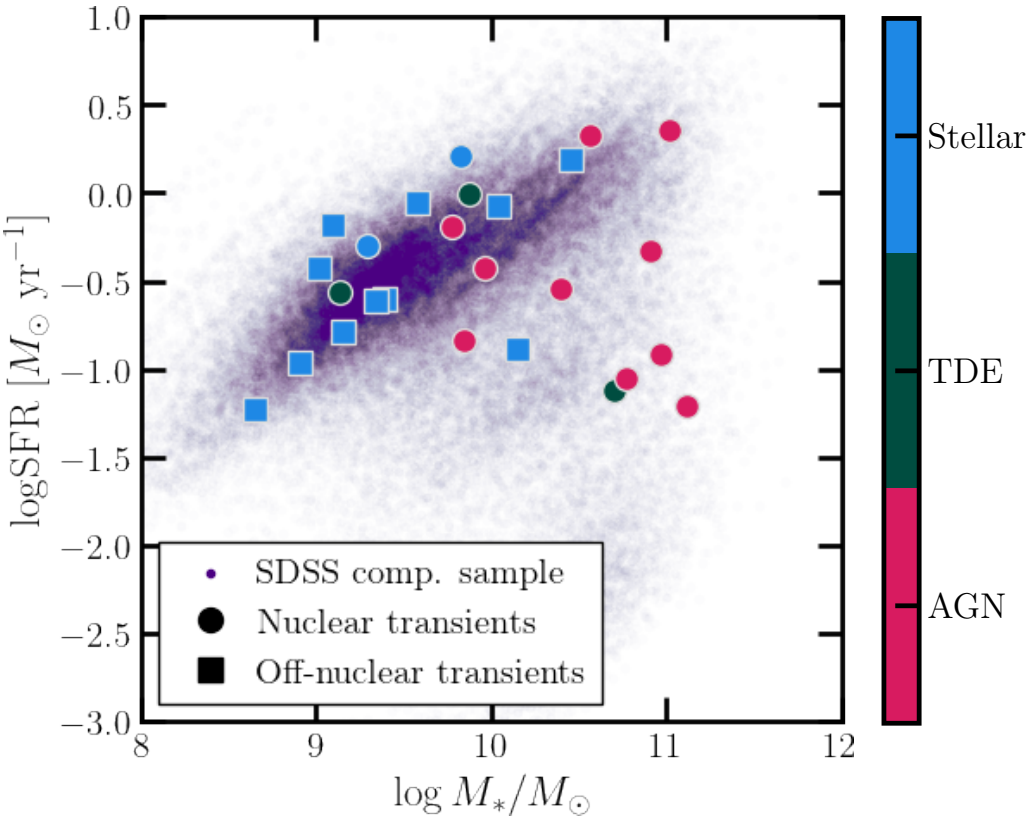

Figure 2.10: Star-formation versus stellar mass for our transient sample, as compared to a selection the SDSS spectroscopic sample within 200 Mpc. SDSS comparison galaxies are shown in purple. Nuclear transients in our sample are shown as circles where off-nuclear transients are shown as squares. The transients are colored by their classification, using the same color scheme as previous plots. Off-nuclear transients classified as stellar explosions dominate the high star-formation regime. Nuclear transients show a larger spread in SFR.

These SFR trends are highlighted again in Figure 2.10, where we show star formation versus stellar mass for our transients compared to SDSS. This figure also highlights the differences between the nuclear and off-nuclear transients: the off-nuclear transients are almost entirely at galaxies with higher SFRs, whereas the nuclear transients show a larger spread in SFR.

In Figure 2.11, we show the host galaxy V-band extinction for our galaxies and

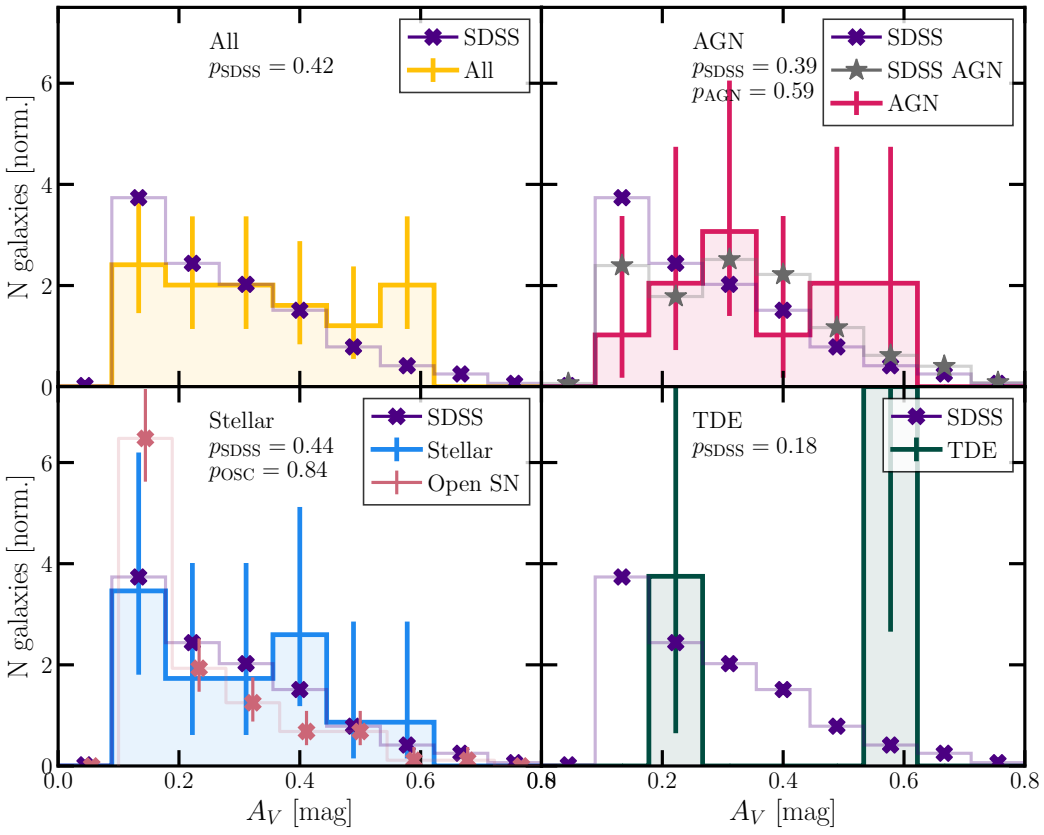

Figure 2.11: V-band host galaxy intrinsic extinction A_V distributions for our transient sample and subsamples compared the the SDSS spectroscopic survey, in the same format as Figure 2.8. The extinction A_V only includes contributions from the host galaxies, with no contribution from the Milky Way. Ours may be slightly biased toward higher A_V, but there are no significant trends.

the comparison samples. This extinction only includes contributions from the host galaxy as opposed to extinction due to the Milky Way. The observed histograms may be slightly biased toward higher A_V, but there are no significant trends.

Finally, in the left panel of Figure 2.12, we show the distribution of BPT classifications of our transients relative to the general SDSS population. Note that we are using the SDSS BPT classification, rather than the BPT classification we determined by inspection to classify the sources (Section 2.4). As expected, there is a significant overabundance of star-forming, off-nuclear transients relative to SDSS. The nuclear transients, in contrast, seem to match the SDSS BPT distribution, with a slight deficit ($\sim 3\sigma$) of star-forming hosts. Intriguingly, there may be an excess of nuclear transients in LINER galaxies ($\sim 3\sigma$ significance). The off-nuclear sample is

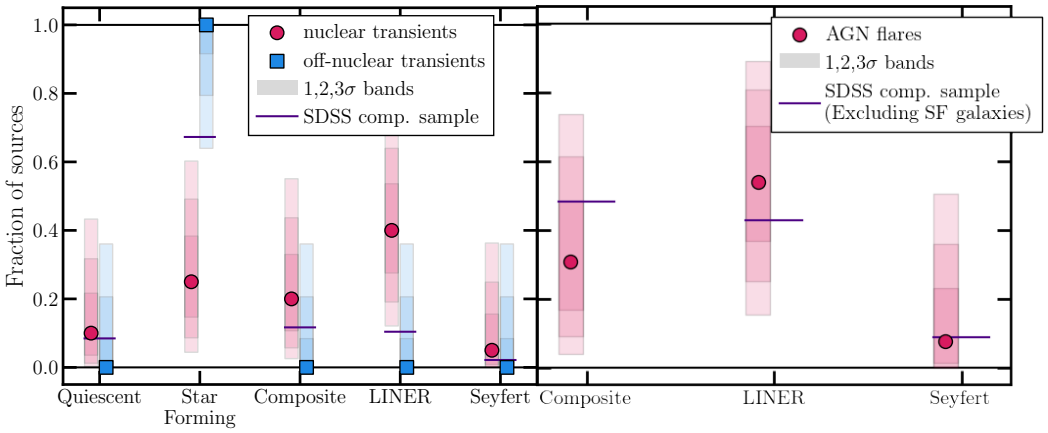

Figure 2.12: In the *left* panel, we show the fraction of SDSS spectroscopic galaxies in each BPT class (purple) as compared to our nuclear sources (red circles) and off-nuclear sources (blue squares). The off-nuclear sources significantly prefer star-forming galaxies relative to SDSS. The nuclear sources appear to prefer LINERs and show a deficit of star-forming galaxies. These trends are due to the fact that our nuclear sample is dominated by AGN flares, as can be seen in the *right* panel. The *right* panel is the same as the *left* panel but only includes AGN flares and, for the comparison SDSS sample, BPT AGN. The excess of LINERs disappears when only considering AGN.

dominated by AGN flares, so to investigate this excess in more detail, in the right panel of Figure 2.12 we show the BPT classification for BPT AGN in SDSS relative to the AGN flares in our sample, which will include LINER flares. The excess of LINERs is removed when only considering AGN, so it was driven by the overall excess of AGN in our nuclear sample.

In summary, we have compared the host galaxy properties of our transient sample to a comparison 200 Mpc SDSS spectroscopic galaxy sample. In particular, we have considered stellar mass, star formation rate, host galaxy extinction, and BPT classification. We see two significant differences: a $\sim 3\sigma$ excess of off-nuclear transients in star-forming galaxies and a $\sim 3\sigma$ deficit of nuclear transients in star-forming galaxies (Figure 2.12). There are some marginal trends toward higher extinction values in TDEs and stellar explosions relative to comparison samples from the Open SN catalog and SDSS galaxies respectively. However, our sample size is still too small for these trends to be considered robust.

2.6 Radio Properties

In addition to the properties of the host galaxy, the properties of the radio flares themselves inform our understanding of the population. In particular, in this section, we use the statistical properties of our sample to constrain the luminosity function, rates, and light curve properties of the broad radio flare population.

Luminosity Function and Rates

First, we briefly summarize our methodology. A detailed description of our techniques is presented in Appendix 2.9. Later, we will discuss the luminosity function shape and transient rates for the full sample, and for a number of subsamples.

The observed luminosity function is largely set by two factors: the shape of the function and the transient rate. We assume the luminosity function is a power-law in luminosity, valid for $L > L_{\rm min}$:

$$\frac{dN}{dL} \propto L^{-\Gamma},\ L > L_{\rm min}, \tag{2.3}$$

where $\Gamma > 0$ is the spectral index. The minimum luminosity $L_{\rm min}$ is defined as the minimum luminosity to which we are sensitive. In our case, it is reasonably approximated as the luminosity corresponding to a source at the minimum distance $d_{\rm min,\,obs}$ of any of the observed sources with flux density at the limit of the VLASS sensitivity, $f_{\rm lim=0.7}$ mJy; i.e., $L_{\rm min} = 4\pi d^2_{\rm min,\,obs} f_{\rm lim}$.

We fiducially adopt a volumetric rate: the transient rate $\dot{n}$ is defined as the number of radio transients per Gpc^3 per year between 10^{26-30} erg s^{-1} Hz^{-1}. This luminosity range was chosen to roughly match the observed luminosity range, but $\dot{n}$ can be easily scaled to different luminosity ranges by integrating Equation 2.3. To calculate the total number of transients expected given $\dot{n}$, we define d_M to be the distance of the farthest transients considered. We assume all distances are uniformly distributed within a sphere. The probability of measuring a distance d is then

$$P_d(d) \propto d^2. \tag{2.4}$$

We also define $f_A = 0.24$, the fraction of the sky probed, which is roughly the fraction of the sky covered by FIRST. Finally, we define $f_S = 0.47$ to be the radio transient host galaxy spectroscopic completeness within 200 Mpc, which we calculate as the fraction of the transient host galaxies within 200 Mpc in the SDSS

field that have SDSS spectra. This spectroscopic completeness is not exact, as it is appropriate for only those galaxies with SDSS spectra. The true spectroscopic completeness of the full sample will be higher than $f_S = 0.47$, so our measured $\dot{n}$ will be overestimated. The true completeness is also likely distance dependent, as nearby, bright galaxies are slightly more likely to have a spectrum. We ignore these effects, as statistical uncertainties dominate our results: if we restrict our analysis to only those transients with SDSS spectroscopic hosts, our measured rates and slopes change by $< 1\sigma$. Future, larger transient samples will need to consider the spectroscopic selection function more carefully.

We assume the time between FIRST and VLASS E1 for all sources is $\Delta t = 20$ years. Δt is, in reality, a function of position on the sky and ranges from $\sim 10 - 20$ years. It is possible to account for this when modelling the luminosity function by assuming a form for the typical radio lightcurve and, assuming random, uniformly distributed launch dates for each transient, calculating the exact number of transient expected as a function of sky location, lightcurve parameters, and luminosity function parameters, which can then be fit to the observations. This method would be particularly powerful for surveys where there are multiple epochs of detections for each transient, allowing the light curve evolution to be directly constrained. Because we have a relatively small sample with only two epochs of detections (VLASS E1/E2), which show little flux evolution for most transients (see Section 2.6), it is unlikely that the more complex fit including lightcurve parameters would result in any reliable information. Hence, we simplify our analysis by assuming a constant $\Delta t = 20$ years. The implicit assumption here is thus that each transient has a constant lightcurve that lasts for $\sim \Delta t$ years. Reducing Δt would increase the measured rate $\dot{n}$.

With the definitions above, the total number of radio transients within the field-of-view considered and with a spectroscopic host is given by

$$N_0 = \frac{4}{3}\pi d_M^3 f_A f_S \dot{n} \Delta t \frac{L_{\rm min}^{1-\Gamma}}{(10^{27(1-\Gamma)} - 10^{30(1-\Gamma)})}, \tag{2.5}$$

where $L_{\rm min}$ is in units of erg s^{-1} Hz^{-1}. The final term involving $L_{\rm min}$ scales the number of transients expected in the luminosity range 10^{26-30} erg s^{-1} Hz^{-1} to the total number we should observe, which includes all those transients with $L > L_{\rm min}$.

This equation does not account for our incompleteness due to the VLASS flux density limit $f_{\rm lim} = 0.7$ mJy. As described in Appendix 2.9, we can calculate the fraction of sources with $f > f_{\rm lim}$, which we write $P(f > f_{\rm lim})$. The observed number of sources is then $N_0 P(f > f_{\rm lim})$.

We can use this value and the probabilities of obtaining a given luminosity, $P_L(L)$, and distance, $P_d(d)$, to calculate the Poisson log-likelihood for a given set of parameters $\log \dot{n}$ and Γ (Equation 2.6):

$$\log \mathcal{L} = -N_0 P_f(f > f_{\rm lim}) + \sum_{i=0}^{N_{\rm obs}} \log \left[\frac{N_0}{N_{\rm obs}} P_L(L_i) P_d(d_i) \right]. \tag{2.6}$$

Here, i sums over each transient with luminosity L_i and distance d_i. $N_{\rm obs}$ is the observed number of transients, in contrast to N_0, which is the predicted number of transients for a given $\dot{n}$ and Γ.

We fit this log-likelihood for Γ and $\log \dot{n}$. We perform the fit using the `dynesty` dynamic nested sampler (Higson et al., 2019; Skilling, 2006; Speagle, 2020; Skilling, 2004; Feroz, Hobson, and Bridges, 2009) with uninformative tophat priors:

$$\log \dot{n} \in [-100, 100], \ \Gamma \in [1, 5]. \tag{2.7}$$

We perform this fit for all the transients and the transients in each class (AGN flares, TDEs, stellar explosions). Because we only detect two strong TDE candidates, we fix the slope at $\Gamma = 2$. We chose $\Gamma = 2$ because, as we will discuss, we obtain values consistent with $\Gamma = 2$ for the fits to every other class and the full transient sample.

In Table 2.1, we summarize the results of our `dynesty` fits. We report the results separately for all transients, AGN flares, TDEs, and stellar explosions. Note that some events are not included in any of these subsamples, so we do not expect the rates of these two subsamples to sum to the total rate. We also show the luminosity functions in Figure 2.13 for the full sample and each subsample.

In Table 2.1, we include the luminosity function index Γ, the volumetric rate, the areal rate, and the rate within 200 Mpc per year. We also include the rate within 200

Table 2.1: Luminosity function and rate parameters measured as described in Section 2.6. Reported uncertainties are 1σ. The rate per galaxy is determined by normalizing the observed rate for each transient class to the number of galaxies with the corresponding BPT classification.

Selection	Γ	log Rate $\mathrm{Gpc^{-3}\ yr^{-1}}$	log Rate $\mathrm{deg^{-2}\ yr^{-1}}$	log Rate $\mathrm{yr^{-1}}$	log Rate $\mathrm{Galaxy^{-1}\ yr^{-1}}$
All transients	$1.91^{+0.08}_{-0.08}$	$3.81^{+0.09}_{-0.10}$	$-1.66^{+0.09}_{-0.10}$	$2.34^{+0.09}_{-0.10}$	$-2.42^{+0.09}_{-0.10}$
SMBH Flares	$1.97^{+0.14}_{-0.13}$	$3.56^{+0.15}_{-0.15}$	$-1.91^{+0.15}_{-0.15}$	$2.09^{+0.15}_{-0.15}$	$-2.05^{+0.15}_{-0.15}$
TDEs	2 (fixed)	$2.62^{+0.28}_{-0.38}$	$-2.85^{+0.28}_{-0.38}$	$1.15^{+0.28}_{-0.38}$	$-2.53^{+0.28}_{-0.38}$
Stellar Explosions	$1.99^{+0.14}_{-0.14}$	$3.57^{+0.15}_{-0.16}$	$-1.91^{+0.15}_{-0.16}$	$2.09^{+0.15}_{-0.16}$	$-2.48^{+0.15}_{-0.16}$
SDSS transients	$1.87^{+0.09}_{-0.10}$	$3.64^{+0.11}_{-0.11}$	$-1.83^{+0.11}_{-0.11}$	$2.17^{+0.11}_{-0.11}$	$-2.59^{+0.11}_{-0.11}$
SDSS SMBH Flares	$1.98^{+0.19}_{-0.19}$	$3.36^{+0.22}_{-0.22}$	$-2.12^{+0.22}_{-0.22}$	$1.88^{+0.22}_{-0.22}$	$-2.26^{+0.22}_{-0.22}$
SDSS TDEs	2 (fixed)	$2.61^{+0.29}_{-0.36}$	$-2.87^{+0.29}_{-0.36}$	$1.13^{+0.29}_{-0.36}$	$-2.54^{+0.29}_{-0.36}$
SDSS Stellar Explosions	$1.92^{+0.15}_{-0.14}$	$3.45^{+0.17}_{-0.17}$	$-2.03^{+0.17}_{-0.17}$	$1.97^{+0.17}_{-0.17}$	$-2.61^{+0.17}_{-0.17}$

Mpc per galaxy, where the total number of galaxies is calculated from SDSS. For the all transients category, we divide the total rate within 200 Mpc by the total number of SDSS spectroscopic galaxies within 200 Mpc, corrected for spectroscopic and areal completeness. For the AGN flares category, we divide by the number of BPT AGN galaxies in SDSS within 200 Mpc. For TDEs, we divide by the number of quiescent galaxies in SDSS within 200 Mpc. Finally, we divide the stellar explosion rate by the number of star-forming galaxies within 200 Mpc to calculate the rate per galaxy.

We also report the results for the full sample and each subsample when only considering those events with SDSS spectroscopic hosts. The results for the SDSS-only samples are, in all cases $< 1\sigma$ consistent with the full samples, supporting our hypothesis that we are dominated by statistical uncertainty rather than uncertainty in our assumptions about spectroscopic completeness.

For all subsamples, the slope of the luminosity function is $\Gamma \sim 2$ within 1σ.

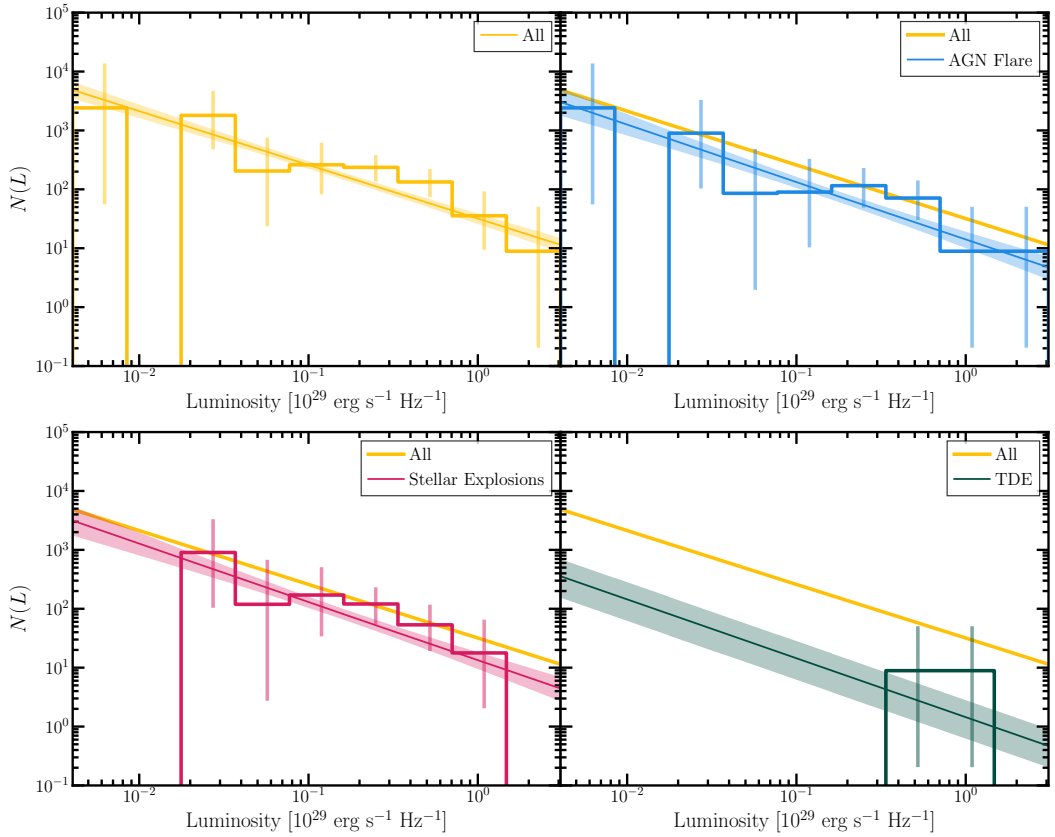

Figure 2.13: The observed luminosity function for all transients (*top left*), AGN flares (*top right*, stellar explosions (*bottom left*) and TDEs (*bottom right*). The best-fit model is shown as a shaded region with 1σ uncertainties. The median best-fit model for the full transient sample is overlaid on each panel in yellow.

This consistency of the luminosity function slope between all subsamples is intriguing. Interpretation of this result is complicated: our luminosity function is not measured using, e.g., the peak luminosity of each transient. We expect that most of our transients are detected at peak because VLASS is flux limited and the volume in which a given source is detectable will be maximized at its light curve peak. With the limited sample size and poorly sampled radio light curves available, we cannot confirm this expectation. If we are not observing each source at peak, the luminosity function is determined by both the peak luminosities and the lightcurve shapes. For example, suppose we are observing sources that all have the same peak luminosity but are decaying as $L_\nu(t) \propto t^{-1}$, where t is measured relative to the transient launch date. This assumed lightcurve is consistent with the lightcurve expected for a spherical outflow shocking against a dense medium. If the launch dates are uniformly distribution between FIRST and VLASS, then the luminosity

function will be related to the probability distribution of t^{-1}, i.e., the probability distribution of the inverse of a uniform variable. Thus, $\frac{dN}{dL} \propto L^{-2}$, as observed. Our constraint of a constant luminosity function shape for all sources could thus be explained by taking into account the fact that we are not observing each source at peak.

The total transient rate is $\sim 10^{3.81}$ Gpc^{-3} yr^{-1}, or $\sim$200 transients within 200 Mpc per year in the luminosity range 10^{27-30} erg s^{-1} Hz^{-1}. This rate includes roughly equal contributions from SMBH flares and stellar explosions. Stellar explosions occur at a rate of $\sim 10^{3.56}$ Gpc^{-3} yr^{-1}, or 123 events per year. SMBH flares occur at roughly the same rate. Normalized to the number of galaxies, stellar explosions occur a factor of $\sim$3 more frequently than SMBH flares, although the rates per galaxy are consistent within uncertainties. TDEs are the least frequent event, at $10^{2.62}$ Gpc^{-3} yr^{-1}, or 400 events per year.

Timescales

As briefly discussed in the previous section, we do not have sufficient data to perform a detailed fit to the transient timescales. We can, however, qualitatively comment on the typical timescales using the change in flux between VLASS E1 and E2. In Figure 2.14, we show histograms of the ratio of VLASS Epoch 1 to Epoch 2 flux. Those sources that are not significantly detected in VLASS E2 are shown as upper limits. Seven of the sources rose between E1 and E2 (14%) and fourty-four of the sources faded (86%). This immediately suggests that the transients in our sample fade on much slower timescales than those on which they rise.

If we split the transients by classification (SMBH flare or stellar explosion, it is clear that SMBH flares are more strongly biased toward fading sources than the general population: 91% of SMBH flares are fading in contrast to 9% rising. This SMBH flare sample is likely contaminated with GPS sources, which could bias our result as these sources would not evolve between VLASS E2 and E1. However, removing sources with similar E1 and E2 fluxes (within uncertainties) only increases the ratio of fading to rising flares.

These percentages are difficult to interpret directly as we are most sensitive to sources near the peak of their lightcurves since VLASS is flux-limited, so we expect cases where VLASS E1 was observed during the flare rise and VLASS E2 was observed during the flare decay. The fact that the large majority of SMBH flares

are decaying tells us that the lightcurve shape is such that $\gtrsim 91\%$ of the time during which the flare is above the VLASS sensitivity, the E1 observation was either taken (a) before the lightcurve peak but sufficiently close in time to the lightcurve peak that the flare appears to have faded ∼2 years later or (b) the E1 observation was taken post-peak.

Stellar explosions are also biased toward fading sources, but not as significantly. 18% of stellar explosions are rising and 82% are fading. This suggests that the ratio of the rise-to-fade time for stellar explosion flares is higher than that for SMBH flares.

2.7 Discussion

In the previous sections, we presented the first uniformly selected sample of extragalactic radio transients large enough for statistical analysis. We also presented contextual information about the radio flares and the galaxies that host them. These transients have a diverse set of astrophysical origins. In the following sections, we will investigate these origins. Before discussing each class of transients, we will present a summary of our results.

AGN Flares

We have identified 16 transients located in extragalactic nuclear regions that have optical spectra unambiguously consistent with Seyfert or LINER activity. We classify these events as high probability AGN flares. We have identified an additional five transients in hosts with weak lines or significant nuclear star formation in addition to AGN-like lines. We classify these sources as medium-confidence AGN flares. There are 10 more events in host galaxies with low-quality spectra (e.g., without flux cabliration) sufficient to measure redshifts but not test for AGN activity. We classify these as low-confidence AGN, though based on the host colors and morphologies, we expect that most if not all of them would be reclassified as high-confidence AGN given better data. In summary, there are 31 transients in our sample consistent with AGN flares of which 16 are classified with high confidence according to our scheme. The host galaxies of the AGN flare sample have stellar masses, extinctions, and star-formation rates that are generally consistent with a comparison sample of AGN selected from SDSS. The transient luminosities are in the range $L_\nu(3\ \mathrm{GHz}) \sim 10^{27.3-28.7}$ erg s^{-1} Hz^{-1}, with the exception of one source with $L_\nu(3\ \mathrm{GHz}) \sim 10^{29.5}$ erg s^{-1} Hz^{-1}. These AGN flares occur at a rate of

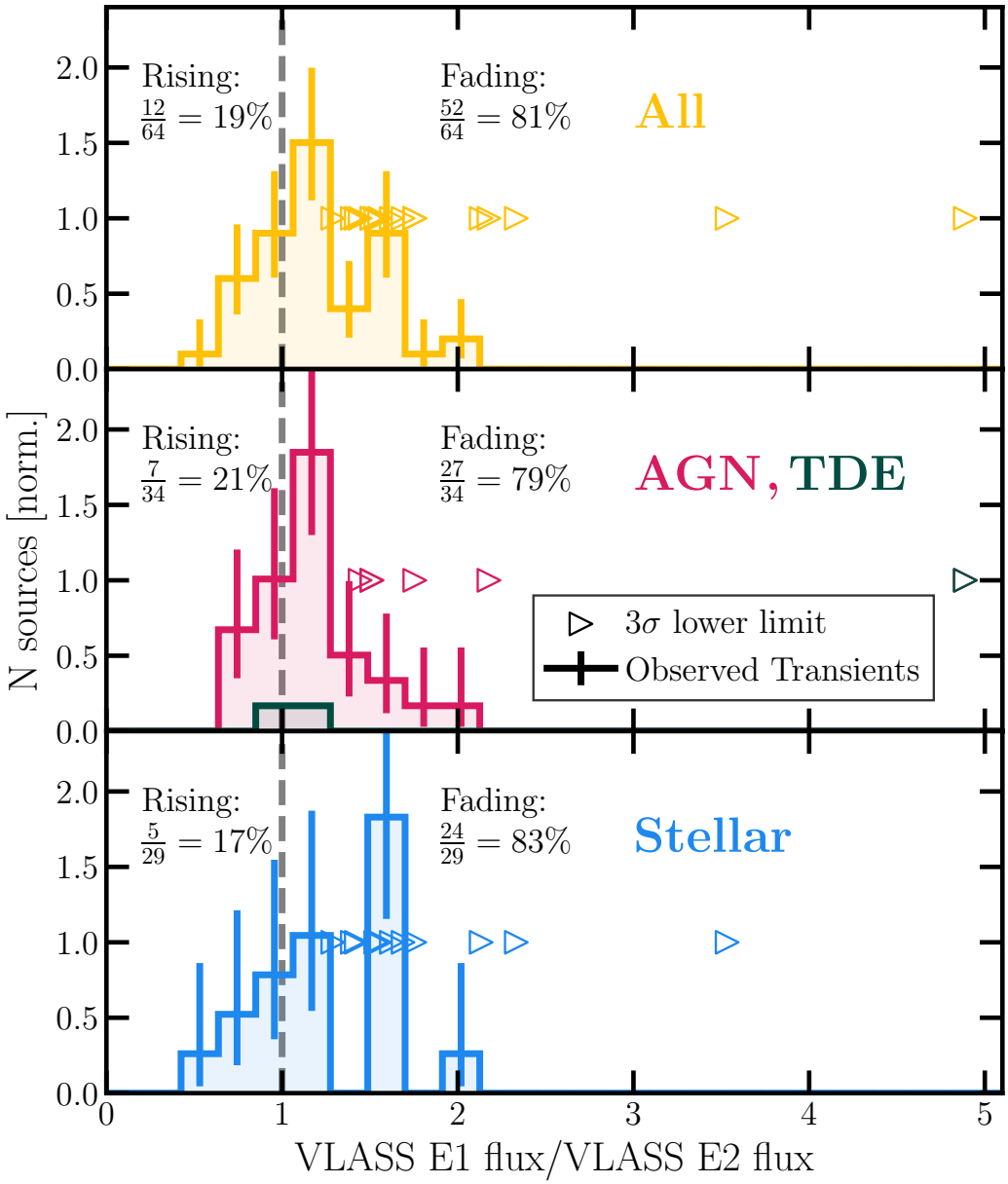

Figure 2.14: VLASS E1 to E2 flux ratios for the full transient sample (*top* panel), SMBH flares (middle panel), and stellar explosions (*bottom* panel). Those sources that are not detected in VLASS E2 are shows as 3σ lower limits. The large majority of sources are fading, and this trend becomes more extreme for just SMBH flares. Stellar explosions show a slightly wider range of flux ratios.

4000 $\mathrm{Gpc^{-3}\ yr^{-1}}$ for $10^{27} < L_\nu/\mathrm{erg\ s^{-1}Hz^{-1}} < 10^{30}$ or 4×10^{-2} per year per galaxy within 200 Mpc in the same luminosity range.

Previous observations of transient radio emission from AGN have been biased toward more luminous sources at higher redshifts. Wołowska et al., 2021 identified AGN flares in a comparison between the 2012 Caltech-NRAO Stripe 82 Survey (CNSS) at 3-GHz and FIRST. These authors presented a sample of twelve radio transients in AGN. They obtain follow-up VLBA observations and VLA SEDs, as well as optical and X-ray observations in select cases. These events fall into the class of Gigahertz-Peaked Spectrum (GPS) sources. GPS sources, and the closely related Compact Steep Spectrum (CSS) sources, are thought to be AGN with young, pc-scale jets. There have been a number of observational studies of these young jets, both through searches for AGN with radio emission peaking in the GHz range, which are indicative of a young jet, or through searches for transient radio emission from AGN on year to decade timescales (e.g., Nyland, Dillon Z. Dong, et al., 2020). Some of these young jets are the precursors to FR I/II galaxies Fanaroff and Riley, 1974, which contain AGN with spatially-extended, kpc-scale radio emission suggestive of old, powerful jets. However, there is an excess of compact jets relative to kpc-scale jets. The remaining jets may have been frustrated by a dense circumnuclear medium or they may be produced during short-timescale ($< 10^4$–10^5 year) radio variable periods. The latter possibility is analogous to the short-timescale radio variability that occurs in X-ray binaries, which produce variable radio jets when they are in low accretion rate states that are then suppressed in high accretion rate states.

Our sample is distinct from the GPS and CSS sources, and in particular those presented by Wołowska et al., 2021. The most notable difference is in the luminosities: our sample is the luminosities of our AGN flares are remarkably low: all but one of sources lie in the range $L_\nu(3\ \mathrm{GHz}) \sim 10^{27.3-28.7}\ \mathrm{erg\ s^{-1}\ Hz^{-1}}$. Moreover, from the discussion on synchrotron emission in Section 2.3, the physical size of the radio-emitting regions are $\sim 10^{16}$ cm$\sim$0.01 pc, and the average speed of these regions since launch is likely extremely sub-relativistic. This suggests that it is unlikely that we are observing young, relativistic jets: the observed sources are moving too slowly and are too small. If we are observing jets, they are very weak jets that have been frustrated at very low radii. These jets could be sub-pc precursors to the GPS/CSS sources that failed and will not successfully form pc-scale jets, as some of the pc-scale jets fail to reach galactic scales. They could also be transient,

X-ray-binary-like jets.

Alternatively, we may be observing non-relativistic outflows from AGN. Multiwavelength observations, including of broad absorption lines in quasars and blue-shifted absorption lines in the X-ray, strongly suggest that AGN accretion disks can launch winds with $v/c \lesssim 0.2$. The mechanisms by which winds can be driven from accretion disks remain unknown. At sufficiently low densities, portions of the disk may experience a higher heating rate than a cooling rate, producing thermally driven winds (Begelman, McKee, and Shields, 1983). Radiation pressure can accelerate line-driven winds off of the disk (Proga, Stone, and Kallman, 2000), or AGN may produce MHD winds (Contopoulos and Lovelace, 1994). These models are generally able to match the observed velocities, although whether the density structure above the wind-launching region of the disk is conducive to ∼decade timescale radio emission is unconstrained. It is plausible to imagine a wind propagating slowly through a relatively low-density medium, possibly consisting of the remnants of previous outflows. Alternatively, there are more exotic models that may be able produce the observed emission, such as stellar explosions within the accretion disk (Jermyn et al., 2022; Perna, Lazzati, and Cantiello, 2021), although it is not established that the shocks created during the stellar explosions could break through the disk. Multiwavelength follow-up of our AGN sample combined with simulations of the evolution of the emission produced by these wind mechanism would enable tighter constraints on the origin of our transients.

Regardless of the precise triggers of our AGN flares, they are almost all consistent with low velocity, weak jets, or outflows. As mentioned earlier, one of the AGN flare candidates, ID 11, has a luminosity almost one order of magnitude brighter than any other AGN flare: $L_\nu(3\,\mathrm{GHz}) \sim 10^{29.5}$. This source can be clearly seen in the AGN luminosity function in Figure 2.13, alone in the highest luminosity bin. We briefly summarize the properties of this source in more detail here. This source was discovered by Wołowska et al., 2021, who obtained extensive follow-up observations. In 2015, they observed this source with the VLBA and observed a core-jet structure. One year later, only the core was visible. VLA SEDs for this source show evolution of the peak frequency and flux from ∼6 GHz and ∼12 mJy in 2014 to ∼4 GHz and ∼16 mJy in 2015 to ∼3 GHz and ∼12 mJy in 2016. Finally, this sources shows faint $\sim 10^{40}$ erg s^{-1} X-ray emission. This source can be interpreted as a weak, young jet that failed to expand.

In summary, we have discovered a population of ∼20 AGN flares between FIRST and VLASS that probe a completely unexplored regime of luminosity: $26 \lesssim \log L_\nu/\mathrm{erg\ s^{-1}\ Hz^{-1}} \lesssim 29$. Based on the physical parameters of the radio emitting regions inferred earlier in this work, we expect that the observed flares are caused by weak jets that are frustrated at very low radii $\lesssim 10^{17}$ cm, weak jets produced as part of a transient phenomenon, or non-relativistic outflows. In any case, the observed population is distinct from previous populations of compact radio sources.

TDEs

Tidal disruption events occur when a star ventures within the tidal radius $R_T \sim (M_{\mathrm{BH}}/M_*)^{1/3}$ of the SMBH in the center of a galaxy and is shredded (Frank and M. J. Rees, 1976; Martin J. Rees, 1988; van Velzen, Farrar, et al., 2011; Donley et al., 2002). The galaxy black hole mass must be $\lesssim 10^8\ M_\odot$ for a TDE to be possible; outside of this limit, the star is swallowed whole rather than shredded. TDEs are thought to produce streams of stellar debris that collide due to Lense-Thirring precession, resulting in shocks that dissipate energy and allow the formation of an accretion disk (Bonnerot and Lu, 2020). Some fraction of the stellar debris will become unbound, forming an outflowing wind (e.g., Lu and Bonnerot, 2020).

Radio emission from tidal disruption events is particularly poorly understood, largely due to a dearth of observations. Until recently, radio detected TDEs appeared to form a dichotomy: the extremely luminous ($L_\nu \gtrsim 10^{40}$ erg s^{-1}) jetted TDEs and the lower luminosity non-relativistic events ($L_\nu \lesssim 10^{38}$ erg s^{-1}) (Kate D. Alexander et al., 2020). In both cases, the emission starts in the days or weeks post-disruption. The advent of full sky radio surveys like VLASS, and the commencement of programs to follow-up TDEs in the radio months to years post-flare have dramatically changed the landscape. There is now evidence for weakly jetted TDEs with $L_\nu \gtrsim 10^{39}$ erg s^{-1} (e.g., Somalwar, Ravi, Dillon Z. Dong, et al., 2022), radio flares that turn ∼6 months post-disruption (e.g., Horesh, Cenko, and Arcavi, 2021), and radio flares that show multiple peaks (e.g., Sfaradi et al., 2022). Generally, the mechanisms thought to produce TDE radio emission are (1) a jet shocking against the circumnuclear material, (2) internal shocks in a jet, (3) outflowing stellar debris colliding with the circumnuclear material, or (4) an outflow launched from the accretion disk colliding with circumnuclear material (see Kate D. Alexander et al., 2020, and references

therein). Whether these are all the possible mechanisms and the relative dominance of each is still unknown. It is also possible that multiple jets/outflows are launched during a single TDE; for example, stellar debris can form a wind that emits in the radio after colliding with the circumnuclear medium, and later a jet could launch that would produce a second radio peak.

We identified TDE candidates as nuclear flares in quiescent galaxies. We have discovered one strong TDE candidate (ID 18), and two moderate candidates (ID 39 and ID 40). All events have low black holes masses $\lesssim 10^8\ M_\odot$, based on the fact that SDSS cannot resolve the line widths in the stellar continuum. They are at moderate luminosities $\sim 10^{28}$ erg s^{-1} Hz^{-1}.

The presence of TDE candidates in our sample suggests that TDEs can produce radio emission that evolves on decade timescales. Before this work, only a few events had been discovered that may have radio emission on such timescales, but they tend to be hosted by Seyferts and so could be an AGN flare (Somalwar, Ravi, Dillon Z. Dong, et al., 2022). This event (VT J024345.70-284040.080) was also at a much higher luminosity $\sim 10^{40}$ erg s^{-1}, suggesting that it was jetted. In contrast, the TDE candidates in our sample are at luminosities $\sim 10^{38}$ erg s^{-1}, implying that TDEs can produce long-lived radio emission at luminosities near $\sim 10^{38}$ erg s^{-1}. Given that we expect the outflow radius to be $\sim 10^{17}$ erg s^{-1} and the outflow to have a very slow average velocity, we could be observing a very weak jet that slammed into dense material near the black hole. This jet would have to be decelerated extremely quickly to match our expected non-relativistic average velocity, rendering this possibility unlikely. We could be observing unbound stellar debris that has collided with circumnuclear material. Yalinewich et al., 2019 predict a velocity $\sim 10^4$ km s^{-1} for unbound debris, which is higher than our average velocity but not impossible given the large uncertainties in our average velocity calculation.

The TDE rates inferred from our sample constrain the rate of $\sim 10^{28}$ erg s^{-1} Hz^{-1}, decade-long radio flares from TDEs. Theoretical and observational work has suggested that TDEs occur at a rate of $10^{-(4-5)}$ galaxy^{-1} yr^{-1} (van Velzen, Holoien, et al., 2020). We observe a rate $\sim 10^{-2.53\pm0.4}$ galaxy^{-1} yr^{-1} in the luminosity range $36 \lesssim \log L/\mathrm{erg\ s^{-1}} \lesssim 39$, although we fixed the luminosity function slope in this fit so the uncertainties are underestimated. Moreover, we do not have strong constraints on the luminosity range expected for TDE radio emission. Considering only events

with $L \sim 10^{29}$ erg s^{-1} Hz^{-1}, like those observed, we expect a rate that is a factor $\sim$100 – 1000 lower, in which case $\sim$1 – 30% of TDEs would produce radio emission like that observed. Hence, we cannot exclude the possibility that a large fraction of TDEs emit in the radio on decade timescales.

We have neglected the possibility of TDEs in AGN in the above analysis. Our TDE selection criteria will likely miss events. TDEs can happen in AGN (e.g., Chan et al., 2019), which means that our AGN sample may be contaminated by TDEs. We will briefly discuss this possibility later. Our rate may be enhanced if some of the objects we identified as AGN are in fact TDEs. ID30, for example, was published by M. M. Anderson et al., 2020 as a TDE candidate, although we identify it as an AGN flare because the host galaxy is a Seyfert. In doing so, we are defining an AGN flare to include any event that produces transient radio emission in an AGN, while a TDE exclusively refers to stellar disruptions in quiescent galaxies. We choose these definitions as it is reasonable to expect that the mechanisms that produce radio emission from TDEs in AGN will be affected by the presence of a pre-existing accretion disk, and thus analyzing those events in combination with TDEs in quiescent galaxies will produce erroneous results. As we have discussed, there are many possible mechanisms at play in the observed AGN flare population, even when disregarding possible TDEs. In the future, when large multiwavelength datasets are readily available, it will be more feasible to distinguish between TDEs in AGN and other radio flare triggers. For now, definitively identifying TDEs in AGN remains an unsolved problem.

Our TDE selection may also include interlopers. We could be identifying new or restarted LERGs, since these AGN such low accretion rates that optical narrow-line emission that is either undetectable or not present. The stellar mass of our strong TDE candidate ($\sim 10^{9.1}\ M_\odot$) is on the low tail of the LERG stellar mass distribution, which peaks near $\sim 10^{10.5}\ M_\odot$ in SDSS, whereas it is very consistent with TDE stellar masses. The moderate candidate has a higher stellar mass $\sim 10^{9.8}\ M_\odot$ that is more consistent with the LERG population, but also consistent with TDEs. Further exploring the possibility of low accretion rate AGN flares masquerading as TDEs requires extensive multiwavelength follow-up.

In summary, we have identified two strong TDE candidates. These events indicate that $\sim$1 – 30% of TDEs may produce radio emission that is very long lived

(~decade timescales) without requiring a jet. We suggest that this radio emission is caused by a non-relativistic outflow colliding with circumnuclear material. A wind formed of unbound stellar debris may be able to reproduce our observations.

Stellar Explosions

Summary of the Sample

In our sample of 64 galaxy-associated radio transients, 23 are off-nuclear, with positions that are astrometrically distinct from their host galaxy nuclei. Of these, 22/23 (95.7%) are located in regions that are either confirmed by SDSS spectroscopy to be dominated by star formation or have blue optical colors suggestive of being an HII region. The host galaxies themselves are also predominantly star-forming; 21/23 have SDSS spectra of which 20/21 (95.0%) have BPT ratios consistent with star formation at the location of the SDSS fibers (typically nuclear). The BPT ratio fraction is directly comparable to the fraction in the host galaxy reference catalog and, assuming Poisson uncertainties, is a $\sim 3\sigma$ excess relative to the overall prevalence of star-forming spectra in local universe SDSS galaxies. The preference for off-nuclear transients to be located in star-forming regions is consistent with our interpretation of these transients as stellar explosions (which are expected to track the often off-nuclear sites of recent star formation) as opposed to SMBH flares (which are expected to track galaxy nuclei). Other theoretical non-stellar explosions are possibly present in our sample. These include flares from wandering black holes (Reines, James J. Condon, et al., 2020; Eftekhari, E. Berger, B. Margalit, B. D. Metzger, et al., 2020), and rapidly inflating hyper-nebulae caused by highly super-Eddington accretion onto stellar mass black holes (Sridhar and Brian D. Metzger, 2022). However, more observational evidence would be required to make a strong case for any of these theories. The one off-nuclear transient not located on a star-forming region (ID 58) is offset by ~100" from a massive elliptical galaxy in the Virgo cluster, and is one of only two sources separated by more than 20" from its potential host. This source, while intriguing, carries a higher risk of being a background source due to large area subtended by the galaxy. We do not give a classification for this source and defer analysis to a future paper. Among the remaining 41 nuclear transients, we have classified 7 as stellar explosions. We assign 5 of the 7 classifications with high-confidence due to unambiguous BPT ratios and in some cases the presence of an optical supernova counterpart. The remaining 2 are low-to-medium confidence classifications with the potential of either being TDEs or AGN flares. Altogether, we have 29 likely stellar explosions in our sample with

an expected contamination rate of $0.9^{+5.1}_{-0.9}$ background sources (Section 2.3) and 2 ambiguous classifications.

Stellar Explosions are Diverse, Though we Expect Many are Supernovae

In our classification scheme, we chose to use the term “stellar explosion” rather than “supernova" because we are classifying the transients by their co-location with star-forming regions rather than by their spectroscopic properties. This distinction is highlighted by one of our transients (VT 1137-0337 / ID 50) which has a flat and slowly evolving radio spectrum that is inconsistent with being a supernova. Instead, it is better explained as an emerging pulsar or magnetar wind nebula where the ejecta from the ~decades-old stellar explosion is a source of free-free absorption rather than significant radio emission (D. Dong and Gregg Hallinan, 2022). Despite the possibility of there being more VT 1137-0337-like (or other unusual) objects in our sample, initial radio follow-up of a subset of transients suggests that the majority are consistent with being supernovae (Dong et al. in prep). Additionally, as we will discuss below, all 6 stellar explosions with optical counterparts (Section 2.3) have features consistent with being supernovae. We therefore proceed with the remainder of this section under the assumption that we are primarily sampling a population of radio supernovae.

Jets or CSM interaction?

Luminous radio emission from supernovae (SNe) is caused by the shock interaction of a high-velocity outflow with the surrounding circumstellar medium (CSM). Two types of outflows have been observed from SNe: ejecta and jets.

A small fraction of supernovae launch relativistic jets in low-luminosity or long gamma ray bursts (GRBs). Observing the high-energy bursts characteristic of GRBs requires that the jets are relativistically beamed, such that for each detected event, there are many more that go undetected because their jets are pointed away from our line of sight (Frail, Kulkarni, R. Sari, et al., 2001). Due to the uncertain fraction that are missed, their volumetric rate is poorly constrained. One way proposed to address this problem is to detect off-axis jets via their radio emission, which at late times should be close to isotropic. Due to the high velocity of a GRB jet (which is able to shock a large volume of gas in a short time), jetted events generally do not necessarily require a dense CSM to reach luminosities detectable by VLASS.

However, such jets sweep past the characteristic ~ 0.1 pc scale where our senstivity is maximized in a span of just months. As an example, GRB 030329 reached its peak 2.3 GHz luminosity just 1 month after explosion. In the span of ~3 years, it faded by an order of magnitude at that frequency (A. J. van der Horst et al., 2007). Such an explosion would be detectable in our search for $\gtrsim 3$ years if it were luminous enough to be $\gtrsim 50\sigma$ at peak. While this would have been the case for GRB 030329 if it were located within 200 Mpc, there are many examples of jets that are less luminous (e.g., Corsi, A. Gal-Yam, et al., 2016) and would require us to get lucky to detect them at peak. Candidates for these jets, if present in our sample, might be drawn from the 10 stellar explosions that are detected in Epoch 1 but not Epoch 2. It is, however, difficult to test this possibility without more observational evidence and more detailed modeling (particularly because off-axis jets should fade slower than on-axis ones like GRB 030329). We therefore defer this analysis to a future paper where we will present broadband radio spectra of the stellar explosion sample.

Nearly all SNe launch roughly spherical ejecta made of the bulk of the star unbound by the explosion. These ejecta have masses ranging from fractions to tens of solar masses, and have velocities within a factor of a few of $\sim 10^4$ km s^{-1} (e.g., Taddia, Sollerman, et al., 2015; Martinez et al., 2022). In the absence of dense gas surrounding the SN (as is the case with many type Ia SNe; e.g., Chomiuk et al., 2016), much of the $\sim 10^{51}$ erg of energy stored in these ejecta is dissipated in the surrounding ISM on a timescale of $\sim 10^3$ years. The resulting radio supernova *remnants* tend to peak at luminosities $L_\nu \sim 10^{24}$ erg s^{-1} Hz^{-1} (Sarbadhicary et al., 2017), far lower than the $\gtrsim 10^{28}$ erg s^{-1} Hz^{-1} required for detection by VLASS in most of our searched volume. Instead, in order for ordinary supernova ejecta to reach a luminosity detectable in VLASS, there must be a reservoir of dense gas to shock in the immediate vicinity (~0.1 pc) of the explosion.

Clouds of sufficiently dense gas can be found throughout the interstellar medium (ISM). However, any star massive enough to explode in a supernova should have long since blown away the ambient ISM within a ~1 pc radius with its radiation pressure and winds. Instead, the sub-parsec region relevant for GHz radio emission is filled with a circumstellar medium (CSM) made of gas ejected from the star itself. For many stars, this region is filled with an approximately spherical stellar wind with a density profile $\rho(r) = \frac{\dot{M}}{4\pi r^2 v_{\rm wind}}$, where $\dot{M}$ is the average mass loss rate and $v_{\rm wind}$ is the wind velocity. The mass loss rate and velocity depend on the type of

star (see Smith, 2014, for a review). For most massive stars, the (number) density of CSM particles at a distance ~ 0.1 pc from the star due to this wind is not much more than the $\sim 10^1 - 10^3$ cm^{-3} characteristic of HII regions. These relatively low CSM densities are consistent with the low peak radio luminosities of typical core collapse supernovae (a median value of $L_\nu \sim 10^{25.5}$ erg s^{-1} Hz^{-1}; Bietenholz, Bartel, et al., 2021). Some massive stars (particularly luminous blue variables and supergiants) can have much denser winds owing to their high mass loss rates and/or low wind velocities. These may be the progenitors of some type II narrowline (IIn) supernovae (Smith, 2014) which are characterized by early optical signatures of CSM interaction and tend to have higher peak radio luminosities (a median value of $L_\nu \sim 10^{26.5}$ erg s^{-1} Hz^{-1}; Bietenholz, Bartel, et al., 2021). However, despite the relatively high radio luminosities of IIn SNe, they are still on average more than an order of magnitude less luminous than the typical stellar explosion in our sample. In order for CSM interaction to produce the characteristic luminosities that we are observing, there need to be even higher CSM densities within the radio-emitting region. Additionally, the luminous 3 GHz emission that is produced needs to not be entirely attenuated by synchrotron self-absorption or free-free absorption. This combination of high density and weak absorption requires specific physical conditions in the CSM and can be seen in all six supernovae where we have deeper contextual information through the presence of optical counterparts. We discuss these case studies below.

Three SNe with Archival Optical Counterparts

We begin with the three stellar explosions (two nuclear and one off-nuclear) that are associated with archival optical supernovae. All 3 supernovae exploded in 2011 or 2012, roughly 5-8 years before detection in VLASS Epoch 1. Each supernova was initially classified with as a different optical spectral type, but by selection, all of them share the property of being substantially more radio-luminous than typical optically-detected supernovae of any class.

Of the three archival supernovae, PTF 11mpv (ID 24) is the least well-studied. It was first detected on September 17th, 2011 by the Palomar Transient Factory (N. M. Law et al., 2009). A follow-up spectrum was taken ~1 week later with the Intermediate-dispersion Spectrograph and Imaging System (ISIS) on the William Herschel Telescope (WHT), leading to its classification as a type II supernova (Avishay Gal-Yam et al., 2011). As discussed in Section 2.3 and shown in Figure

2.5, there is some ambiguity to this classification. Due in part to the unknown epoch of discovery, a number of stripped envelope classifications including IIb, Ic, and Ic-BL are all reasonable. A spectrum taken with Keck/LRIS at an epoch of ∼6 years post-explosion is consistent with emission from the host galaxy (Figure 2.6). Regardless of its optical classification, PTF 11mpv is more radio luminous than typical supernovae of any class. In VLASS Epoch 1 (6.1 years post-explosion), it had a flux of 0.7 ± 0.14 mJy, corresponding to a luminosity of $(3.1 \pm 0.6) \times 10^{28}$ erg s^{-1} Hz^{-1}. By comparison, both type II and type Ib/c supernovae have a median peak radio luminosity of $\sim 10^{25.5} - 10^{26.5}$ erg s^{-1} Hz^{-1} (Bietenholz, Bartel, et al., 2021), and most but not all type Ic-BL supernovae have radio luminosities $\lesssim 10^{27.5}$ erg s^{-1} Hz^{-1} (Corsi, A. Gal-Yam, et al., 2016).

As further confirmation of the radio transient and as a probe of its radio properties, we took two follow-up radio spectra with the VLA under programs 18A-481 (6.7 years post-explosion) and 19A-422 (7.6 years post-explosion). We calibrated and imaged the data using standard procedures in CASA (McMullin et al., 2007). The transient is clearly detected in both follow-up spectra, with a peak in the first follow-up epoch of ∼2 GHz (as expected from selection biases; Section 2.3) and a similar value in the second follow-up epoch (Dong et al. in prep). Nine years after explosion in VLASS Epoch 2, the supernova has faded below the VLASS detection threshold, with a 3σ upper limit of 0.42 mJy, corresponding to $L_\nu \lesssim 2 \times 10^{28}$ erg s^{-1} Hz^{-1}.

Given that PTF 11mpv is potentially associated with a Ic-BL (the only type of supernova that has been associated with relativistic jets; e.g., Kulkarni, Frail, et al., 1998), it might seem reasonable at first to expect that the luminous radio emission is due to a jet. However, the shock radius implied by the follow-up radio spectra is $r_{\rm shock} = (1.1 \pm 0.1) \times 10^{17}$ cm, implying a very sub-relativistic average velocity of $v_{\rm shock} \sim 5000$ km s^{-1}. Though it is possible that PTF 11mpv launched a relativistic jet at explosion, such a jet would have promptly escaped to a much larger radius than the present-day shock (since even the densest CSM is not sufficient to stop a relativistic jet; e.g., Duffell and A. Y. Q. Ho, 2020). We thus conclude that any such just has long since faded, and that the recent radio emission observed for PTF 11mpv is due to CSM interaction.

PTF 11qcj (ID 49) was first observed spectroscopically ∼2 weeks after its photometric discovery on November 1, 2011. Similar to PTF 11mpv, the early spectrum

had a broad line of width ∼22,000 km/s in its near IR Ca II triplet (8498 - 8662 Å). However, the rest of the spectrum did not show any signs of H or He emission, leading the automated supernova classifier *Superfit* to classify it as a type Ic-broadline (Ic-BL) supernova. Due to this classification, Corsi, A. Gal-Yam, et al. (2016) began a multi-wavelength monitoring campaign of this supernova. Later spectra taken as part of this campaign at epochs of ∼2 - 3 months post discovery more closely resemble the stripped-envelope (type Ib) supernovae 2008D and 1985F (Corsi, E. O. Ofek, et al., 2014). A final spectrum taken ∼5 years post-explosion was consistent with host-galaxy emission (Palliyaguru et al., 2019). At no observed point did its spectra show evidence of the narrow or intermediate-width hydrogen lines typically used as indications of CSM interaction in optical supernovae.

Two weeks after first detection in the optical, PTF 11qcj was detected in a 6 GHz VLA observation at a flux of 0.42 ± 0.03 mJy, corresponding to a luminosity of $L_\nu \sim 8 \times 10^{27}$ erg s^{-1} Hz^{-1} (Corsi, E. O. Ofek, et al., 2014). Over the next ∼2 months, it rose to an initial plateau of $\sim 3 \times 10^{28}$ erg s^{-1} Hz^{-1} which it maintained for ∼1 year before continuing to rise in luminosity to a second peak at 5 GHz of $\sim 2 \times 10^{29}$ erg s^{-1} Hz^{-1} extending all the way to 5.1 years post-explosion (Palliyaguru et al., 2019). By the time of VLASS Epoch 1 (7.4 years post-explosion), PTF 11qcj's 3 GHz flux had faded to 6.4 mJy, from its 3.4 GHz peak of 9.9 mJy in Year 5. It continued to fade into VLASS Epoch 2 (10.0 years post-explosion), reaching a 3 GHz flux of 3.2 mJy.

Though PTF 11qcj was initially speculated to have launched a jet due to its high radio luminosity and Ic-BL classification, the slow evolution and subsequent VLBI-based upper limit of $\lesssim 5 \times 10^{17}$ cm on the late-time shock radius show that the late-time radio emission is dominated by CSM interaction rather than a jet. Its double radio peak suggests that there is structure in the radial density profile of the CSM, with the second peak potentially being due to a density enhancement at $\sim 10^{17}$ cm (Palliyaguru et al., 2019). The structured CSM scenario stands in contrast to widely-adopted models of supernova CSM interaction where the ejecta encounter a smooth power-law wind (e.g., Roger A. Chevalier, 1998).

Unlike PTF 11qcj, SN 2012ab (ID 12) showed immediate signs of CSM interaction in the form of both broad and intermediate-width components to its Hα line. This led to its classification as a type IIn supernova (Bilinski et al., 2018). At early

times (days 16-52), the broad component is dominated by blueshifted Hα emission, extending out to $-14,000$ km s^{-1} at its zero-flux point. At later times (days $\sim$ 137 - 289), the broad component is dominated by a redshifted Hα wing extending out to $\sim 20,000$ km s^{-1}. At around day 119, the intermediate width component emerged from being blended with the broad component to become the dominant Hα feature. On day 137, it was centered at a redshifted velocity of $\sim$800 km s^{-1} and had a width of $\sim$4500 km s^{-1}. Signatures of this intermediate width component remained in the spectrum on day 1206 (3.3 years), though the broad component had since faded. The asymmetric and shifting Hα components led Bilinski et al. (2018) to propose a unifying model with an aspherical high-density shell at a radius of $\sim 2\times10^{16}$ cm that has a higher density and is physically located at a larger radius on the far (redshifted) side. This CSM asymmetry is reinforced by the relatively strong continuum polarization (typically a hallmark of asymmetric emission or absorption) coupled with the depolarization of the Hα emission, which suggests that the continuum polarization is intrinsic rather than due to CSM dust. Altogether, this model suggests asymmetric and heavy mass loss at an average rate of $\sim 5 \times 10^{-2} \left(\frac{v_{\rm CSM}}{100 \text{ km s}^{-1}}\right)^{-1} M_\odot$ yr^{-1}. As discussed by the authors, this type of mass loss is likely due to the influence of a binary companion which will tend to cause mass to be ejected in the plane of the binary.

Shocks propagating in dense, extended CSMs are powerful engines for creating luminous radio transients with synchrotron self-absorption peaks at $\sim$GHz frequencies (Section 2.3). When the CSM is aspherical, there will be many lines of sight along which the density is lower and where the shock will have already swept through rapidly and superheated the gas to $\sim 10^8$ K. Both the lower density and high temperature suppress free-free absorption, allowing the GHz radio transient to shine through along those lines of sight (D. Z. Dong et al., 2021). The detection of SN 2012ab as a 3 GHz transient with a high luminosity of $\sim 4 \times 10^{28}$ erg s^{-1} Hz^{-1} in Epoch 1 of VLASS (7.0 years after discovery) thus supports the picture of heavy, aspherical mass loss presented in Bilinski et al. (2018). The fact that it faded between Epoch 1 and Epoch 2 (9.7 years post-explosion) suggests that the peak has passed through 3 GHz and, assuming synchrotron self-absorption, that the shock is now at a radius of $\gtrsim 5 \times 10^{16}$ cm. The relatively small degree of fading ($\sim$ 30% in 2.7 years) suggests that there continues to be CSM interaction at this radius, consistent with the mass loss episode starting even earlier than previously proposed: $\gtrsim 1.5 \left(\frac{v_{\rm CSM}}{100 \text{ km s}^{-1}}\right)^{-1}$ centuries before core collapse.

Three SNe with Follow-up Optical Counterparts

In addition to the three supernovae found in optical transient searches, we have found emission lines reminiscent of nebular emission from CSM-interacting supernovae in 3 additional stellar explosions: IDs 56, 57, and 59 (Figure 2.6). All 3 transients were first discovered in an early version of the search presented in this paper which covered only VLASS Epoch 1.1. We discuss these transients below.

VT 1210+4956 (ID 56, analyzed in detail in D. Z. Dong et al., 2021) is located in a dwarf star-forming galaxy at distance $d_L = 153.6$ Mpc, and is associated with an X-ray burst detected by the MAXI Gas Slit Camera on August 14, 2014 (Serino et al., 2014a). The short duration of the X-ray burst coupled with its luminosity and spectral softness (a peak at ∼5 keV) implies a jet of Lorenz factor $\Gamma > 2$, presumably launched on the day of explosion. In Epoch 1 of VLASS, 3.3 years after explosion, VT 1210 had 3 GHz luminosity of $\sim 7.5 \times 10^{28}$ erg s^{-1} Hz^{-1}. In two follow-up radio SEDs taken at 3.8 and 4.7 years after explosion, VT 1210 was observed to have a slowly evolving spectral peak at ∼5 GHz of luminosity $\sim 2 \times 10^{29}$ erg s^{-1} Hz^{-1}. In both epochs, the optically-thick part of the spectrum dropped too shallowly toward low frequency to be explained by free-free absorption, implying that the peaks are due to synchrotron self-absorption. In Epoch 2 (6.0 years post-explosion), VT 1210+4956's 3 GHz luminosity has risen to 1×10^{29} erg s^{-1} Hz^{-1}, suggesting that the peak is now closer to 3 GHz, consistent with the slow SED evolution observed in the radio follow-up epochs.

Based on the follow-up radio SEDs, we concluded that the radio emission was produced by a slow moving shock ($v_{\rm shock} \sim 2000$ km s^{-1}) at a radius of $\sim 10^{17}$ cm, interacting with a high CSM density of $\sim 10^6$ cm^{-3}. The slow shock velocity and high CSM density suggests that the radio emission at this late time is not due to the jet, and is instead due to the interaction of slower, more massive ejecta with the CSM. In order to explain the combination of high density and negligible GHz-frequency free-free absorption, we proposed a scenario similar to SN 2012ab where the CSM is aspherical and we are looking along a line of sight where the free-free absorption is suppressed. This scenario is reinforced by the presence of an intermediate-width Hα feature (observed 3.7 years post-explosion; Figure 2.6) reminiscent of the one seen persisting in SN 2012ab at an epoch of 3.3 years. Similar to Bilinski et al. (2018), we concluded that the aspherical CSM at large radius is due to binary interaction-driven eruptive mass loss, in our case ∼a few centuries before

explosion. This delay of ∼centuries is difficult to explain with either pre-supernova instabilities (which should take place just a few years before explosion; e.g., Wu and Fuller, 2021), or coincidental binary interaction (which at the slightly sub-solar metallicity of VT 1210's host galaxy should take place $\sim 10^4 - 10^6$ years before core collapse; e.g., Klencki et al., 2020). This suggests a causal link between the binary interaction and the stellar explosion. To explain this link, and to explain the relativistic jet (which would require a compact object to launch), we proposed that the stellar explosion was driven by the inspiral of the compact object in a high-mass X-ray binary undergoing unstable mass transfer. This scenario, first presented in Roger A. Chevalier (2012), has been referred to as a merger-driven explosion (e.g., Schrøder et al., 2020) or as a common envelope jets supernova (e.g., Soker, Grichener, and Gilkis, 2019). In this scenario, during either Roche lobe overflow (e.g., Pejcha et al., 2017) or the common envelope phase (e.g., Ivanova et al., 2013), the compact object ejected mass at a rate $\gtrsim 10^{-2} M_\odot$ yr^{-1}, sending it outwards in a spiral in the plane of the binary (e.g., Smith, 2014). After entering the star (likely as it reached the core; Roger A. Chevalier, 2012), the compact object then started a phase of extremely rapid accretion, launching the jet and causing the stellar explosion. The ejecta from the explosion then crashed into the dense spiral of CSM which had been expanding for centuries, creating the luminous shock traced by the radio and intermediate-width Hα emission (D. Z. Dong et al., 2021).

As seen in Figure 2.6, both of the other stellar explosions with late-time optical features also have a similar intermediate-width Hα line. One of these is VT 1441+2913 (ID 57), which is located in another star-forming dwarf galaxy at a distance $d_L = 55.2$ Mpc. In Epoch 1, VT 1441+2913 had a 3 GHz luminosity of 1.8×10^{28} erg s^{-1} Hz^{-1} and in Epoch 2 (2.9 years after Epoch 1), it had a barely changed luminosity of 1.6×10^{28} erg s^{-1} Hz^{-1}. The extremely slow evolution of its radio lightcurve suggests that it has a very slow shock velocity, keeping its peak frequency roughly in the same position. This picture is corroborated by its exceptionally narrow Hα feature, which has a velocity dispersion of 820 ± 15 km s^{-1} (measured using the same MCMC-based multiple Gaussian fitting technique used in D. Z. Dong et al., 2021). Interpreting the velocity dispersion as the post-shock velocity in the dense Hα emitting gas (e.g., Heng, 2010) suggests that the gas likely has a density of order $\sim 10^7$ cm^{-3}. If (similar to all of the supernovae discussed above) the CSM is located in the range where our search is most sensitive $\sim 10^{16} - 10^{17}$ cm, an even heavier episode of eruptive mass loss likely took place $\gtrsim 1$ century before explosion.

In addition to the intermediate-width Hα, VT 1441+2913 has a pair of much broader emission features of width $\sim 7500 \pm 1000$ km s^{-1} corresponding to the [OIII] 4959, 5007 Å doublet. Similar oxygen features have been seen in the late-time nebular features of a number of supernovae (e.g., Dan Milisavljevic, Fesen, et al., 2012), including SN 2014C (which transitioned from a type Ib to a type IIn SN) where it is attributed to a reverse shock back-propagating through the oxygen rich ejecta (D. Milisavljevic et al., 2015; Margutti, Kamble, et al., 2017) and the type Ib-peculiar SN 2012au where it is attributed to a candidate emerging pulsar wind nebula (Dan Milisavljevic, Patnaude, et al., 2018). Given the strong evidence for CSM interaction from the slowly evolving radio emission and low-velocity Hα emission, we favor the reverse shock explanation in this case. Under this interpretation, the sharp velocity contrast between the [OIII] and Hα emission suggests that in between the reverse shock and the forward shock, the supernova ejecta has sharply decelerated from $\sim$ 7500 km s^{-1} to $\sim$ 1000 km s^{-1}. This suggests that instead of having a smoothly declining CSM density profile, the dense CSM is concentrated in a heavy clump at the current radius of the forward shock. If so, the mass loss may have taken place in a sudden eruption instead of a smooth flow leading up to explosion.

The other stellar explosion with nebular features in our sample is VT 1252+2203 (ID 59), located on a bright star-forming region in a dwarf galaxy at distance d_L = 98 Mpc. Similar to VT 1441+2913, there is relatively low-velocity Hα emission (FWHM 1300 ± 370 km s^{-1}) along with much broader [OIII] emission $\sim$ 6000 km s^{-1}. The [OIII] velocity is difficult to fit in part because there is visually apparent substructure in the line profile (Figure 2.6) that cannot be described with single narrow/broad components centered at the doublet's rest frequencies. As evidence of this, the best-fit single broad Gaussian for the 5007 Å line has a width of 7600 ± 700 km s^{-1}, while the equivalent for the 4959 Å line has width 5500 ± 750 km s^{-1}. The same substructure is also apparent in the other oxygen lines (OI and OII) seen in the spectrum. In the context of CSM interaction, this suggests that there are multiple zones with different red/blueshifts and sharper/weaker velocity contrasts between the forward and reverse shocks. Such substructure would be a natural consequence of an aspherical and structured CSM which, as we have seen, seems to be ubiquitous among the radio-luminous supernovae found in our search.

Unifying Properties of the 6 Case Studies

Altogether, all of the 6 stellar explosions discussed above are likely caused by the interaction of supernova ejecta with a dense and structured CSM located at a typical radius of $\sim 10^{16} - 10^{17.5}$ cm. In each of the cases where we have early optical spectra, there are high-velocity features of width $\sim 20,000$ km s^{-1}. Two out of 3 of these spectra are consistent with Ic-BL supernovae, the only type to have been associated with jets. However the only transient with direct evidence for a jet is VT 1210+4956, which was not detected in optical transient surveys (likely due to incomplete coverage, as it passed behind the sun shortly after the X-ray flare; D. Z. Dong et al., 2021). The type of CSM responsible for our transients is a natural byproduct of certain types of binary interaction (including inspirals of compact objects), provided that they occur at the right time (~centuries) before explosion. The timing, asymmetry, and scale of mass loss are difficult to explain with non-binary mechanisms, though much remains to be learned about eruptive mass loss in the late stages of a star's life.

It is striking that despite the rapid growth in the supernova detection rate throughout the 2010s, all 3 supernovae detected in optical surveys exploded between 2011 and 2012 (5-8 years before detection in VLASS), and the only other one with an explosion date (VT 1210+4956) was first detected ~3 years after explosion. Though the sample is small and our coverage of the radio lightcurve is sparse, we speculate that this may be because the stellar explosions do not reach their peak 3 GHz luminosity until after a delay of $\gtrsim 5$ years, and are therefore less likely to be detected in our survey at early times. This is supported by the fact that VT 1210+4956 (which at an age of 3.3 years in VLASS Epoch 1 is the youngest stellar explosion in our sample with an explosion date) is even brighter in VLASS Epoch 2 than at first detection.

Physically, this explanation is consistent with a general picture where the ejecta initially interacts with a less dense CSM (slowing down slightly and producing a lower luminosity that peaks at higher frequency), and then crashes into a dense shell located at $\gtrsim 10^{16}$ cm (slowing down substantially and producing a much higher 3 GHz luminosity). At early times, if the exterior CSM is dense enough ($\gtrsim 10^4$ cm^{-3}), the GHz radio emission may also be suppressed by free-free absorption. CSM densities much larger than this are likely required to produce the slow moving shocks and intermediate-width Hα emission seen in SN 2012ab and the 3 explosions with nebular features. However at late times, the explosions become

detectable at GHz frequencies due to the asymmetry of the CSM which suppresses free-free absorption through the mechanisms described above. This hypothesis can be tested with further epochs of VLASS, which will provide late-time radio fluxes for an even larger sample of optically-detected supernovae.

Diversity and Rates of Stellar Explosions

The stellar explosions in our sample are a diverse group of transients. The sample includes ≥ 1 likely pulsar/magnetar wind nebulae (D. Dong and Gregg Hallinan, 2022), and ≥ 6 supernovae, of which at least one was likely triggered by the merger of a compact object and a massive star (D. Z. Dong et al., 2021). The data and analysis presented in this chapter are only a first step toward diagnosing the nature of this sample.

Based on the analysis in Section 2.6, stellar explosions at the high luminosities probed by our search are rare. Their volumetric rate of 350^{+85}_{-70} Gpc^{-3} yr^{-1} is roughly 0.3% of the volumetric core-collapse supernova rate (Taylor et al., 2014). More data and analysis are required to test our hypothesis that the sample is dominated by supernovae. However, based on the 6 supernovae with optical counterparts, we can conclude that $\sim 0.05 - 0.3\%$ of supernovae have 3 GHz luminosities $\sim 10^{28}$ erg s^{-1} Hz^{-1} and peak at $\sim$5 years post-explosion. These luminous and slowly evolving radio supernovae are predominantly fueled by ejecta interacting with a dense and asymmetric CSM, likely ejected by binary interaction in the $\sim$centuries before explosion.

2.8 Summary and Conclusions

- We have identified a sample of 64 radio transients that appeared in the $\sim$20 years between FIRST and VLASS Epoch 1. All the transients are statistically associated with galaxies within 200 Mpc, with an estimated background contamination of $0.9^{+5.1}_{-0.9}$ sources. To date, this is the largest uniformly-selected sample of extragalactic slow radio transients (Section 2.3, 2.3).

- The parameters of our survey (detection frequency 3 GHz, epoch separation $\sim$20 years, sensitivity $\sim$1 mJy, and maximum distance 200 Mpc) create a selection bias in our search favoring long-lived transients with spectral peaks of $\sim$3 GHz at the detection epoch and luminosities $\sim 10^{28}$ erg s^{-1} Hz^{-1}. Physically, these parameters select for energetic and relatively slow-moving

shocks in dense environments (Section 2.3).

- Six of the off-nuclear transients in our sample have optical counterparts identified in either archival surveys (3 events) or our follow-up observations (3 events). All six transients are located in star-forming galaxies and their spectra are consistent with supernovae (Section 2.3).

- Based on the properties of the host galaxies and the offset between the host nuclei and the transient positions, we developed a simple classification scheme. We identified 31 transients as AGN flares (16 with high confidence), 3 transients as TDEs (1 with high confidence), and 29 objects as stellar explosions (6 confirmed with optical counterparts, and 22 others with high confidence). We leave one object (ID 58) unclassified due to the combination of its unusual potential host (the only off-nuclear transient on a non star-forming galaxy) and its large angular offset from the host nucleus (97″ compared to a median of $\sim 5''$ among all non-nuclear transients) which increases the chance of it being a background source. (Section 2.4).

- The transients' host galaxy properties are largely consistent with those of a comparison sample from SDSS. We see one major difference: nuclear transients prefer galaxies with non star-forming BPT ratios, and off-nuclear transients prefer star-forming galaxies at a $\sim 3\sigma$ significance. We see two additional trends that are not yet statistically significant, but can be tested with larger future samples: (1) Radio TDEs appear to be in substantially dustier galaxies than SDSS galaxies as a whole, (2) Radio stellar explosions appear to be found in slightly dustier galaxies than optically selected core collapse supernovae (Section 2.5).

- Modelling the transient radio luminosity function as a power-law with index Γ and normalization determined by the transient rate $\dot{n}$, we predict an overall transient rate of $10^{3.81\pm0.1}$ Gpc^{-3} yr^{-1}. Considering only the SMBH flares only, the rate is $10^{3.56\pm0.15}$ Gpc^{-3} yr^{-1}. The rate of stellar explosions is $10^{3.57\pm0.15}$ Gpc^{-3} yr^{-1}. The slopes of the lumionsity functions for all three populations are $\Gamma \sim 2$ (Section 2.6.

- While we cannot set stringent constraints on the timescales of the lightcurves of our events, inspection of the VLASS E1 to E2 flux ratios suggests that most of our sources are fading. This trend becomes even more extreme when considering only SMBH flares. The high fraction of fading sources is

consistent with typical lightcurves that fade more slowly than they rise and that remain around their peak luminosity for several years (Section 2.6).

- The AGN flares in our sample are at substantially lower luminosities and redshifts than others that have been previously reported. The lower luminosities suggest that they come from sub-pc regions. If they are due to jets, the jets are quickly frustrated by a dense circumnuclear medium. Alternatively they may be due to slower, more isotropic outflows driven by transient disk winds. Such winds may be driven by radiation pressure, MHD processes within the disk, or more unusual mechanisms such as stellar explosions within the disk (Section 2.7).

- TDEs are the least common classification in our sample. This is due in part to the stringent criteria that we have applied in classifying these events (i.e total quiescence with no evidence for present or past AGN activity on the narrow-line region formation timescale $\sim 10^3$ years). The events in our sample are also unusually long-lived for TDEs; the inferred rate suggest that $\sim 1-30\%$ of TDEs eventually produce radio emission that persists for at least a few years and perhaps more than a decade. Unlike the most radio-luminous TDEs, which are jetted, these events are also due to slower shocks propagating through a dense circum nuclear medium (Section 2.7).

- The stellar explosions in our sample are diverse, including a likely pulsar/magnetar wind nebula, and six optically confirmed supernovae of which at least one was likely caused by the merger of a compact object and a massive star. The optically confirmed supernovae in our sample all have extremely high radio luminosities relative to typical supernovae. As with TDEs, their high luminosities are not due to relativistic jets, but are instead due to interaction with a dense and structured CSM, likely produced by binary-driven eruptive mass loss in the ∼centuries before explosion. The remaining 23 objects have not been studied in-depth, though our prior is that they are predominantly supernovae. Other unusual scenarios are possible, such as flares from wandering black holes (Section 2.7).

The sample presented in this paper is distinct from previously reported samples of extragalactic radio transients (e.g., Mooley, G. Hallinan, et al., 2016; Nyland, Dillon Z. Dong, et al., 2020; Wołowska et al., 2021; F. Zhang et al., 2022), in a number of ways. First, our total sample size (n = 64) has, as far as we are aware,

roughly doubled the total number of such transients in the literature to date. Additionally, previous samples have focused almost exclusively on nuclear transients, which are easier to identify with their host galaxies. Our work is the first to robustly extend this analysis to off-nuclear transients, thus opening a new window into radio-luminous stellar explosions. Our nuclear transients are also distinct due to their lower luminosities, which probe more compact regions than previously studied.

Based on the parameters of our survey, we have argued that there is a characteristic size $\sim 10^{17}$ cm, velocity ~few thousand km s^{-1}, and density $\sim 10^5$ cm^{-3} of the emitting regions that produce the transients we are detecting. These order-of-magnitude estimates are supported by more detailed analysis of the stellar explosions with optical counterparts. However, despite the similarities in the transient emitting regions, the astrophysical origins of the transients are varied and require more data and theoretical analysis to confirm. Our classifications of transients as AGN flares, TDEs, and stellar explosions is oversimplified. These classes reflect the contextual information at hand (or lack thereof), more than the nature of the transients themselves. If the diversity within these sub-classes is to be revealed, the transients within them must be investigated in more depth. This can be done in quite a few ways.

First, there can be a wealth of information to be learned from follow-up observations of slow radio transients in spite of (or in some cases because of) their old age. Though for any given transient the available information can be scattered and heterogeneous, basic analyses can be done for most transients. In particular, all of the transients in our samples are bright enough to be detected in VLASS, a survey with an effective integration time of 5 seconds per field. Direct measurement of radio lightcurves and SED evolution through VLA follow-up observations is thus feasible for all but the fastest fading transients. With sufficiently careful analysis, the forward evolution of the transient (e.g., the growth in size of the emitting region) can be modelled using standard synchrotron theory. Similar analyses have been done for many single objects found in follow-up of optical transients (e.g., K. D. Alexander, E. Berger, et al., 2016; Eftekhari, E. Berger, Zauderer, et al., 2018; Palliyaguru et al., 2019; A. Y. Q. Ho, E. Sterl Phinney, et al., 2019; A. Y. Q. Ho, Daniel A. Perley, et al., 2020; Horesh, Cenko, and Arcavi, 2021) and directly detected in radio surveys (e.g., C. J. Law et al., 2018; M. M. Anderson et al., 2019; D. Z. Dong et al., 2021; Somalwar, Ravi, D. Dong, et al., 2021; Somalwar, Ravi, Dillon Z. Dong, et al., 2022; D. Dong and Gregg Hallinan, 2022). Additionally, as seen in

Figure 2.6, there may be surprising multi-wavelength features that show up at non radio wavelengths which can shed light on e.g., asymmetry of the circum-explosion medium. We therefore encourage multi-wavelength follow-up observations of these transients and will be conducting some follow-up of our own.

There is also important contextual information to be gained from finding archival transient counterparts. As seen in our discussion of archival supernovae (Section 2.7), the identification of more archival supernovae in Stroh et al. (2021), the association of an archival X-ray transient with VT 1210+4956 in D. Z. Dong et al. (2021), and the in-depth characterization of a nuclear radio flare with an infrared precursor in Somalwar, Ravi, D. Dong, et al. (2021), the identification of late-time radio counterpart can shed much light on otherwise innocuous archival transients. This avenue of inquiry is set to grow in the near future as the delayed radio emission from transients detected in modern optical surveys such as the Zwicky Transient Facility (Bellm, 2014) start to become detectable in later epochs of VLASS. Even larger and more varied samples of potential transient counterparts will come from near-future transient surveys such as eROSITA (Predehl et al., 2021), WINTER (Lourie et al., 2020), and the Rubin Observatory LSST (Ivezić et al., 2019).

Multiwavelength surveys designed to study quiescent objects (e.g., galaxies) rather than transients are also critical parts of the effort to systematically characterize the universe's impulsive particle accelerators. As seen in our classification scheme and a number of works in the literature (e.g., Fruchter et al., 2006; Taggart and D. Perley, 2019; Christopher D. Bochenek, Ravi, and D. Dong, 2021), host galaxy environments at the locations of transients can be used as first-line diagnostics of the transients' origins. This tool becomes more powerful as sample sizes grow and statistical trends emerge. Near-future spectroscopic surveys such as the Dark Energy Spectroscopic Instrument (DESI; DESI Collaboration et al., 2016) and SPHEREx (Doré et al., 2014) will also help in this regard by increasing the redshift completeness of galaxy catalogs and providing more detailed diagnostics of those galaxies (e.g., through BPT diagrams). As estimated in Section 2.3, a complete census of galaxies within 200 Mpc should roughly double our sample size. Extending this search to larger distances would expand the sample further and also open the door to finding faster, rarer, and more luminous events such as relativistic jets. This extension of our sample requires only additional contextual information from spectroscopic surveys and can be done after the fact. After-the-fact transient identi-

fication does make follow-up more challenging, though this can be addressed with samples of newer transients from ongoing radio sky surveys such as ASKAP/VAST (T. Murphy, Shami Chatterjee, et al., 2013), LOFAR (Stappers et al., 2011), and further epochs of VLASS (Dong et al. in prep).

Looking at the broader context, this paper demonstrates that radio surveys such as VLASS are now at a scale where transients can be identified en-masse. These transients can be classified and studied in-depth with the help of contextual information from multiwavelength surveys, and follow-up observations. Ongoing developments in surveys across the electromagnetic spectrum (and beyond) will lead to substantial improvements in this process in the near future. With current and upcoming surveys, we are moving ever closer toward the goal of identifying the diversity of cosmic explosions and tracking their evolution throughout the electromagnetic spectrum from start to finish.

Appendix

2.9 Luminosity Function and Rates Methodology

Consider a survey sensitive to all transients above a minimum luminosity $L_{\rm min}$, set by the minimum distance considered and the flux sensitivity. Let the volumetric transient rate for luminosities L where $L_{\rm min} < L$ be $\dot{n}$, the maximum distance probed be $d_M = 200$pc, the fraction of the sky probed be f_A, and the average spectroscopic completeness f_S. The total number of observations is $N_{\rm obs.}$, and the time between each FIRST observations and VLASS E1 observation is Δt. We adopt a power-law form for the luminosity function, valid for luminosities L where $L_{\rm min.} < L$, with index Γ. The luminosity function can be shown to be

$$\frac{dN}{dL} = \frac{4}{3}\pi d_M^3 f_A f_S \dot{n} P_L(L) \Delta t \tag{2.8}$$

$$P_L(L) = \frac{\Gamma - 1}{L_{\rm min}^{1-\Gamma}} L^{-\Gamma},\ L_{\rm min.} < L. \tag{2.9}$$

Equation 2.9 gives the probability of detecting a source at a given luminosity. The luminosity function is normalized to the total number of sources between $L_{\rm min} < L < L_{\rm max}$. However, we aim to fit this distribution to our observations, and our observations are flux-limited, not luminosity-limited. To incorporate this, we must calculate the expected number of sources above the VLASS sensitivity.

Table 2.2: Summary of the 200 Mpc sample.

ID	RA	Dec	r_{norm}	$\Delta\theta$	D_L	FIRST	E1	E2	Class.	Confidence
	hms	dms		arcsec	Mpc	mJy	mJy	mJy		
ID01	09:41:50.08	+14:58:00.34	0.01	0.15	112.3	0.13	0.96	0.78	AGN	high
ID02	11:56:54.24	+32:09:31.77	0.02	0.08	44.4	0.27	0.95	0.85	AGN	high
ID03	16:01:40.23	+21:21:10.62	0.02	0.09	142.0	0.35	0.89	< 0.46	AGN	high
ID04	16:17:35.23	+13:29:31.45	0.03	0.26	149.4	0.3	0.83	0.64	AGN	high
ID05	14:38:56.84	+28:21:11.70	0.03	0.18	198.2	0.25	1.23	1.28	SN/TDE	medium
ID06	07:46:28.59	+58:57:45.33	0.03	0.17	97.1	0.28	0.84	0.75	AGN	low
ID07	16:43:04.22	+61:34:43.96	0.04	1.08	83.4	0.26	0.74	0.56	AGN	high
ID08	12:28:15.46	+28:37:12.76	0.05	0.95	9.5	0.31	0.55	< 0.4	AGN/SN	low
ID09	12:41:34.27	+44:26:39.15	0.05	0.35	186.3	-0.01	1.45	1.3	SN	high
ID10	16:39:00.22	+51:30:29.61	0.05	0.23	131.9	0.21	0.93	0.8	AGN	medium
ID11	03:09:25.99	+01:14:57.93	0.06	0.2	189.9	-0.08	6.82	3.84	AGN	high
ID12	12:22:47.60	+05:36:24.39	0.06	0.3	78.6	-0.07	5.9	3.37	SN	very high
ID13	00:35:26.46	+04:52:19.83	0.07	0.49	171.0	0.31	2.32	2.05	AGN/SN	low
ID14	07:47:51.16	+18:33:07.50	0.08	0.24	200.2	0.16	0.83	0.61	AGN	medium
ID15	11:01:27.20	-00:43:05.61	0.08	0.45	197.4	0.21	0.8	< 0.59	AGN	high
ID16	01:10:22.29	+03:31:10.93	0.08	0.65	188.1	0.26	0.77	0.73	AGN/TDE	low
ID17	11:03:57.81	+38:14:16.21	0.08	0.25	134.8	0.11	1.21	0.85	AGN	medium
ID18	10:33:28.17	+49:19:12.44	0.09	0.12	192.2	-0.38	3.05	2.46	TDE	high
ID19	13:36:32.63	+33:52:33.78	0.09	0.23	180.5	0.28	0.7	0.81	AGN	high
ID20	08:35:36.46	+49:35:42.66	0.09	0.32	188.6	0.07	1.08	0.87	AGN	high
ID21	22:10:51.73	+02:06:21.36	0.09	0.4	183.1	0.15	1.42	1.68	AGN	low
ID22	02:58:35.35	-01:59:18.18	0.09	0.19	29.2	0.34	0.75	0.62	AGN/TDE	low
ID23	01:41:40.57	-06:09:48.26	0.11	0.7	156.8	0.28	0.67	< 0.47	AGN	medium
ID24	15:41:42.95	+37:27:29.57	0.11	0.24	192.2	-0.1	0.71	< 0.43	SN	very high
ID25	02:18:45.02	-06:38:19.75	0.14	3.65	76.5	0.36	1.06	1.76	SN	high
ID26	23:33:34.70	+04:27:58.15	0.15	0.4	149.6	0.29	0.9	0.83	AGN	medium
ID27	08:55:34.59	+56:12:07.60	0.18	0.89	200.0	0.29	0.73	0.78	AGN	high
ID28	02:04:31.21	+06:38:09.29	0.19	0.61	48.8	0.28	0.84	0.82	SN/AGN/TDE	low
ID29	14:52:55.49	+09:52:30.75	0.19	1.33	130.3	0.19	1.65	1.39	SN	high
ID30	00:19:47.34	+00:35:27.18	0.21	0.31	77.3	0.15	1.08	< 0.55	AGN	high
ID31	15:16:28.28	+06:06:53.41	0.21	0.31	154.3	0.28	0.91	0.61	AGN	high
ID32	09:20:45.60	+19:33:27.81	0.22	0.3	130.7	-0.11	2.27	1.73	AGN	high
ID33	23:59:19.55	+04:45:38.36	0.22	0.93	56.2	0.12	0.68	0.93	AGN	low
ID34	00:34:24.63	+12:16:06.95	0.23	1.16	140.0	0.24	0.65	< 0.53	AGN/SN	low
ID35	23:38:42.05	+09:03:26.54	0.23	0.6	179.7	0.19	1.06	1.24	AGN	low
ID36	12:38:21.83	+42:12:19.55	0.25	0.54	127.3	0.24	1.13	0.82	AGN	high
ID37	15:51:03.42	+20:14:06.93	0.25	0.34	159.6	0.26	0.64	< 0.46	SN	high
ID38	10:26:56.14	+08:09:07.78	0.26	0.44	141.7	0.31	0.69	< 0.49	AGN	high
ID39	13:43:07.35	+30:55:15.10	0.28	0.45	192.4	0.14	0.7	0.57	TDE/AGN	medium
ID40	17:21:53.46	+57:13:13.02	0.3	0.46	114.5	-0.03	2.21	< 0.43	TDE/AGN	medium
ID41	11:34:49.44	-03:20:54.92	0.34	2.1	178.7	0.32	0.76	< 0.51	SN	high
ID42	10:13:16.91	-02:31:53.27	0.35	2.48	187.3	0.23	0.76	< 0.49	SN	high
ID43	10:42:08.74	-02:31:41.62	0.4	0.7	169.0	0.3	1.06	0.8	AGN	low
ID44	12:10:16.63	+39:18:17.51	0.41	0.53	96.6	0.08	0.68	0.59	AGN	high
ID45	16:53:51.51	+22:23:50.21	0.43	1.87	156.9	0.06	1.02	< 0.44	SN	high
ID46	09:59:51.20	+38:39:09.00	0.52	3.91	94.4	0.33	0.82	< 0.35	SN	high
ID47	00:12:33.97	-02:53:10.96	0.55	1.74	132.0	-0.12	1.17	< 0.45	SN	high
ID48	12:18:08.85	-01:03:49.35	0.58	4.42	83.1	-0.01	1.76	1.54	SN	high
ID49	13:13:41.48	+47:17:56.72	0.6	1.68	123.6	-0.03	6.58	3.18	SN	very high
ID50	11:37:06.21	-03:37:36.81	0.65	0.51	121.6	0.2	1.71	1.04	PWN	very high
ID51	03:20:10.04	-06:15:41.34	0.67	5.63	33.8	0.16	1.65	< 0.67	SN	high
ID52	10:44:40.27	+38:33:22.06	0.78	5.79	145.3	-0.12	0.68	0.49	SN	high
ID53	15:04:57.27	+02:48:47.46	0.9	7.55	156.6	0.02	1.49	1.31	SN	high
ID54	09:23:38.97	+54:28:52.17	1.0	9.11	50.6	-0.01	0.63	< 0.43	SN	high
ID55	15:04:50.84	+24:24:34.81	1.08	3.15	179.6	0.01	0.78	0.49	SN	high
ID56	12:10:01.35	+49:56:46.93	1.17	4.71	153.6	0.17	2.82	3.52	SN	high
ID57	14:41:35.74	+29:13:44.27	1.41	17.12	55.2	0.11	5.09	4.32	SN	high
ID58	12:42:55.70	+02:41:56.46	1.59	96.83	13.5	0.15	1.93	1.26	?	low
ID59	12:52:34.16	+22:03:54.46	1.59	6.08	98.0	0.12	0.75	< 0.45	SN	very high
ID60	14:28:35.46	+59:10:58.53	1.6	6.08	171.7	0.33	0.59	< 0.44	SN	high
ID61	08:04:24.32	+29:30:56.71	1.72	7.11	80.2	0.14	0.75	0.98	SN	high
ID62	12:09:17.36	+29:54:07.78	2.15	89.45	9.2	0.12	0.63	0.4	SN	high
ID63	08:23:37.36	+39:06:16.61	2.22	14.1	129.5	0.33	1.16	0.75	SN	high
ID64	10:03:29.48	+15:40:19.72	2.24	4.97	186.2	-0.21	0.96	0.59	SN	high

First, we require a form for the flux probability distribution. We expect the source distances to be distributed in $[0, d_M]$ Mpc, where $d_M = 200$ Mpc is the maximum distance, as $P_d = \frac{3}{d_M}(\frac{d}{d_M})^2$. Given our luminosity function lower limit $L_{\rm min}$, for flux $f = \frac{L}{4\pi d^2}$, the minimum distance at which this source can be observed is $\sqrt{\frac{L_{\rm min}}{4\pi f}}$. Then, one can show that the probability of flux f is given by

$$P_f(f) = \int_{\frac{L_{\rm min}}{4\pi f}}^{d_M^2} 4\pi x P_L(4\pi f x) P_{d^2}(x) dx \tag{2.10}$$

which evaluates to

$$P_f(f) = \begin{cases} \frac{3}{f}\frac{\Gamma-1}{5-2\Gamma}\left(\frac{4\pi d_M^2 f}{L_{\rm min}}\right)^{1-\Gamma}\left[1 - \left(\frac{L_{\rm min}}{4\pi d_M^2 f}\right)^{\frac{5}{2}-\Gamma}\right] & (\Gamma \neq \frac{5}{2}) \\ \frac{9}{4f} & \\ \left(\frac{L_{\rm min}}{4\pi d_M^2 f}\right)^{\frac{3}{2}} \ln\left(\frac{4\pi d_M^2 f}{L_{\rm min}}\right) & (\Gamma = \frac{5}{2}), \end{cases} \tag{2.11}$$

Here, we use the probability distribution function for the source distance squared ($x = d^2$):

$$P_{d^2}(x) = \frac{3}{2d_M^2}\left(\frac{\sqrt{x}}{d_M}\right)dx. \tag{2.12}$$

We can include the total number of sources expected to calculate

$$\frac{dN}{df} = \frac{4}{3}\pi d_M^3 f_A f_S \dot{n} \Delta t P_f(f) \tag{2.13}$$

With Equation 2.11, we can calculate the fraction of sources with $f > f_{\rm lim}$, where $f_{\rm lim} = 0.7$ mJy is the VLASS E1 detection limit. If we define $f_{\rm min} = \max\left(f_{\rm lim}, \frac{L_{\rm min}}{4\pi d_M^2}\right)$, this fraction is given by

$$P_f(f > f_{\rm lim}) = \int_{f_{\rm min}}^{\infty} P_f(f) df = 2\frac{\Gamma-1}{5-2\Gamma}\left(\frac{L_{\rm min}}{4\pi d_M^2 f_{\rm lim}}\right)^{\Gamma-1}\left[\frac{3}{2(\Gamma-1)} - (\frac{L_{\rm min}}{4\pi d_M^2 f_{\rm lim}})^{\frac{5}{2}-\Gamma}\right].$$

It can be seen that if $f_{\rm lim} = \frac{L_{\rm min}}{4\pi d_M^2}$, then $P(f > f_{\rm lim}) = 1$, as expected. The total number of sources above $L_{\rm min}$ is $\frac{4}{3}\pi d_M^3 f_A \dot{n} \Delta t$, so the observed number of sources with $f > f_{\rm lim}$ is $\frac{4}{3}\pi d_M^3 f_A \dot{n} \Delta t \times P(f > f_{\rm lim})$.

Now, we want to fit our observations to $\frac{dN}{df}$, with free parameters $\dot{n}$ and Γ. First, we require the unbinned log-likelihood (see Appendix C of Drlica-Wagner et al., 2020, for a detailed derivation):

$$\log \mathcal{L} = -N_0 P_f(f > f_{\rm lim}) + \sum_{i=0}^{N_{\rm obs}} \log\left[\frac{N_0}{N_{\rm obs}} P_L(L_i) P_d(d_i)\right] \tag{2.14}$$

$$N_0 = \frac{4}{3}\pi d_M^3 f_A f_S \dot{n} \Delta t. \tag{2.15}$$

This is the final log-likelihood we use in Section 2.6.

Chapter 3

VT 1210+4956: A MERGER-DRIVEN EXPLOSION

Dong, D. Z. et al. (Sept. 2021). "A transient radio source consistent with a merger-triggered core collapse supernova". In: *Science* 373.6559, pp. 1125–1129. DOI: 10.1126/science.abg6037. arXiv: 2109.01752 [astro-ph.HE].

Dillon Z. Dong[1], Gregg Hallinan[1], Anna Y. Q. Ho[1,3,4], Andrew K. Hughes[5], Kenta Hotokezaka[6], Steven T. Myers[7], Kishalay De[1], Kunal P. Mooley[1,7], Vikram Ravi[1], Assaf Horesh[8], Mansi M. Kasliwal[1], Shri R. Kulkarni[1]

[1] Division of Physics, Mathematics, and Astronomy, California Institute of Technology, Pasadena, California 91125, USA
[2] School of Physics and Astronomy, Tel Aviv University, Tel Aviv, 69978, Israel
[3] Department of Astronomy, University of California, Berkeley, 94720, USA
[4] Miller Institute for Basic Research in Science, Berkeley, CA 94720, USA
[5] Department of Physics, University of Alberta, Edmonton AB T6G 2E1, Canada
[6] Research Center for the Early Universe, Graduate School of Science, University of Tokyo, Bunkyo-ku Tokyo 113-033, Japan
[7] National Radio Astronomy Observatory, Socorro, NM 87801, USA
[8] Racah Institute of Physics, The Hebrew University of Jerusalem, Jerusalem, 91904, Israel

3.1 Abstract

A core-collapse supernova occurs when exothermic fusion ceases in the core of a massive star, typically due to exhaustion of nuclear fuel. Theory predicts that fusion could be interrupted earlier, by merging of the star with a compact binary companion. We report a luminous radio transient, VT J121001+495647, found in the Very Large Array Sky Survey. The radio emission is consistent with supernova ejecta colliding with a dense shell of material, potentially ejected by binary interaction in the centuries prior to explosion. We associate the supernova with an archival X-ray transient, which implies a relativistic jet was launched during the explosion. The combination of an early relativistic jet and late-time dense interaction is consistent with expectations for a merger-driven explosion.

3.2 Main Text

Most massive stars (those > 8 solar masses, $M_\odot$) are born in close binaries, within which expansion of one star during its evolution can lead to mass transfer with the companion (Sana et al., 2012; Moe and Di Stefano, 2017). In some systems,

the faster evolving (more massive) star explodes as a supernova, leaving behind a compact object (neutron star or black hole) remnant in a close orbit with its companion. When the companion (second star) later expands, it transfers mass in the other direction, onto the compact object. Systems of this type with wide orbits have been observed in the Milky Way (Orosz et al., 2011). Those with closer orbits undergo unstable mass transfer, causing the compact object to spiral into the atmosphere of the massive star, forming a common envelope binary.

During the common envelope phase, the outer atmosphere of the donor star becomes unbound, forming a dense and expanding toroidal shell around the binary (MacLeod, Ostriker, and Stone, 2018). The physics of the common envelope are difficult to model. Some inspirals halt before reaching the donor's core. This process is a leading candidate for producing the close double-compact-object binaries detected by gravitational wave observatories (Tauris et al., 2017). Other systems are expected to spiral inwards until the compact object reaches the star's core. Theory predicts that some of these systems tidally disrupt the core, forming a rapidly accreting neutrino-cooled disk (Roger A. Chevalier, 2012). This energetic accretion is predicted to launch a jet and cause a merger-driven explosion (Roger A. Chevalier, 2012; Schrøder et al., 2020; Soker, 2017).

We performed a systematic blind search for radio transients in the Very Large Array Sky Survey (VLASS; Lacy et al., 2020). We identified and followed up luminous point sources associated with galaxies closer than 200 megaparsec (Mpc) that are present in the first half-epoch (Epoch 1.1; Sep 2017 - Feb 2018) of the survey but absent from the earlier (1994-2005) Faint Images of the Radio Sky at Twenty-Centimeters (FIRST) survey (Becker, R. L. White, and Helfand, 1995). The most luminous source we identified was VLASS transient VT J121001+495647 (hereafter abbreviated VT 1210+4956), located in an off-nuclear region of the dwarf star-forming galaxy SDSS J121001.38+495641.7 (Fig 3.1)(Aguado et al., 2019). This galaxy has stellar mass $\sim 10^{9.2} M_{\odot}$, specific star formation rate ~0.25 $M_{\odot}$ Gyr^{-1} $M_{\odot}^{-1}$ and an abundance of elements heavier than helium (metallicity) of ~80% the solar value (Aguado et al., 2019).

We observed two follow-up epochs with the Karl G. Jansky Very Large Array (VLA), finding a peak radio luminosity of 1.5×10^{29} erg s^{-1} Hz^{-1} at 5 GHz (Fig. 3.1), ten times more luminous than any other non-nuclear transient found in our search. We obtained an optical spectrum of the radio transient location using the Low Resolution

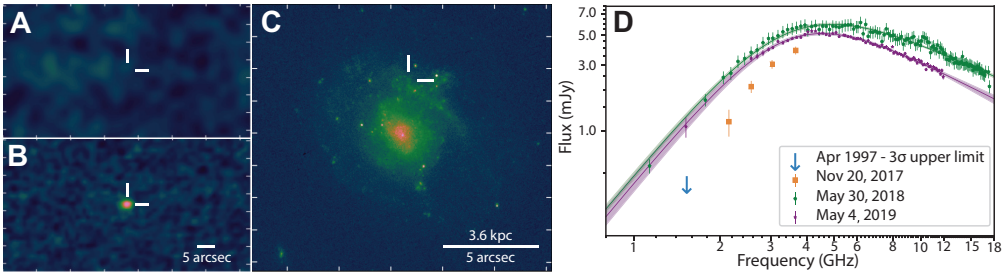

Figure 3.1: The luminous radio transient VT 1210+4956. A. Non-detection in the FIRST survey at 1.4 GHz, with a 3 upper limit of 0.41millijansky (mJy) on 1997 April 17. B. Detection in VLASS at 3 GHz at 2.7 ± 0.1 (stat) ± 0.5 (sys) mJy on 2017 November 20, 20.59 years after the FIRST observation, at right ascension 12h10m01.32s, declination +49°5647.006 (indicated by white crosshairs in panels A-C). C. Optical image of the location of VT 1210+4956 taken from the Hubble Space Telescope archive (PI: T. Schrabback). D. The radio spectrum of VT 1210+4956 measured from the VLASS observation and follow-up epochs observed with the VLA, plotted with 1 uncertainties. Follow-up epochs are fitted with a synchrotron self-absorption model.

Imaging Spectrometer on the Keck I telescope, which exhibits a hydrogen-alpha (Hα at 6563Å) emission line with luminosity (7.3 ± 0.3) × 10^{38} erg s^{-1} and full-width half maximum ~1340 ± 60 km s^{-1} (Fig. 3.2). This emission line implies a massive, ionized outflow associated with the radio source (Dan Milisavljevic, Fesen, et al., 2012; Heng, 2010), and its redshift z = 0.03470 ± 0.00003 confirms its association with the host galaxy, which is at z = 0.03472 ± 0.00003 (Aguado et al., 2019). In addition to the broad component, we observe spectrally unresolved (narrow) emission lines consistent with a co-located star-forming region. The environment, broad line, and high radio luminosity indicate a likely association with the explosion of a massive star.

Radio emission from supernovae is powered by synchrotron emission from fast ejecta driving a shock into the ambient circumstellar medium (CSM) (Roger A. Chevalier, 1998). The most luminous events require exceptionally fast material, such as relativistic (close to the speed of light) jets driven by central compact-object engines, or interaction with a particularly dense CSM. All known supernovae with radio emission peaking at $\geq 10^{29}$ erg s^{-1} Hz^{-1} are high-luminosity examples of transient classes that involve central engines (e.g., A. J. van der Horst et al., 2007; A. Y. Q. Ho, E. Sterl Phinney, et al., 2019; A. Y. Q. Ho, Daniel A. Perley, et al., 2020; Corsi, E. O. Ofek, et al., 2014; Kulkarni, Frail, et al., 1998). Supernovae featuring dense CSM interaction are typically over an order of magnitude less lu-

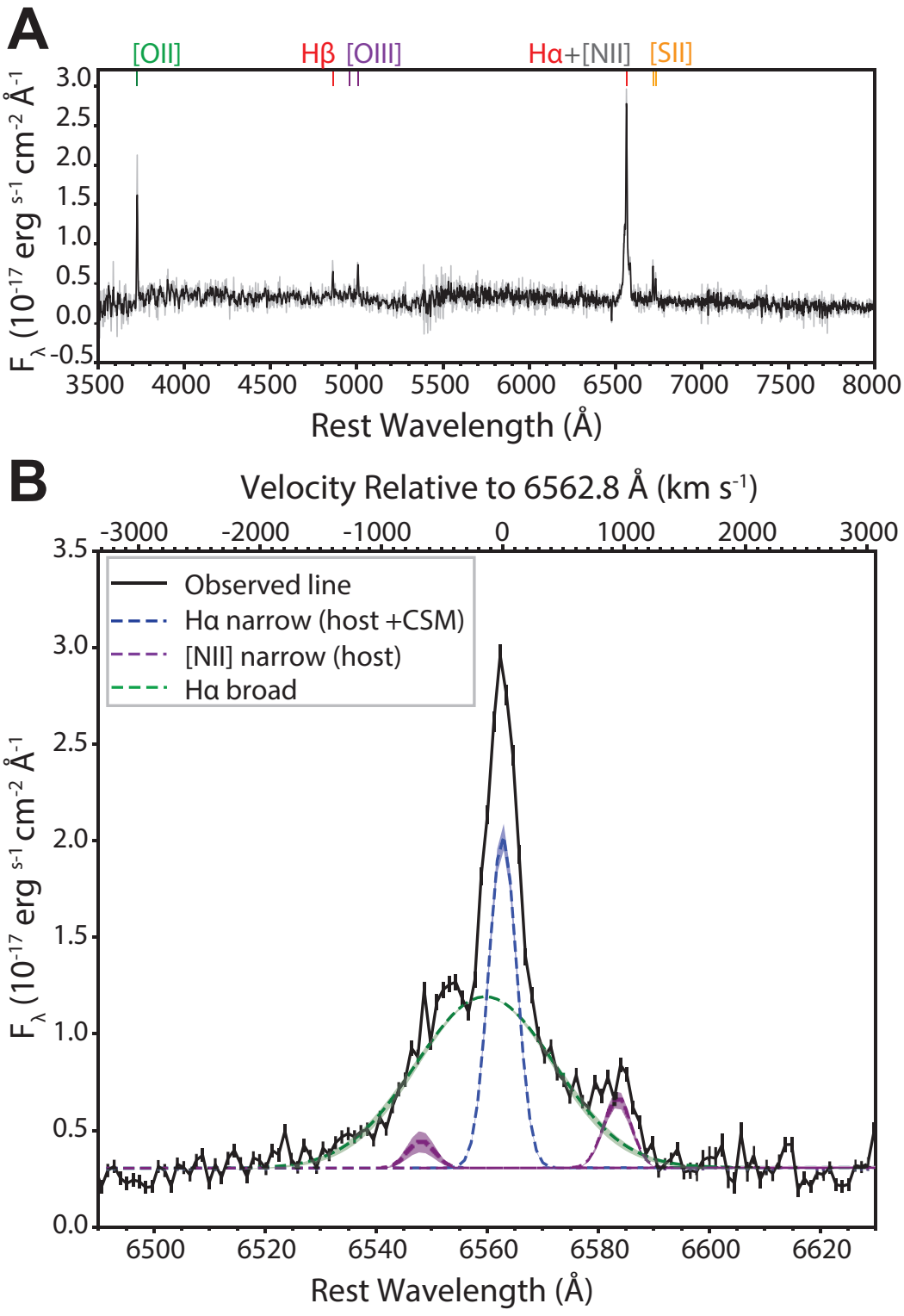

Figure 3.2: Optical spectrum of VT 1210+4956. Taken with Keck/LRIS on 2018 April 13, ~4.45 months after the detection in VLASS. A. The full spectrum, including spectrally unresolved emission lines from the host galaxy. Unbinned data are shown in gray; data shown in black were smoothed with a 3Åboxcar kernel. B. Details of the Hα and [N II] part of the spectrum, with Gaussian models fitted to the lines. The narrow Hα and [N II] lines are unresolved, while the broad component has a FWHM of 1340 ± 60 km/s. The best fitting model parameters and their uncertainties are listed in Table 3.1.

minous. Given the high luminosity of VT 1210+4956, we checked for early-time signatures of a central engine by searching archival optical, X-ray, and gamma-ray transient catalogs for a counterpart source. This search yielded one match: GRB 140814A, an unusual soft X-ray burst detected by the Monitor of All Sky X-ray Image (MAXI) instrument on the International Space Station, using its Gas Slit Camera (GSC) (Serino et al., 2014b).

GRB140814A was detected by the GSC at 2-4 keV and 4-10 keV in a 15 ± 3s window centered at 07:12:23 Universal Time on 2014 August 14, with a similar flux in both bands. It was not detected in a simultaneous observation with a similar sensitivity in the GSC 10-20 keV band, suggesting a characteristic energy of ∼5 keV. The position of VT 1210+4956 is consistent with the MAXI data and implies a short, fading burst that occurred at the beginning of the GSC's 40 second transit (Fig 3.3). We estimate a false alarm probability for the spatial association of (1.2 - 4.8) $\times 10^{-3}$. We performed several additional consistency checks: (a) the shock properties of VT 1210+4956 are consistent with an explosion on the date of GRB 140814A, (b) upper limits from contemporaneous optical observations do not rule out a stripped envelope supernova at the location of VT 1210+4956 and time of GRB 140814A, and (c) alternative classes of X-ray transients are not consistent with the observational data.

Our association of VT 1210+4956 with GRB 140814A implies that the X-ray emission had a peak 2-10 keV luminosity of $\sim 4 \times 10^{46}$ erg/s. This combination of high luminosity, short duration, and soft spectrum is unlike other X-ray transients with measured luminosities. Known transients with similar spectral peaks and durations, such as the shock breakout of supernova SN 2008D (Soderberg, E. Berger, et al., 2008), are more than 3 orders of magnitude less luminous. Transients with similar luminosities, such as X-ray flashes and low-luminosity GRBs, typically maintain this luminosity for at least an order of magnitude longer duration (Campana et al., 2006), or peak at $\geq$ 1 order of magnitude higher energy (Ghirlanda et al., 2015). The luminosity and duration of MAXI 140814A implies a relativistic outflow with Lorentz factor $\Gamma \geq 2.5$, and the characteristic energy of the photons implies a jetted geometry. Producing such a relativistic jet requires the presence of a central engine at the time of explosion.

Unlike the early relativistic jet, the radio emission detected in our follow-up epochs (observed >3 years after GRB140814A) is powered by a low-velocity shock prop-

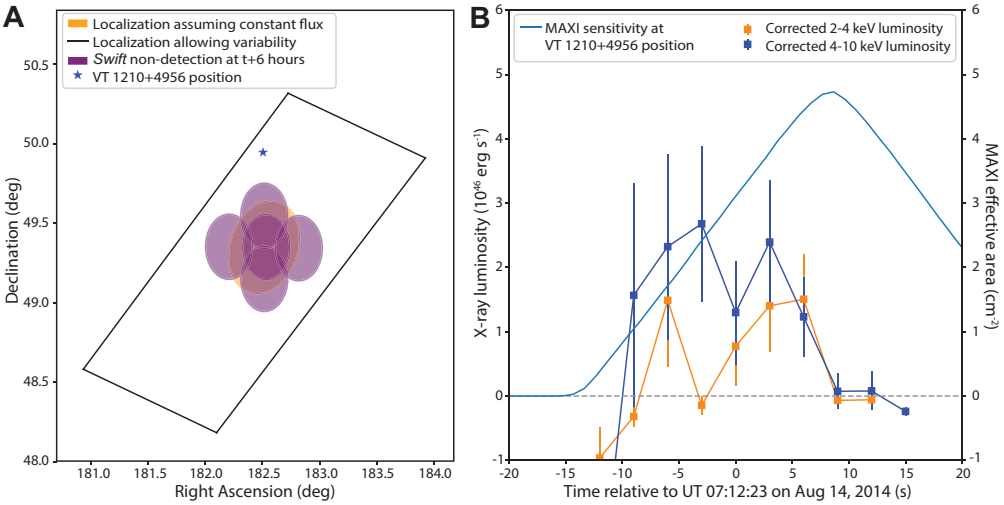

Figure 3.3: The X-ray transient MAXI 140814A which we associate with VT 1210+4956 (observed 3.268 years before VLASS detection). A. The location of VT 1210+4956 compared to published MAXI localizations: orange ellipse assuming constant flux and black rhombus allowing for variability. This position is consistent within 1σ of the expectation from the lightcurve in panel B. The purple ellipses show fields with non-detections in Swift observations, with upper limits of 60,000 times fainter than the MAXI 140814A ~6 hours after the burst. B. MAXI 2-4 keV (orange) and 4-10 keV (blue) light curves, corrected for instrumental sensitivity at the location of VT 1210+4956.

agating in a dense, extended CSM. The spectral peaks of the radio spectra are due to synchrotron self-absorption rather than free-free absorption, suggesting that the CSM is asymmetric, observed along a lower-density line of sight. The peak luminosities and frequencies imply forward shock radii R $\sim 9 \times 10^{16}$ cm, post-shock magnetic fields B $\sim$ 0.35 G, and energies dissipated in the shock U $\sim 7 \times 10^{49}$ erg. The change in R between follow-up epochs implies a forward shock velocity of $\sim$ 1800 km/s. This velocity, which is similar to the width of the broad Hα line, implies a high density of $\sim 10^6$ cm^{-3} for the CSM swept-up in the $\sim$1 year between follow-up epochs. This density is sufficient to allow the shocked gas to cool, on a timescale of $\sim$1 year, from a shock-heated temperature of $\sim 10^7$ K to a $\sim 10^4$K dense shell, cool enough to produce the Hα emission (Draine, 2011). Compared to known explosive radio transients, VT 1210+4956 has a highly energetic shock propagating at low-velocity, and a high CSM density at large radius (Fig 3.4).

Measurements of the CSM density as a function of radius trace the rate and timing of pre-explosion mass loss. Accounting for both the cool Hα emitting gas and the hot synchrotron emitting gas, we find a lower limit to the total swept-up CSM mass

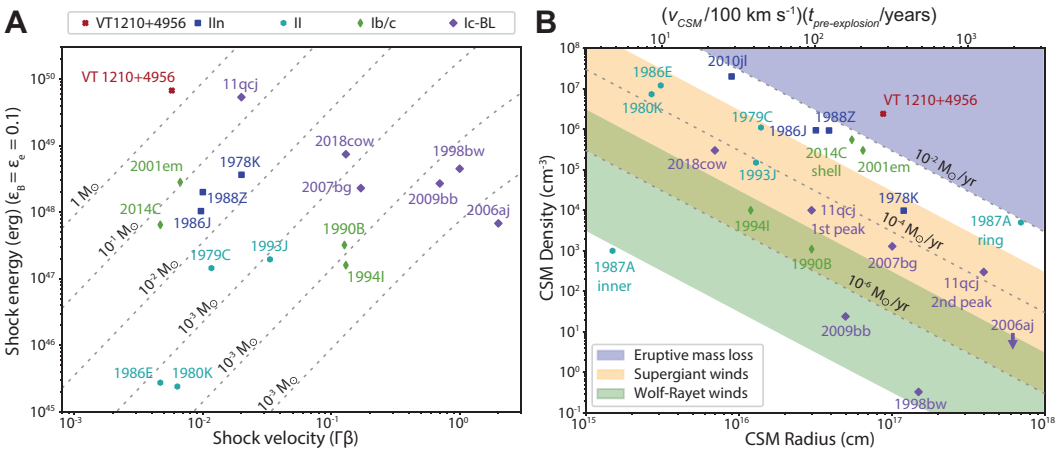

Figure 3.4: Comparison of inferred shock properties for VT 1210+4956 and other luminous radio supernovae (sources listed in Table 3.5). A. Shock energies derived from broadband radio spectra vs shock velocities. The dashed curves show constant shocked mass, assuming that the shock energy is equal to the kinetic energy. B. CSM density vs CSM radius with values derived from optical and radio spectra. The upper axis gives the time between mass loss and explosion, normalized to a CSM velocity of 100 km/s. The dotted and dashed lines indicate constant mass flow rates /v, with the colored shaded regions indicating approximate ranges of values for winds and eruptive mass loss from different types of systems (Smith, 2014).

of $\geq 1\ M_\odot$. The high density and total mass at a radius of $\sim 10^{17}$ cm requires a pre-explosion mass loss rate $\dot{M} \approx 4 \times 10^{-2}$ (v/100 km s^{-1})$M_\odot$ yr^{-1}, where v is the pre-shock CSM velocity. This is over an order of magnitude higher than the densest-observed stellar winds and requires a pre-supernova eruption (Smith, 2014). With these observed and inferred constraints on the CSM velocity, we find that the eruption occurred a few centuries before the explosion (Fig. 3.4).

Similar pre-explosion eruptive mass loss has been inferred from the dense and extended CSM around a few peculiar supernovae, including SN 2014C (Margutti, Kamble, et al., 2017; G. E. Anderson et al., 2017; Sun, Maund, and Crowther, 2020) and SN 2001em (N. N. Chugai and Roger A. Chevalier, 2006; Chandra, Roger A. Chevalier, N. Chugai, Dan Milisavljevic, et al., 2020), which both transitioned from stripped envelope (type Ib/c) to interacting (type IIn) spectral classifications. Several models have been proposed to explain the synchronization of this eruptive mass loss with core collapse, including nuclear burning instabilities (Wu and Fuller, 2021; Klencki et al., 2020), binary interaction timed coincidentally with core collapse (Margutti, Kamble, et al., 2017; Sun, Maund, and Crowther, 2020),

and merger driven explosions (Roger A. Chevalier, 2012; Margutti, Kamble, et al., 2017; Schrøder et al., 2020). For VT 1210+4956, the detection of a central engine allows us to distinguish between these scenarios, and the order of magnitude higher radio luminosity and shock energy suggests the possibility of a different origin to SN 2014C and SN 2001em.

Nuclear burning instabilities strong enough to produce VT 1210+4956's pre-explosion mass loss rate are predicted to occur in only the final few years before core collapse (Wu and Fuller, 2021), so would produce shells that are over an order of magnitude more compact at the time of interaction than we observed. Binary mass transfer is common in massive stars and is more consistent with the early eruptive mass loss. Roughly 70% of massive stars are found in orbits that will eventually lead to mass transfer, with an estimated 1/3 of these interactions leading to common envelope inspiral (Sana et al., 2012; Moe and Di Stefano, 2017). Such interactions are predicted to drive mass loss at or above the rate inferred for VT 1210+4956 (Smith, 2014). Unlike in single-star models, the mass is ejected in the plane of the binary (Schrøder et al., 2020; MacLeod, Ostriker, and Stone, 2018), providing a natural explanation for the inferred asymmetry of the CSM.

Binary interactions can occur at any time during the life of a star and can thus produce shells at any radius. However, the delay time between eruption and core collapse constrains the specific type of interaction. At the near-solar metallicity of VT 1210+4956's host galaxy, most interactions are expected to occur while the mass donor is undergoing fusion of hydrogen or helium, roughly 10^4 - 10^7 years before core collapse (MacLeod, Ostriker, and Stone, 2018). Interactions synchronized coincidentally within $\sim 10^2$ years of core collapse are expected to be extremely rare (Klencki et al., 2020), though uncertainties in the rates from binary population synthesis modeling allow this to be a viable scenario for previous events such as SN 2014C (Margutti, Kamble, et al., 2017; Sun, Maund, and Crowther, 2020).

The synchronization is more naturally explained if the interaction itself triggers the core collapse. To do so, an inspiraling object must disrupt the donor star's core. A non-compact merging body (e.g., a main sequence star) is unable to do so, as it would replenish fuel in the core, producing a rejuvenated massive star (Langer, 2012). In contrast, an inspiraling neutron star or black hole is capable of tidally disrupting the core, leading to a merger driven explosion (Roger A. Chevalier, 2012;

Schrøder et al., 2020). During the inspiral phase, the compact object is expected to eject mass from the donor star at a similar rate to our calculated value (Taam and Sandquist, 2000). When it reaches the core, theory predicts the formation of an accretion disk and launching of a jet (Roger A. Chevalier, 2012; Schrøder et al., 2020). Of the models we consider for eruptive mass loss, this scenario is most consistent with the jetted X-ray transient.

The high mass loss rate we infer occurred centuries before explosion, much longer than the dynamical timescale of the inspiraling compact object, which may indicate that the donor star had an envelope with a steep density profile. This would be theoretically expected for a star undergoing core helium fusion, for example (Taam and Sandquist, 2000). A steep density profile is thought to be required for merger during the dynamical inspiral phase (Taam and Sandquist, 2000; Ivanova et al., 2013). Flatter density profiles would lead to full envelope ejection before merger, producing close compact object – evolved star binaries. These binaries may subsequently evolve into double compact object systems, with orbits close enough to merge within the lifetime of the Universe, and therefore contribute to gravitational wave events (Tauris et al., 2017; Taam and Sandquist, 2000; Ivanova et al., 2013). Our proposed scenario for VT 1210+4956 is an alternative outcome to the formation of such systems.

Based on our blind search, we estimate a rate of (1-8) $\times$ 10^{-8} Mpc^{-3} yr^{-1} for transients with similar 3 GHz luminosities to VT 1210+4956. However, given the continuous distributions of stellar binary periods and mass ratios (Sana et al., 2012; Moe and Di Stefano, 2017), there may be a wider range of delays between interaction and core collapse, thus producing CSM shells at smaller or larger radii. If so, these events may be more easily identified at other frequencies, so we regard this rate as a lower limit on the rate of merger driven explosions.

3.3 Materials and Methods

3.4 Transient Identification in the VLA Sky Survey

We assembled a catalog of sources detected with a significance of $\geq 5\sigma$ in the quick-look images for the first half-epoch of VLASS (Epoch 1.1) (Lacy et al., 2020) using the source extractor PYBDSF (Mohan and Rafferty, 2015b). Within this catalog, we flagged the set of VLASS source separated by >10" from the nearest catalogued source in FIRST (Richard L. White et al., 1997) as our initial set of

transient candidates. Through visual inspection of all candidates, we selected those that are unresolved and have no identifiable uncatalogued counterpart in FIRST. To identify the population associated with nearby galaxies and exclude background sources (e.g., flaring active galactic nuclei (AGN)), we use the fact that background sources are isotropically distributed (J. J. Condon, Cotton, and Broderick, 2002), while known classes of extragalactic transients are concentrated within a few exponential radii ($r_{\rm exp}$) of their host galaxies (Fong and E. Berger, 2013). In our sample, we find an excess of transient candidates within $2r_{\rm exp}$ of their host galaxies, where the $r_{\rm exp}$ of a galaxy is taken to be the median among all detected bands in Data Release 15 of the Sloan Digital Sky Survey (SDSS) (Aguado et al., 2019). There are 20 sources within $2r_{\rm exp}$ of a d $<$ 200 Mpc galaxy, with an expected isotropic background rate of 0.6, given the full set of visually confirmed VLASS sources not in FIRST.

Of these 20 sources, 12 have astrometry consistent with their host galaxy's nuclei, while 8 are in off-nuclear positions. To avoid likely contamination from AGN, we focused on the off-nuclear transients. Follow-up optical spectra of the $\sim$1 arcsecond regions surrounding each radio transient revealed that 4 of the 8, including VT 1210+4956, have $\sim$1000 km/s hydrogen emission lines at the redshift of the host galaxy, indicating that the transient radio sources are associated with their apparent host galaxies. These lines are too broad to be due to star formation (Terlevich and Melnick, 1981). Among these 4 sources, VT 1210+4956 was the most radio luminous by an order of magnitude (with a peak radio luminosity of $\sim 2 \times 10^{29}$ erg/s/Hz), and the only one lacking other broad emission lines in its optical spectrum.

VT 1210+4956 is located at right ascension 12h10m01.3s, declination +49d56'47.0" in a star-forming region on the outskirts of the galaxy SDSS J121001.38+495641.7. This position is derived from VLA follow-up imaging described below, and has an uncertainty smaller than 0.1". From broadband spectral energy distribution modeling listed in the SDSS data products (Aguado et al., 2019), this galaxy has a stellar mass of $\sim 10^{9.2} M_{\odot}$, a star formation rate of $\sim 0.3 M_{\odot}$ yr^{-1}, and a metallicity of 0.8 $Z_{\odot}$.

3.5 Optical Follow-up Spectroscopy

Five to 20 months after the VLASS observations and $\sim$10-20 years after non-detections in FIRST, we obtained optical spectra at the location of the 8 off-nuclear

radio transients with the Low Resolution Imaging Spectrometer (LRIS) on the 10m Keck I telescope on Maunakea. We used the 560 nm dichroic to split the light between the red and blue arms. We dispersed the light with the 400/8500 grating in the red arm, and the 400/3400 grating on the blue arm, resulting in a ∼7Å FWHM spectral resolution on both arms. To acquire the target locations, we centroided on nearby bright stars and applied an offset corresponding to the difference between the SDSS coordinate of the star and the best-fitting coordinate of the radio transient. We observed each target in spectroscopic mode for 20 minutes, with 2×1 (spatial × spectral) CCD binning in the red arm, and 2×2 CCD binning in the blue arm. These settings correspond to a 3σ sensitivity of ∼23 mag (AB) throughout the red arm and a wavelength dependent 3σ sensitivity peaking at ∼24 mag (AB) at 5000Åin the blue arm and dropping on either side to ∼23 mag at 4000Å and the 5600Å dichroic. We reduced the LRIS observations using the data reduction pipeline LPIPE (Daniel A. Perley, 2019).

Four of the resulting spectra are consistent with an underlying star-forming region only, while the other four contain additional broad hydrogen and oxygen features at the same redshift. We focus on the spectrum of VT 1210+4956, taken on 2018 April 13, which contains a broad Hα line that is blended with spectrally unresolved Hα and [N II] lines. We fitted this complex with a model of four Gaussian components, corresponding to the broad and narrow Hα lines, and the narrow [NII] host galaxy lines. The narrow line components have central wavelengths fixed to their respective wavelengths at the host galaxy redshift z = 0.03472 (Aguado et al., 2019). Their widths were fixed to the 7ÅFWHM instrumental resolution, while their amplitudes were allowed to vary. The broad profile was allowed to vary in its amplitude, width (up to 10,000 km/s) and central wavelength (up to 6Å). We additionally marginalized over three nuisance parameters corresponding to i) an overall zero-point offset for the spectrum, ii) an overall shift in the wavelength solution (corresponding to a redshift uncertainty of < 0.002), and iii) a local slope for the continuum emission. We fitted this model using the Markov Chain Monte Carlo code *emcee* (Foreman-Mackey et al., 2013) and find that the data are sufficient to constrain each parameter to a roughly Gaussian posterior probability distribution. The model spectrum is shown in Fig. 3.2, and the best-fitting values are listed in Table 3.1.

3.6 Radio Follow-up Observations

Using the VLA, we took two broadband radio follow-up observations of VT 1210+4956. The first epoch was observed on 2018 May 30 and spans the frequency range 1-18 GHz in five bands with central wavelengths 1.5, 3, 6, 10, and 15 GHz. The second epoch spans 1-12 GHz, and was observed in two scheduling blocks, with the 1.5 and 3 GHz bands observed on 2019 April 30, and the 6 and 10 GHz bands observed on 2019 May 8. We used standard procedures in the radio data reduction package CASA (McMullin et al., 2007) to calibrate and image the data. The photometric measurements based on the images in each band are listed in Table 3.2. Where permitted by signal to noise, we increased the frequency resolution by producing sub-band images from groups of independently calibrated spectral windows. After verifying in each sub-band image that the target is detected, unresolved, and not substantially affected by image artifacts, we measured the peak flux using the CASA task *imstat* and estimated the uncertainty by taking the root mean square pixel value in an area of the image with no substantial emission. In both epochs, we detected the peak of the radio spectrum, allowing for standard synchrotron blast wave modeling described below. In our first follow-up epoch, taken ∼20.6 years after nondetection at 1.5 GHz in FIRST, we measured a 1.5 GHz source at a flux of 1.22 ± 0.04 mJy (Table 3.2). After adding the 0.13 mJy RMS noise in the FIRST image in quadrature with our measurement uncertainty, this corresponds to a 9σ detection of variability relative to the nondetection in FIRST, confirming that VT 1210+4956 is a transient source.

3.7 Archival X-ray Source

We searched the MAXI Gamma Ray Burst (GRB) catalog (Serino et al., 2014b), the INTernational Gamma-Ray Astrophysics Laboratory (INTEGRAL) GRB catalog (Rau et al., 2005), the Swift GRB catalog (Lien et al., 2016), and the Open Supernova Catalog (Guillochon et al., 2017) for counterparts to VT 1210+4956. We considered an archival transient to be a match to VT 1210+4956 if it fell within the astrometric uncertainty of that source's localization region. For MAXI, INTEGRAL and Swift, we used the published uncertainties and localization regions, and for optical supernovae in the Open Supernova Catalog, we took this region to be a circle of radius 2 arcseconds. We excluded the Fermi GRB catalog (von Kienlin et al., 2020), because the large localization regions and the ∼2000 bursts detected before the VLASS detection in 2017 lead to a high false alarm probability (an expected value of ∼13 spurious matches per source as estimated by cross matching the

catalog with a set of random coordinates). Among the catalogs adopted, we found one match: an association between VT 1210+4956 and the soft X-ray flash GRB 140814A (Serino et al., 2014b).

GRB 140814A was detected by the MAXI Gas Slit Camera (GSC) in the 4-10 keV band during five consecutive 3-second time bins, centered between Universal Time (UT) 07:12:17 and 07:12:29 on 2014 August 14. The integrated 4-10 keV flux in this time window is $\sim$11$\times$ greater than the upper limits from the previous transit at UT 5:39 and the subsequent transit at UT 8:43 (Uchida et al., 2014). The burst was simultaneously detected in the GSC's 2-4 keV band in four of the five time bins (Fig. 3.3). There was no detection in the simultaneous observation with the GSC 10-20 keV band, which has similar 1σ sensitivity to the other two bands (Sugizaki et al., 2011). This burst is one of 9 MAXI GRBs that has been classified as a MAXI Unidentified Short Soft Transient (MUSST), due to the lack of counterparts in follow-up observations (Sugizaki et al., 2011), (Lipunov et al. 2014, GCN#16688, Vargas et al. 2014, GCN#16689) and the non-detection in the highest energy MAXI band.

3.8 Consistency of VT 1210+4956's Position with the GRB 140814A Localization

Sources detected with the MAXI GSC are localized by the MAXI team by modeling the observed light curve with the position-dependent instrumental response (Serino et al., 2014b). Along the direction of the slit, point sources appear as a roughly Gaussian point spread function (PSF) with a standard deviation of 0.42-0.64 degrees depending on the angle at which they pass over the slit (Sugizaki et al., 2011). As these sources transit over the slit, their flux is modulated by a triangular effective area function dependent on the orthogonal separation between the source and the slit (Sugizaki et al., 2011). The observed light curve is proportional to the product of the intrinsic light curve with the effective area. Sources with intrinsically constant flux can thus be localized by fitting a joint model of the triangle function in the time direction and a Gaussian in the direction along the slit (Serino et al., 2014b). For sources that vary during the observation, the light curve cannot be properly represented by the triangle function, which produces a systematically too small localization region. To roughly compensate for this effect, the MAXI team produced a variable source localization region by first fitting a model to the data assuming the flux were constant, then extending the localization in the direction of

the scan by a factor of $d\Theta(T_{transit} - T_{duration})/T_{transit}$ where $d\Theta$ is the angular-width of the triangle function, $T_{transit}$ is the time-width of the triangle function, and $T_{duration}$ is the observed width of the transient. This method is estimated to localize the position of GRB afterglows up to a ~0.1 deg systematic error (Serino et al., 2014b).

Figure 3 shows the position of VT 1210+4956 relative to the published MAXI localization regions for constant and variable sources, after incorporating the systematic error. We used the *MXSCANCUR* function from the MAXI software package to compute the angular separation of the VT 1210+4956 position and the center of the constant flux ellipse as a function of time. At the time of the burst the separation is ~0.34 deg, smaller than the 1σ uncertainty of the Gaussian response. We additionally used *MXSCANCUR* to check that the effective area at the position of VT 1210+4956 is nonzero at the time of the burst detections. We find that this is the case, with all $> 1\sigma$ detections occurring during the first half of the sensitivity window (Fig. 3.3).

VT 1210+4956 is located in the variable source region, but not the constant X-ray flux region (Fig. 3.3). This is as expected if the observed duration of the burst (~15s) is shorter than the MAXI transit duration (~40s). To check that this short duration cannot be explained as an artifact of the time-variable GSC sensitivity, we ran a Monte Carlo simulation. If the true light curve were constant and longer than the ~40s transit duration, then the observed light curve can be modeled with a top hat function of width >40s, multiplied by the effective area function. We thus fitted the observed light curve with a model product of these functions, allowing the duration and flux of the burst to vary freely and using the effective area function at the center of the constant source localization region. We adopted flat priors in both the duration and flux, with the height constrained to be greater than 0 and less than 5x the highest data point, and the width constrained to be greater than 0 and less than 100s. We fit the 4-10 keV data because it has a higher signal-to-noise ratio than at 2-4 keV. From this simulation, we found that the best fitting top hat model has a duration of 15.1 ± 2.3s (where the uncertainty reflects the 50th-16th and 84th-50th percentile ranges). Burst durations of >40s are ruled out at the 99% level, consistent with GRB 140814A being located in the variable source region.

A location for GRB 140814A outside the constant flux region is reinforced by the non-detection in 0.3-10 keV follow up observations by the Swift X-ray tele-

scope taken ∼6 hours after MAXI. These data cover the constant flux localization region (Fig. 3.3) and do not detect any new X-ray sources with an upper limit of 3×10^{-3} counts/s (Vargas et al. 2014, GCN#16689). This corresponds to a flux of $\sim10^{-13}$ erg cm^{-2} s^{-1}, approximately 60,000× fainter than the MAXI detection in a similar band, a substantially faster fade rate than typical for GRB afterglows at this epoch (Bernardini et al., 2012).

3.9 False Alarm Probability

We test the false alarm probability (FAP) for GRB 140814A being located in the variable source region, excluding the constant source region. After incorporating the systematic uncertainty, this region spans an area of ∼1.54 deg^2. Due to the uncertainty in the intrinsic light curve of the burst and its degeneracies with the localization, we do not attempt to further subdivide this area. We treat all points within this area as being equally likely to be the true position.

VT 1210+4956 was identified in a blind search of the overlap between the VLASS Epoch 1.1 and the FIRST fields, spanning 6195 deg2. The probability that a random point from the searched area falls within the GRB 140814A region is 1.54 deg^2 / 6195 deg^2 = 2.5×10^{-4}. Because GRB 140814A is the only MUSST within the Epoch 1.1 / FIRST overlap that occurred before the end of Epoch 1.1 in February 2018, this is the FAP for a cross match between VT 1210+4956 and MUSSTs.

If we relax the softness condition, there are 3 other MAXI bursts (GRB 150110A (Negoro et al. 2015, GCN #17290), GRB 120528C (Morii et al. 2012, GCN #13349), and GRB 111024A (Toizumi et al. 2011, GCN #12489)) with no definitive counterparts . The collective area spanned by the localizations of all 4 bursts (including GRB 140814A) is 6.6 deg^2, corresponding to a FAP of 1.1×10^{-3}. Expanding the sample to account for other catalogs of potential matches only changes this result by small amount. The 12 INTEGRAL GRBs (Rau et al., 2005) in the Epoch 1.1/FIRST overlap are localized to a few arcminutes and span a total area of 0.053 deg^2. The Swift GRBs (Lien et al., 2016) span 0.6 deg^2, and the Open Supernova Catalog supernovae (Guillochon et al., 2017) span 0.017 deg^2 assuming a 2 arcsecond match radius. The joint false alarm probability for all those catalogs combined is 1.2×10^{-3}. We regard this value as the lower limit of the FAP.

There are 3 other VLASS transients among the sample that are associated with

galaxies and have broad Hα lines in follow-up spectroscopy. These transients are ∼an order of magnitude less radio luminous than VT 1210+4956. Their optical spectra all contain broad oxygen lines, which VT 1210+4956's spectrum lacks. None of the other 3 are associated with observed X-ray bursts. Their radio and optical properties are also consistent with supernovae interacting with massive CSM shells ejected in the centuries before core collapse. If we consider all four to be part of the same sample, the FAP rises by a factor of 4 to 4.8×10^{-3}. We consider this to be an upper limit on the FAP.

3.10 Peak Flux and Frequency

To infer properties of the shock from our broadband radio SEDs, we used *emcee* (Foreman-Mackey et al., 2013) to fit the sub-band radio photometry with a synchrotron spectral break model [Granot and Re'em Sari (2002), their equation 1]. We adopt top-hat priors over wide ranges in all parameters and find that each radio epoch is well fitted by this model (Fig. 3.1). The peak frequencies and fluxes are listed along with their uncertainties in Table 3.3, and have statistical uncertainties of less than 1% in both epochs. The dominant sources of uncertainty in the derived shock properties are systematic, due to the unmeasured parameters ϵ_e, ϵ_B, and f described below.

3.11 Shock Radius and Magnetic Field

The frequency and luminosity of a shock's synchrotron self-absorption peak can be used to estimate the shock's radius R and magnetic field B. Assuming an optically thin spectral index of $\alpha_{\rm thin} = 1$ (appropriate for VT 1210+4956; see Table 3.3), we calculate R and B using equations in units scaled roughly to VT 1210+4956.

$$R = 7.5 \times 10^{16} \left(\frac{\epsilon_e}{\epsilon_B}\right)^{-\frac{1}{19}} \left(\frac{f}{0.2}\right)^{-\frac{1}{19}} \left(\frac{L_p}{10^{29}\ \mathrm{erg/s/Hz}}\right)^{\frac{9}{19}} \left(\frac{\nu_p}{5\ \mathrm{GHz}}\right)^{-1}\ \mathrm{cm}, \qquad (3.1)$$

$$B = 0.21 \left(\frac{\epsilon_e}{\epsilon_B}\right)^{-\frac{1}{19}} \left(\frac{f}{0.2}\right)^{-\frac{4}{19}} \left(\frac{L_p}{10^{29}\ \mathrm{erg/s/Hz}}\right)^{-\frac{2}{19}} \left(\frac{\nu_p}{5\ \mathrm{GHz}}\right)\ \mathrm{G}, \qquad (3.2)$$

where ϵ_B and ϵ_e are the fraction of shock energy in the magnetic field and in relativistic (energy > 511 keV) electrons respectively, f is the fraction of the spherical volume of radius R that is emitting the synchrotron emission, and L_p and ν_p are the luminosity and frequency of the radio spectrum's spectral peak. The strongest

dependencies in these equations are on L_p and ν_p, which are directly measured from the radio spectrum (Table 3.3). Both R and B are weakly dependent on the unmeasured quantities ϵ_e/ϵ_B , and f. We adopt a similar convention to studies of other non-relativistic radio supernovae in assuming $\epsilon_e = \epsilon_B = 0.1$ [see (A. Y. Q. Ho, E. Sterl Phinney, et al., 2019) for a discussion]. Because of the likely aspherical CSM geometry, we marginalize over f by assuming it is drawn from a uniform distribution between 0.1 and 0.5. The resulting values are listed in Table 3.4.

3.12 Energy in the Shock

The energy U dissipated in the shock is:

$$\begin{aligned} U &= \left(\frac{1}{\epsilon_B}\right)\frac{4}{3}\pi f R^3 \frac{B^2}{8\pi} \\ &= 2.7\times10^{49}\left(\frac{\epsilon_B}{0.1}\right)^{-1}\left(\frac{\epsilon_e}{\epsilon_B}\right)^{-\frac{-11}{19}}\left(\frac{f}{0.2}\right)^{\frac{8}{19}}\left(\frac{L_p}{10^{29}\ \mathrm{erg/s/Hz}}\right)^{-\frac{23}{19}}\left(\frac{\nu_p}{5\ \mathrm{GHz}}\right)^{-1}\ \mathrm{erg}. \end{aligned} \tag{3.3}$$

We make the same assumptions for ϵ_e,ϵ_B, and f as before; the dependence on these parameters is much stronger for the energy. The largest systematic uncertainty arises from the factor $(1/\epsilon_B)$, with all other uncertainties likely amounting to less than a factor of 2 in the energy. In gamma ray bursts, ϵ_B has been estimated to be as small as $\sim10^{-6}$, however, for non-relativistic radio supernovae, it is often assumed to be between 0.1 - 0.5. For our comparison with other radio supernovae in Fig. 3.4, we normalize all values to $\epsilon_B = 0.1$. Under this assumption, we find an energy of $(5.4^{+0.9}_{-1.2})\times10^{49}$ erg in follow up epoch 1 (Table 3.4). If instead we assume that ϵ_B is drawn from a log-uniform distribution between 10^{-3} and 0.1, we find a $\sim3\times$ larger value of $(14^{+13}_{-7})\times10^{49}$ erg.

Radio shock velocity and CSM density

By measuring the shock radius R at two epochs, using identical values for ϵ_e,ϵ_B, and f for both epochs in each instance of the Monte Carlo simulation, we can determine the average shock velocity between the two: $v_{\mathrm{radio}} = \Delta R_{\mathrm{Epoch\ 1\text{-}2}}/\Delta t_{\mathrm{Epoch\ 1\text{-}2}}$. We find a shock velocity for VT 1210+4956 of 1780 ± 290 km s^{-1}. If we adopt the wide range of ϵ_B described above, we find a value of 1570^{-270}_{+290} km s^{-1}. Both values are similar to the FWHM velocity of the Hα line, 1345^{-64}_{+56} km s^{-1}, consistent with our interpretation of the Hα emission coming from a dense shell behind the forward

shock (Heng, 2010). Because the Hα velocity is more tightly constrained than the radio velocity, we use its value as a proxy for the shock velocity in estimating the CSM density. Using measurements of the magnetic field and the shock velocity, we can estimate the density of the gas swept up between the follow-up epochs. Applying the shock jump conditions in the limit of a strong shock: $\mathrm{P}_1+\rho_1\ \mathrm{v}_1^2 = \mathrm{P}_2+\rho_2\ \mathrm{v}_2^2$ and $\rho_2/\rho_1 = v_1/v_2 = 4$, where P is the pressure, v is the forward shock velocity, ρ is the mass density, and the subscripts 1 and 2 refer to pre- and post-shock quantities respectively. The post-shock (thermal) pressure is given by $P_2 = (1/\epsilon_B)B^2/8\pi$. Material is swept up by the shock at a speed of $v_1 \approx v_{\rm shock}$ and the mass density is related to the number density by $\rho = \mu m_p n$, where μ is the mean atomic mass. Combining these relations, the pre-shock CSM density is:

$$n_1 = \frac{4}{3\mu m_p}\frac{(1/\epsilon_B)(B^2/8\pi)}{v_{\rm shock}^2}. \tag{3.4}$$

Scaled to typical values for the VLASS transients and assuming a pure hydrogen gas ($\mu = 1$), the pre-shock density is

$$n_1 = 3.9\times10^6\left(\frac{\epsilon_B}{0.1}\right)^{-1}\left(\frac{\epsilon_e}{\epsilon_B}\right)^{-\frac{8}{19}}\left(\frac{f}{0.2}\right)^{\frac{8}{19}}\left(\frac{L_p}{10^{29}\ \mathrm{erg/s/Hz}}\right)^{-\frac{4}{19}} \left(\frac{\nu_p}{5\ \mathrm{GHz}}\right)^2\left(\frac{v_{\rm shock}}{1000\ \mathrm{km/s}}\right)^{-2}\ \mathrm{erg}. \tag{3.5}$$

Assuming that $\epsilon_B = \epsilon_e = 0.1$, f is uniformly distributed between 0.1 and 0.5, and adopting the Hα velocity as discussed above, we find a density of $n_1 = 1.1^{+0.3}_{-0.2}\times 10^6\ \mathrm{cm}^{-3}$. Allowing ϵ_B to vary in a wide range as with the energy changes this estimate to $n_1 = 4^{+7}_{-2}\times10^6\ \mathrm{cm}^{-3}$. The resulting density of $\sim 10^6\ \mathrm{cm}^{-3}$ is higher than the densities observed in non-nuclear regions of galaxies, with the exception of giant molecular cloud (GMC) cores and extreme stellar outflows (Draine, 2011). This high gas density is located within a radius of 0.05 pc of a highly energetic explosion associated with an evolved star-forming region. Within this radius, GMC cores would be disrupted through feedback within the lifetime of any massive star (Elmegreen, 2007). We conclude that this mass was deposited through a pre-explosion outflow from the progenitor.

3.13 Total Shocked Mass in the Circumstellar Shell

From the inferred densities, velocities and shock radii, we set a lower limit on the mass swept up within the shock. The total mass swept up in the Δt $\sim$1 year between our two radio follow-up epochs is $M_{\rm shocked} \approx 4\pi R^2 f_{\rm shell}(v_{\rm shock}\Delta t) m_p n_1 = 0.8 M_\odot (f_{\rm shell})$, where $f_{\rm shell}$ is the fraction of the shocked shell that is emitting radio emission, and m_p is the mass of an ionized hydrogen atom. The radio component of the mass estimate scales with the density and can thus be scaled downwards by $\sim$3$\times$ or upwards by 10$\times$ for the range of ϵ_B values considered above. The gas producing the radio emission is shock heated to a temperature of 10^7 K, a temperature at which hydrogen recombination is too inefficient to produce the Hα line. Thus, there is an additional cooler component of gas at a temperature where recombination is efficient, providing the Hα emission associated with the shock. We estimate the mass in this phase using the luminosity of the Hα line, which scales inversely with the density. The total mass of this cool ionized gas is given by $M_{\rm ionized} = (m_p\ L_{H\alpha})/(\alpha_B\ n_1\ (hc/6563\text{Å}))$ where $\alpha_B = 1.17 \times 10^{-13}$ cm^3 s^{-1} is the effective Case B recombination coefficient for Hα at a temperature of 10^4 K (Draine, 2011), and $L_{H\alpha}$ is the Hα luminosity, and hc is the product of Planck's constant and the speed of light. Assuming that the Hα producing gas has a similar density to the pre-shock gas, we find an ionized mass of $\sim 0.7 M_\odot$ for VT 1210+4956. Combining the two phases, we find that the minimum shell mass (responsible for radio and optical emission at the time of our observations) is $\sim 0.8 M_\odot$.

3.14 Mass Loss Rates and CSM Velocities

The mass density ρ at a given radius R is related to the pre-explosion mass loss rate $\dot{M}$ and CSM velocity v by $\dot{M}/v = 4\pi R^2 \rho$, assuming constant $\dot{M}$ and v over the scale probed by a given observation. For a pure hydrogen CSM, we have:

$$\dot{M} = 3.3 \times 10^{-2} \left(\frac{n}{10^6\ \text{cm}^{-3}}\right) \left(\frac{R}{10^{17}\ \text{cm}}\right)^2 \left(\frac{v}{100\ \text{km/s}}\right)\ M_\odot\ \text{yr}^{-1}. \qquad (3.6)$$

For VT 1210+4956, we find a mass loss rate of $\dot{M}/(v/100\,\text{km s}^{-1}) = 4{\times}10^{-}2 M_\odot\ yr^{-1}$.

Mass lost from stars has a terminal velocity similar to the escape velocity of the star. These velocities range from 10s of km/s for systems with loosely-bound atmospheres such as giant stars and common envelopes, to $\sim$1000 km/s for Wolf Rayet stars (Smith, 2014). The densest observed winds tend to move at velocities closer to $\sim$50 km/s, given the additional luminosity needed to drive the extreme mass loss

(Smith, 2014). Given that our observed mass loss rates are higher, we take this as a rough lower bound on the mass loss velocity in wind scenarios. For binary mass loss, the same escape velocity principle applies. Given that the majority of interactions occur on the main sequence or during first expansion to a red giant, we adopt the same fiducial lower bound on the mass loss velocity. In type IIn supernovae, the narrow Hα line indicates the velocity of the pre-explosion mass loss. The LRIS velocity resolution sets an upper limit of ~270 km/s. With the velocity range of 50-270 km/s, the gas accounting for the massive shell we infer must have been lost ~100-1000 years prior to explosion.

3.15 Constraints on the Source of MAXI 140814A

MAXI 140814A has a spectrum that is much softer than that of gamma-ray bursts. It is more reminiscent of SN 2008D, which has been interpreted as a sub-relativistic shock breakout from an optically thick stellar wind. However, MAXI 140814A's luminosity is three orders of magnitude brighter than the SN 2008D X-ray flare (Soderberg, E. Berger, et al., 2008).

We first assume that the source is a spherical sub-relativistic stellar explosion, with velocity βc, where c is the speed of light, and scale to a total burst energy $E \approx 3 \times 10^{47}$ erg, a burst duration $t \approx 15$s, and a typical photon energy $\epsilon_\gamma \approx 5$ keV. The radiated energy in such explosion from any fluid element is at most equal to its kinetic energy, so the mass of the source must satisfy:

$$\tau \approx \kappa \frac{m}{4\pi R^2} \geq 250 \frac{E}{3 \times 10^{47}\ \mathrm{erg}} \frac{\kappa}{0.2\ \mathrm{cm^2 g^{-1}}} \left(\frac{t}{15s}\right)^{-2} \beta^{-2}, \tag{3.7}$$

where κ is the opacity of the source material per unit of mass. For GRB 140814A, $\tau >> \beta^{-1}$, which implies that the radiation is trapped in the source and cannot diffuse to the observer over the observed duration. Thus, the source cannot be non-relativistic and spherical. For an aspherical non-relativistic source, the optical depth is higher for the same amount of mass, and so is the diffusion time unless the outflow geometry is finely tuned. Therefore, we conclude that the outflow is relativistic.

A relativistic explosion solves the high diffusion time problem. A relativistic spherical source that is shocked to a Lorentz factor γ, has an internal energy E $\approx mc^2\gamma(\gamma - 1)$ and therefore,

$$m \geq \frac{E}{\gamma(\gamma-1)c^2} = 1.5\times10^{-7}M_\odot\frac{E}{3\times10^{47}\ \mathrm{erg}}(\gamma(\gamma-1))^{-2}, \quad (3.8)$$

at the same time, relativistic effects dictate $R < 2ct\gamma = 13R_\odot(t/15s)\gamma^2$, so

$$\tau \approx \kappa\frac{m}{4\pi R^2} \geq 125\frac{E}{3\times10^{47}\ \mathrm{erg}}\left(\frac{t}{15s}\right)^{-2}\left(\frac{\kappa}{0.2\ \mathrm{cm^2\ g^{-1}}}\right)^{-2}\gamma^{-4}(\gamma-1)^{-2}. \quad (3.9)$$

The requirement $\tau < \beta^{-1}$ implies $\gamma > 2.5$.

However, a relativistic spherical explosion is also inconsistent with the data. First, accelerating enough mass to relativistic velocities in a spherical explosion of a star requires an extreme energy of $\sim10^{53}$ erg (Ehud Nakar and Re'em Sari, 2012). Second, if the stellar envelope is at rest at the time that the explosion energy is released (i.e., there is no double explosion) the photons that are generated behind the shock are radiated upon the breakout of the shock and their typical observed energy is 100 keV (Ehud Nakar and Re'em Sari, 2012), higher than observed.

We conclude that the most likely explanation for GRB 140814A is a non-spherical relativistic expansion, such as a jet. A collimated outflow does not change the lower limit on the source Lorentz factor derived above. If the radiation of the source is beamed towards the observer (i.e., the angle between the source velocity and the line of sight is smaller than $1/\gamma$) the limits are similar to the spherical case, and if the radiation is beamed away from the observer the limits are more severe (Matsumoto, Ehud Nakar, and Piran, 2019).

3.16 Supplementary Text

3.17 Consistency Checks

Other than requiring that high-energy transients occur before the first radio observation of VT 1210+4956, we did not explicitly consider the inferred explosion date in the FAP calculation. However, the timing of GRB 140814A is consistent with the evolution of the radio spectrum. When supernova ejecta begin to interact with a dense CSM, the forward shock velocity decreases suddenly, due to the large density jump. The shock velocity is then reaccelerated by the pressure produced by the shocked supernova ejecta. The properties of the ejecta and CSM can thus be used

to estimate the forward shock velocity as a function of time. Assuming an ejecta mass of $\sim 2 M_{\odot}$ and kinetic energy of $\sim 10^{51}$ erg, similar to SN 2014C (Margutti, Kamble, et al., 2017) and SN 2001em (N. N. Chugai and Roger A. Chevalier, 2006), we find that the forward shock velocity reaches ~2000 km/s approximately 3 years after the explosion (Roger A. Chevalier and Liang, 1989). We assume a CSM shell of uniform density $\sim 2 \times 10^6$ cm^{-3} with total mass $\sim 1 M_{\odot}$ at radius $\sim 9 \times 10^{16}$ cm, as inferred from the radio analysis (Table 3.4, see discussion below). This is consistent with the ~3.5 year delay between GRB 140814A and the epoch at which we infer a radio-based shock velocity of ~1800 km/s for VT 1210+4956.

The column density of hydrogen, N_H, in a spherical CSM shell with the assumed values is $N_H \sim 2 \times 10^{22}$ cm^2, at which the optical depth at 2 keV is ~1, rapidly decreasing at higher energies. The column density would be lower for an off-axis line of sight in a toroidal CSM geometry. This is consistent with GRB 140814A's observed soft X-ray spectrum being intrinsic rather than a product of obscuration.

We considered other potential sources of short, soft X-ray transients. One such class is a shock breakout from a supernova similar to the one observed in SN 2008D, which was 3 orders of magnitude less luminous than MAXI 140814A (Soderberg, E. Berger, et al., 2008). For MAXI to detect such a breakout, it would have to be at a distance within ~5 Mpc. At that distance, the contemporaneous All Sky Automated Survey for Supernovae (ASASSN) (Shappee et al., 2014) was complete to supernovae with a V or g band absolute magnitude brighter than -12, easily sufficient to detect core collapse and stripped envelope supernovae months after explosion. There are no cataloged supernovae that are located within the variable source region and exploded within ~1 month of the X-ray transient (Guillochon et al., 2017). This rules out shock breakout as an explanation for the MAXI transient. At the ~149 Mpc distance of VT 1210+4956, the ASASSN limiting magnitude of > –20.5 is not constraining for a wide range of supernova types (Hicken et al., 2017; Taddia, M. D. Stritzinger, Sollerman, et al., 2013; Taddia, M. D. Stritzinger, Bersten, et al., 2018).

Another potential class is a flare from a Galactic source, such as a star or X-ray binary. MAXI 140814A is located at a Galactic latitude of +66 deg, where the column density of Galactic sources is low. In a search of the SIMBAD database, we did not find any known flare stars or X-ray binaries within the MAXI localization region.

X-ray flares from stars generally last from minutes to hours, as opposed to ∼15s for MAXI 140814A (Pye et al., 2015). The peak luminosity of these flares is generally 1-2 orders of magnitude brighter than the quiescent X-ray luminosity from the star. To search for a potential quiescent counterpart, we checked the Röntgensatellit (ROSAT) all sky catalog (Boller et al., 2016) and found that the brightest X-ray source within a 3-degree radius of the MAXI 140814A constant flux localization has a ROSAT count rate of 0.2 counts/s in the 0.1-2.5 keV band. This corresponds to a flux < 1000× the 2-4 keV flux of MAXI 140814A for a range of power law and blackbody models, further disfavoring a flare star origin.

X-ray binaries are known to brighten by several orders of magnitude when transitioning between the low-hard state and high-soft state. These transitions typically last for days to months (Fender, Homan, and Belloni, 2009), whereas GRB 140814A was detected for ∼15s in only one 92-minute orbit of the ISS. Luminous shorter timescale flares have been observed from accreting compact object systems, with some burst-only systems displaying quiescent fluxes > 3 orders of magnitude lower than the peak of the bursts (Campana, 2009). The vast majority of known bursters have a Galactic latitude between -15 and +15 deg (in't Zand et al., 2019) in contrast to the +66.4 deg Galactic latitude of GRB 140814A. Additionally, these bursts are observed to, and theoretically expected to repeat (Sivakoff, Sarazin, and Jordán, 2005; Galloway and Keek, 2021). In particular, bursts with durations of 10-100s have typical recurrence timescales of hours to days (Galloway and Keek, 2021). No other bursts from the localization region of GRB 140814A have been reported from X-ray follow-up observations of the field, or the >11 years of observations from the MAXI GSC.

AGN are known to display variability at all wavelengths, and have been observed to launch new jets (Nyland, Dillon Z. Dong, et al., 2020). However, it is difficult to explain a 15s X-ray flare from an AGN. The characteristic X-ray variability timescale for an AGN scales with its supermassive black hole mass, M_{BH}, at 5 days × (M_{BH} / 10^8 $M_\odot$)^2 (Ishibashi and Courvoisier, 2009). Thus, the characteristic black hole mass for a variability timescale of ∼1 minute is ∼10^4 $M_\odot$. The peak X-ray luminosity of MAXI 140814A is ∼4 × 10^{46} erg/s × (d/150 Mpc)^2, which corresponds to ∼10^4 times the Eddington luminosity for a 10^4 $M_\odot$ black hole at distance d = 150 Mpc. A luminosity at the Eddington limit would require an intermediate-mass

black hole at ∼1.5 Mpc; no such sources are known. There are also no catalogued galaxies within the MAXI variable source localization region closer than 10 Mpc (Cook et al., 2019).

3.18 Constraints on an Optical Supernova

Due to its proximity to the Sun, the optical sky survey coverage of the location of VT 1210+4956 at the time of MAXI 140814A was sparse. Nevertheless, available observations can constrain the possibility of a supernova at the position of VT 1210+4956 in the months following MAXI 140814A.

The only optical constraint reported in the literature comes from the Mobile Astronomical System of Telescope Robots (MASTER) II telescope in Kislovodsk, which followed up a region that likely contains VT 1210+4956 (Lipunov et al. 2014, GCN#16688) starting 10.3 hours after the MAXI transient time. The upper limit from this observation is an apparent magnitude of >18.5 in single 180s frames and >20.0 in 10 images co-added. The latter limit corresponds to an absolute magnitude of -15.9 at the distance of VT 1210+4956. The Balmer decrement of 4.9 from the ratio of the narrow Hα and Hβ lines in the 2018 optical spectrum of VT 1210+4956 implies a reddening E(B-V) = 0.46. Assuming a standard reddening curve (Calzetti et al., 2000), this corresponds to an extinction of 0.8 – 2.8 magnitudes in the MASTER II bands (B, V, R, and I), making the effective limit somewhat shallower (≥ -16.7 to -18.7). Due to the rise time of days to weeks for all but the fastest supernovae (A. Y. Q. Ho, Daniel A. Perley, et al., 2020) this limit does not rule out most types of supernova.

We measured two additional constraints using data from the Palomar Transient Factory (PTF) (N. M. Law et al., 2009) and the Panoramic Survey Telescope and Rapid Response System (Pan-STARRS) (Chambers et al., 2016). The PTF observations were taken in g band ∼2.2 months after GRB 140814A in October 2014. There are no g band PTF observations of the field prior to this date, so we convolved the PTF image to the resolution of a pre-explosion Pan-STARRS image and subtracted the two using a difference imaging pipeline (De et al., 2020). We do not detect a source in the difference image to limits of g > 19.6, g > 20.0, and g > 20.4 on 2014 October 19, 20, and 23 respectively. The deepest of these limits corresponds to an absolute magnitude G > -15.5, or an extinction corrected limit of G > -18.1. The Pan-STARRs observations were taken in I band on 2015 January 12. We stacked all

available images from this epoch and used the pipeline to subtract them from a stack of Pan-STARRS I band images from 2014 May 9. We do not detect any transient or variable emission to a limiting apparent magnitude of I > 21.1, corresponding to an absolute magnitude of -14.8 and an extinction corrected value of I > -15.6. The PTF and Pan-STARRS limits rule out superluminous supernovae (e.g., De Cia et al., 2018), and luminous type IIn supernovae with large amounts of mass lost close to explosion (Fransson et al., 2014). However, they are not constraining for other types of stripped envelope supernovae (Taddia, M. D. Stritzinger, Bersten, et al., 2018), including analogs of SN 2014C (Margutti, Kamble, et al., 2017) and PTF 11qcj (Palliyaguru et al., 2019). This is consistent with the early time counterpart of VT 1210+4956 having been a stripped envelope supernova, though does not require this.

3.19 Free-free Absorption and Asymmetric CSM

In our radio follow-up observations of VT 1210+4956, we measured peaks in the broadband radio spectra at 5.06 ± 0.02 GHz in the first epoch and 4.49 ± 0.03 GHz in the second epoch (Fig. 3.1). In the previous sections, we assumed that this peak was due to synchrotron self-absorption, leading to results that are consistent with the optical spectrum of VT 1210+4956. Here we test whether the spectra could instead be explained with free-free absorption.

The free-free optical depth τ_ν of radio emission passing through a plasma is given by:

$$\tau_\nu = 3.28 \times 10^{-7} \left(\frac{\nu}{\mathrm{GHz}}\right)^{-2.1} \int_{LOS} \left(\frac{T}{10^4 \mathrm{K}}\right)^{-1.35} \left(\frac{n_e}{\mathrm{cm}^{-3}}\right)^2 \frac{ds}{\mathrm{pc}}, \tag{3.10}$$

where ν is the frequency of light being absorbed/transmitted, and T and n_e are the electron temperature and density in a region of length ds along the line of sight (LOS) (James J. Condon and Ransom, 2016a). The optical depth scales as $\tau_\nu \propto \nu^{-2.1}$, which implies that on the optically thick side, the flux density scales super-exponentially with frequency as $\S_\nu \propto \nu^{-1} exp(-\tau_\nu) \propto \nu^{-1} \propto exp(\nu^{-2.1})$, where the additional factor of ν^{-1} arises from the intrinsic spectral index of the emission, which is ~ 1 (Table 3.3).

Combining this relation with our lowest frequency detection of 0.56 ± 0.07 mJy at 1.14 GHz, we set an upper limit on the optical depth to free-free absorption at the

5.87 ± 0.02 mJy peak at 5.06 GHz in the first epoch. If there is no synchrotron self-absorption, all of the drop in flux from the peak at $S_5 = 5.87$ mJy to the low frequency measurement of $S_1 = 0.56$ mJy is due to free-free absorption. In that case, we have that $S_5 / S_1 = (5.06/1.14)^{-1} \exp(-(\tau_{5,ff} - \tau_{1,ff}))$, where $\tau_{5,ff}$ and $\tau_{1,ff}$ are the free-free optical depth at 5.06 and 1.14 GHz respectively. This implies that $\tau_{5,ff} - \tau_{1,ff} = 3.9$. Simultaneously, we find that $\tau_{5,ff}/\tau_{1,ff} = (1.14/5.06)^{-2.1} \approx 22.9$. This then implies that $\tau_{5,ff} = 0.17$. Thus, the maximum possible attenuation from free-free absorption at the 5 GHz peak is $\sim 1\text{-}e^{-0.17} = 16\%$, with any contribution from synchrotron self-absorption reducing this even closer to 0.

We improve this limit by attempting to reproduce the detailed shape of the observed peak with free-free absorption. To do so, we assume that a synchrotron source with unabsorbed spectrum $S_\nu = A\nu^\alpha$ (where α is the spectral index and A is a scale factor) is being attenuated by a slab of material with constant temperature T and emission measure $\mathrm{EM} = \int_{LOS} \left(\frac{n_e}{\mathrm{cm}^{-3}}\right)^2 \frac{ds}{\mathrm{pc}}$. We used *emcee* to explore the parameter space of EM, T, A, and α, assuming uninformative priors for all parameters. This model can approximate the radio spectrum at frequencies > 2 GHz. However, at lower frequencies, the super-exponential decay in flux becomes dominant. At 1.5 GHz, the predicted flux drops to 0.359 ± 0.006 mJy, nearly 4× lower than our measured value of 1.22 ± 0.04 mJy. At 1.14 GHz, the model predicts 0.0169 ± 0.0007 mJy, over 30× lower than our measured value of 0.56 ± 0.07 mJy. This confirms that the peak cannot be explained by free-free absorption.

The lack of free-free absorption requires an explanation, given the high CSM density. Above we estimated the density of the CSM to be $\sim 2.2 \times 10^6$ cm^{-3}. This density depends primarily on the shock velocity (which is independently and consistently measured using both the Hα line width and the change in shock radius), the peak frequency (which has uncertainty less than 1%), and the assumed value of 0.1 for the magnetic field energy fraction ϵ_B (which can vary, but cannot decrease the density by more than a factor of 3). If we approximate the CSM between the first and second epochs as a spherical shell with uniform density and temperature, the free-free optical depth at 5 GHz is $\tau_\nu \sim 88 \left(T/10^4 K\right)^{-1.35} \left(\frac{n_e}{2.2\times10^6 \mathrm{cm}}\right)^{-3}$ for the estimated density at typical H II region temperatures. Any dense ionized gas that has yet to be shocked along the line of sight would only increase the free-free absorption.

To reconcile the inferred lack of free-free absorption at 5 GHz with the implied

density, we require either a high temperature in the pre-shock CSM, a lower density along the line of sight, or both. A high temperature, driven by Compton heating from the central X-ray source, was invoked to explain a similar phenomenon in the fast blue optical transient AT 2018cow (A. Y. Q. Ho, E. Sterl Phinney, et al., 2019). However, the X-ray flux of this source faded by a factor of $\sim 10^3$ within the first 100 days of discovery (Margutti, B. D. Metzger, et al., 2019). An analogous source would have to be substantially longer-lived to maintain a temperature necessary to suppress the free-free absorption, or would have to be powerful enough at early times to heat the dense CSM to $>> 10^7$ K where it would not have enough time to cool to the typical HII region equilibrium temperature of 10^4 K in the years before encountering the shock. A simpler solution is if the CSM is asymmetric, with the line of sight being along a lower density direction. Asymmetric mass loss has been predicted for binary interactions. Hydrodynamic simulations have found that the CSM from binary interaction generally forms a toroidal geometry that can be orders of magnitude denser in the midplane than along the poles (Schrøder et al., 2020; MacLeod, Ostriker, and Stone, 2018). If our line of sight is not oriented directly along the midplane, it would be through a substantially smaller column density of gas. Much of that gas may already be shocked, because shocks propagate faster through lower density regions. For a shock velocity $v_{\rm shock}$, the pre-shocked gas would be heated to a temperature of $T = 3/16\, m_p/k_B\, (v_{\rm shock})^2 \sim 5.7 \times 10^8$ K $(v_{\rm shock}/(5000\ {\rm km/s}))^2$, far above the $\sim 10^5$ K temperature required to suppress free-free absorption.

3.20 Rate of similar radio transients

VT 1210+4956 was identified in a search for distance $d < 200$ Mpc off-nuclear extragalactic transients with a flux-limited detection limit of ~0.7 mJy. With its 3 GHz luminosity at the detection epoch of 7.1×10^{28} erg/s, it would have been detectable out to 291 Mpc. Its host galaxy has an r-band apparent magnitude of 17.7 at a distance of 150 Mpc, and would be easily detectable at 200 Mpc. Likewise, the broad emission feature would be detectable by the same follow-up Keck observation at 200 Mpc. This leaves only one major source of incompleteness: the 6195 deg^2 overlap between VLASS Epoch 1.1 and FIRST. The expected all-sky number of 3 GHz transients at this radio luminosity is thus ~6.7 within 200 Mpc, corresponding to $\sim 2 \times 10^{-7}$ transients Mpc^{-3}. To convert this density to a volumetric rate, we require the duration for which each event would be detectable in our search. The lower limit is set by the time between the first detection in VLASS Epoch 1.1 and the latest detection in VLASS Epoch 2.1, spanning ~2.5 years (Table 3.2). Given

the unknown CSM profile outside the current radius reached, it is unclear how long it will take before the source fades below our detection limit. However, there is a maximum effective timescale probed by our search: the time between non-detection in FIRST and detection in VLASS, which is ~7500 days for VT 1210+4956. Sources that are older than this will appear as variable sources rather than transients, and thus are not included in our sample. Using this range of detectable ages, we estimate a range of volumetric rates for similarly luminous transients of $\sim$ (1-8) $\times$ 10^{-8} transients Mpc^{-3} yr^{-1}.

3.21 Supplementary Tables

Table 3.1: Best fitting emission line model components for VT 1210+4956. Based on the Keck/LRIS spectrum on 2018 April 13 (0.37 years after detection in VLASS). Columns are the name of the emission line component, the rest wavelength of the line $\lambda_{\rm rest}$, the best-fitting central wavelength of the line component $\lambda_{\rm fit}$, the velocity full-width-half-maximum (FWHM) of the line component, the total flux of the component, and its luminosity. Upper and lower uncertainties are respectively the 86th and 14th percentiles of the posterior probability distribution.

Line	$\lambda_{\rm rest}$ (Å)	$\lambda_{\rm fit}$ (Å)	FWHM (km/s)	Integrated flux (10^{-17} erg s^{-1} cm^{-2})	Luminosity (10^{36} erg s^{-1})
Hα broad	6562.8	6559^{49}_{45}	1345^{+64}_{-56}	$27.7^{+1.1}_{-0.9}$	727^{+29}_{-25}
Hα narrow	6562.8		< 270	$10.7^{+0.5}_{-0.4}$	282^{+13}_{-11}
NII 6583Å	6583.45		< 270	$2.3^{+0.3}_{-0.3}$	61^{+7}_{-7}
NII 6548Å	6548.05		< 270	$0.9^{+0.3}_{-0.3}$	23^{+8}_{-8}

Table 3.2: Radio fluxes from single-band images of VT 1210+4956. Columns are the observation date relative to detection in VLASS on 2017 November 20 Δt, the fluxes S_ν in VLA bands centered at frequency ν and. Uncertainties are the RMS noise in a nearby patch with no emission. The upper limit from FIRST is 3× the RMS noise. There is an additional ∼5% systematic uncertainty in the overall flux density scale, which is correlated between bands and constant between epochs, as we used the same calibrators. There is an additional uncertainty of ∼20% in fluxes from VLASS quick-look imaging (Epochs at t = 0 and t = 2.454 years after VLASS detection) (Lacy et al., 2020).

Δt	$S_{1.5\ \rm GHz}$	$S_{3\ \rm GHz}$	$S_{6\ \rm GHz}$	$S_{10\ \rm GHz}$	$S_{15\ \rm GHz}$
	Years	mJy	mJy	mJy	mJy
-20.59	< 0.41				
0		2.8 ± 0.1			
0.5233	1.22 ± 0.04	4.54 ± 0.02	6.11 ± 0.01	5.22 ± 0.01	3.85 ± 0.01
1.441	1.3 ± 0.3	4.13 ± 0.05			
1.463			4.62 ± 0.01	3.04 ± 0.02	
2.454		4.0 ± 0.2			

Table 3.3: Fitted properties of VT 1210+4956's radio spectrum from follow-up observations with the VLA. The columns are the relative observation date (same definition as table 3.2), the spectral peak frequency $\nu_{\rm peak}$, the flux at the peak frequency $S_{\nu_{\rm peak}}$, and the asymptotic optically thin spectral index α. Upper and lower uncertainties are the 86th and 14th percentiles of the posterior probability distribution. We jointly fit the two observations in follow up epoch 2.

Δt (years)	$\nu_{\rm peak}$ (GHz)	$S_{\nu_{\rm peak}}$ (mJy)	α
0.5233	$5.06^{+0.03}_{-0.02}$	$5.87^{+0.02}_{-0.02}$	$-1.04^{+0.02}_{-0.02}$
1.452	$4.48^{+0.03}_{-0.02}$	$5.10^{+0.02}_{-0.02}$	$-1.05^{+0.11}_{-0.17}$

.

Table 3.4: Derived properties of the VT 1210+4956 shock and the CSM in which it is propagating. The columns are the relative observation date (same definition as Table 3.2), the shock radius R, the shock magnetic field B, the energy dissipated within the shock U, the pre-shock CSM density n, and the assumed distributions of microparameters ϵ_e, ϵ_B, and f. For the microparameters assumed, A denotes $\epsilon_e = \epsilon_B = 0.1$, with f drawn from a uniform distribution between 0.1 and 0.5, while B denotes the same distributions for ϵ_e and f with ϵ_B drawn from a log-uniform distribution between 10^{-3} and 0.1, (see text). The uncertainties are the 86th and 14th percentiles of the posterior probability distribution. Values between epochs are positively correlated assuming no evolution in ϵ_e, ϵ_B, and f, with an implied velocity from the change in R between the two epochs of 1780^{+290}_{290} km s^{-1} for microparameter set A, and 1570^{+270}_{290} km s^{-1} for microparameter set B (see text).

Δt (years)	R (10^{16} cm)	B (mG)	U (10^{49} erg)	n (10^6 cm^{-3})	Distribution
0.5233	$8.9^{+0.3}_{-0.2}$	392^{+5}_{-2}	$5.4^{+0.9}_{-1.2}$	$1.1^{+0.3}_{-0.2}$	A
0.5233	$7.9^{+0.6}_{-0.6}$	246^{+10}_{-7}	14^{+13}_{-7}	4^{+7}_{-2}	A
1.452	$9.4^{+0.3}_{-0.2}$	353^{+5}_{-3}	$5.1^{+0.9}_{-1.1}$		A
1.452	$8.4^{+0.7}_{-0.7}$	221^{+8}_{-6}	13^{+12}_{-6}		B

.

Table 3.5: Energies, velocities, radii, densities, and references for sources plotted in Fig. 4. Columns U, R, and n are as defined in table 3.4 and are either calculated from radio data presented in references assuming $\epsilon_e = \epsilon_B = 0.1$ (see text) or taken directly from the reference(s). Dimensionless shock velocities $\Gamma\beta$, where Γ is the bulk Lorentz factor and β is the velocity divided by the speed of light, are either taken from the reference(s) or estimated from R assuming a constant velocity since explosion. References are as follows: (1: Roger A. Chevalier, 1998), (2: A. Y. Q. Ho, E. Sterl Phinney, et al., 2019), (3: Soderberg, Chakraborti, et al., 2010), (4: Margutti, Kamble, et al., 2017), (5: Fransson et al., 2014),(6: Palliyaguru et al., 2019), (7: A. Y. Q. Ho, E. Sterl Phinney, et al., 2019; Kulkarni, Frail, et al., 1998; Z.-Y. Li and Roger A. Chevalier, 1999), (8: A. Y. Q. Ho, E. Sterl Phinney, et al., 2019; Salas et al., 2013), (9: Soderberg, Kulkarni, et al., 2006; Peters et al., 2019), (10: Seppo Mattila et al., 2010)

Object	U (10^{49} erg)	$\Gamma\beta$ (10^{-2})	R (10^{16} cm)	n (10^6 cm^{-3})	Reference(s)
SN 1978 K	0.36	2.0	12	9.8×10^{-3}	(1)
SN 1979C	1.4×10^{-2}	1.2	1.4	1.1	(1)
SN 1980K	2.4×10^{-4}	0.63	0.27	7.4	(1)
SN 1986E	2.7×10^{-4}	0.47	0.31	13	(1)
SN 1986J	0.1	0.97	0.32	1.1	(1)
SN 1988Z	0.2	1	3.9	0.94	(1)
SN 1990B	3.2×10^{-2}	13	3.0	1.1×10^{-3}	(1)
SN 1993J	1.9×10^{-2}	3.3	1.3	0.15	(1)
SN 1994I	1.6×10^{-2}	13	1.2	1×10^{-2}	(1)
AT 2018cow	0.74	13	0.73	1.3	(2)
SN 2009BB	0.27	70	5	2.4×10^{-5}	(3)
SN 2014C (shell)	6.5×10^{-2}	0.5	5.5	0.55	(4)
SN 2010jl			0.9	20	(5)
PTF 11qcj	7.1	2.6	13	6.3×10^{-2}	(6)
SN 1998bw	0.45	100	15	3×10^{-7}	(7)
SN 2007bg	0.23	17	10	1.3×10^{-3}	(8)
SN 2006aj	6.8×10^{-2}	200	6.2	$< 9 \times 10^{-6}$	(9)
SN 1987A (ring)	5.9×10^{-6}	17	70	5×10^{-3}	(10)
SN 1987A (inner)			0.1	1×10^{-3}	(10)

Chapter 4

VT 1137-0337: AN EMERGING PULSAR WIND NEBULA

Dong, Dillon and Gregg Hallinan (June 2022). "A Flat-Spectrum Radio Transient at 122 Mpc consistent with an Emerging Pulsar Wind Nebula". In: *arXiv e-prints*, arXiv:2206.11911, arXiv:2206.11911. arXiv: 2206.11911 [astro-ph.HE].

Dillon Z. Dong[1], Gregg Hallinan[1]

[1] Division of Physics, Mathematics, and Astronomy, California Institute of Technology, Pasadena, California 91125, USA

4.1 Abstract

We report the discovery and follow-up observations of VT 1137-0337: an unusual radio transient found in our systematic search for extragalactic explosions in the VLA Sky Survey (VLASS). VT 1137-0337 is located in the brightest region of a dwarf starburst galaxy at a luminosity distance of 121.6 Mpc. Its 3-GHz luminosity is comparable to luminous radio supernovae associated with dense circumstellar interaction and relativistic outflows. However, its broadband radio spectrum - proportional to $\nu^{-0.35}$ over a range of $\gtrsim 10\times$ in frequency and fading at a rate of 5% per year - cannot be directly explained by the shock of a stellar explosion. Jets launched by various classes of accreting black holes also struggle to account for VT 1137-0337's combination of observational properties. Instead, we propose that VT 1137-0337 is a decades old pulsar wind nebula that has recently emerged from within the free-free opacity of its surrounding supernova ejecta. If the nebula is powered by spindown, the central neutron star should have a surface dipole field of $\sim 10^{13} - 10^{14}$ G and a present-day spin period of $\sim 10 - 100$ ms. Alternatively, the nebula may be powered by the release of magnetic energy from a magnetar. Magnetar nebulae have been proposed to explain the persistent radio sources associated with the repeating fast radio bursts FRB 121102 and FRB 190520B. These FRB persistent sources have not previously been observed as transients, but do bear a striking resemblance to VT 1137-0337 in their radio luminosity, spectral index, and host galaxy properties.

4.2 Introduction

Recent advances in hardware (R. A. Perley, Chandler, et al., 2011) and observing techniques (Mooley, Myers, et al., 2019) used at the Jansky Very Large Array (VLA) have made it possible to efficiently survey large areas of the GHz radio sky at arcsecond resolution. These technologies are key components of the VLA Sky Survey (VLASS), which is observing the full sky north of declination $\delta = -40^\circ$ over multiple epochs (Lacy et al., 2020). VLASS's survey speed and wide areal coverage (~34,000 deg^2) has led to a rapid uptick in the detection rate of slow radio transients, which typically peak on timescales of months to decades post explosion in the 2-4 GHz VLASS band. Previously, slow radio transients were primarily detected via follow-up observations of events identified at other wavelengths. With VLASS, new transients can be directly identified at radio frequencies at scale, enabling an exploration of the radio transient phase space unbiased by the detectability of emission at other wavelengths. This has facilitated the systematic discovery of representatives from both known and previously hypothetical transient classes (e.g., Brian D. Metzger, Williams, and Edo Berger, 2015; Roger A. Chevalier, 2012). Examples include a diversity of nuclear radio flares including tidal disruption events (M. M. Anderson et al., 2019; Ravi et al., 2021; Somalwar, Ravi, D. Dong, et al., 2021) and a population of newly launched jets from quasars (Nyland, Dillon Z. Dong, et al., 2020), a compelling candidate for an off-axis long gamma ray burst (C. J. Law et al., 2018), and the first known supernova set off by the merger of a compact object with a massive star (D. Z. Dong et al., 2021).

Broadband radio spectra of a transient's synchrotron emission are powerful diagnostic tools of the transient's physical properties. Thus far, these spectra have primarily revealed spectral peaks, and/or steep power law tails where $S_\nu \propto \nu^{-\alpha}$ with $\alpha > 0.5$. This is in line with predictions for synchrotron emission from electrons accelerated with diffusive shock acceleration (Roger Blandford and Eichler, 1987; Jones and D. C. Ellison, 1991; Pelletier et al., 2017) modified by free-free/synchrotron self absorption (James J. Condon and Ransom, 2016b). The consistency is unsurprising, given that previously identified radio transient classes are associated with fast outflows that drive strong shocks in the surrounding gas.

In this paper, we present VLASS Transient J113706.19-033737.3 (hereafter VT 1137-0337), a new radio transient with a spectral index ($\propto \nu^{-0.35}$ measured over more than a factor of 10$\times$ in frequency) that is inconsistent with diffusive shock

acceleration. In Section 4.3, we discuss the discovery of VT 1137-0337 and its association with its host galaxy, a starbursting dwarf. We additionally estimate the rate of transients with similar observational properties. In Section 4.4, we present radio and optical follow up spectra at the location of the transient and discuss our procedure for fitting power-law and emission line models to these spectra. In Section 4.5, we use these observations to derive constraints on the emitting region and its surroundings. In Section 4.6, we assess the consistency of VT 1137-0337 with a wide range of transient, variable, and persistent radio source classes. In Section 4.7, we summarize our conclusions. Throughout this paper, we assume a flat ΛCDM cosmology where H_0 = 69.6 km s^{-1} Mpc^{-1} (Bennett et al., 2014), implying a luminosity distance to the source of 121.6 Mpc and an angular diameter distance of 115.2 Mpc (Wright, 2006).

4.3 Discovery of VT 1137-0337

VT 1137-0337, located at RA = 11:37:06.19, Dec = -03:37:37.3, was discovered through a blind search of VLASS Epoch 1.1 (the first half-epoch of VLASS) for transients associated with galaxies within a distance of 200 Mpc. For this search, we chose the Faint Images of the Radio Sky at Twenty-cm (FIRST) survey (Becker, R. L. White, and Helfand, 1995) as our reference epoch for its comparable resolution and sensitivity over a large area of sky (6195 deg^2 overlapping with Epoch 1.1). Full details of the search will be presented in an upcoming paper (Dong et al. in prep). Here we provide an overview of our methodology.

We used the source extractor PyBDSF (Mohan and Rafferty, 2015a) to assemble a catalog of all sources detected at ≥5 times the local RMS noise the Epoch 1.1 quicklook images[1] (Lacy et al., 2020). We used methods implemented in the `astropy.skycoord` class (Astropy Collaboration, Robitaille, et al., 2013; Astropy Collaboration, Price-Whelan, et al., 2018) to cross match these sources against the FIRST catalog (Becker, R. L. White, and Helfand, 1995), identifying all VLASS sources that are separated by >10" from the nearest known FIRST source as transient candidates. Through visual inspection, we rejected image artifacts, spatially resolved VLASS sources, and faint FIRST sources that fell under the 0.7mJy FIRST catalog threshold. After this process, we are left with ∼3000 point sources that are ≳ 0.7mJy in VLASS and < 0.3-0.4 mJy in FIRST. Due to the slight frequency

[1]VLASS quicklook images are available at `https://archive-new.nrao.edu/vlass/quicklook/`

mismatch between the reference and detection epochs, some of these transient candidates are due to non varying or slowly varying AGN at redshift >> 0 which have rising spectral indices between the 1.5 GHz FIRST band and the 3 GHz VLASS band. Because our search was focused on transients within the local universe, we cross matched the transient candidates against spectroscopically verified galaxies within 200 Mpc from the Sloan Digital Sky Survey Data Release 15 (SDSS DR15; Aguado et al., 2019), the Census of the Local Universe (CLU; Cook et al., 2019) galaxy catalog, and the NASA Extragalactic Database (NED)[2]. This process revealed 20 likely transients with statistically significant local universe galaxy associations. None of these likely transients show indications in multiwavelength data of being background sources (Dong et al. in prep).

Among the 20 local universe sources, VT 1137-0337 stood out for its starbursting host galaxy (Section 4.5) and unusual flat spectrum (Sections 4.4, 4.5). It was detected in VLASS Epoch 1.1 with a 3 GHz flux of 1.7 ± 0.4 mJy in January 2018, but is absent from FIRST with a 3σ upper limit at 1.5 GHz of < 0.35 mJy in September 1998. Three VLA followup observations taken in May 2018, March 2019, and February 2022 confirmed the presence of a new 1.5 GHz source that would have been easily detectable in FIRST (Section 4.4, Table 4.1). Figure 4.1 shows the reference, discovery, and a follow-up image of this source, which is located within 0.4 arcseconds of the nucleus of the dwarf starburst galaxy SDSS J113706.18-033737.1 (Aguado et al., 2019).

In our searched catalogs, there are ~70,000 galaxies within the 6195 deg^2 VLASS/FIRST overlap. The fraction of the overlap area that falls within 0.4 arcseconds of one of their nuclei is 1.4×10^{-7}. There are ~3000 VLASS transient candidates that could have been located within this area. Thus, the expected number of coincidental associations within this sample is $\sim 4 \times 10^{-4}$. Among the 20 galaxy-associated transients, we observed 12 that are within 0.4" of their host galaxy's nucleus. The probability of one or more of these being falsely associated is $\approx 4 \times 10^{-4}$ (formally, 1 - Poisson($\lambda = 4 \times 10^{-4}$, $k = 0$), where λ is the mean and k is the number of false positive occurrences). Given the small false alarm probability, we conclude that VT 1137-0337 is not a foreground or background source, and is indeed associated with SDSS J113706.18-033737.1.

[2]The NASA/IPAC Extragalactic Database (NED) is operated by the Jet Propulsion Laboratory, California Institute of Technology, under contract with the National Aeronautics and Space Administration.

The $>$ 500% variability at 1.5 GHz is inconsistent with refractive scintillation which, given the estimated critical frequency of ∼8.5 GHz at the location of the transient (J. M. Cordes and T. J. W. Lazio, 2002), would imply a typical point source modulation of ∼40% (Walker, 1998). If the source diameter d is resolved on the scale of the scattering disk (corresponding to a diameter of $d_{rs} \sim 2 \times 10^{17}$ cm at the distance to the host galaxy), the RMS modulation is further reduced by a factor of $(d_{rs}/d)^{7/6}$. Diffractive scintillation is suppressed at even smaller scales, being reduced by a factor of (d_{ds}/d), where for our source $d_{ds} \sim 10^{15}$ cm. Additionally, the modulations would be decorrelated on a bandwidth of ∼6 MHz and would be substantially reduced by averaging over a single VLA spectral window. This implies that the variability of VT 1137-0337 between FIRST and VLASS is not primarily due to propagation effects in the Milky Way, and is instead intrinsic to the source itself or its immediate surroundings.

Implied detection rate

In our search of ∼6195 deg^2 out to ∼200 Mpc, we detected no other transients similar to VT 1137-0337, which we define as having an optically thin spectral index flatter than $\alpha = 0.5$ and being located in a galaxy at or above the star-forming main sequence. This suggests that (1) the phenomenon is rare, or (2) we have detected one of the easiest ones to detect, or (3) both. Here we present a rate estimate assuming that VT 1137-0337 is a representative example of the population from which it is drawn (option 1). If instead there are less luminous analogs or if they are predominantly located in faint galaxies, this estimate should be treated as a lower limit.

Based on VT 1137-0337's 1.7 mJy flux in the detection epoch, we estimate that the transient would have been detectable in our search out to ∼190 Mpc. The host galaxy, which has a g band magnitude of ∼17.5, would have easily been detectable by SDSS out to that distance. The effective searched volume is $V_{\rm search} \approx \frac{4}{3}\pi\,(190\,{\rm Mpc})^3\,(6195\,{\rm deg}^2/41253\,{\rm deg}^2) \approx 4 \times 10^6\,{\rm Mpc}^3$. Within this volume, Kulkarni, D. A. Perley, and Miller (2018) estimate that the overall redshift completeness f_z of all NED galaxies is ∼60%. This fraction is lower for low-mass galaxies but higher for star-forming galaxies. If we use the host galaxy's K band absolute magnitude (a proxy for mass), $f_z \approx 10\%$, but if we use its NUV flux (a proxy for star formation), $f_z \approx 75\%$. We adopt an intermediate value of $f_z \approx 50\%$ for the redshift completeness, noting that this may be uncertain by a factor of a few. Finally, VT 1137-0337 appeared in

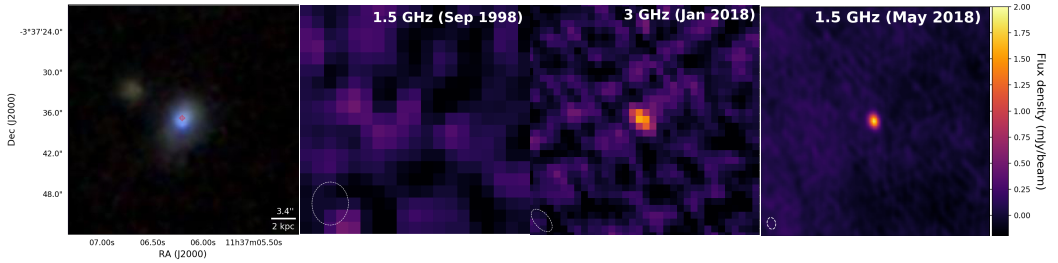

Figure 4.1: The detection of VT 1137-0337. Left to right: (1) The host galaxy, located at a luminosity distance of 121.6 Mpc. The radio transient position is marked with a red cross. (2) Non-detection at 1.5 GHz in the FIRST survey. (3) First detection at 3 GHz in VLASS quicklook imaging (observed in the VLA's B configuration; (Lacy et al., 2020)). (4) A follow-up image at 1.5 GHz taken with the VLA in the A configuration. All images are at the same size scale, and all radio images use the same colorscale shown by the colorbar. The synthesized beam of each radio image is shown by the ellipse in the bottom left.

the radio sky on a timescale of $t_{\rm span} < 19.3$ years, and persisted for $t_{\rm span} \gtrsim 4.1$ years (Table 4.1). We thus estimate that the volumetric birth rate for flat spectrum radio transients of similar radio luminosity in similar galaxies is $R = \left(V_{\rm search} t_{\rm span} f_z\right)^{-1} \approx$ (20 to 600) Gpc^{-3} yr^{-1}.

In addition to astrophysical systematics (e.g., less luminous transients that are not detected in VLASS), the rate based on a sample of 1 should be regarded as having a large margin of error due to Poisson noise. Adopting a 95% confidence interval leads to a range of (1 - 3000) Gpc^{-3} yr^{-1} (Gehrels, 1986). For comparison, this corresponds to between 0.001% and 3% of the volumetric core collapse supernova rate (Taylor et al., 2014). The rate is consistent with the estimated birth rate of FRB persistent source candidates ($\sim$ 500 Gpc^{-3} yr^{-1}) found by Eran O. Ofek (2017).

4.4 Observations and Model Fitting

We used a combination of follow-up and archival observations to characterize the observational properties of VT 1137-0337 and its surrounding environment. In this section, we describe the observations and associated data processing. We also discuss the model function used to fit the radio and optical follow-up spectra.

Radio follow up observations

Four months after initial discovery in VLASS, we observed VT 1137-0337 with the VLA in its A configuration with the L, S, C, and X bands (1-12 GHz) under program 18A-481 (hereafter referred to as Epoch 1). We used 3C286 as the flux calibrator and J1150-0023 as the phase calibrator. We repeated these broadband radio observations at post-discovery epochs of 1.2 and 4.1 years with the VLA in the B and BnA configurations under programs 19A-422 (Epoch 2) and 21B-393 (Epoch 3). In the second epoch, we also observed in the Ku band (12-18 GHz). To calibrate and image the data, we used standard tasks from the Common Astronomical Software Applications (CASA) package (McMullin et al., 2007). In the first two epochs, we excluded the S band (2-4 GHz) observations which could not be reliably calibrated due to gain compression in the receivers. This is likely due to severe radio frequency interference from geosynchronous satellites in the Clarke Belt during the S band setup scans. For all other observations, we made single-band images of the target using the CASA implementation of `CLEAN` (Schwab, 1984). We additionally made sub-band images from groups of (or individual) independently calibrated 128 MHz spectral windows. In each image, we verified that the target location is not substantially contaminated by image artifacts. We then used the CASA task `imstat` to measure its flux, which is taken to be the value of the peak pixel. To avoid pixelation noise in this method of photometry, we chose a pixel scale that oversamples the beam size by a conservative margin ($\gtrsim 10\times$) in all images. To estimate the uncertainty, we use the RMS pixel value in a nearby aperture with no sources or image artifacts. The single-band fluxes and uncertainties are listed in Table 4.1. The sub-band fluxes are used for model fitting, and are shown in Figure 4.3 along with the fluxes from VLASS observations and the FIRST nondetection.

As a check on the calibration in our follow up observations, we made images of the phase calibrator J1150-0023 (a quasar seperated by ~4.7 degrees from the target) in every VLA spectral window, representing frequency chunks of 128 MHz with independent phase, amplitude, and bandpass calibrations. In standard VLA observations (including ours), the target flux is established by applying the fluxscale corrections derived for the phase calibrator (which suffers from nearly the same atmospheric and instrumental effects as the target) to the target. Any major issues in the calibration of the target spectrum should therefore show up as irregularities in the calibrated fluxes of the phase calibrator. As shown in the top panel of Figure 4.2, the calibrated phase calibrator spectrum in each epoch varies smoothly within

and across all receiver bands. Since each receiver band contains 2-3 independent hardware basebands, this suggests that there are no substantial systematics due to the instrument. In the first two epochs, the phase calibrator spectrum is well described by a single power law. In Epoch 3, we measure some spectral curvature which is well described in log-space by a parabola. The bottom panel of Figure 4.2 shows that the flux measured in Epoch 2 is offset from the flux in Epoch 1 by ∼3% with marginal frequency structure. Due to the new spectral curvature, the phase calibrator is up to 5% dimmer and 10% brighter in Epoch 3 relative to Epoch 1 in our observed frequencies. We take this range to be an upper limit on the systematic fluxscale error introduced by calibration, though we suspect that the true error is smaller since (1) this level of variability is commonly observed in quasars (e.g., Liodakis et al., 2017), and (2) we independently measure the same spectral index for VT 1137-0337 in all 3 epochs (Section 4.4, Figure 4.3). By rerunning the fits described in Section 4.4 with fluxes scaled by the phase calibrator model ratio, we find that if the full difference between calibrator epochs were attributed to systematic calibration errors, Epoch 3's best fit spectral index would change from $\alpha = 0.35 \pm 0.02$ to $\alpha = 0.38 \pm 0.02$.

Modeling the radio spectra

In each epoch, we used the Markov Chain Monte Carlo code `emcee` (Foreman-Mackey et al., 2013) to fit the sub-band fluxes with a simple optically-thin synchrotron emission model:

$$S_{\nu,mod} = S_3 \left(\frac{\nu}{3\ \mathrm{GHz}}\right)^{-\alpha}, \tag{4.1}$$

where $S_{\nu,mod}$ is the model flux at frequency ν, α is the optically thin spectral index, and S_3 is the flux at 3 GHz. We used the following log likelihood function which assumes that the uncertainties are Gaussian:

$$\ln \mathcal{L} = -\frac{1}{2} \sum_n \left[\frac{(S_{\nu,obs,n} - S_{\nu,mod,n})^2}{\sigma_n^2} + ln(2\pi\sigma_n^2) \right], \tag{4.2}$$

where for the n-th data point, $S_{\nu,obs,n}$ and $S_{\nu,mod,n}$ are the observed and model fluxes at the data point's frequency ν, and σ_n is its uncertainty. In all epochs, we assumed top hat priors, with cutoffs of $0 < \alpha < 1$ and 1 mJy $< S_3 <$ 2 mJy. For Epoch 1, we found that the data are well described with the parameters $S_3 = 1.470^{+0.026}_{-0.026}$ mJy, and $\alpha = 0.345^{+0.018}_{-0.019}$, where the central value and upper and lower uncertainties are

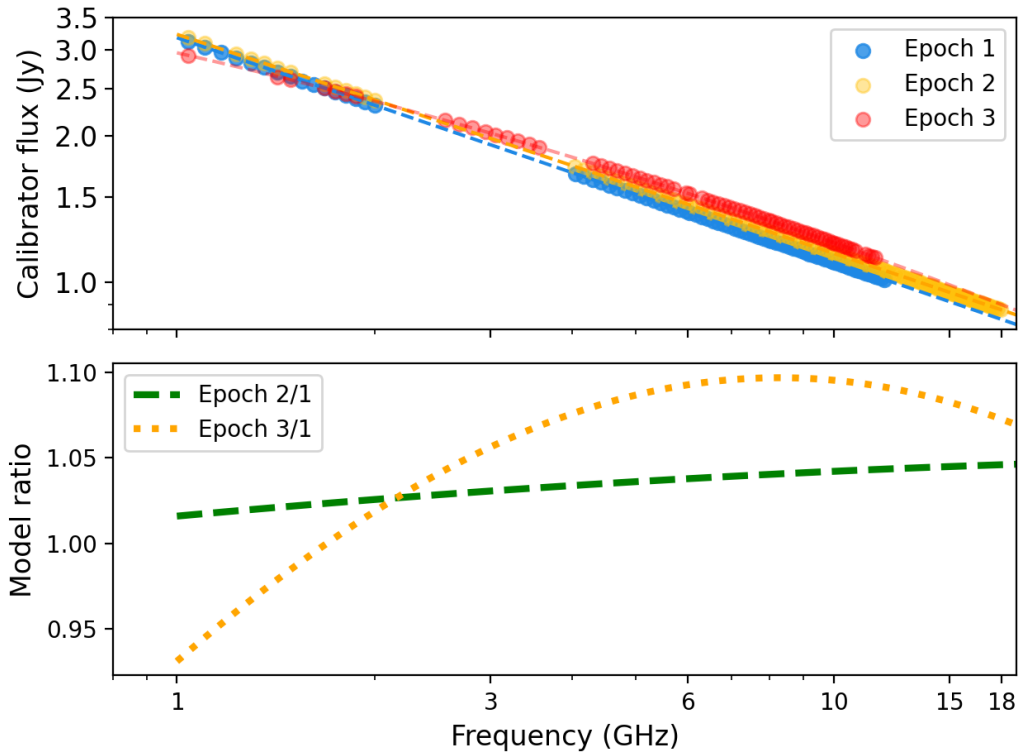

Figure 4.2: The phase calibrator (J1150-0023) observed in each VLA follow-up epoch, plotted as a consistency check for our calibration. **Top:** The calibrator spectrum after correction with the calibration applied to VT 1137-0337. Data points are measured from images of each VLA spectral window, described in Section 4.4. Dashed lines show best fit parabolic models for each epoch. **Bottom:** The ratio of calibrator models, showing $\lesssim$ 10% variability between epochs at all observed frequencies.

taken from the 50th, 86th - 50th and 50th - 14th percentile values of their posterior distributions. For Epoch 2, the best fit power-law model is $S_3 = 1.44^{+0.20}_{-0.020}$ mJy and $\alpha = 0.355^{+0.011}_{-0.012}$. For Epoch 3, we find that $S_3 = 1.171^{+0.012}_{-0.012}$ mJy and $\alpha = 0.347^{+0.018}_{-0.017}$. The data and best fit models are plotted in Figure 4.3.

In Epochs 1 and 2, VT 1137-0337's best fit radio spectra are consistent within 1σ uncertainties in each parameter, indicating slow evolution (or a lack thereof) over the ~1 year between epochs. The implied fade rate from the first two epochs is (2.3 ± 2.8)% per year. In Epoch 3, its spectral index remains constant but the spectrum's overall amplitude is fainter than that of Epoch 1 by a margin of $(S_{3,\text{Epoch 1}} - S_{3,\text{Epoch 3}})/S_{3,\text{Epoch 1}} = (20 \pm 2)\%$, corresponding to a fade rate of (5.3 ± 0.4)% per year. If we attribute the full difference in the phase calibrator's spectrum

to systematic calibration errors, the overall level of fading increases to (25 ± 2)%, or (6.9 ± 0.4)% per year.

Table 4.1: Fluxes from single-band imaging of VT 1137-0337. Uncertainties are estimated using the RMS in a region of the image free of sources. There is an additional ∼5% systematic fluxscale uncertainty in imaging of followup epochs (R. A. Perley and Butler, 2017), and a ∼20% systematic error in fluxes derived from VLASS quicklook images (Epochs in Jan 2018, Aug 2020).

Date	Δt	$S_{1.5\ \mathrm{GHz}}$	$S_{3\ \mathrm{GHz}}$	$S_{6\ \mathrm{GHz}}$	$S_{10\ \mathrm{GHz}}$	$S_{15\ \mathrm{GHz}}$
	Years	mJy	mJy	mJy	mJy	mJy
Sep 16, 1998	-19.3	< 0.34				
Jan 12, 2018	0		1.69 ± 0.14			
May 31, 2018	0.38	1.86 ± 0.06		1.21 ± 0.02	1.01 ± 0.01	
Mar 29, 2019	1.21	1.86 ± 0.14		1.23 ± 0.03	0.99 ± 0.01	0.77 ± 0.01
Aug 22, 2020	2.61		1.23 ± 0.14			
Feb 14, 2022	4.09	1.41 ± 0.10	1.19 ± 0.03	0.914 ± 0.02	0.75 ± 0.01	

Optical spectra

The host galaxy of VT 1137-0337 was observed as part of the SDSS Legacy Survey on January 20, 2002 (∼3.35 years after nondetection in FIRST and ∼16 years before first detection in VLASS). The SDSS spectrum has a spectral resolution of $\Delta\lambda/\lambda \sim 2000$, and detects numerous emission lines characteristic of star formation. It is sensitive to a 3" diameter region encompassing the location of the radio transient.

To check for any spectral evolution or new spectrally resolved features, we took a follow-up spectrum with the Keck Low Resolution Imaging Spectrograph (LRIS) (Oke et al., 1995) on Feb 13, 2021 (∼3 years after first detection). We used the 1 arcsecond-wide longslit setup with the 400/3400 grism on the blue arm and the 400/8500 grating on the red arm with a central wavelength of 7830 Å. These settings correspond to a wavelength coverage of ∼3100 - 10,000 Å at a FWHM spectral resolution of $\Delta\lambda/\lambda \sim 1000$. To acquire the target, we applied a blind offset from a nearby star, resulting in a spectrum of the region around the radio transient of order the slit width (1.0"). We exposed for 20 minutes in both arms, resulting in a typical per-pixel 1σ noise of $\sim (1-2)\times 10^{-18}$ erg/s/cm^2. We processed the optical spectra using the LRIS data reduction pipeline `LPIPE` (Daniel A. Perley, 2019).

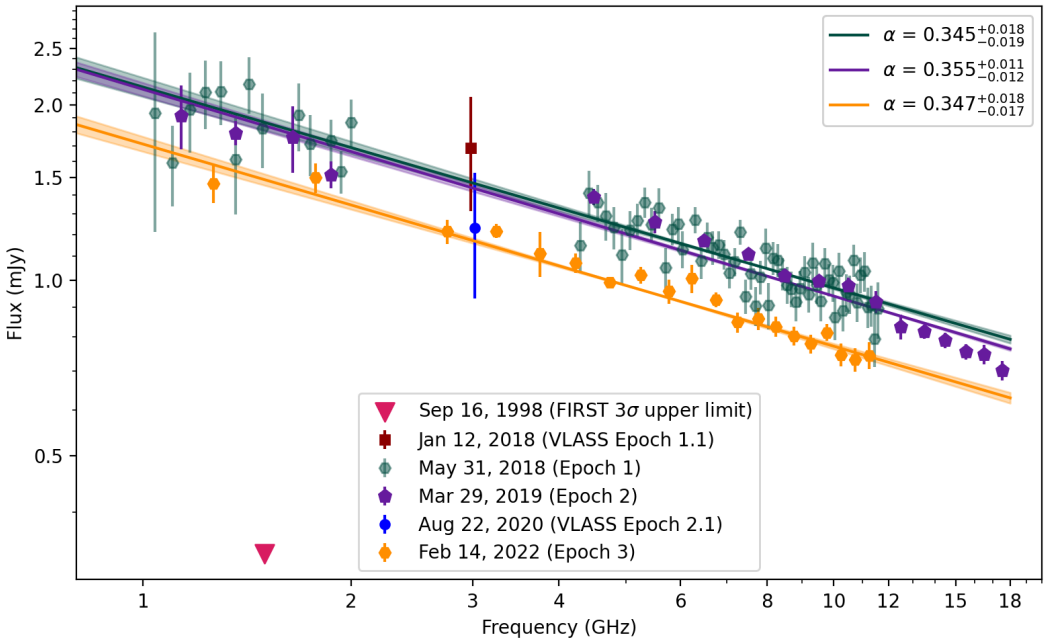

Figure 4.3: Radio observations of VT 1137-0337 from initial nondetection in FIRST to detections in VLASS and VLA followup epochs, along with single power law fits to followup epochs. To avoid overlap of the plotted errorbars, the frequencies of the VLASS epochs are shown with an arbitrary offset of ± 0.02 GHz from 3 GHz. The green line shows the median MCMC fit to Epoch 1, observed ~20 years after FIRST: $S_\nu = (1.470 \pm 0.026\ \mathrm{mJy})\ (\nu/3\ \mathrm{GHz})^{-0.345\pm0.019}$. The purple line shows the median single power law fit to Epoch 2, observed ~1 year after Epoch 1: $S_\nu = (1.441 \pm 0.020\ \mathrm{mJy})\ (\nu/3\ \mathrm{GHz})^{-0.355\pm0.012}$. The orange line shows the median fit to Epoch 3, observed ~4 years after Epoch 1: $S_\nu = (1.171 \pm 0.012\ \mathrm{mJy})\ (\nu/3\ \mathrm{GHz})^{-0.347\pm0.018}$.

Fitting the optical emission features

We used `emcee` to fit a number of optical emission features in both the LRIS and SDSS spectra. We fit these features in six separate wavelength chunks: 6490-6630Å (Hα/NII), 4750-5200Å (OIII 4959+5007/Hβ), 4350-4380Å (OIII 4363), 6700-6750Å (SII 6716/6730), 7300-7350Å (OII 7320/7330), and 6270-6350Å (OI 6300). We modeled each emission feature as a single-component Gaussian where the amplitude and width are allowed to vary freely (with both constrained to be positive and less than a large value for the purposes of convergence). Within each complex, we marginalized over three additional nuisance parameters: a linear slope and flux offset for the underlying continuum, and a wavelength shift to correct for wavelength calibration errors. We used a uniform prior that loosely constrains the slope and offset to within an order of magnitude of an initial guess from a least-squares fit to the data with the emission lines masked. The wavelength shift was limited to ±1Å.

The best fit fluxes and their uncertainties listed in Table 4.2, and the gas properties inferred from these features are discussed in Section 4.5. No features are spectrally resolved in either observation. We find that despite the ∼20 year gap and the difference in spatial scales, the fluxes are similar in all measured lines. The ∼5% higher fluxes in the SDSS spectrum are easily explained by either systematic flux calibration uncertainties, or the larger effective aperture of the SDSS fiber. Thus, on the scale of ∼1", corresponding to ∼550 pc at the distance to the host galaxy, we do not detect any significant evolution in the optical spectrum at the location of the transient between 2002 (∼3 years after nondetection in FIRST) and 2021 (∼22 years after nondetection in FIRST and ∼3 years after first detection in VLASS).

We additionally checked for emission from the high ionization potential [Fe X] line at 6374Å, used in a search for AGN in dwarf galaxies by Molina, Reines, Latimer, et al. (2021). We do not detect this line in either spectrum above the local noise.

Table 4.2: Emission line fluxes at the location of VT 1137-0337. The reported uncertainties are statistical, reflecting the 86th-50th and 50th-16th percentiles of the posterior distributions. There is an additional relative systematic uncertainty between the two spectra due to the different apertures as well as an absolute systematic uncertainty in the spectrophotometric flux calibration in each epoch.

Line	$\lambda_{\rm rest}$ (Å)	Flux (SDSS) (10^{-16} erg s^{-1} cm^{-2})	Flux (LRIS) (10^{-16} erg s^{-1} cm^{-2})
Hα	6562.8	$387.7^{+0.4}_{-0.4}$	$357.6^{+0.5}_{-0.5}$
Hβ	4861.4	$112.6^{+0.2}_{-0.2}$	$107.8^{+0.5}_{-0.5}$
NII	6548.0	$5.8^{+0.5}_{-0.4}$	$5.0^{+0.1}_{-0.1}$
NII	6583.5	$18.6^{+0.6}_{-0.6}$	$17.2^{+0.2}_{-0.2}$
OIII	4363.2	$5.7^{+0.9}_{-0.8}$	$5.5^{+0.3}_{-0.3}$
OIII	4958.9	$176.7^{+0.3}_{-0.3}$	$174.0^{+0.6}_{-0.5}$
OIII	5006.8	$519.3^{+0.7}_{-0.7}$	$499.8^{+0.9}_{-0.9}$
OI	6300.3	$5.2^{+0.5}_{-0.5}$	$4.6^{+1.9}_{-1.8}$
SII	6716.4	$28.9^{+0.8}_{-0.8}$	$26.6^{+0.2}_{-0.2}$
SII	6730.8	$21.9^{+0.7}_{-0.8}$	$19.9^{+0.2}_{-0.2}$
OII	7320.1	$4.1^{+0.8}_{-0.8}$	$3.0^{+0.2}_{-0.2}$
OII	7330.2	$2.7^{+0.5}_{-0.5}$	$3.0^{+0.2}_{-0.2}$

X-ray upper limit from 2006

VT 1137-0337 is located near the edge of an archival XMM-Newton image (observation ID 0305801101; PI Ponman) observed with the European Photon Imaging Camera (EPIC) PN CCD for 21.8 kiloseconds on June 10, 2006. It is not significantly detected in the image. Assuming a galactic HI column of 3×10^{20} cm^2 and a power law model with photon index of 1.34 (equal to the radio spectral index), one count corresponds to 3.7×10^{-12} erg s^{-1} as calculated with the WebPIMMS tool. This flux, which corresponds to a luminosity of 6.5×10^{42} erg/s at the distance to VT 1137-0337 is an approximate upper limit to the X-ray emission in 2006. We caution, however, that the radio emission first appeared sometime between September 1998 and January 2018 (Table 4.1). If the radio emission predates June 2006 and was at the same flux or brighter, then the X-ray / radio luminosity ratio was $\lesssim 2 \times 10^4$ at that time. If not, this is an upper limit on the quiescent X-ray luminosity of the galaxy.

Nondetection of archival transient counterparts

We searched a variety of archival catalogs for potential transient counteparts to VT 1137-0337. These included the CHIME FRB catalog (The CHIME/FRB Collaboration et al., 2021), the Open Supernova Catalog Guillochon et al., 2017, the MAXI (Serino et al., 2014a), INTEGRAL (Rau et al., 2005), and Swift (Lien et al., 2016) GRB catalogs, and the Transient Name Server[3]. We found no significant matches. We additionally used the ASASSN lightcurve service (Kochanek et al., 2017; Shappee et al., 2014) to check for optical variability at this location, and found no significant increase in the optical flux beyond the typical ASASSN V band detection limit of ∼17 (corresponding to an absolute magnitude of -18.4). This rules out association with superluminous supernovae that exploded after the first ASASSN observation on Jan 29, 2012 (Avishay Gal-Yam, 2019), but does not rule out the majority of core collapse supernovae (e.g., Taddia, M. D. Stritzinger, Sollerman, et al., 2013; Taddia, M. D. Stritzinger, Bersten, et al., 2018; Hicken et al., 2017).

4.5 Properties of the transient and its environment

In this section we explore the physical conditions that can produce the observed features of VT 1137-0337 and its environment, and in Section 4.6, we discuss possible astrophysical scenarios that can give rise to these conditions.

[3]The Transient Name Server (TNS) is the official IAU repository for reporting transients and can be found at `https://www.wis-tns.org/`

Properties of the Surrounding Starburst

One contextual clue to the origin of VT 1137-0337 comes from the properties of the host galaxy and the local region surrounding the radio transient. We can diagnose the state of the ionized gas near the transient using the optical emission lines discussed in Section 4.4. We use the LRIS flux values due to the tighter spatial area probed around the transient. The quantities presented are averaged over the ∼1" LRIS slit width, corresponding to a linear diameter of ∼560 pc. The region directly influenced by the transient is much smaller (< 6pc; Section 4.5), and may have different properties.

The Hα/Hβ ratio can be used to estimate the extinction due to dust along the line of sight. We measure a ratio of 3.32 ± 0.02, corresponding to a reddening of E(B-V) ∼ 0.13 (Domınguez et al., 2013). This reddening corresponds to an extinction of ∼0.42 mag for the Hα line (Calzetti et al., 2000).

The [SII] 6717Å /6731Å ratio is sensitive to the density of the emitting region, with a small dependence on the metallicity. We measure a ratio of 1.34 ± 0.02, corresponding to an electron density of ∼60 cm^{-3} (Lisa J. Kewley, Nicholls, et al., 2019).

The faint OIII 4363Å line allows us to directly measure the temperature of electrons in the ionized gas producing the emission lines. Since the inferred density is well within the limit where collisional de-excitation is negligible, the temperature can be determined by the ratio of oxygen lines using the relation from Osterbrock and Ferland (2006):

$$\frac{j_{4959} + j_{5007}}{j_{4363}} = \frac{7.90 \exp(3.29 \times 10^4 / T)}{1 + 4.5 \times 10^{-4}\, n_e / T^{1/2}}. \tag{4.3}$$

We measure a line ratio of 122 ± 7, corresponding to a temperature of ∼12,000 K.

The density and temperature of the surrounding region is consistent with values commonly observed in star-forming regions (Draine, 2011). The electron temperature can be used to measured the metallicity of the region to a typical intrinsic scatter of ∼0.1 dex (Lisa J. Kewley and S. L. Ellison, 2008). To do so, we adopt the calibration of Izotov et al. (2006) assuming that the total oxygen abundance is the sum of the O^+ and O^{++} abundances (Lisa J. Kewley and S. L. Ellison, 2008). We find that 12 + log O^+/H = 7.68 and 12 + log O^{++}/H = 7.99, for a total metallicity of 12 + log O/H = 8.16. This metallicity is 30% of the solar value (12 + log O/H =

8.69; Asplund et al., 2009).

To check for signs of AGN activity and to further diagnose the state of the ISM, we plotted the nucleus of the galaxy on the classical BPT diagram (Baldwin, Phillips, and Terlevich, 1981b). As shown in Figure 4.4, the source lies on the star-forming side, indicating that any AGN activity is not apparent in optical diagnostics. The position of VT 1137-0337 on the left side of the star-forming sequence (log OIII 5007/Hβ = 0.66, log NII 6584/Hα = -1.32) indicates that the overall star-forming complex is irradiated by a hard ionizing photon spectrum (e.g., Richardson et al., 2016). At the metallicity inferred above, both line ratios are higher than expected for the highest ionization parameter model presented in Figure 1 of (Lisa J. Kewley, Michael A. Dopita, et al., 2013). This suggests that the ionization parameter q exceeds $10^{8.3}$ cm/s, which is substantially harder than the range measured in both local HII regions (M. A. Dopita et al., 2000) and star-forming galaxies (Moustakas et al., 2010). This suggests that the transient is surrounded by young, massive, hot stars (e.g. O stars and Wolf-Rayet stars) (Lisa J. Kewley, Michael A. Dopita, et al., 2013).

Another indication of a young starburst comes from the high extinction-corrected Hα luminosity of 9.3×10^{40} erg/s measured in the ~1 arcsecond region around VT 1137-0337. Adopting the calibration of (E. J. Murphy et al., 2011), this corresponds to a star formation rate (SFR) of ~0.5 $M_{\odot}$/yr. If the star formation were to continue at a constant rate, the galaxy (of stellar mass $10^{8.3} M_{\odot}$; Salim, Médéric Boquien, and Lee (2018)) would double its stellar mass in the next ~1 Gyr. Nearly all of the star formation is concentrated in the ~ 280 pc radius region surrounding VT 1137-0337, as evidenced by the similar Hα fluxes in the LRIS and SDSS spectra which probe radii of $r \sim 280$ pc and 840 pc respectively. The star formation surface density within a circle of radius $r = 280$ pc is $\Sigma_{\rm SFR} \approx 6$ M$_{\odot}$ yr^{-1} kpc^{-2}. This value is in the high star formation density tail of blue compact star-forming galaxies measured by Pérez-González et al. (2003) and luminous circumnuclear star-forming regions (Kormendy and J. Kennicutt R. C., 2004; R. C. Kennicutt and Evans, 2012). The surrounding HII region would be among the most Hα luminous of the ~18,000 star-forming regions compiled by Bradley et al. (2006). This Hα flux traces ionizing photons from O and B stars, with disproportionate contributions from the youngest, most massive stars. As these stars explode in supernovae over the course of a few Myr, the Hα flux is expected to fade rapidly as the gas recombines. The high

observed Hα luminosity therefore indicates that massive stars were recently formed in the region surrounding VT 1137-0337. In particular, the Hα flux of a Salpeter (1955) initial mass function of stars formed at any given time is expected to fade by $\sim$2 orders of magnitude after $\sim$10 Myr (Leitherer et al., 1999). If the present-day massive stars are relics of an earlier generation, the star formation rate and surface density at that the time of formation would have been $\sim$2 orders of magnitude more extreme than what we have already observed. This is not likely, so we infer that the massive stars powering the high Hα luminosity surrounding VT 1137-0337 must be younger than a few Myr.

Table 4.3: The environment around VT 1137-0337. The host galaxy mass is from SED fitting reported in the GALEX-SDSS-WISE Legacy Catalog (GSWLC; Salim, Médéric Boquien, and Lee, 2018). The SFR is from the extinction-corrected Hα flux, and is consistent with the GSWLC value $0.46 M_{\odot}$/yr. The transient position is fitted from a 10 GHz VLA follow-up observation. All other quantities are derived from a Keck I/LRIS spectrum and are representative of a $\sim$280 pc radius region surrounding VT 1137-0337.

Galaxy center RA		11:37:06.18
Transient RA		11:37:06.19
Galaxy center Dec		-03:37:37.16
Transient Dec		-03:37:37.29
Galaxy stellar mass	M_*	$10^{8.3} M_{\odot}$
Electron temperature	T_e	12000 K
Electron density	n_e	60 cm^{-3}
Reddening	E(B-V)	0.13 mag
Hα extinction	A(Hα)	0.42 mag
Metallicity	Z	0.3 $Z_{\odot}$
Star formation rate	SFR	0.5 $M_{\odot}$ yr^{-1} height

Flat-spectrum radio emission mechanisms

Broadband emission at GHz frequencies from extragalactic sources is typically thought to originate from either free-free or synchrotron emission. In Section 4.5 we outline why VT 1137-0337's luminosity and variability timescale are not consistent with having a substantial free-free emission fraction. A full argument is presented in Appendix 4.8. In Section 4.5, we discuss how synchrotron emission is consistent with the observations, though the flat spectrum is unlike typical synchrotron transients in that it cannot be explained with a single shock-accelerated

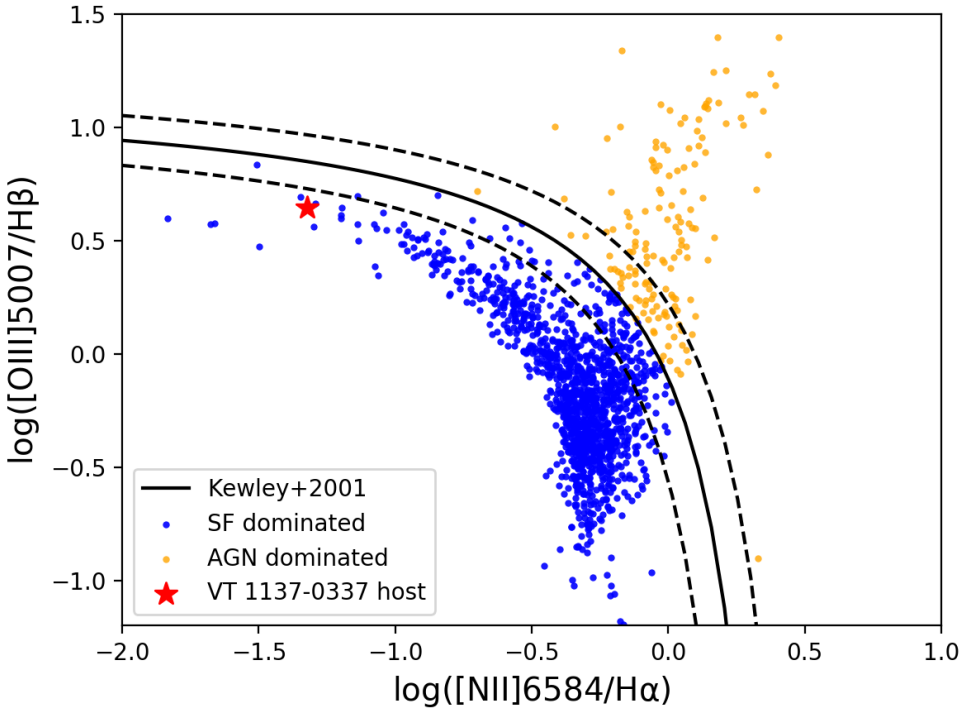

Figure 4.4: The position of VT 1137-0337's host galaxy on a BPT diagram (Baldwin, Phillips, and Terlevich, 1981b). The dividing line between AGN and star formation dominated galaxy spectra from L. J. Kewley et al. (2001) is shown with $\pm 1\sigma$ uncertainties (dotted lines). Blue and orange dots show SDSS galaxies classified respectively as star-forming or AGN according to this scheme by Vanderplas et al. (2012).

particle distribution.

Free-free emission

Free-free emission is a tempting explanation for the radio emission of VT 1137-0337, given that its natural flat spectrum ($\nu^{-0.12}$; Draine (2011)) can add on to a steeper spectrum component to create a power law similar to what we observe. This combination is commonly observed in extragalactic star-forming regions (e.g., Linden et al., 2020). However, with reasonable temperatures and densities, high luminosities of $\sim 10^{28}$ erg/s/Hz can only be produced via free-free emission from a region ~hundreds of parsecs in size. The required size is not compatible with transient emission appearing on human timescales. In Appendix 4.8, we show that the conditions required to produce VT 1137-0337's luminosity within the upper

limit on size set by causality ($R < c$ (20 years) = 6.1 pc) are extreme: a temperature $T \gtrsim 10^7$ K and a thermal energy $U \gtrsim 10^{54}$ erg. We conclude that the fraction of VT 1137-0337's observed radio luminosity due to free-free emission is << 1. We also note that the expected 3 GHz flux due to free-free emission from star formation in the host galaxy is $\sim 50\mu$Jy (E. J. Murphy et al., 2011, Figure 4.9), far lower than the ∼1.5 mJy we observe.

Synchrotron emission

Having ruled out free-free emission, we are left with synchrotron emission as the likely source of VT 1137-0337. However, its spectral index of $\alpha = 0.35$ (Section 4.4), is much flatter than other synchrotron transients and most synchrotron sources in general and requires further explanation. As we discuss below, the flat spectrum cannot be produced by an ordinary shock and instead requires an alternate model.

The simplest model for a power law synchrotron spectrum is a single population of emitting electrons with a power law energy distribution $N(E) \propto E^{-p}$. At frequencies below the synchrotron cooling spectral break, the spectral index α is related to the energy index p by $\alpha = (p-1)/2$. Above the cooling break, the spectral index steepens by 0.5 to $\alpha = p/2$. The single population model implies an energy index $p < 2$, which is too hard to be produced by diffusive shock acceleration (DSA), the mechanism thought to be responsible for most synchrotron transients. In non relativistic shocks, DSA predicts that $p = (r+2)/(r-1)$, where r is the ratio by which the shocked gas is compressed (e.g., Roger Blandford and Eichler, 1987). The compression ratio is given by the shock jump conditions: $r = \frac{(\gamma+1)M^2}{(\gamma-1)M^2+2}$, where M is the Mach number (the ratio of the shock speed to the sound speed in the pre-shock gas), and γ is the adiabatic index, equal to 5/3 for a monatomic gas. In the limit of a strong shock ($M \gtrsim 10$) in a monatomic gas, $r \approx 4$, and thus $p = 2$. Nonlinear factors such as the dynamical effect on the shock of the accelerated particles themselves can steepen the energy distribution to $p = 2.5 - 3$ (Jones and D. C. Ellison, 1991), a range of values often seen in astrophysical sources. If the shock is relativistic, there are further complications due to e.g. particles being unable to return to the shock front after first crossing. In these conditions, the limiting steepness is estimated to be p ≈ 2.3 (Pelletier et al., 2017). In all cases, ordinary shocks are expected to produce substantially steeper spectra than what we observe.

A variety of astrophysical source classes do display power law spectra that are

flatter (over a large bandwidth) than $\alpha = 0.5$, the spectral index corresponding to the $p = 2$ DSA limit. These include pulsar wind nebulae, X-ray binaries in the low/hard state, and a subset of AGN which tend to have jets pointed along our line of sight. Theoretical explanations for their flat spectra often invoke one or more of the following: (1) an alternate particle acceleration mechanism capable of producing an intrinsically hard electron energy distribution, (2) a regular electron energy distribution with a flattened spectrum due to propagation in a non uniform magnetic field, or (3) a flat spectrum constructed from the (discrete or continuous) sum of ordinary self-absorbed synchrotron spectral components. We discuss these mechanisms further in Section 4.7, where we consider the possible astrophysical sources that may be powering VT 1137-0337.

Constraints on the emitting region

Even with a possibly multi-component synchrotron spectrum where we do not know the value of p, we can still derive useful constraints from the overall luminosity of the emission and upper limits on the synchrotron self-absorption and free-free absorption frequencies. In this section, we use these properties to roughly constrain the size and magnetic field of the emitting region, the cooling timescale of the emitting electrons, and the line-of-sight column density of ionized gas. For simplicity, we assume that the emission is from a single hard distribution of electrons with $p = 1.7$. These arguments depend only weakly on p. Likewise, if the emission is the sum of components at different optical depth, the arguments should still be applicable to the lowest frequency component observed, which would comprise a large fraction of the total luminosity. In all cases, we stress that the results presented in this section should be regarded as order of magnitude estimates.

From the lack of an observed peak in our follow up observations, we infer that the $\tau = 1$ frequencies for synchrotron self-absorption (ν_a) and free-free absorption (ν_{ff}) are both < 1 GHz. The upper limit $\nu_a < 1$ GHz allows us to set a lower limit on the size of the nebula producing the synchrotron emission. If we assume energy equipartition between the radiating particles and the magnetic field, the angular diameter of the emitting source is $\theta \gtrsim 0.2$ mas (Scott and Readhead, 1977). At the 115 Mpc angular diameter distance to the source, this corresponds to $D \gtrsim 0.1$ pc. The lower limit on the source size corresponds to a volume: $V = \frac{4}{3}\pi(D/2)^3 \gtrsim 10^{52}\mathrm{cm}^3$. From the 20 year separation between FIRST and Epoch 1, light travel time arguments require that the region responsible for the excess emission is $\lesssim 6.1$ pc in size.

We can use this limit on the source size along with classical energy minimization arguments (G. R. Burbidge and E. M. Burbidge, 1957; Scott and Readhead, 1977) to estimate the typical strength of the magnetic field B in the emitting region. To do so, we note that the energy stored in the magnetic field is $U_B = V\frac{B^2}{8\pi} = \frac{4}{3}\pi R^3 \frac{B^2}{8\pi}$ for a spherical emitting region of radius R. Meanwhile, the energy in particles is $U_p = Ag(\alpha)LB^{-3/2}$ (Scott and Readhead, 1977), where A is a constant equal to 1.586×10^{12} in cgs units, L is the region's synchrotron luminosity in the range from ν_1 to ν_2 (in units of Hz), $\alpha = -0.35$ is the spectral index in the convention of Equation 4.4, and $g(\alpha)$ is a quantity from an integral over the electron energy distribution that encapsulates the dependency on frequency range and spectral index:

$$g(\alpha) = \frac{2\alpha + 2}{2\alpha + 1}\left[\frac{\nu_2^{(2\alpha+1)/2} - \nu_1^{(2\alpha+1)/2}}{\nu_2^{\alpha+1} - \nu_1^{\alpha+1}}\right]. \tag{4.4}$$

The two energies $U_B \propto B^2$ and $U_p \propto B^{-3/2}$ have opposite dependencies on B. Thus, there is a value $B_{\rm min}$ that minimizes the total energy $U = U_B + U_p$, which can be found by setting $dU/dB = 0$. The solution is

$$B_{\rm min} = \left(\frac{6\pi A g(\alpha) L}{V}\right)^{2/7}. \tag{4.5}$$

To estimate the value of $B_{\rm min}$ for VT 1137-0337, we integrate over our observed epoch 2 spectrum (from $\nu_1 = 1 \times 10^9$ Hz to $\nu_2 = 1.8 \times 10^{10}$ Hz), resulting in $L \approx 3.2 \times 10^{38}$ erg s^{-1}. Over this frequency range g(α) = 1.3×10^{-5}. For the minimum emitting region size of $R \approx 10^{17}$ cm, we then have $B_{\rm min} \approx 0.04$ G. If R is greater, $B_{\rm min}$ decreases as $R^{-6/7}$, to a minimum value of $\sim 6 \times 10^{-4}$ G at the causality limit of $R = 6.1$ pc.

The quantity $B_{\rm min}$ is a reasonable order-of-magnitude estimate for the true magnetic field B. If $B >> B_{\rm min}$, then the total energy must increase by $(B/B_{\rm min})^2$. Likewise, if $B << B_{\rm min}$, the total energy must again increase by $(B/B_{\rm min})^{-3/2}$. Perturbations of more than an order of magnitude will thus lead to large increases in the energy. Such an increase may be difficult to explain when considering the energy already required in the emitting region. At the lower limit of $R \approx 10^{17}$ cm, the minimum energy in the magnetic field alone is $U_B = \frac{4}{3}\pi R^3 (B_{\rm min}^2/8\pi) \approx 4 \times 10^{47}$ erg, comparable to the magnetic energy in an energetic supernova-driven shock (e.g.,

A. Y. Q. Ho, E. Sterl Phinney, et al., 2019). If R is greater, then the energy scales as $U_B \propto R^{9/7}$, up to $\sim 4 \times 10^{50}$ erg at $R = 6.1$ pc.

One consequence of our magnetic field estimate is that the spectral break frequency ν_c associated with synchrotron cooling is not likely to be < 1 GHz. The timescale for synchrotron cooling is

$$t_c \approx 1300 \left(\frac{B}{0.01G}\right)^{-3/2} \left(\frac{\nu_c}{\mathrm{GHz}}\right)^{-1/2} \text{years}, \tag{4.6}$$

and the maximum value of B_{min} with our radius constraints is ~0.04 G. This implies that the minimum synchrotron cooling time at 1 GHz is $t_{c,min} \approx 120$ years. At our highest observed frequency of 18 GHz, $t_{c,min} \approx 27$ years. Both timescales are longer than the ~20 year span over which the new emission appeared. If the electrons radiating at those frequencies were accelerated after the FIRST nondetection in 1998, they have not yet had enough time to cool. In the case of a single-component nonthermal electron energy distribution, this implies that our observed spectrum of $S_\nu \propto \nu^{-0.35}$ maps to $p = 1.7$ rather than $p = 0.7$.

Finally, the lack of free-free absorption along the line of sight at 1 GHz ($\tau << 1$) implies either a low column density of ionized electrons along the line of sight, or a high temperature for those electrons. We first check that this is the case for a source embedded in the HII region surrounding VT 1137-0337. From the density and temperature in Section 4.5, and equation 4.20, the optical depth to free-free absorption at 1 GHz is $\tau \approx 0.09(R/100\ \mathrm{pc})$, where R is the distance that the radio photons must travel through the ionized gas. The effective size of the ionized region is of order the size of a Strômgren sphere with the ionizing photon production rate implied by the extinction-corrected Hα emission $Q_0 \approx 6.9 \times 10^{52}$ s^{-1} (E. J. Murphy et al., 2011), which is ~90 pc (Draine, 2011). Thus, the surrounding HII region should not contribute substantially to the free-free absorption, though if the source were embedded at its center, it may become a factor for observations at frequencies of a few hundred MHz. However, a high density ionized shell at a typical HII region temperature is excluded. From Equation 4.20, the limit $\tau << 1$ at 1 GHz indicates that at a temperature of T = 10^4 K, the quantity $\left(n_e/\mathrm{cm}^{-3}\right)^2 (s/\mathrm{pc}) < 3 \times 10^6$, where n_e is the average density of ionized gas and s is the thickness of the ionized region. If a hypothetical shell has thickness $s \sim 10^{16}$ cm, the density $n_e < 3 \times 10^4$ cm^{-3}. If it is more extended, the density constraint becomes more stringent. This excludes the

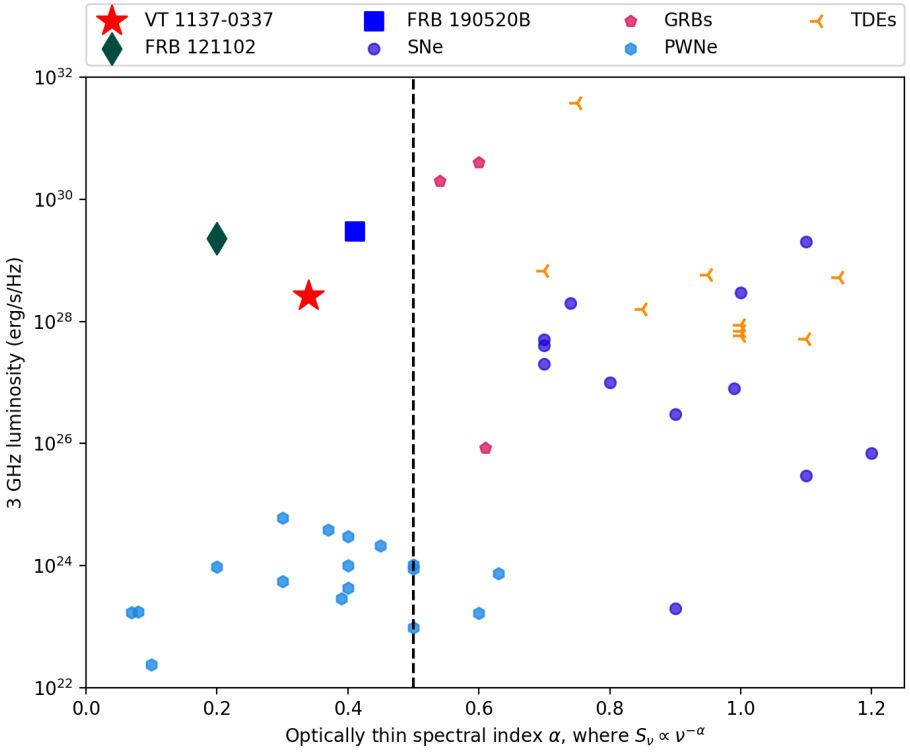

Figure 4.5: The 3-GHz luminosity and optically thin spectral index of VT 1137-0337 compared against values in the literature from radio observations of supernovae (SNe), gamma ray bursts (GRBs), tidal disruption events (TDEs), pulsar wind nebulae (PWNe), and fast radio burst (FRB) persistent sources. Sources left of the dotted line have harder spectra than the theoretical limit for diffusive shock acceleration: $\alpha = 0.5$. The values plotted and their references are listed in Appendix 4.9.

densest winds that have been observed around some supergiant stars (Smith, 2014), though we note that the constraint applies only along the line of sight and dense but asymmetric gas from e.g. binary interaction is allowed (D. Z. Dong et al., 2021).

4.6 Astrophysical Analogues and Possible Models

As discussed in Section 4.4, VT 1137-0337 is characterized by the following observational properties:

- Located near the nucleus of a dwarf galaxy of stellar mass $\sim 10^{8.3} M_\odot$ at redshift at z = 0.02764;

- A flat radio spectrum $S_\nu \propto \nu^{-0.35}$ with no observed peak between 1 to 15 GHz;
- A high radio luminosity of $L_{1.5\ \mathrm{GHz}} \sim 3 \times 10^{28}$ erg/s/Hz, and a νL_ν luminosity of 2×10^{38} erg s^{-1} at our highest observed frequency (∼15 GHz);
- Transient-like behavior (an increase of $> 5\times$ in luminosity at 1.5 GHz) on the timescale of ∼2 decades;
- Slow, broadband fading (∼20%) at 1-12 GHz over ∼4 years with a constant spectral index.

In Section 4.5, we used these features to argue that VT 1137-0337 is:

- Surrounded by massive stars that have formed in the past few Myr with no indications of AGN activity in the BPT diagram (Section 4.5);
- Characterized by a synchrotron spectrum that cannot be explained by a single shock under standard magnetic conditions (Section 4.5);
- Produced by an emitting region of present-day radius $\gtrsim 0.05$ pc and $\lesssim 6$ pc, where the synchrotron cooling time is $\gtrsim$ decades at the GHz frequencies observed. This region contains a magnetic energy that is comparable to or greater than radio-luminous supernovae, and is not presently obscured by a high density ionized shell or wind (Section 4.5).

In this section, we discuss astrophysical source classes known to produce luminous and variable and/or flat-spectrum radio emission. We assess whether they are consistent with the properties summarized above.

Exploding stars: radio SNe and long GRBs

VT 1137-0337 is located in the midst of a young starburst which, from its star formation rate (SFR) of ∼0.5 $M_\odot$ / yr, is expected to produce a core collapse supernova (SN) every ∼2 centuries. A small fraction of these explosions are expected to reach our observed luminosity of $\sim 10^{28}$ erg s^{-1}, either through interaction with a dense shell in the circumstellar medium (CSM) or by harboring a relativistic outflow such as a gamma ray burst (GRB). The slow evolution and low-frequency peak of the radio spectrum can potentially be explained if the explosion were caught at a late epoch (∼years for CSM interaction and $\gtrsim$1 decade for a GRB). However, the flat radio spectrum is unlike any SN or GRB that has been previously observed. Figure

4.5 shows a compilation of radio SNe and GRBs with published optically thin spectral indices. As can be seen in the figure, the spectral indices are > 0.5 in each case, consistent with DSA under standard conditions.

If VT 1137-0337 is indeed a supernova or GRB, we would likely need to invoke a model such as unusual magnetic conditions in the shock (e.g., Schlickeiser and Fuerst, 1989; Gregory D. Fleishman, 2006) to explain its flat spectrum. This has not been observed before in the sample of SNe and GRBs discovered in optical and high energy transient surveys. Though we cannot rule out that VT 1137-0337 is drawn from a new class of volumetrically rare flat spectrum stellar explosions discovered at radio wavelengths, the lack of flat spectrum analogs leads us to believe that a SN or GRB is an unlikely explanation. Instead, as discussed in Section 4.6, VT 1137-0337 may be associated with the compact remnant of a stellar explosion, rather than the shock.

Black hole jets: XRBs, ULXs, TDEs, and AGN

Synchrotron emission from a black hole (BH) jet is a potential explanation for the flat spectrum and variability of VT 1137-0337. Flat radio spectra spanning orders of magnitude in bandwidth have been observed from BHs with a wide range of masses, from stellar mass BHs in X-ray binaries (XRBs) (e.g., Fender, Pooley, et al., 2000) to supermassive BHs in active galactic nuclei (AGN) (e.g., Kellermann and Pauliny-Toth, 1981). The classical model of R. D. Blandford and Königl (1979) interprets flat AGN spectra as emission from relativistic electrons that are continuously accelerated by compact conical jets. In this model, the effective area of the emitting region varies with frequency in a way that cancels out the intrinsic optically thick spectral index. This optical depth effect, which can be understood as a continuous superposition of synchrotron components, results in an overall flat spectrum. This general picture is supported by very long baseline interferometry (VLBI) observations of flat spectrum AGN cores, which in some cases directly resolve the roughly conical jets (e.g., Asada and Nakamura, 2012), and in others, show a core shift towards the black hole at high frequencies (e.g., Plavin et al., 2019), which are both predictions of the model. A similar model from Hjellming and Johnston (1988), where the jet has a hollow conical geometry due to jet precession or orbital motion of the binary, is often invoked to explain the flat spectrum radio emission from XRBs.

In addition to producing flat spectra, BH jets are both theoretically expected and

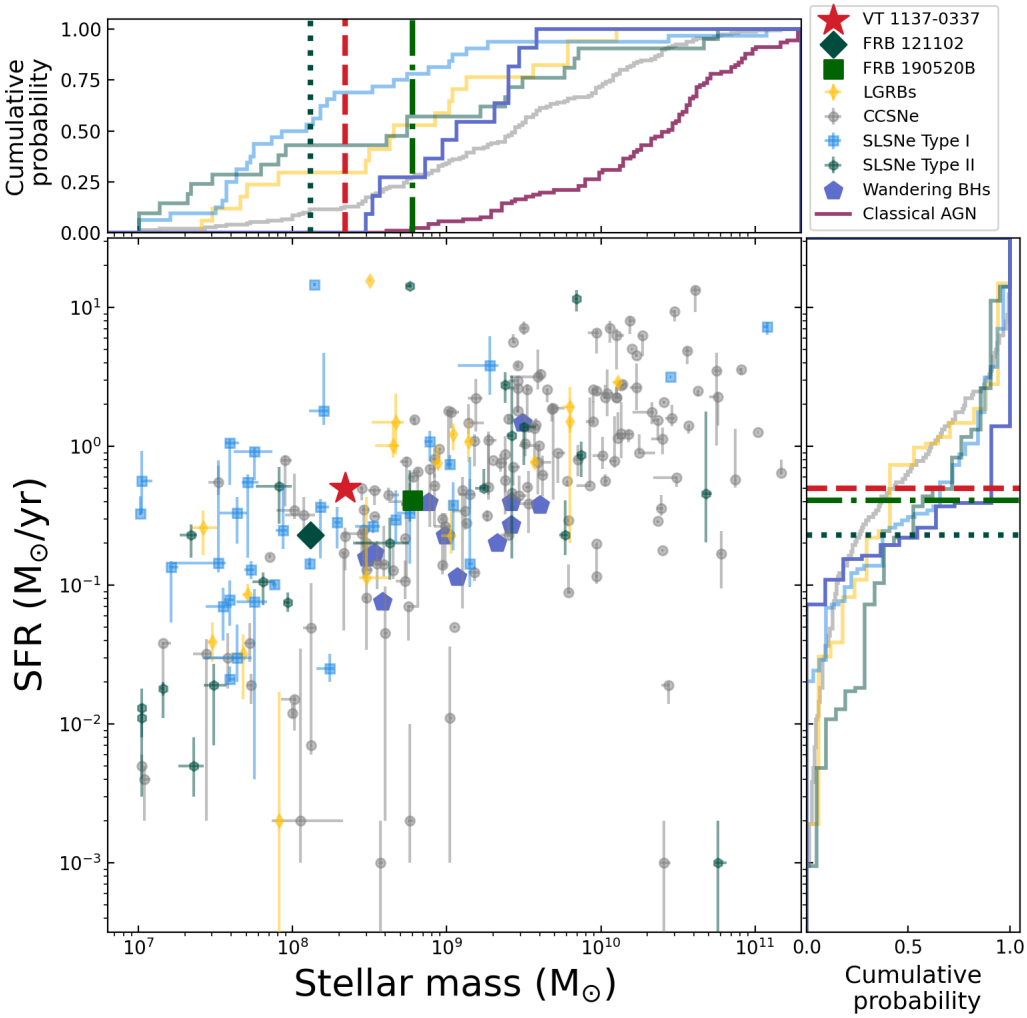

Figure 4.6: The star formation rate and stellar mass of VT 1137-0337's host galaxy in comparison with the hosts of FRB 121102 (Bassa et al., 2017), FRB 190520B (Niu et al., 2021), wandering black holes in dwarf galaxies (Reines, James J. Condon, et al., 2020, their sample A), optical/high energy transients compiled by Taggart and D. Perley (2019), and broadline AGN host masses from Reines and Volonteri (2015). For all populations with more than one source, the top and right panels show the cumulative distribution in stellar mass and star formation rate respectively. The dotted, dot-dash, and dashed lines show the positions of FRB 121102, FRB 190520B, and VT 1137-0337's host galaxies relative to these histograms.

observed to be variable. In jets that are pointed within a few degrees of our line of sight, small changes in either the jet angle or jet power can lead to substantial changes in the flux due to relativistic beaming (R. D. Blandford and Königl, 1979; Lister, 2001). Stochastic radio variability on timescales of days to months at the ∼10 to 40% level is often observed in blazars and flat spectrum radio quasars, which both have nearly on-axis jets. In some cases, their moving average flux density can change by factors of a few on timescales of years (Liodakis et al., 2017). BHs can also brighten substantially due to new jets being launched. During state changes, XRBs have been observed to brighten by orders of magnitude at radio frequencies while displaying flat radio spectra (Yao et al., 2020; Egron et al., 2021). Quasars have also recently been observed to launch new jets, brightening by 2 to >25× on decade timescales, albeit with peaked rather than flat spectra (Nyland, Dillon Z. Dong, et al., 2020).

To assess the viability of a BH jet model in explaining the specific observational properties of VT 1137-0337, we consider BHs in three mass ranges that may exist in its $M_* \approx 10^{8.3} M_\odot$ host galaxy: stellar mass BHs ($\lesssim 100 M_\odot$), intermediate mass BHs ($10^2 - 10^5 M_\odot$), and supermassive BHs ($\gtrsim 10^5 M_\odot$). Where possible, we draw analogies to known phenomena from these BH classes in the Milky Way and other galaxies.

Stellar mass BHs are expected to exist in large numbers in all galaxies of appreciable mass. While the majority of these BHs are likely isolated and do not emit strongly, a small fraction will reside in rapidly accreting systems such as XRBs that could in principle be detected (Wiktorowicz et al., 2019). There are, however, a number of orders-of-magnitude mismatches between VT 1137-0337's properties and those of known XRBs. VT 1137-0337's radio luminosity of $L_\nu \sim 10^{28}$ erg s^{-1} Hz^{-1} is $\gtrsim$ 4 orders of magnitude higher than even extreme flares from Galactic XRBs (e.g., Corbel et al., 2012). Likewise, its slow fading and lack of spectral index evolution over ∼4 years stands in sharp contrast with the large changes in luminosity and spectral shape observed in flaring XRBs over the span of hours to weeks (e.g., Pietka, Fender, and Keane, 2015; Yao et al., 2020). These issues of scale arise because black holes in this mass range have relatively short dynamical times and are limited in the rate at which they can accrete. In particular, the radio power - jet power relation from Cavagnolo et al. (2010) (which contains radio sources of similar luminosity to VT 1137-0337 in its calibration set) predicts that the jet power corresponding to

the luminosity we observe is $P_{\rm jet} \approx 1.4 \times 10^{42}$ erg s^{-1} with a scatter of ∼0.7 dex. This jet power is comparable to the Eddington luminosity of a $M_{\rm BH} = 10^4 M_\odot$ BH, given by $L_{\rm Edd} = 1.26 \times 10^{42} \left(M/10^4 M_\odot\right)$ erg s^{-1}. This suggests that to explain VT 1137-0337, a jet from stellar mass BH would need to suddenly increase in power over ∼20 years by a factor of ∼5× to ∼100 to 1000 times its Eddington luminosity, and it would need to maintain this new power level for at least the ∼4 years over which we have observed the source.

The rate of mass siphoned from a close binary $\dot{M}_*$ can substantially exceed the Eddington accretion rate $\dot{M}_{\rm Edd}$ of the accreting BH. Though the vast majority of this mass is lost through disk winds, the accretion rate $\dot{M}_{\rm BH}$ onto the BH can itself exceed $\dot{M}_{\rm Edd}$ due to photon trapping within the accretion flow. This is thought to occur in most ultra-luminous X-ray sources (ULXs; e.g, Sutton, T. P. Roberts, and Middleton, 2013). Using 3D GR radiation-MHD simulations, Sądowski and Narayan (2016) predict that a rapidly rotating black hole accreting in the super-Eddington regime can launch a jet with a power of a few percent of $\dot{M}_{\rm BH} c^2$ via the R. D. Blandford and Znajek (1977) process. In order to explain VT 1137-0337 with such a super-Eddington jet, $\dot{M}_{\rm BH}$ should be ∼2 to 3 orders of magnitude higher than Eddington requiring $\dot{M}_*$ to be a few orders of magnitude higher still.

An alternate explanation for the high radio luminosity is relativistic beaming. For a jet with a velocity $\beta = v/c$ oriented at an angle θ from our line of sight, the Doppler factor is defined as $\delta = (\Gamma - \sqrt{\Gamma^2 - 1}\,\cos\,\theta)^{-1}$, where $\Gamma = (1 - \beta^2)^{-1/2}$ is the bulk Lorenz factor. The jet's luminosity is magnified (or demagnified) by a factor of $\delta^{p_{\rm mag}}$, where the exponent $p_{\rm mag}$ depends on a number of factors including the spectral index of the emission, the structure of the jet, and (if relevant) the lifetime of the emitting blob (see Appendix B of Urry and Padovani (1995) for a discussion). For a steady, uniform jet, $p_{\rm mag} = 2 + \alpha$ where α is the spectral index (equal to +0.35 for VT 1137-0337). If the emission arises from a discrete blob of plasma travelling down the jet (i.e., a flare), it will be enhanced by a further factor of δ due to time dilation, making $p_{\rm mag} = 3 + \alpha$. In either case, beaming can magnify the radio luminosity by a large factor. For a steady jet pointed at $\theta \sim 20°$, the magnification is a factor of ∼10 depending on Γ (see Figure 4.7). At $\theta \sim 10°$, the luminosity is magnified by a factor of ∼100, and for $\Gamma \gtrsim 10$ jets pointed at $\theta \approx 0°$, beaming can enhance the luminosity by a factor of $\gtrsim 1000$. In Galactic XRBs, Γ has been measured to be in the range 1.3 - 3.5 (Saikia et al., 2019), a range in which the max-

imum magnification for a steady jet is $\sim$100$\times$ even if it is completely on-axis ($\theta = 0$).

Figure 4.8 shows the Eddington luminosity fraction required to explain VT 1137-0337's inferred jet power for various BH masses and under varying levels of beaming. For stellar mass BHs, highly super-Eddington accretion, strong beaming, or a combination of the two are required to explain the jet power we infer. These scenarios may be difficult to reconcile with the rapid transient behavior between FIRST and VLASS and subsequent slow fading. A large increase in the beaming magnification can occur if the the jet precesses into our line of sight. However, the timescale of this precession should be comparable to the orbital timescale of the binary which, given the high accretion rates, should be $\sim$weeks. Depending on the degree of beaming, the issue of timescales is compounded by time dilation, since the timescale in the jet's rest frame is longer by a factor of δ than the time we measure on Earth. Alternatively, a sudden increase in the instantaneous jet power may occur if $\dot{M}_{\rm BH}$ increases rapidly. Such increases are observed in XRBs as they transition between the high-soft and low-hard states. However, this increased accretion rate typically happens on a timescale of order the disk dynamical time, which is again much shorter than the $\sim$4 years over which we have observed slow fading. Overall, though it may be possible to explain VT 1137-0337's radio luminosity with the direct emission from a stellar mass BH jet, the characteristic timescales of such systems are not conducive to explaining the broadband lightcurve we observe.

We now consider the possibility of an intermediate mass BH (IMBH) in the mass range $10^{2-5} M_\odot$. To date, no examples of IMBHs have been conclusively established, though there are some promising candidates, particularly at masses $\gtrsim 10^4 M_\odot$ (see Greene, Strader, and L. C. Ho, 2020, and references therein). In the lower half of the mass range $\sim 10^{2-3.5} M_\odot$, many of the same arguments regarding stellar mass BHs apply. Beaming is still required if the accretion flow is sub or near-Eddington, though for near-Eddington accretion, the required magnification is only $\sim$10$\times$, corresponding to $\theta \lesssim (30^\circ \text{ to } 15^\circ)$ for $\Gamma = (2 \text{ to } 10)$. If the near-Eddington accretion is due to a close binary companion, the orbital timescale will still be of order $\sim$weeks, so the orbital plane would still have to be aligned close to face-on to avoid precessing the jet by more than a few degrees. A flare would need to span 4δ years ≈ 1 decade in its rest frame and would be more akin to a new jet turning on. It is again unclear what could cause the sudden but sustained change in accretion required to power such a flare. Tidal disruption events (TDEs) can launch jets and drive super-Eddington

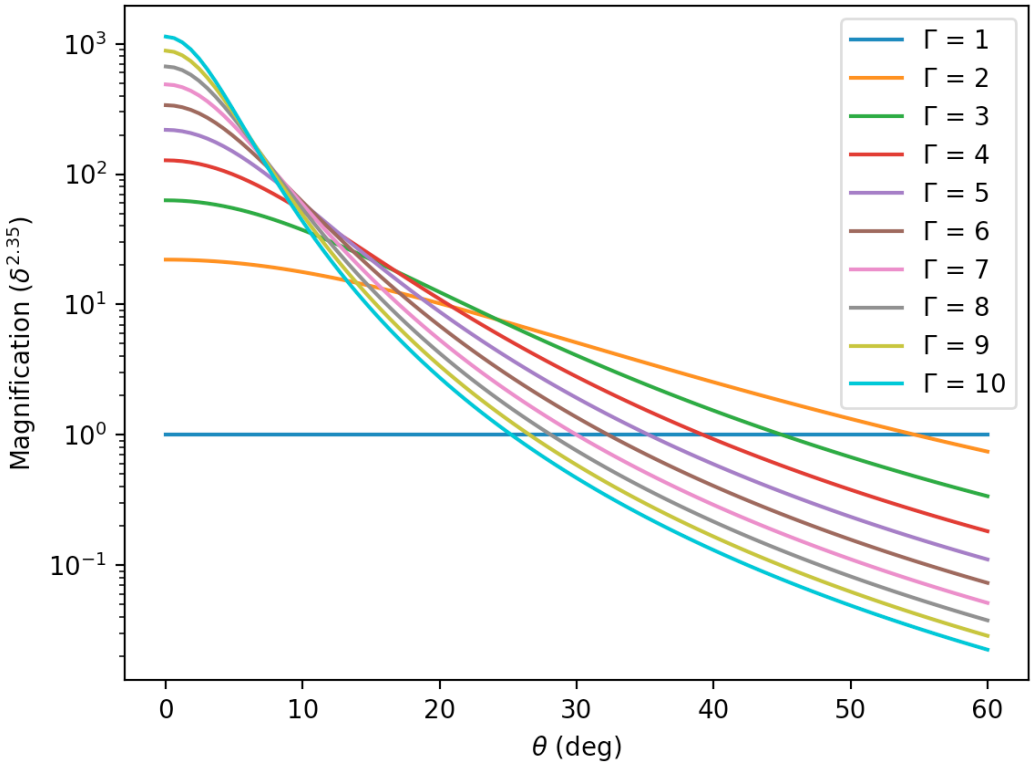

Figure 4.7: The magnification (or demagnification) due to relativistic beaming for a steady $\alpha = 0.35$ jet with bulk Lorenz factor Γ oriented at angle θ relative to our line of sight.

accretion (Zauderer et al., 2011), but the mass fallback rate is expected to decline steeply over time (canonically as $t^{-5/3}$; E. S. Phinney (1989)) and the jet's characteristic fading timescale would be ~months, not ~decades (Tchekhovskoy et al., 2014). Likewise, accretion disk instabilities will operate on timescales far too short to explain our observations.

The upper half of the IMBH mass range $\sim 10^{3.5-5} M_\odot$ is more plausible, and is particularly important to consider given the potential presence of a central black hole in VT 1137-0337's $M_* \approx 10^{8.3} M_\odot$ host galaxy. Due to selection bias in traditional AGN diagnostics, central black hole detections have historically been limited to galaxies with stellar mass $M_* \gtrsim 10^{9.5} M_\odot$ (e.g., Reines and Volonteri, 2015), where typically $M_{\rm BH} >> 10^5 M_\odot$. However, there is strong evidence of $\sim 10^5 M_\odot$ BHs in $\sim 10^9 M_\odot$ galaxies (e.g., Nyland, Davis, et al., 2017; Davis et al., 2020) and simulations suggest that the BH occupation fraction should be $\gtrsim 50\%$ in $10^{8-9} M_\odot$ galaxies (Bellovary et al., 2019). Additionally, new selection methods based on

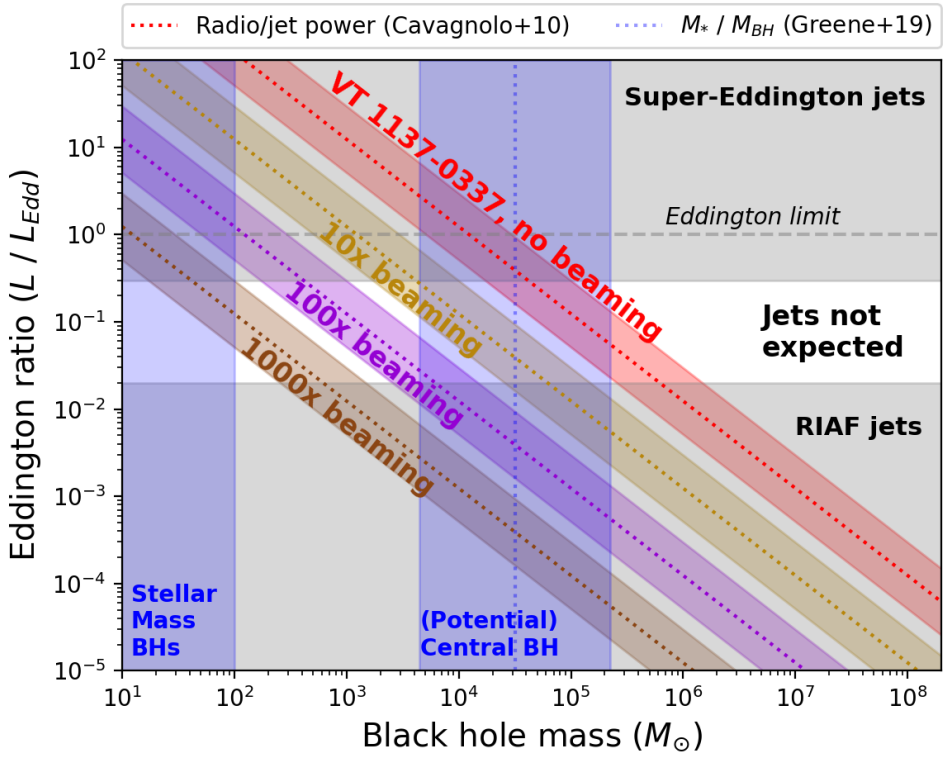

Figure 4.8: Approximate constraints on the mass and accretion scale required to explain VT 1137-0337 with a BH jet. The dashed lines show the predicted jet power from the radio power - jet power relation of Cavagnolo et al. (2010) with varying levels of magnification by beaming, with the corresponding shaded regions showing the scatter in the relation. The blue shaded regions show the estimated mass ranges for stellar mass BHs and central massive BHs as predicted by the galaxy mass - black hole mass relation (Greene, Strader, and L. C. Ho, 2020). The gray shaded regions show the accretion regimes (super-Eddington accretion and radiatively inefficient accretion flows) where the inflow is expected to be geometrically thick and thus capable of supporting jets.

luminous radio emission (Reines, James J. Condon, et al., 2020) and the high ionization potential [FeX] line (Molina, Reines, Greene, et al., 2021; Molina, Reines, Latimer, et al., 2021) have identified promising AGN candidates in dwarf galaxies as low mass as $\sim 10^{7.5} M_{\odot}$. For VT 1137-0337's host galaxy, a slight extrapolation of the most recent stellar mass - BH mass relation (Greene, Strader, and L. C. Ho, 2020) predicts a central BH mass of $10^{4.5\pm0.8} M_{\odot}$ when considering all galaxy types, or $10^{4.7\pm0.8} M_{\odot}$ when considering only late-type galaxies.

There are some additional complications that are particularly relevant for jet models in the predicted central BH mass range. First, there is a range of Eddington ratios between ~a few percent and ~30% for which jets are not observed or theoretically predicted. In this range, the accretion disk is expected to be geometrically thin and incapable of supporting the vertical magnetic fields required to collimate jets (Meier, 2001). This jet quenching effect has been observed in XRBs (e.g., Fender, Belloni, and Gallo, 2004), and has been used to explain the abrupt drop in the X-ray flux from the jetted TDE Swift J1644+57 (Tchekhovskoy et al., 2014). The quenched jet zone excludes a substantial part of the BH mass - Eddington ratio parameter space relevant to higher mass IMBHs (Figure 4.8). Second, the optical emission lines in the ~280 pc radius region surrounding VT 1137-0337 have intensity ratios that are very far from the region typically associated with AGN (Figure 4.4), and all of the lines are spectrally unresolved at the ~150 km/s level. This is likely ok for lower mass BHs or those accreting at low Eddington ratios, since sub-Eddington BHs with masses $\lesssim 10^4 M_{\odot}$ are predicted to have weak narrow lines with ratios consistent with star formation, (albeit in a different region of the BPT diagram than VT 1137-0337's host) (Cann et al., 2019). However, for near-Eddington BHs with mass $\gtrsim 10^5 M_{\odot}$, the expected narrow line luminosity is comparable to what we observe, and their intensity ratios are inconsistent with the ones we measure.

At the lower end of the predicted mass range ($\sim 10^4 M_{\odot}$), avoiding the quenched jet zone requires either near-Eddington accretion and little to no beaming, or very strong beaming and accretion in the radiatively inefficient accretion flow (RIAF) regime (an Eddington ratio of $\lesssim$ a few percent). If the accretion rate is near Eddington, it is once again difficult to explain the sudden and sustained accretion. If instead the emission is highly beamed, the slow variability is again problematic given time dilation and the expected variability timescale (~months) for sources in this luminosity range (e.g., Pietka, Fender, and Keane, 2015).

At the high end of the predicted mass range ($\sim 10^5 M_\odot$), the two scenarios are demagnification from beaming and near-Eddington accretion, or moderate beaming and accretion in the RIAF regime. As discussed above, the near-Eddington scenario is disfavored by the lack of AGN-like emission ratios in addition to issues with fueling the BH at the right rate on the right timescales. In the RIAF scenario, the power requirement for the jet is more easily satisified, so we investigate it in more detail. If a $\sim 10^5 M_\odot$ BH experienced an increase in its accretion rate to a few percent of Eddington and subsequently launched a flat spectrum jet at an angle where it is magnified by $\sim 10\times$ by beaming, that could potentially explain the appearance of VT 1137-0337 between FIRST and VLASS. However, in order to explain the slowly fading flat spectrum, the jet would need to maintain a nearly constant luminosity on scales of $\sim 10^{-3} - 10^{-1}$ pc (the linear scales corresponding to synchrotron self-absorption frequencies of 15 GHz to 1 GHz at the luminosity of VT 1137-0337; Scott and Readhead, 1977) for an observer-frame timescale of ∼4 years. Plasma moving at relativistic velocities in the jet will cycle through these length scales on timescales of ∼days to weeks. Thus, the jet would have to maintain a stable power on all scales probed over ∼tens to thousands of plasma crossing times. This type of stability is not observed in AGN dominated by their flat spectrum cores. For scale, the 15 GHz length scale for a 1 Jy flat spectrum AGN at a distance of 100 pc is ∼0.07 pc, corresponding to a plasma crossing time of ∼80 days. Maintaining a constant flux for ∼1000 crossing times would be analogous to having that flat-spectrum radio quasar or blazar be stable for ∼2 centuries, which is far longer than the typical variability timescale of ∼months (Liodakis et al., 2017). Additionally, to avoid spectral index evolution and sharp variability due to changes in beaming, the jet orientation would need to remain stable, excluding models involving a pre-existing jet that precessed into our line of sight. We do not consider any of the above scenarios to be likely.

Finally, we consider the possibility of a jet from a supermassive BH. Black holes with mass $>> 10^6 M_\odot$ are not generally expected to exist in VT 1137-0337's dwarf host galaxy, though ones in the range $10^{5-6} M_\odot$ are within the scatter of the stellar mass - BH mass relation. Many of the same arguments against $\sim 10^5 M_\odot$ BHs apply in this mass range. While fueling the jet power is no longer an issue, maintaining a low-luminosity flat-spectrum core with only ∼20% variability over ∼4 years and no change in the spectral index is once again difficult due to the size scales involved.

In summary, BH jet models at all mass scales face substantial challenges when attempting to explain VT 1137-0337's luminosity, variability properties, and flat spectrum. Stellar mass BHs would require extreme and rapidly changing accretion rates or heavy beaming to produce the required luminosity. Such jets would most likely appear as fast transients (flickering on and off on timescales of ∼days) rather than the relatively stable one that we have observed. An IMBH, particularly one towards the higher mass end ($\sim 10^5 M_\odot$), is potentially expected to exist in VT 1137-0337's host galaxy and would be able to accrete at a rate that could power the luminosity we observe. However such a BH cannot explain the flat spectrum and slow variability, since the length scales responsible for emitting at each of our observed frequencies would have been traversed by tens to thousands of separate blobs of relativistic plasma over the course of 4 years. The modest ($\sim 20\%$) and consistent variability we have observed at all frequencies would require any stochastic jet-power process to be auto-correlated over unrealistic timescales. Supermassive BHs are ruled out by the same argument, and are furthermore not expected to exist in such a low-mass galaxy. These arguments, though approximate in nature, show that the specific properties of VT 1137-0337 (particularly its sudden appearance, flat spectrum, and slow fading, which have not been observed for other BHs or BH candidates) are not easily explained by a BH jet. Instead, we believe that there is a more compelling explanation: a young and energetic pulsar wind nebula. We discuss this in the next section.

Neutron star nebulae: pulsar winds and magnetar field decay

The most distinctive feature of VT 1137-0337 is its flat and slowly evolving radio spectrum. Pulsar wind nebulae (PWNe) are one of the only well-observed source classes with this type of spectrum. The vast majority of known PWNe are observed to have spectra flatter than the $\alpha = 0.5$ Fermi acceleration limit (Kaspi, M. S. E. Roberts, and Harding, 2006; Bryan M. Gaensler and Slane, 2006; Green, 2019) that evolve very slowly on human timescales. As an example, the Crab Nebula has a power law spectrum with no radio-frequency substructure, which fades by only 0.167 ± 0.015 percent per year (Aller and S. P. Reynolds, 1985). Its spectral index was measured in the 1960s to be $\alpha = 0.299 \pm 0.009$ (Baars et al., 1977), and least squares fitting of a compilation of measurements from the 1970s to the early 2000s gives $\alpha = 0.296 \pm 0.006$ (Macıas-Pérez et al., 2010).

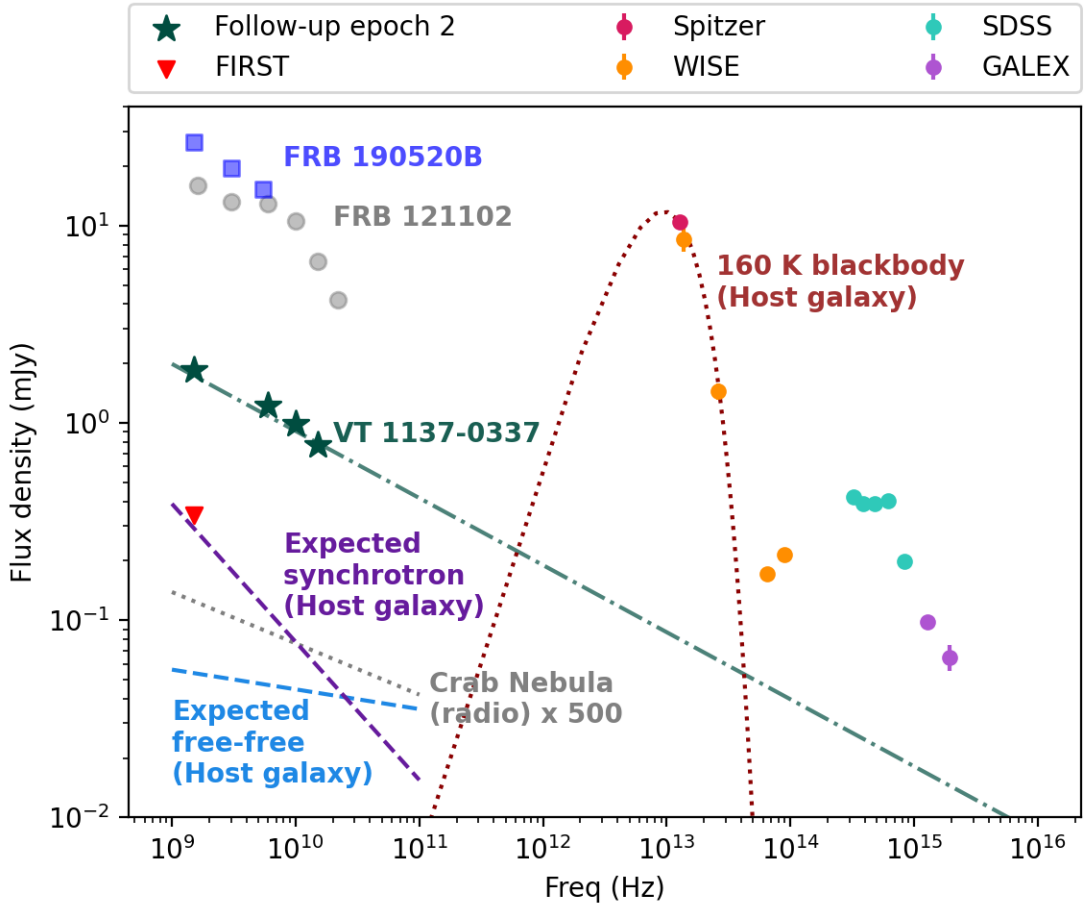

Figure 4.9: The radio spectrum of VT 1137-0337 superimposed on the spectral energy distribution of its host galaxy. The dotted and dashed green line shows VT 1137-0337's extrapolated spectrum in Epoch 2. The blue and purple dashed lines show the expected host galaxy radio emission due to star formation, assuming a typical synchrotron spectral index of 0.7 (E. J. Murphy et al., 2011). The dotted red line shows a blackbody approximation to the host galaxy's infrared dust emission, normalized to the Spitzer 24μm flux. For comparison, the gray circles and blue squares show the spectrum of the persistent counterparts to FRB 121102 (S. Chatterjee et al., 2017) and FRB 190520B (Niu et al., 2021). The gray dotted line shows the integrated radio spectrum of the Crab Nebula (Atoyan and Aharonian, 1996) multiplied by a factor of 500×. The FRB persistent source and scaled-up Crab fluxes are normalized to the distance of VT 1137-0337.

Many theoretical mechanisms have been proposed to explain the flat spectra of PWNe. Unlike in BH jets, where the time-variable flat spectra are typically explained with optical depth effects that can change rapidly, most PWN theories invoke an intrinsically hard spectrum with an electron energy index $p < 2$. Atoyan (1999) proposes that the hard energy distribution is assembled over time from electrons injected at high energy that cool rapidly and pile up at the synchrotron cooling break. As the PWN expands and its magnetic field weakens, the break drifts upwards in energy, freezing in the old low energy electrons and piling up new ones to fill out the higher energy parts of the spectrum. This model ties the spectral index to the evolution of the PWN in a way that reproduces the observed flat spectra for standard energy injection via spindown. It predicts that the current radio-producing electrons in the Crab Nebula were injected at a very early time (∼decades). If this were the case, the Crab Pulsar may have had a spin period of a few milliseconds at birth rather than the $\sim$ 19 ms inferred from tracing back its spindown from parameters measured in the present day (e.g., Kou and Tong, 2015).

There is, however, evidence that radio-emitting electrons in the Crab Nebula are still being accelerated today, given the morphological similarity of radio wisps with much shorter lived optical wisps (Bietenholz, Frail, and Hester, 2001). In that case, the hard distribution may instead be produced at the acceleration site. Schlickeiser and Fuerst (1989) propose that $p < 2$ in extremely magnetic dominated shocks, due to second-order Fermi acceleration. By their analytic estimates, reducing p to 1.7 requires that the magnetic energy dominates over the thermal energy by over an order of magnitude (a plasma β of ∼0.05). Alternatively, simulations of particles accelerated by relativistic magnetic reconnection are consistently able to produce distributions with $p < 2$ with Lorentz factors appropriate for GHz radio emission (e.g., Kagan, Ehud Nakar, and Piran, 2018). This too requires a highly magnetized plasma at the acceleration site. Werner et al. (2016) found that $p \approx 1.7$ when σ (the ratio of the magnetic to relativistic energy density) is ∼8. Reconnection-driven acceleration can potentially occur at the termination shock of the highly magnetized and relativistic pulsar wind (Sironi and Spitkovsky, 2011) or within the bulk of the nebula itself (Lyutikov et al., 2019).

Flat spectra can potentially be produced even without a hard electron distribution if the electrons are propagating within a magnetic field that, due to turbulence, is randomly oriented on scales smaller than the particles' orbits. In this scenario, there

is a frequency range where $\alpha = (q-1)/2$, where q is the index of the turbulent power spectrum (G. D. Fleishman and Bietenholz, 2007). Intriguingly, Kolmogorov (1941) turbulence has $q = 5/3$, which implies a spectral index of $\alpha = 1/3$ similar to our observed value of $\alpha = 0.35$. This mechanism has also been proposed to explain the Crab Nebula's flat radio spectrum (Tanaka and Asano, 2017). Recent particle-in-cell simulations have also shown that particles accelerated (typically by magnetic reconnection) within turbulent plasmas have an energy-dependent anisotropy, which for most viewing orientations would also lead to hard spectra $\alpha \sim 0.3$ to 0.5 (Comisso, Sobacchi, and Sironi, 2020).

At the moment, the theory of PWNe spectra is an evolving field with new ideas being put forward regularly. We therefore remain agnostic to the mechanism and instead point out that VT 1137-0337's flat spectrum and slow fading are *empirically* very similar to what's observed for PWNe. The biggest differences to be explained are that (1) VT 1137-0337 appears as a transient (on a timescale of ~20 years), (2) it is fading at a moderate rate (~5% per year, much faster than the Crab's 0.17% per year), and (3) it is far more radio luminous than any known PWN ($\sim 10^4\times$ the Crab's luminosity).

All three of these differences are, at least qualitatively, *expected* for a PWN if the central neutron star (NS) is young. VT 1137-0337's starbursting host galaxy is expected to produce young NSs via core collapse supernovae at a relatively high rate. Shortly after birth, a NS will start to spin down, launching a relativistic wind of particles and Poynting flux through the rapid rotation of its magnetic field (Goldreich and Julian, 1969). For the most strongly magnetized NSs, there may be a non-negligible or even dominant component of the wind powered by the direct decay of the internal magnetic field, possibly in discrete flares (e.g., Beloborodov, 2017; Ben Margalit and Brian D. Metzger, 2018). Regardless of the power source, the wind will deposit its energy in a termination shock, inflating a bubble within the surrounding supernova ejecta and forming a PWN. After some time, the ejecta will expand and dilute to the point where it becomes optically thin to free-free absorption. At that point, the PWN will suddenly appear as a radio transient (Roger A. Chevalier and Fransson, 1992). Young PWNe are expected to reach their peak luminosity after just a few years (with the rise time generally occurring while they are still obscured). Those powered by neutron stars with fast periods or high magnetic fields could be orders of magnitude more luminous at early times than the centuries- to millenia-old

PWNe observed in the Milky Way. Such young nebulae are also expected to fade at their fastest per-year rate (S. P. Reynolds and R. A. Chevalier, 1984). Together, these qualities make a young, energetic PWN an intriguing potential explanation for VT 1137-0337. In the remainder of this section, we describe some order-of-magnitude properties of PWN models embedded in supernova ejecta, and check whether they are able to explain VT 1137-0337's observed properties.

Age constraints

We begin by constraining the range of PWN ages ($t_{\rm age}$) consistent with VT 1137-0337's observables, under the assumption that it was born in a supernova. There are thought to be other ways of forming young neutron stars (such as the accretion induced collapse of a white dwarf), but VT 1137-0337's location within an extreme starburst suggests that a supernova would be the most likely channel. The age constraints will be applicable regardless of the nebula's power source.

To start, there is a hard lower limit of $t_{\rm age} > 4$ years in February 2022 based on the duration that we have observed the source. This minimum age is pulled upwards by two requirements: (1) that the supernova ejecta must expand to the point where it is optically thin to free-free absorption, and (2) that the nebula has time to grow to a size $R \gtrsim 10^{17}$ cm, as we inferred in Section 4.5. The time for the ejecta to become transparent to free-free absorption is given by Brian D. Metzger, Edo Berger, and Ben Margalit (2017):

$$t_{ff} \approx 9.85 \left(\frac{f_{\rm ion}}{0.1}\right)^{2/5} T_4^{-3/10} M_{10}^{2/5} v_9^{-1} \nu_{\rm GHz}^{-2/5} \text{ years} \tag{4.7}$$

where $f_{\rm ion}$ is the ionization fraction of the ejecta, T_4 is the ejecta temperature in units of 10^4K, M_{10} is the ejecta mass in units of $10 M_\odot$, v_9 is the ejecta velocity in units of 10^4 km/s, and $\nu_{\rm GHz}$ is the observing frequency in GHz. Even for a high intensity of ionizing radiation from the nebula, $f_{\rm ion}$ is expected to be $\lesssim 0.25$ on a timescale of ∼decades, with full ionization occurring on a timescale of ∼centuries (Brian D. Metzger, Edo Berger, and Ben Margalit, 2017). For typical supernova kinetic energies and ejecta masses (e.g., Nicholl et al., 2015; Taddia, Sollerman, et al., 2015; Barbarino et al., 2020; Martinez et al., 2022), the quantity $M_{10}^{2/5} v_9^{-1}$ is ~ 0.5 for Ic broadline supernovae, ~ 1 for superluminous supernovae, ~ 1.5 for stripped envelope (type Ib/c) supernovae, and ~ 3.5 for type II supernovae. For these various classes, $t_{ff} \approx 1$ to 4 decades for our lowest observed frequencies of ∼1 GHz.

Next, the radius of a PWN expanding within supernova ejecta is given by Roger A. Chevalier (2004):

$$R = 2 \times 10^{17} \dot{E}_{42}^{1/5} E_{51}^{3/10} M_{10}^{-1/2} t_{20}^{6/5} \text{ cm}, \tag{4.8}$$

where $\dot{E}_{42}$ is the rate of energy injection into the PWN in units of 10^{42} erg s^{-1}, E_{51} is the energy of the supernova in units of 10^{51} erg, and t_{20} is the age normalized to 20 years. For the various supernova types, the quantity $E_{51}^{3/10} M_{10}^{-1/2} \approx 0.9$ to 3. For reasonable values of $\dot{E}$ discussed in the sections below, $\dot{E}_{42}^{1/5} \gtrsim 0.25$. The timescale $t_{ff} \gtrsim 10$ years is sufficient to expand the nebula to $\gtrsim 10^{17}$ cm for fiducial values, though less energetic supernovae with higher ejecta masses will require longer to reach this radius. Adding the duration that we have observed the source to t_{ff}, we adopt a fiducial lower limit to the nebula's age in 2022 of $t_{\rm age} \gtrsim 14$ years.

We note that at an age of $\gtrsim 10$ years, the shock emission from most (but not all) supernovae should be orders of magnitude fainter than what we can detect. VT 1137-0337 has a radio spectral luminosity of $\sim 10^{28}$ erg s Hz^{-1}, which is $\sim$2.5 orders of magnitude more luminous than the median peak of supernova radio lightcurves. These peaks tend to occur at an epoch of $\sim$months to years after explosion (Bietenholz, Bartel, et al., 2021). At an epoch of $\sim$decades, typical supernovae will be one or more orders of magnitude fainter yet (Roger A. Chevalier, 1998). We also note that for typical NS kick velocities, the radius of the nebula should be larger than the distance the NS has travelled, given by $R_{\rm kick} = 1.9 \times 10^{16}\ v_{300}\ t_{20}$ cm, where v_{300} is the kick velocity in units of 300 km/s. Even for the largest kick velocities of $\sim$1000 km/s, the NS should still be embedded within the nebula, though the distance travelled and the implied asymmetry of the ejecta would contribute to the nebula partially breaking out at a slightly earlier time. Thus, supernova shocks and neutron star kicks should not be issues for the general picture presented here.

An upper limit to the age of the nebula can be inferred from the fact that VT 1137-0337 was detected as a transient. If $t_{ff} \gtrsim 10$ years is the time that it takes for the ejecta to become transparent at 1 GHz, the upper limit to the age in 2018 is $t_{ff} + 20$ years, since if VT 1137-0337 were older than that, it should have been clearly detected in FIRST. Our estimate of $t_{ff} \approx 1 - 4$ decades, therefore suggests that the source is no more than $\sim$ 6 decades old.

A complementary upper limit comes from the ∼5.5% per year fading that we measure between Epoch 2 and Epoch 3. In both spindown and magnetar models, the rate of fading can be approximated with a power law that at early times is generally not steeper than $\sim t^{-4}$ (e.g., S. P. Reynolds and R. A. Chevalier, 1984; Ben Margalit and Brian D. Metzger, 2018). Figure 4.10 shows the observed fade rate in comparison with power laws of various steepness. Past an age of ∼80 years, even a fade rate of t^{-4} will be slower than the rate that we measure.

Altogether, the allowable age range for VT 1137-0337 is a ∼20 year window with the lower edge set by t_{ff} (Figure 4.10). Different values of $t_{\rm age}$ also correspond to different power-law rates of fading when combined with the observed per-year fade rate. In the next section, we use this to constrain the allowable parameter space in the $P - \dot{P}$ diagram for a spindown model.

Spindown implies a strongly magnetized NS

We now consider a nebula powered by the spindown of a central NS, the mechanism thought to power most Galactic PWNe. In standard spindown models, the rate of energy input to the nebula $\dot{E}$ is assumed to be equal to the rate of rotational energy dissipation (the spindown luminosity $L_{\rm sd}$), which can be expressed as a function of the NS's rotational period P and its time derivative $\dot{P}$:

$$L_{\rm sd} = 4 \times 10^{41} I_{45} \dot{P}_{-11} P_{10}^{-3} \text{ erg s}^{-1}. \tag{4.9}$$

Here, I_{45} is the NS moment of inertia in units of 10^{45} g cm^2 (equal to 1.1 for a 1.4 $M_\odot$ sphere of radius $R_{\rm NS} = 10$ km), $\dot{P}_{-11}$ is the period derivative in units of 10^{-11} seconds per second, and P_{10} is the period in units of 10 ms. As the NS's magnetic field rotates, it emits magnetic dipole radiation with a luminosity of

$$\dot{E}_d = 4 \times 10^{41} B_{d,13}^2 P_{10}^{-4} \text{ erg s}^{-1}, \tag{4.10}$$

where $B_{d,13}$ is the strength of the surface dipole field in units of 10^{13} G. By equating $\dot{E}_d$ with $L_{\rm sd}$, we can get an expression for B_d (where we have dropped a constant within a few percent of unity):

$$B_{d,13} = (\dot{P}_{-11} P_{10})^{1/2}. \tag{4.11}$$

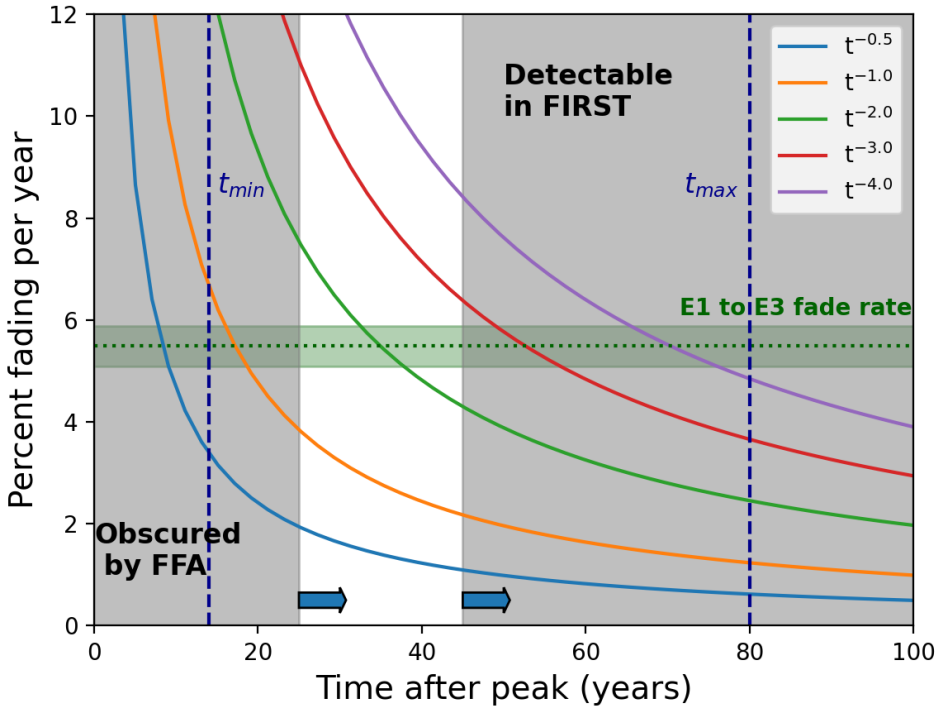

Figure 4.10: Age constraints for a pulsar wind nebula model of VT 1137-0337. The minimum age of the nebula is $t_{min} \approx 14$ years, while the maximum age is $t_{max} \approx 80$ years. The true age lies within a ~20 year sliding window starting from the age t_{ff} when the ejecta becomes transparent to free-free absorption at 1 GHz (shown in the figure with a fiducial value of $t_{ff} = 25$ years). The measured per-year fade rate and its uncertainty is shown with the green dotted line and its corresponding shaded region. When combined with an assumed true age, this per-year rate determines the present-day steepness of VT 1137-0337's fading lightcurve, as illustrated by the various power laws plotted as solid lines.

The spindown luminosity evolves over time (Bryan M. Gaensler and Slane, 2006):

$$\dot{E}_d = \dot{E}_0 \left(1 + \frac{t}{\tau_0}\right)^{-\frac{n+1}{n-1}}, \tag{4.12}$$

where $\dot{E}_0$ is the initial value of $\dot{E}_d$, $n = 2$ to 3 is the braking index, and τ_0 is the initial spindown time:

$$\tau_0 = \frac{P_0}{(n-1)\dot{P}_0}. \tag{4.13}$$

At early times $t << \tau_0$, $\dot{E}_d$ will be nearly constant. Later, when $t >> \tau_0$, $\dot{E}_d$ will

decrease as a power law $\propto t^{-2}$ to t^{-3}. By combining Equations 4.11 and 4.13 and assuming $n = 3$, the spindown time can also be recast in terms of the dipole field:

$$\tau_0 = 15.9\, B_{d,13}^{-2}\, P_{10}^{2} \text{ years.} \tag{4.14}$$

From this, we can see that the initial spindown time depends strongly on both the initial period and the magnetic field. We will return to this later in this section and the next, but first, we attempt to constrain the values of $\dot{E}_d$ and τ_0 consistent with VT 1137-0337's radio luminosity and lightcurve.

In Galactic PWNe, the spindown luminosity can be measured precisely through pulsar timing. However, for our model, the best we can do is to estimate what it should be from the radio luminosity. The conversion between radio and spindown luminosity is often expressed with the fraction $\eta_R \equiv L_R/L_{sd} = L_R/\dot{E}_d$. For well-characterized radio PWNe in the Green (2019) catalog, the median value of η_R is 3×10^{-4}, with a scatter of ~ 0.85 dex, where we have taken properties of the corresponding pulsars from *psrcat* (Manchester, Hobbs, et al., 2005). This is in agreement with results in the literature (e.g., Frail and Scharringhausen, 1997; B. M. Gaensler et al., 2000), who find $\eta_R \sim 10^{-4}$ for young and energetic pulsars, though some older pulsars with undetected nebulae have values $< 10^{-5}$.

The value of η_R is expected to evolve over time as the NS spins down ($\dot{E}_d$ decreases, as described above) and its PWN fades (L_R decreases). The behavior of the radio lightcurve depends on $\dot{E}_d$, the adiabatic cooling of the radio-emitting electrons and the evolution of the magnetic field in the nebula. An analytic model for the lightcurve of a spindown powered PWN expanding within spherically symmetric supernova ejecta undergoing homologous expansion can be found in S. P. Reynolds and R. A. Chevalier (1984). Their model predicts that for $t < \tau_0$, a single injected electron energy distribution of $p = 1.7$, and an observing frequency below the synchrotron cooling break, L_R should fade approximately as a power law of $t^{-0.75}$ to $t^{-1.35}$, depending on the degree to which the PWN has swept up the ejecta. After τ_0, when the spindown luminosity begins to drop, the radio lightcurve fades much more steeply, as $\approx t^{-3.4}$ for $p = 1.7$. Later, after the PWN is compressed by the passage of the reverse shock, the luminosity will undergo a sharp enhancement followed by a slow decline $\approx t^{-1}$. This occurs at a time $\sim 10^4$ years for a thin wind or an ISM-like density, though may occur much sooner if there is a dense shell

of circumstellar material around the supernova. The net result is that before the reverse shock sweeps through (both before and after τ_0), η_R should very roughly decrease as $\sim t^{-0.75}$ to $t^{-1.5}$. After the reverse shock, η_R should increase as $\sim t^1$ to t^2.

In Section 4.5, we argued that VT 1137-0337 is not surrounded by a dense shell (so the reverse shock is not relevant at our inferred $t_{\rm age}$ of ~decades), and that our radio observations likely lie below the cooling break. We therefore expect that η_R should be decreasing with time, and that the value of of η_R in Galactic PWNe is likely an underestimate. Extrapolating backwards from the youngest known PWNe (including the Crab Nebula) which have characteristic ages ~1000 years and $\eta_R \sim 10^{-4} - 10^{-3}$, we estimate that a reasonable range of values for a PWN with an age of a few decades is $\eta_R \sim 10^{-1} - 10^{-3}$. For VT 1137-0337's radio luminosity of $L_R \sim 10^{38}$ erg s^{-1}, the corresponding spindown luminosity range is $\dot{E}_d \sim 10^{39}$ to 10^{41} erg s^{-1}.

Using the age constraints in Section 4.6, we can separately constrain the value of the initial spindown time τ_0. As can be seen in Figure 4.10, if the true age of the nebula $t_{\rm age}$ were close to the minimum age $t_{\rm min} \approx 14$ years, the measured per-year rate of fading corresponds to a rather shallow power law $\approx t^{-1}$. In the framework of S. P. Reynolds and R. A. Chevalier (1984), this would imply that the NS has not yet appreciably spun down, so $\tau_0 \gtrsim t_{\rm age} \gtrsim 14$ years. Alternatively, if $t_{\rm age}$ is closer to the maximum value $t_{\rm max} \approx 80$ years, we would require a steep power law $\sim t^{-4}$ to reach the ~5% per-year fading we observe. Such a steep power law would imply that the NS has already begun to spin down substantially, and so 80 years $\gtrsim t_{\rm age} \gtrsim \tau_0$. Intermediate values of $t_{\rm age}$ correspond to power laws of intermediate steepness that would appear when $t_{\rm age} \approx \tau_0$. This implies that for a spindown powered nebula, τ_0 is between $\sim$ 14 to 80 years.

As shown in Figure 4.11 the constraints on $\dot{E}_d$ and τ_0 combine to form a rather tight region in the classic pulsar parameter space of P and $\dot{P}$. The allowed region corresponds to a dipole field of slightly less than 10^{13} G to a few $\times$ 10^{14} G, roughly an order of magnitude stronger than that of the Crab Pulsar ($\sim 10^{12.5}$ G). Such strongly magnetized neutron stars should spin down rapidly (Equation 4.14). Within ~100 years, $\dot{E}$ will have decreased by $\sim 10 - 30\times$ and, due to the expected drop in η_R, the radio luminosity will have decreased by an even larger margin. Within a few thousand years, the central NS should fall within the distribution observed in the Milky Way. If the magnetic field is $\sim 10^{14}$ G, the NS may eventually

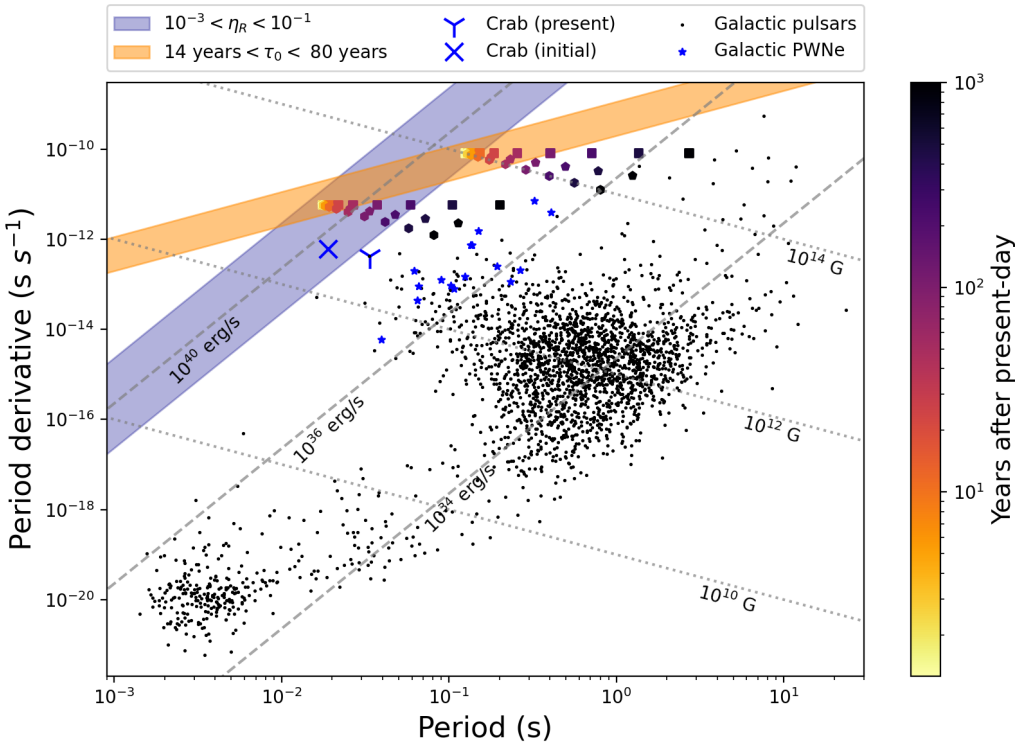

Figure 4.11: Constraints on a spindown-powered pulsar wind nebula model of VT 1137-0337, plotted in comparison with Galactic pulsars (black points; Manchester, Hobbs, et al., 2005). The dashed and dotted lines show curves of constant spindown luminosity $\dot{E}_d$ and surface dipole field B_d respectively. Pulsars from the Green (2019) catalog with well-characterized nebulae are shown with blue stars. Using the Y and X symbols, we highlight the present position of the Crab Pulsar (Lyne, Pritchard, and Graham Smith, 1993) and its estimated initial position from tracing back its spindown (Kou and Tong, 2015). In our model, VT 1137-0337's present day position is in the intersection of the orange shaded region (derived from limits on the initial spindown time τ_0) and the blue shaded region (derived from our estimate of $\dot{E}_d$). The colored tracks show the spindown over 1000 years of neutron stars currently located at two different positions in the intersection ($B_d = 10^{14}$ G, $\dot{E}_d = 2 \times 10^{39}$ erg s^{-1}) and ($B_d = 10^{13}$ G, $\dot{E}_d = 5 \times 10^{40}$ erg s^{-1}). In these tracks, the squares, pentagons, and hexagons represent braking indices of n = 2, 2.5, and 3, respectively.

resemble the population of Galactic magnetars (Kaspi and Beloborodov, 2017). If instead B is closer to $\sim 10^{13}$ G, it might eventually resemble a highly magnetized pulsar, similar to the NS at the center of the composite supernova remnant Kes 75 (e.g., Gavriil et al., 2008; Stephen P. Reynolds, Borkowski, and Gwynne, 2018).

Magnetar activity as an alternate power source

As discussed above, VT 1137-0337's luminosity and lightcurve are consistent with a ∼decades old PWN powered by spindown. However, the only part of the argument that depends specifically on spindown is the evolution of $\dot{E}$. In principle, any source of power that can approximately reproduce $\dot{E}$ (and also satisfy one of the mechanisms for producing a flat spectrum) would suffice. A change in the time-dependence of $\dot{E}$ would change the PWN's lightcurve, but as shown in Figure 4.10, our per-year fading measurement can be reconciled with a broad range of power-law fade rates from $\sim t^{-1}$ to $\sim t^{-4}$ simply by changing $t_{\rm age}$. This leads us to consider a different energy source often used in modeling magnetars: the direct decay of the NS's magnetic field.

Galactic magnetars typically have spindown-inferred surface dipole fields of $B \sim 10^{14} - 10^{15}$ G (Kaspi and Beloborodov, 2017). Their total surface fields may be even stronger if a large fraction is "hiding" in higher order multipoles (those components fall off more rapidly with radius and make only marginal contributions to the torque at the light cylinder radius where the pulsar wind is launched; J. M. Cordes, Wasserman, et al., 2021). Fields within the NS should be even stronger. Galactic magnetars maintain high blackbody temperatures for much longer than their initial neutrino cooling timescale, suggesting that their internal fields (which heat the NS through their decay) can be as strong as $B_{\rm int} \sim 10^{16}$ G. The strong internal field corresponds to a large energy reservoir $E_B \sim (\frac{4\pi}{3} R_{\rm NS}^3) \frac{B_{\rm int}^2}{8\pi} \sim 2\times10^{49} B_{\rm int,16}^2$ erg. This reservoir is primarily released via ambipolar diffusion on a characteristic timescale of roughly $t_{\rm amb} \sim 400\ B_{\rm int,16}^{-1.2}\ L_{\rm km}^{1.6}$ years, where $B_{\rm int}$ is normalized to 10^{16} G, and L in kilometers is the length scale of magnetic field fluctuations being dissipated in the core (Beloborodov and X. Li, 2016). The corresponding average luminosity is roughly

$$\dot{E}_{\rm mag} \sim \frac{E_B}{t_{\rm amb}} \sim 10^{39}\ B_{\rm int,16}^{3.2}\ L_{\rm km}^{-1.6}\ {\rm erg\ s^{-1}} \tag{4.15}$$

which scales sharply with the internal magnetic field, and should be able to power VT 1137-0337 (i.e., produce $\dot{E} = 10^{39} - 10^{41}$ erg s^{-1}) provided that $B_{\rm int} \gtrsim 10^{16}$ G.

The energy released by ambipolar diffusion should on average decline as a power law with time as the length scale L grows from small scales to the radius of the NS and the internal magnetic field decays (Beloborodov and X. Li, 2016). Though on

short timescales the energy may be released in discrete magnetar flares, these flares should combine to form a variable or intermittent wind which also gets decelerated in a termination shock and transfers its energy to particles in the nebula through wave heating (Beloborodov, 2017). The evolution of a magnetar wind nebula with a power law energy input $\dot{E}_{\rm mag} = \dot{E}_0(t/t_0)^{-\alpha_B}$ where the magnetar switches on at a time t_0 and injects relativistic electrons through its flares has been modeled semi-analytically by Ben Margalit and Brian D. Metzger (2018). They find that at an age of ∼decades, nearly all of the properties of the persistent radio source associated with the repeating fast radio burst FRB 121102 (including its radio luminosity, which is $\sim 10\times$ that of VT 1137-0337; S. Chatterjee et al., 2017) can be reproduced with $E_B \sim 5 \times 10^{50}$, $\alpha_B \sim 1.3$, and $t_0 \sim 0.2$ years. By changing the parameters slightly, they are able to scale the luminosity upwards or downwards by an order of magnitude, including to the luminosity of VT 1137-0337. At frequencies below the synchrotron cooling break, their model predicts that the nebula's lightcurve should decrease as $t^{-(\alpha_B^2+7\alpha_B-2)/4} \sim t^{-1.5}$ to t^{-4} for $\alpha_B = 1$ to 2. This range of fade rates is consistent with the range inferred for VT 1137-0337 for $t_{\rm age} \sim 20 - 80$ years.

These order-of-magnitude considerations suggest that the decay of a young magnetar's internal field is a plausible alternative to spindown for explaining VT 1137-0337's luminosity and lightcurve. If this is the case, then the field decay should be the nebula's primary power source in the present day, since NSs born with strong enough magnetic fields should have long since spun down. When normalized to a surface dipole field $B_d = 10^{15}$ G (a reasonable value for the strong required internal fields), the initial spindown time (Equation 4.10) becomes $\tau_0 \sim 14\ B_{d,15}^{-2}\ P_{10}^2$ hours. For a braking index $n = 3$, the age at which the spindown luminosity drops below the level required to power a radio luminosity L_R is roughly

$$t_{\rm brake} \sim \tau_0 + (1\ {\rm year})\ B_{d,15}^{-1} L_{38}^{-\frac{1}{2}} \left(\frac{\eta_R}{0.01}\right)^{\frac{1}{2}}, \tag{4.16}$$

where $L_{38} = L_R/10^{38}$ erg s^{-1}. For initial periods $P_0 \lesssim 300$ ms and $B_d = 10^{15}$ G, $t_{\rm brake} \lesssim$ years is much less than $t_{\rm age} \sim$ decades. If the initial period is much longer, the spindown luminosity never reaches the level required to power the nebula (Figure 4.11), and if n is closer to 2, spindown occurs even more rapidly.

At early times, the energy released by a magnetar's spindown could influence the expansion of the nebula and the luminosity of the supernova. If $B_d \sim 10^{15}$ G, a large fraction of the NS's rotational energy will have been released while the ejecta

is still coupled to the internal radiation via electron scattering. If the magnetar has an initial period $P_0 \sim$ a few to a few 10s of milliseconds, its rotational energy would be $\gtrsim 10^{50}$ erg, which is enough to power a superluminous supernova when released at this early time (Kasen and Bildsten, 2010). Such rapid rotation may be related to the generation of the strong fields (Raynaud et al., 2020), and due to the age of VT 1137-0337, such a luminous explosion is not ruled out by the lack of an archival supernova detection (Section 4.4). In this scenario, the radius of the nebula might be larger than expected for its age due to the additional energy imparted to the ejecta and the increase in $\dot{E}$ (Equation 4.8). If instead $P_0 \gtrsim 100$ ms, the total rotational energy would be closer to $\sim 10^{47} - 10^{48}$ erg. In this case, the early spindown luminosity (comparable to $\dot{E}_{\rm mag}$) would have a small effect on the initial expansion of the nebula, and a negligible effect on the supernova.

Comparison with FRB persistent sources

Much of the recent work on luminous magnetar wind nebulae has been done in the context of persistent radio sources (PRSs) associated with repeating fast radio bursts (FRBs), a connection that has recently been strengthened by the detection of a low-luminosity FRB from the Galactic magnetar SGR 1935+2154 (C. D. Bochenek et al., 2020; CHIME/FRB Collaboration et al., 2020). There are a number of observational similarities between VT 1137-0337 and PRSs. The two PRSs identified to date are associated with FRB 121102 (S. Chatterjee et al., 2017) and FRB 190520B (Niu et al., 2021). Both of the PRSs have have comparably flat spectral indices at frequencies of a few GHz and radio luminosities $\sim 10\times$ higher than that of VT 1137-0337 (Figure 4.5). Both PRSs are hosted by starbursting dwarf galaxies of stellar mass $\sim 10^8 - 10^9\ M_\odot$ and star formation rate $\sim 0.2 - 0.5\ M_\odot$/yr (Figure 4.6). These galaxies have specific star formation rates (SSFRs) comparable to the hosts of long GRBs and superluminous supernovae, but there is considerable overlap with the SSFRs of ordinary core collapse supernova hosts (Figure 4.6, Taggart and D. Perley, 2019). Neither PRS has thus far been observed to fade, but the measurement uncertainties for these faint sources ($\sim 250\mu$Jy at $\sim$1.5 GHz in both cases) do not preclude fading at the level that we have observed. Likewise, neither PRS has been observed to appear as a transient, but the lack of sufficiently deep reference epochs does not exclude this scenario. Some of the best available constraints come from the the NRAO VLA Sky Survey (NVSS), which gives 1.5 GHz 3σ upper limits at both PRS locations of $\sim$1.5 mJy roughly two decades before detection (J. J. Condon, Cotton, Greisen, et al., 1998), suggesting that the average fade rate of these sources

on ∼2 decade timescales is $\lesssim 10\%$ per year.

One feature of the FRB 121102 PRS not present in VT 1137-0337 is the break at ∼10 GHz where the spectrum steepens from $\sim \nu^{-0.2}$ to $\sim \nu^{-1.2}$ (S. Chatterjee et al., 2017). This break is confirmed by Chen, Ravi, and G. W. Hallinan (2022) who find a low variability amplitude at 15 and 22 GHz, suggesting that the break is intrinsic rather than a chromatic artifact of refractive scintillation. A potential break at the same frequency is unconstrained by currently available observations of FRB 190520B, which span 1 - 6 GHz (Niu et al., 2021). The origin of the FRB 121102 break is still somewhat unclear. The most straightforward explanation might be synchrotron cooling, which is generically expected to deplete high-energy electrons radiating at high frequencies where cooling is efficient, piling them up at a lower energy E_c and creating a spectral break at the corresponding cooling frequency ν_c. However, cooling of a single electron population predicts a steepening from $\alpha = (p-1)/2$ for $\nu < \nu_c$ to $p/2$ for $\nu > \nu_c$ for a difference $\Delta\alpha = 0.5$, less than the observed value $\Delta\alpha \sim 1$. One potential solution is if more electrons are injected at early times where the magnetic field is stronger and the cooling frequency lower. As discussed in Atoyan (1999), this would flatten the spectrum at frequencies lower than ν_c, thus alleviating the tension in $\Delta\alpha$. It is likely, however, that other solutions exist.

Regardless of the mechanism, if the break were caused by a cooling frequency, the lack of a detected break in VT 1137-0337 is unsurprising given its lower radio luminosity, which suggests an older age, a lower $\dot{E}$, or both. Either of these differences could lead to the cooling break ν_c being located at a higher frequency than the range we have observed. For electrons with age t and a nebula with field strength B_n, the cooling frequency scales as $\nu_c \propto t^{-2}\ B_n^{-3}$. In young nebulae, the weakening of the magnetic field (which is primarily driven by adiabatic cooling as the nebula expands) should be the dominant factor, causing the cooling frequency to rise rapidly with time. In the case of spindown, $B_n \propto t^{-1.3}$ to t^{-2}, so $\nu_c \propto t^{1.9}$ to t^4 (S. P. Reynolds and R. A. Chevalier, 1984). For a power law magnetic energy injection $\dot{E} \propto (t/t_0)^{-\alpha_B}$ and a nebula radius $R_n \propto \dot{E}^{1/5}\ t^{6/5}$ (Equation 4.8), integrating Equation 11 from Ben Margalit and Brian D. Metzger (2018) yields $B_n \propto t^{-(3\alpha_B+13)/10} \sim t^{-1.6}$ to t^{-2} for $t >> t_0$ and $\alpha_B = 1$ to 2. This leads to a similar evolution for the cooling break: $\nu_c \propto t^{2.8}$ to t^4. Even for the shallowest power laws, raising ν_c from 10 GHz to $\gtrsim$ 15 GHz (beyond our observing frequencies)

would only require that VT 1137-0337 is $\gtrsim$ 20% older than FRB 121102. For a fixed nebula age, the value of B_n could also be lowered by reducing $\dot{E}$, though this effect is weaker than that of aging. Roughly, $B_n \propto E_B^{1/2} R_n^{-3/2}$, where E_B is the magnetic energy in the nebula and the nebula radius is a weak function of $\dot{E}$, scaling as $R_n \propto \dot{E}^{1/5}$ (Equation 4.8). If we neglect the differential adiabatic cooling due to the slightly different expansion rate, $E_B \propto \dot{E}$ for fixed age. Altogether, this leads to $B_n \propto \dot{E}^{0.2}$, implying $\nu_c \propto \dot{E}^{-0.6}$. If we assume that a 10× smaller radio luminosity corresponds to a 10× lower $\dot{E}$, this would lead to a $\sim 4\times$ higher ν_c at the same age. This too would be enough to explain the lack of a cooling break at $\nu < 15$ GHz.

Overall, we find the two FRB persistent sources to be intriguing possible analogues for VT 1137-0337, given the theoretical connections to magnetar wind nebulae and the many observational similarities. However, a link between the two cannot be firmly established without the detection of associated FRBs. The best publicly available constraints come from the first CHIME data release, which does not report any detections consistent with VT 1137-0337 between July 2018 and July 2019 (The CHIME/FRB Collaboration et al., 2021). The lack of detections is not particularly constraining however, since VT 1137-0337 is located close to CHIME's southern declination limit ($-11°$) where their observations are likely not as sensitive and since our observations do not constrain the free-free opacity at CHIME's observing frequencies (400 - 800 MHz). From Figure 4 of The CHIME/FRB Collaboration et al. (2021), CHIME's total integration time at VT 1137-0337's location in the reported span was < 10 hours, and depending on the exact configuration of their synthesized beams, the actual effective integration time may have been much less. In the most tightly constrained scenario, this implies that VT 1137-0337 is not much more active than FRB 121102, which had one detection by CHIME in a total integration time of 11.3 hours (Josephy et al., 2019). It remains to be seen whether there are fast timescale bursts detectable from VT 1137-0337. We have started to monitor the source for bursts and will report on our results in a future paper.

4.7 Summary and Conclusions

We have discovered VT 1137-0337, a luminous, flat spectrum radio transient in a dwarf starburst galaxy at redshift z = 0.02764 with mass $\sim 10^{8.3} M_\odot$, star formation rate $\sim 0.5 M_\odot$ yr^{-1}, and metallicity $\sim 0.3 Z_\odot$. The transient source became detectable at radio frequencies some time between 1998 and 2018, brightening by >550% at 1.5 GHz. Between 2018 and 2022, it has faded at an average rate of ~5% per year

while maintaining a stable power-law spectrum $S_\nu \propto \nu^{-0.35}$ from $\sim$ 1 to 15 GHz (Sections 4.3, 4.4).

VT 1137-0337 is surrounded by massive young stars that have formed in the past few Myr, suggesting an association with the massive stars or their remnants. The lack of a self-absorption break in its synchrotron spectrum implies an emitting region larger than $\sim 10^{17}$ cm and causality requires an emitting region smaller than $\sim$ 6 pc. Its luminosity implies a magnetic energy similar to the shocks of radio-luminous supernovae. However, its flat spectrum and slow fading is unique among known radio transients of similar luminosity and cannot be explained by diffusive shock acceleration under standard conditions (Section 4.5).

We considered several possible origins for this transient (Section 4.6), summarized by the following:

- Shocks from stellar explosions such as supernovae and gamma ray bursts have not been observed to (and are generally not expected to) have a flat spectrum. In the absence of observational analogues or theoretical expectations for such transients, we consider this explanation to be unlikely.

- Jets launched from black holes can have flat spectra through the continuous superposition of synchrotron self-absorbed components. However, black holes of this radio luminosity are not typically expected to reside in galaxies of this mass, and there are no optical or X-ray indications of accretion onto a black hole. More importantly, the size scale implied by self-absorption is not consistent with the slow and steady fading that we have observed from 1-10 GHz over four years. We do not believe that a black hole jet is a likely explanation, though future observations including radio monitoring will provide important tests for this argument. In particular, stochastic behavior in the radio lightcurve (in excess of expectations for scintillation) or a change in the radio spectral index would reopen the case for an AGN, while continued slow and steady fading would further strengthen our arguments against this scenario.

- Pulsar wind nebulae are one of the only known source classes that are *expected* to have flat spectra and fade slowly. They will appear as radio transients once the surrounding supernova ejecta becomes optically thin to free-free

absorption. Though VT 1137-0337 is much more luminous than pulsar wind nebulae found in the Milky Way, all of its observed properties can be explained with the spin-down of a ∼decades old neutron star with a dipole field $B_d \sim 10^{13-14}$ G and a period $P \sim 10 - 100$ ms. Alternatively, VT 1137-0337 could be powered by the decay of internal magnetic fields in the core of a magnetar (possibly through discrete flares), provided that the internal field is stronger than $\sim 10^{16}$ G. We find a nebula powered by either spindown or field decay to be a reasonable explanation for VT 1137-0337.

- The two known persistent radio sources associated with repeating FRBs have similar radio luminosities, spectral indices and host galaxies to VT 1137-0337. Though FRB persistent sources have not previously been observed as transients, they have been theorized to be ∼decades old magnetar wind nebulae. If that were the case, they should have appeared as transients in the recent past. We consider these sources to be intriguing potential analogs to VT 1137-0337. This scenario can be tested by further monitoring for associated bursts.

Among the scenarios considered, we find that the most compelling explanations for VT 1137-0337 involve highly magnetized neutron stars at an age of $\sim$ 1 to 8 decades. In the case of a spindown-powered pulsar wind nebula, the surface dipole field is constrained by limits on the spindown luminosity and initial spindown time to be approximately $B_d \sim 10^{13-14}$ G. In the case of a nebula powered by magnetar field decay, the injected power scales sharply with $B_{\rm int}$, which should be stronger than $\sim 10^{16}$ G in order to power to the nebula.

Our results establish a general picture for VT 1137-0337, but leave open a rich set of questions for further observational and theoretical analysis. We list a few of these questions below:

- *Where are the breaks in the spectrum and how do they evolve with time?* Synchrotron spectra should generically turn over at a low frequency due to synchrotron self-absorption or free-free absorption, and should break at a high frequency due to synchrotron cooling. The self-absorption and cooling frequencies depend on the radius and magnetic field of the nebula, which in the case of young pulsar wind nebulae, are expected to evolve with time. Locating and tracking these breaks would provide important constraints on

the evolution of the nebula and even nondetections would strengthen the limits we have provided in Section 4.5 (e.g., Resmi, Vink, and Ishwara-Chandra, 2021).

- *What is the origin of the flat spectrum?* Much theoretical work has been done to explain the flat spectra of pulsar wind nebulae, though observational verification of these theories has proven challenging. Many of the theories are motivated by in-depth studies of the Crab Nebula made possible by multi-wavelength, spatially resolved observations. VT 1137-0337 presents an opportunity to probe a very different region of the pulsar wind nebula parameter space. In particular, theories involving electrons injected at early times (e.g., Atoyan, 1999) may be constrained by measurements of the nebula's evolution.

- *Are there associated FRBs or other bursts?* Neutron stars produce a wide range of potentially related bursts, including Crab giant pulses (e.g., Bera and Chengalur, 2019), X-ray bursts (e.g., Tavani et al., 2021), and fast radio bursts (e.g., C. D. Bochenek et al., 2020). Most of these burst types are associated with field-decay powered magnetars, though the line between these sources and the most strongly magnetized spindown powered pulsars is somewhat fuzzy (e.g., Gavriil et al., 2008). Since VT 1137-0337 has an inferred field in the range of strongly magnetized pulsars to full magnetars, it will be particularly interesting to monitor the source for bursts. In particular, the particles injected by bursts may be important in providing the number of relativistic particles required to produce the high radio luminosity we observe (e.g., Beloborodov, 2017).

- *What can VT 1137-0337 teach us about the population of young pulsar wind nebulae as a whole?* In our effective survey volume (Section 4.3), there should be $\sim 10^2 - 10^3$ young neutron stars born per year, of which at least $\sim 10\%$ should be magnetars (e.g., Beniamini et al., 2019). Our detection of only 1 likely pulsar wind nebula in observations spanning 20 years implies that the vast majority of young neutron stars (including magnetars) either produce nebulae that are much less luminous, or do not produce nebulae at all. An even larger gap in rates is inferred for FRB persistent sources by Casey J. Law, Connor, and Aggarwal (2022). Understanding the selection factors that lead to luminous pulsar wind nebula will help interpret future searches for extragalactic nebulae and, if FRB persistent sources are truly magnetar wind

nebulae, may help reveal why some repeating FRBs have luminous persistent sources (S. Chatterjee et al., 2017; Niu et al., 2021) while others do not (e.g., Kirsten et al., 2022).

We conclude with a few thoughts on the selection factors leading to radio-luminous nebulae. In both field-decay and spindown powered scenarios, we find that a flux-limited survey such as VLASS may biased towards neutron stars that are particularly strongly magnetized, though detailed verification requires population synthesis, further transient searches, and theoretical modeling beyond the scope of this paper.

In Galactic magnetars, the typical timescale of field decay is $\sim 10^4$ years (Beniamini et al., 2019) rather than the fiducial few $\times\, 10^2$ years we considered in Section 4.6. These longer decay times translate to weaker internal fields B_{int}, lower averages rates of energy release $\dot{E}$ and, for fixed values of $\eta_R \equiv L_R/\dot{E}$, lower average radio luminosities L_R. Since for our fiducial parameters, $\dot{E}$ is already close to the minimum value for VT 1137-0337 of $\sim 10^{39}$ erg s^{-1} when $B_{int} = 10^{16}$ G, we may only be sensitive to the highest values of $\dot{E}$, corresponding to strong internal fields. This tracks with the lack of radio-detected magnetar wind nebulae in the Milky Way (the strongest candidate for such a nebula is a faint X-ray source not detected in the radio; Younes et al., 2016). Detailed modeling beyond our order-of-magnitude estimates is required to draw firm conclusions, however.

For spindown-powered pulsars, Galactic sources that can be age-dated with associated supernova remnants have initial periods P_0 and dipole fields B_0 drawn from log-normal distributions centered at $P_0 \sim 100$ ms with a scatter of ~ 0.5 dex and $B_0 \sim 10^{12.4}$ G with a scatter of ~ 0.4 dex (Igoshev et al., 2022). By running a Monte Carlo simulation where we assume a volumetrically uniform distance distribution $dN/dr \propto r^3$ and neglect any covariance between B_0 and P_0, we find that the median peak flux due to spindown of these neutron stars is $L_R \sim 6 \times 10^{-4}\ (\eta_R/10^{-2})$ mJy, roughly 1000 times fainter than we can detect. Due to the sharp scaling of $\dot{E}$ with P_0 however, a substantial tail of the distribution ($\sim 8\%$ of nebulae for $\eta_R = 10^{-2}$ or $\sim 3.5\%$ for $\eta_R = 10^{-3}$) should be brighter at peak than ~ 1 mJy and would be detectable by our search. The requirement for nebulae to still be luminous at the time of emergence from free-free absorption shrinks this tail by only a small factor due to the slow spindown from ordinary pulsar-like dipole fields (a median value of $10^{12.7}$ G in the tail). At an age of ~ 40 years, roughly 80% in the tail will still

be brighter than 1 mJy, dropping to 30% after 200 years. Altogether, the combined requirements of youth and escape from free-free absorption downselects the pulsar population by a factor of $\sim 100\times$, leaving us with a further factor of $\sim 10-100\times$ to account for our detection rate.

This can be accomplished if VT 1137-0337's unusually strong dipole field is a selected-for feature rather than a fluke. In the bright tail, only ~30% of neutron stars have dipole fields stronger than 1×10^{13} G, roughly the minimum field strength inferred for VT 1137-0337. The fraction drops to 10% above 2×10^{13} G, and to only 1% above 5×10^{13} G, which is in the middle of the inferred range for spindown. Thus, if a field strength of a few $\times\ 10^{13}$ G is required to produce a nebula as luminous as VT 1137-0337, that could plausibly explain our detection rate. As with magnetars, further analysis is required to draw a firm conclusion.

It is interesting to note that at a dipole field strength of $\sim10^{13.5}$ G, the distinction between spindown powered pulsars and field-decay powered magnetars becomes blurred, with each population displaying features of the other (e.g., Gavriil et al., 2008; Kaspi and Beloborodov, 2017). If magnetar-like flares are required to populate the radio electron population and a large energy input from spindown (or decay of an unusually strong internal field) is required to power those electrons, the highest radio luminosity tail of young pulsar wind nebulae may be populated by unusually magnetized neutron stars. Future detections of flat spectrum radio transients in surveys such as the remaining epochs of VLASS (Lacy et al., 2020), ASKAP/VAST (T. Murphy, Kaplan, et al., 2021), LOTSS (Shimwell et al., 2017), or the DSA-2000 (Gregg Hallinan et al., 2019) will provide a test of this hypothesis.

Appendix

4.8 Appendix: Free-free Emission

Here we show that VT 1137-0337's combination of high luminosity and human-timescale variability cannot be explained by free-free emission, as claimed in Section 4.5. Let us consider the implications of having a substantial fraction of the observed luminosity be due to free-free emission. For simplicity, we assume that the source of the free-free emission is a sphere of ionized gas with a radius R, temperature T, and density n_e. We denote the frequency where the optical depth to free-free absorption equals 1 as ν_{ff} and the thermal fraction (i.e., the fraction of the flux at

ν_{ff} due to free-free emission) as f_{th}. The flux $S_{\nu_{ff}}$ due to free-free emission at frequency ν_{ff} can then be expressed in two ways:

$$S_{\nu_{ff}} \approx 2 \text{ mJy} \left(\frac{\nu_{ff}}{\text{GHz}}\right)^{-0.35} \left(\frac{f_{th}}{1.0}\right), \tag{4.17}$$

from the observed spectrum discussed in Section 4.4 and

$$S_{\nu_{ff}} \approx \frac{2\nu_{ff}^2 kT}{c^2} \pi \left(\frac{R}{120 \text{ Mpc}}\right)^2, \tag{4.18}$$

since at $\tau = 1$ the thermal free-free emission is close to being optically thick.

From the variability timescale and observed spectrum, we have constraints on R and ν_{ff}. Taking the $\Delta t \sim 20$ year span between nondetection at 1.5 GHz in FIRST and and our first follow-up epoch to be an upper limit on the rise time of the transient, we have a maximum length scale for the region responsible for the excess emission of $R < c\Delta t = 6.1$pc. The nondetection in Epoch 1 of any spectral break between ~1-12 GHz and the falling spectrum in that range (Figure 4.3) implies that we are observing the optically thin part of the spectrum and thus that $\nu_{ff} < 1$ GHz.

Combining Equations 4.17 and 4.18, we have

$$T = 8 \times 10^6 \left(\frac{\nu_{ff}}{\text{GHz}}\right)^{-2.35} \left(\frac{R}{6.1 \text{ pc}}\right)^{-2} \left(\frac{f_{th}}{1.0}\right) \text{K}, \tag{4.19}$$

which together with the constraints on R and ν_{ff} indicates a minimum temperature of $\sim 8 \times 10^6$ f_{th} K. If f_{th} is ~1, the corresponding lower bound is extreme for a region emitting radio free-free emission. Moreover, it is likely a substantial underestimate when considering the range of reasonable radii. For instance, a constant velocity blast wave of 10,000 km/s would reach $R \sim 6 \times 10^{17}$ cm in 20 years, and would thus require a temperature $\gtrsim 8 \times 10^9$ K.

We can further highlight the problem of extremes by considering the required density and energy within the emitting region. The density can be constrained from the free-free opacity (James J. Condon and Ransom, 2016b) which, for our constant density sphere of radius R, is approximately

$$\tau \approx 0.082 \left(\frac{T}{K}\right)^{-1.35} \left(\frac{\nu}{\mathrm{GHz}}\right)^{-2.1} \left(\frac{n_e}{\mathrm{cm}^{-3}}\right)^{2} \left(\frac{R}{\mathrm{pc}}\right). \tag{4.20}$$

By definition, $\tau = 1$ at ν_{ff}, so we can combine equations 4.19 and 4.20 to get:

$$n_e = 6.5 \times 10^4 \left(\frac{\nu_{ff}}{\mathrm{GHz}}\right)^{-0.54} \left(\frac{R}{6.1\ \mathrm{pc}}\right)^{-1.85} \left(\frac{f_{th}}{1.0}\right)^{0.68} \mathrm{cm}^{-3}. \tag{4.21}$$

Again if $f_{th} >> 0$, this density is substantially higher than then $\sim 10^2$ cm^{-3} inferred for the surrounding star-forming region (Section 4.5), and would thus require an unusual environment or a significant pre-explosion deposition of mass from the source of the transient. It is also likely underestimated by a similar factor to the temperature, given the similar scaling with R. These issues come together when considering the thermal energy required for the radiating plasma:

$$U = \frac{3}{2}\left(\frac{4}{3}\pi R^3\right) nkT. \tag{4.22}$$

Folding in equations 4.19 and 4.21, we get

$$U = 3 \times 10^{54} \left(\frac{\nu_{ff}}{\mathrm{GHz}}\right)^{-2.9} \left(\frac{R}{6.1\ \mathrm{pc}}\right)^{-0.85} \left(\frac{f_{th}}{1.0}\right)^{1.68} \mathrm{erg}. \tag{4.23}$$

If there is any substantial thermal fraction, the implied lower limit on the energy is orders of magnitude beyond what can be deposited by e.g. a supernova, tidal disruption event, or black hole flare. For scale, the minimum energy would require a black hole of ~20% the stellar mass of the galaxy to be emitting at its Eddington luminosity for 20 years. Varying the assumptions (e.g. a nonspherical geometry, or a non constant temperature and density) does not help by much. Considering that the emission appeared within a dwarf galaxy on the timescale of ~20 years, we conclude that free-free emission is not a reasonable explanation for VT 1137-0337.

4.9 Appendix: Literature Transients and Flat Spectrum Sources

Here we give the luminosities, spectral indices, and references for the points plotted in Figure 4.5. Due to the evolving nature of supernovae, gamma ray bursts and tidal disruption events, the luminosities for sources in those classes are approximate values, valid at *some* point in the evolution of the transient. We have made an effort to choose luminosities at late times where the transient is optically thin at 3 GHz.

Where possible, we use spectral indices that are directly fit from standard peaked SED models. For spectral indices derived from measurements in two bands, we use values from late epochs after the peak has dropped to frequencies below the two bands and the spectral index has converged to its optically thin value.

Fast radio burst persistent sources:

- **PRS/FRB 121102:** From a fit of the the 1 - 10 GHz observations in S. Chatterjee et al. (2017), we estimate a low-frequency spectral index of $\alpha \sim 0.2$. There is evidence of a break at ∼10 GHz, with a spectral index of $\alpha \sim 1.2$ toward higher frequencies. The 3 GHz luminosity is $L_{3\mathrm{GHz}} = 2.3 \times 10^{29}$ erg s^{-1} Hz^{-1} at the redshift reported in Tendulkar et al. (2017).
- **PRS/FRB 190520B:** The spectral index and luminosity come from the values reported in Niu et al. (2021): $\alpha = 0.41 \pm 0.04$ and $L_{3\mathrm{GHz}} = 3 \times 10^{29}$ erg s^{-1} Hz^{-1}.

Gamma ray bursts:

- **GRB 030329:** Our plotted spectral index $\alpha \sim 0.55$ comes from the report in A. J. van der Horst et al. (2007) that $p = 2.1$, though we note that Figure 1 of Granot and Alexander J. van der Horst (2014) suggests a value closer to $\alpha = 0.7$. This GRB has many observations over a span of years. In the figure, we plot a value of $\sim 2 \times 10^{30}$ erg s^{-1} Hz^{-1} in between the 4.8 and 2.3 GHz temporal peaks.
- **GW 170817:** The spectral index $\alpha \approx 0.6$ comes from the fit in Mooley, E. Nakar, et al. (2018), and the luminosity ($\sim 9 \times 10^{25}$ erg s^{-1} Hz^{-1}) comes from their brightest reported 3 GHz data point.
- **GRB 980703:** We estimate a spectral index of $\alpha \sim 0.6$ from the late-time data points plotted in Fig 1 of Granot and Alexander J. van der Horst (2014). The 5 GHz luminosity at the point where the spectral index plateaus is roughly 4 $\times 10^{29}$ erg s Hz^{-1}.

Radio supernovae:

- **SN 1978K:** The spectral index $\alpha = 0.8$ and luminosity 1×10^{27} erg s^{-1} Hz^{-1} are from the 1992.5 epoch in Table 5 of Ryder et al. (1993).

- **SN 1979C:** The spectral index $\alpha = 0.7$ and luminosity 2×10^{27} erg s^{-1} Hz^{-1} are from Table 3 of Kurt W. Weiler, van Dyk, et al. (1991).
- **SN 1983N:** The plotted optically thin spectral index $\alpha = 1.1$ and luminosity 3×10^{25} erg s Hz^{-1} are from Table 8 of K. W. Weiler et al. (1986).
- **SN 1984L:** The spectral index $\alpha = 1.2$ and luminosity 7×10^{25} erg s^{-1} Hz^{-1} are from the Nov 30. 1984 epoch reported in N. Panagia, R. A. Sramek, and K. W. Weiler (1986).
- **SN 1986J:** The spectral index is from the report in Kurt W. Weiler, Nino Panagia, and Richard A. Sramek (1990) that $\alpha = 0.7 \pm 0.1$ from 6 to 2 cm and the luminosity $\sim 5 \times 10^{27}$ erg s^{-1} Hz^{-1} is from Table 5.
- **SN 1987A:** The plotted spectral index $\alpha = 0.9$ is from the report in Manchester, B. M. Gaensler, et al. (2002) that the spectral index has changed from 0.97 to 0.88 and the luminosity $\sim 2 \times 10^{23}$ erg s Hz^{-1} is estimated from their Figure 1.
- **SN 1988Z:** The spectral index $\alpha = 0.74 \pm 0.5$ and luminosity $\sim 2 \times 10^{28}$ erg s Hz^{-1} are from Tables 1 and 2 of van Dyk, Kurt W. Weiler, Richard A. Sramek, and Nino Panagia (1993).
- **SN 1990B:** The spectral index $\alpha = 0.9$ and luminosity 3×10^{26} erg s^{-1} Hz^{-1} are from the Apr 26, 1990 epoch reported in van Dyk, Richard A. Sramek, et al. (1993).
- **SN 1993J:** The spectral index $\alpha \sim -0.99$ is from Table 1 of van Dyk, Kurt W. Weiler, Richard A. Sramek, Rupen, et al. (1994) and the luminosity $\sim 8 \times 10^{26}$ erg s Hz^{-1} is estimated from their Figure 1.
- **SN 1998bw:** The plotted spectral index $\alpha = 0.7$ and luminosity 4×10^{27} erg s Hz^{-1} come from observations presented in Z.-Y. Li and Roger A. Chevalier (1999) at a late epoch where the radio SED is optically thin.
- **SN 2009bb:** The spectral index and luminosity come from Soderberg, Chakraborti, et al. (2010), who report $\alpha \sim 1$ and $S_{3\mathrm{GHz}} \sim 15$ mJy on day 52, corresponding to $L_{3\mathrm{GHz}} \sim 3 \times 10^{28}$ erg s^{-1} Hz^{-1}.
- **PTF 11qcj:** The spectral index ($\alpha \sim 1.1$) and luminosity ($L_{3\mathrm{GHz}} \sim 2 \times 10^{29}$ erg s^{-1} Hz^{-1}) come from the most recent broadband radio spectrum (at day 1887) reported in Palliyaguru et al. (2019).

- **VT 1210+4956:** The spectral index $\alpha = 1.04 \pm 0.02$ and 3 GHz luminosity 1.3×10^{29} erg s Hz^{-1} come from the May 30, 2018 followup epoch in D. Z. Dong et al. (2021).

Tidal disruption events:

- **Sw J1644+57:** We use the report in Eftekhari, E. Berger, Zauderer, et al. (2018) that on day 651, the 3.4 GHz flux was 8.78 mJy, corresponding to $L_\nu = 4 \times 10^{31}$ erg s Hz^{-1}. The optically thin slope at this epoch is consistent with $p = 2.5$, corresponding to $\alpha = 0.75$.

- **IGR 12580+0134:** We use the combined jet model from Perlman et al. (2017), which predicts $p = 2.7$, corresponding to $\alpha = 0.85$. Extrapolating from their 5GHz flux using this spectral index gives a 3 GHz flux of 46 mJy in the 2015 Oct 8 epoch, corresponding to 1.6×10^{28} erg s Hz^{-1}.

- **AT 2019dsg:** The spectral model from Stein et al. (2021) predicts $p = 2.9 \pm 0.1$, corresponding to $\alpha = 0.95 \pm 0.05$, consistent with results in Y. Cendes et al. (2021). On day 178, the 3.24 GHz flux was 0.92 ± 0.08 mJy, corresponding to a luminosity of 5.8×10^{28} erg s Hz^{-1}.

- **Arp 299-B AT1:** We use the spectral model from S. Mattila et al. (2018). Their modeling (Table S8) indicates that p = 3.0 for the jet, corresponding to $\alpha = 1$. From their Table S4, we adopt 3mJy as a representative flux at 3GHz, corresponding to 7×10^{27} erg s Hz^{-1}.

- **CNSS J0019+00:** Spectral fitting in M. M. Anderson et al. (2019) indicates that during the 2015 Oct 15 epoch, the 2.9 GHz flux was 7.25 mJy, corresponding to 5.2×10^{28} erg s Hz^{-1} and the optically thin spectral index was $\alpha = 1.1$.

- **ASASSN 14li:** From modeling in K. D. Alexander, E. Berger, et al. (2016), the transient component in the 2015 June epoch was ~ 0.9 mJy, corresponding to 9×10^{27} erg s Hz^{-1} and the spectral index was $\alpha \sim 1$.

- **XMMSL1 J0740-85:** From K. D. Alexander, Wieringa, et al. (2017), the 2.7 GHz emission was 0.87 mJy at peak, corresponding to 6×10^{27} erg s Hz^{-1}. They find a best fit spectral index of $\alpha = 0.7 \pm 0.1$.

- **VT J1548+2208:** Somalwar, Ravi, D. Dong, et al. (2021) observe a 3 GHz flux of ~ 3 mJy, corresponding to $\sim 7 \times 10^{28}$ erg s Hz^{-1}. We use the spectral index of the high frequency component: $\alpha = 1.1$.

- **FIRST J1533+2727:** This TDE was discovered at a late time where the spectrum is optically thin at all observed frequencies. From Table 1 in Ravi et al. (2021), we calculate a spectral index of $\alpha = 0.84$. At this late time, the 3 GHz luminosity is $\sim 5 \times 10^{27}$ erg s Hz^{-1}.

Pulsar wind nebulae:

The spectral indices and luminosities of plotted PWNe are from the Green (2019) pulsar wind nebula and supernova remnant catalog. We selected every source classified as a PWN with a measured distance, flux, and spectral index. They are: the Crab Nebula, 3C58, Vela X, G284.3-1.8, G292.2-0.5, G292.0+1.8, G308.8-0.1, G320.4-1.2, G341.2+0.9, G343.1-2.3, G5.4-1.2, G11.2-0.3, G21.5-0.9, G29.7-0.3, G34.7-0.4, G54.1+0.3, and G69.0+2.7.

Chapter 5

EXPANDING THE SEARCH FOR SLOW RADIO TRANSIENTS TO THE ENTIRE NORTHERN SKY

5.1 Other samples

All of the science described above was done with a sample of 64 transients identified in spectroscopically verified galaxies within 200 Mpc using only data within the FIRST footprint. The number of qualifiers in that description suggests that there is much more science to be done when those qualifiers are relaxed.

A subset of that work has been done by my collaborator Kristina Nyland, who wrote a paper on a sample of VLASS vs FIRST transients I identified that are associated with quasars (Nyland, Dillon Z. Dong, et al., 2020). Due to their much higher redshifts, they have much higher luminosities than the AGN flares identified in Chapter 2. As such, they are more likely to be new jets being launched, as was the conclusion in her paper.

I also conducted a search for transients in VLASS relative to the NRAO VLA Sky Survey (NVSS; J. J. Condon, Cotton, Greisen, et al., 1998), which is a 1.4 GHz survey contemporaneous with FIRST taken in the VLA's D configuration. NVSS's resolution (~40") is significantly mismatched with VLASS and it has a much worse sensitivity (a RMS of ~500μJy). However, it does cover the entire sky, including the Galactic plane which FIRST avoids. The transients identifiable in that search are too bright in VLASS to be explainable by a rising spectral index. One nuclear transient was recently published as a candidate jetted TDE (Somalwar, Ravi, Dillon Z. Dong, et al., 2022). Others are likely Galactic and are the subject of ongoing work within the Caltech radio group (Miller et al. in prep).

Though there is more to be said about the VLASS vs FIRST and VLASS vs NVSS samples, here I focus on initial results from the sample of transients that VLASS was intended to search for: sources that are present in one epoch but not in another. I identified the first batch of these transients with a modified version of the pipeline from Chapter 2. This pipeline is described below.

5.2 Identification of transients and variables in VLASS Epoch 2 vs Epoch 1

As of the writing of this thesis, two full epochs of VLASS have been observed. Epoch 1 was obseved from 2017-2019, and Epoch 2 was observed from 2020-2022. Each epoch spans ∼34,000 deg^2. Thus far, I have only run a search for Epoch 2 sources not present in Epoch 1. However, my pipeline can be run equally well in the opposite direction to look for disappearing transients, and I have plans to do this in the near future. This work will be done in collaboration with members of the VLASS Survey Science Group and their students toward the goal of releasing a catalog paper of Epoch 2 vs Epoch 1 transients in both directions.

My approach to identifying transients between VLASS epochs is to first find where the sources are in each epoch using a source extractor, and then quantify the level of variability at those locations using forced photometry. The reason why I do it this way instead of simply running a catalog cross match (as is commonly done in the literature) is to get a measure of variability that transitions smoothly from nondetections to faint sub-threshold detections to significant detections. This is akin to what I did to remove faint sub-threshold FIRST sources in the 200 Mpc search.

To find the sources, I ran PyBDSF on the Epoch 2 images with the same settings used in the 200 Mpc search (5σ peak pixel threshold, 3σ island threshold). Then, at the RA and Dec of each Epoch 2 source candidate, I take a 5x5 box of pixels in the corresponding Epoch 1 image. I then take the maximum pixel value in that box to be an estimator of the Epoch 1 flux[1]. I use the 5x5 box in order to guarantee that any underlying source will be accounted for even in the presence of astrometric errors (which at times can be ∼1" in the quicklook images prior to correction of systematics, compared to the 1" pixel size used in VLASS quicklook images). This will likely be tightened to a 3x3 box in the final version of the transient catalog, which will use astrometrically corrected images which should have an astrometric uncertainty closer to 0.5".

The 5x5 box photometry scheme introduces some systematics when there is no clearly detected source in the box. Whereas the flux value for one pixel is well described by a Gaussian, the maximum value over 25 pixels is not, particularly if there is also a faint underlying source. To account for this, I ran a set of Monte Carlo

[1]The units of flux in radio images are Jy per beam, so for point sources which by definition span 1 beam, the peak pixel value is exactly equivalent to its integrated flux.

simulations where I injected noise on top of simulated Gaussian sources of varying fluxes. By running 5x5 box photometry on these simulated sources, I generated expected distributions for the maximum pixel value as a function of intrinsic source brightness. Then, I used these results to calculate the distribution of underlying source fluxes given a measured pixel value. The 16th, 50th, and 84th percentile values of the intrinsic source flux distributions are then saved as a lookup table. For each measured pixel value in Epoch 1, I report the medians as the estimated Epoch 1 flux, and the 50th-16th and 84th-50th percentile values as the lower and upper uncertainties. In addition to measuring the 5x5 flux in Epoch 1, I do the same measurement in the Epoch 2 image. With these results, I can then estimate the probability that the Epoch 1 and Epoch 2 fluxes are different from each other, given the local noise, the overall signal-to-noise ratio, the difference between 5x5 box fluxes, and an estimate of the systematic fluxscale offset from the measured ratio of high signal-to-noise nearby point sources. This probability of variability is then used to find sources that are likely to be variable. In addition to the box photometry process, I also consider the pixels in a much larger box, 1 arcminute in diameter. I apply the same automated artifact filters for near and far sidelobes described in Chapter 2. Any sources that do not pass these filters are flagged for removal from the sample.

More careful statistical analysis is required to assemble a sample of variable sources with well-quantified levels of false positives and false negatives. However, for transients, most of the results can be obtained using just the quantities described above by applying some simple cuts. If I require that (1) the Epoch 2 flux is $> 7\sigma$, (2) the Epoch 1 flux is $< 3\sigma$, (3) the probability of variability is $> 90\%$, and (4) the transient candidate passes both artifact filters, I am left with a sample of 2883 strong candidates for transients appearing between Epoch 1 and Epoch 2. Visual inspection of this sample confirms that the rate of artifacts is low; roughly a few percent. There is some contamination from faint variable sources that were sub-threshold in Epoch 1 but present in Epoch 2. Based on initial visual inspection, the number of actual transients (with no discernible evidence for emission in Epoch 1) is closer to ~2000. Regardless of the precise number, this sample increases the number of known slow radio transients from $O(10^2)$ to $O(10^3)$.

Interesting science can be done with variable sources as well, especially if they are transients on top of quiescent emission. More careful analysis is again required, but preliminary results are that if I remove the requirement that the Epoch 1 flux is

$< 3\sigma$, I arrive at a catalog with ∼50,000 sources with variability not consistent with measurement error.

5.3 A rough blueprint for identifying the origin of the transient and variable radio sources

With this new abundance of radio transients and variables, the next step is to identify their origins. There is a substantial amount of ongoing work being done in this regard, adapting and improving upon the themes and techniques discussed in previous chapters. The specific process is different for each science case, but below, I outline some general considerations.

Given a directly detected slow radio transient or variable source in VLASS, there are several immediately available clues. From the detection and reference epochs, you can measure the source's location, time of detection, flux at detection, level of variability, and a loose constraint on the timescale of variability from the separation between epochs. For bright sources, with some additional data processing, it is possible to get information on the polarization and spectral shape within the band, and to split up the 5 second integration into 0.5 second chunks. With further time on the VLA and other radio telescopes, it is often straightforward to obtain one or more radio spectra of the source, given that any source bright enough to be detected in VLASS should be easily detectable in a follow-up observation[2]. As see in Chapters 2 and 3, it is sometimes possible to detect multi-wavelength counterparts in follow-up observations (e.g., with Keck spectroscopy).

Of these clues, the lowest hanging fruit is the location of the transient. At every point in the sky, there is a wealth of data from modern surveys spanning the entire electromagnetic spectrum from MHz radio to gamma rays. There are also an increasing number of time-domain surveys at optical, infrared, X-ray, and gamma-ray wavelengths, as well as in neutrinos and gravitational waves. Given all of these surveys, there are many opportunities to look for multiwavelength or multimessenger associations. Doing so requires some care to avoid false positives. In particular, as we have seen in the preceeding chapters, there may be a long delay (∼years) between transient activity at other wavelengths and the time that a radio transient first becomes detectable at 3 GHz. Associations based on coincidence in time (which are

[2]Note that this is not the case for most stellar transients, which are inherently on very short timescales.

the standard for associating optical transients with multi-wavelength counterparts) are more difficult for transient classes with delays, and require some detailed modeling in order to make a reasonably strong case. On the other hand, the relatively low numbers of radio transients overall (as compared to optical transients) and the high accuracy to which they can be localized makes it so that spatial coincidence alone can be sufficient to establish association (especially when the class of objects being associated is also rare). For many types of single-object spatial-only associations, you can reasonably expect false alarm probabilities of order $\sim 10^{-4} - 10^{-3}$. This type of analysis is also strengthened when working in the realm of samples instead of single objects. Though I estimated that there are ~5 residual background false positives out of 21 in the off-nuclear transients in the 200 Mpc sample, that level of contamination does not qualitatively change the conclusions, and simply lowers the rate by a small amount.

Given the large increase in the overall number of slow radio transients provided by the Epoch 2 vs Epoch 1 sample and the unique way in which they have been selected, there is much to be learned by simply establishing the demographics of sources in this sample. At this stage, any multiwavelength association (either with a transient or with persistent objects such as stars, galaxies, and quasars) can be the basis of a useful paper. Current sub-samples that are being analyzed by other members of the Caltech radio group include: (1) TDE candidates identified either by association with optical/infrared transient counterparts or as nuclear radio flares from quiescent galaxies, led by Jean Somalwar, (2) transients associated with Gaia stars led by my undergraduate student Carlos Ayala, (3) highly variable Galactic transients led by Jessie Miller, and (4) stellar radio transients associated with TESS superflares led by Ivey Davis.

Once multi-wavelength counterparts are established, all of the observational properties of those objects become further contextual clues that can be used in identifying and characterizing the radio transient. Objects with distances (e.g., galaxies with redshifts, and Galactic objects with parallaxes) turn the measured fluxes to luminosities. Where radio SEDs can be measured, those luminosities can be used alongside the standard synchrotron analysis (Chapter 3) to establish properties of the emitting region. This in turn can provide information about the mechanism responsible for the radio transient. Even “hostless" sources with faint or no multi-wavelength counterparts can be analyzed as a subsample of their own. Roughly 1/3 of the 2000

transients have no apparent counterparts in Panstarrs imaging (at a typical depth of 23rd magnitude in most optical bands). The fraction shrinks when looking at deeper images from the Dark Energy Camera Legacy Survey (which reaches a depth of g = 24.9). Initial Keck/MOSFIRE follow-up has shown that some of the remaining sources have faint infrared counterparts and may be highly obscured, intrinsically very red, or both.

The contextual clues described above are just a few of the possible means by which this new sample of radio transients can be diagnosed. Through the use of these clues (or ones that we have yet to identify), there may be even more new populations of transients waiting to be discovered. The increasing quality and quantity of clues from next-generation multi-wavelength surveys will accelerate this process of discovery. I discuss some of the new possibilities in the Conclusions section below.

Chapter 6

CONCLUSIONS AND NEXT DIRECTIONS

6.1 Summary

In this thesis, I have presented results from the first successful use of radio surveys to directly detect slow radio transients at scale. The 200-Mpc extragalactic transient sample (Chapter 2) represents a significant fraction of the total number of slow radio transients published to date, and has roughly doubled the number that were detected directly in previous radio surveys. With the sample size afforded by this search, we are now able to constrain the rates of slow radio transients in a way that is unbiased by the presence of optical counterparts. The sample identified in Epoch 2 vs Epoch 1 (Chapter 5) has increased the number of directly detected non-FRB radio transients by a further factor of $\sim 30\times$.

The transients found in these samples are different in nature than typical transients identified in previous searches (particularly from targeted follow-up observations). Instead of relativistic jets, which were commonly assumed to dominate the population of the most luminous radio transients, the transients in the 200 Mpc sample are produced by slower outflows shocking dense gas at a radial scale that is often inaccessible in non radio observations. Where there is sufficiently constraining data, there is evidence that the dense gas has an aspherical geometry. Further observations and modeling of these transients and ones that are continually being found will help reveal the structure of this gas and shed light on its origin.

One of the main themes in my thesis is that even though slow radio transients typically appear long after most other transient emission has faded, there can still be a wealth of contextual clues that can be used to conduct in-depth studies of individual transients or sub-samples. These clues can be found in many places including catalogs of archival transients, observations of host galaxies, and multi-wavelength follow-up observations at the locations of the transients. Because the available clues are heterogeneous, it is often necessary to use techniques and theory from multiple astrophysical fields to tie them together into a coherent picture.

Using such clues, I conducted deep-dive investigations into two transients: VT

1210+4956 (Chapter 3), and VT 1137-0337 (Chapter 4). In the case of VT 1210+4956, the duration and luminosity of the associated X-ray transient MAXI 140814A confirmed expectations for the launch of a relativistic jet at the time of explosion. But the shape and evolution of the transient's radio spectrum, and the intermediate width Hα feature in its nebular optical spectrum, indicated that 3 years after the explosion, the luminous radio emission is not actually due to the jet. Instead the radio emission detected in VLASS was produced by a powerful and slow-moving shock interacting with aspherical circumstellar gas. The most natural explanation for the scale and asymmetry of this gas is binary-driven mass loss occurring a few centuries before explosion. But given binary population synthesis models, coincidental interaction is unlikely at such a short delay before explosion. Additionally, there was no clear reason why such a rare coincidence would also happen in an explosion that launched a jet (also a rare phenomenon). This led me toward the conclusion that both the binary-driven mass loss and the jet have a common origin: the merger of a compact object and a massive star. This scenario had previously been predicted (Roger A. Chevalier, 2012), and of the models in the literature, is the only one that ties together all of the observables.

Though VT 1210+4956 is only one object, it does raise the question of whether merger-driven explosions are the reason behind aspherical mass loss at the $\sim 10^{17}$ cm scale that VLASS is selecting for, or whether there is a better alternate explanation. Testing this hypothesis will require the identification of more such events. We are making some progress on this front by finding multiple examples of stellar explosions interacting with asymmetric circumstellar gas (Chapter 2). Given that the high-energy emission from jets is only visible from a small angle, we will either need a large sample with relatively uniform coverage in X-ray surveys, or an alternate indicator of jets in these asymmetric CSM interactors. Such an indicator could come from faster timescale searches for radio transients which could detect the early fast signature of a jet regardless of the angle at which it is launched. Alternatively, searches for "orphan afterglows" in optical surveys may provide the first constraints given the rapid and deep coverage of large areas of the sky expected from LSST. Regardless of the answer, there is much left to be learned about the origin of asymmetric circumstellar gas in stellar explosions, and direct detection in radio surveys is one of the best ways to identify such events.

VT 1137-0337 was an example of what can be done with well-calibrated wide-

bandwidth radio data and order-of-magnitude theory. Its flat spectrum $S_\nu \propto \nu^{-0.35\pm0.02}$, implies an energy distribution $dN/dE \propto E^{-1.70\pm0.04}$, which suggests that the synchrotron-producing electrons are not accelerated by diffusive shock acceleration under standard conditions (Roger Blandford and Eichler, 1987). Both the lack of substructure in its spectrum and its slow, monotonic fading suggests that the spectrum cannot be explained by geometric optical depth effects as has been observed in AGN and X-ray binary jets. Instead, the objects most reminiscent of this transient are pulsar wind nebulae (which have ubiquitously hard radio spectra; Green, 2019) and the persistent sources associated with FRBs (which may also be due to neutron star inflated bubbles; Ben Margalit and Brian D. Metzger, 2018). If interpreted as a pulsar wind nebula, the pulsar is unusual, with a surface dipole field in the range 10^{13-14} G and a present-day spin period of $\sim 10 - 100$ ms. If instead it is a powerful young magnetar, it may be best described by some the same models used to explain the persistent sources associated with repeating FRBs. Other theoretical explanations such as bubbles inflated by highly super-Eddington accretion onto stellar mass black holes may also be possible (Sridhar and Brian D. Metzger, 2022).

Regardless of the correct model, very little observational precedent exists for a transient like VT 1137-0337. The specific type of transient found was unexpected, but the fact that we are finding unusual objects in general was not unexpected given the new parameter space being explored. Among the theoretical possibilities, I chose to highlight the pulsar wind nebula scenario because we know that such objects exist (albeit at much lower luminosity). In fact (and in hindsight), it is somewhat surprising that we are not finding *more* emerging pulsar wind nebulae. Given recent estimates of the initial spin period and magnetic field distributions of pulsars (Igoshev et al., 2022), there should be ∼10-100 young pulsar wind nebulae within the volume probed by the 200 Mpc search with spindown luminosities similar to the one inferred for VT 1137-0337. In the paper, I discussed how this could potentially be explained if the strong magnetic field inferred for VT 1137-0337 is required to produce luminous radio emission. This could be because strong fields cause ejections of mass from the neutron star that are required to fill the nebula with enough radio synchrotron-emitting electrons (Beloborodov, 2017). More theoretical investigation and more careful characterization of the extragalactic transient population is required to test this theory. In the present, more broadband radio follow-up observations are required to check how many more (if any) of the stellar explosions

in the 200 Mpc and Epoch 2 vs Epoch 1 samples are flat spectrum transients. In the near future, this type of spectral characterization may become routine, with wide bandwidth observing bands such as the ones planned for the ngVLA.

6.2 Transient detection ideas for the near future

With the rapid increase in detection rate of radio transients from VLASS, there is too much analysis for any one person or group to do. To address this issue, I will be publicly releasing the catalog of Epoch 2 vs Epoch 1 transients once the sample is well-vetted. The analysis of such a varied sample is naturally broad and can benefit from the inclusion of techniques, theory, and expertise from many fields. To me, the potential for cross-disciplinary bridge building is the most exciting aspect of this work going forward.

Though there is much analysis to be done on this sample, there will be a need for further expansion in radio transient detection for the future. In particular, if we are to find the delayed counterparts to transients detected by LSST, we will need to continue (and ideally automate) the work of radio transient detection going forward. VLASS is scheduled for only one more full epoch; Epoch 3.2 will conclude in October 2024. Past that date, we will need to look to a different source to maintain the flow of new radio transients.

Some of this demand will be addressed by lower frequency surveys such as VAST (the ASKAP transient survey) and various projects being done with LOFAR. However, at GHz frequencies, there are (to my knowledge) no more large sky surveys planned until the DSA 2000 (Gregg Hallinan et al., 2019) comes online in the late 2020s or early 2030s. To bridge the gap, I think that the two most promising areas of growth in the immediate future are (1) non survey-based direct detection relative to VLASS and (2) serendipitous follow-up of transients found by surveys such as LSST and eROSITA.

To explain (1), now that we have mapped the entire sky available to the VLA at 3 GHz, every subsequent 3 GHz observation taken with the VLA is an opportunity to find transients. For every reasonably bright point source ($\gtrsim$ 0.7 mJy) detected, we can check to see whether it was detected in VLASS. If not (and if it should have been), we have found a transient. If so, we can check to see if it has varied in flux. Conversely, we can check every subsequent 3 GHz image at

the location of every cataloged VLASS source to check to see if any of them have faded. Analysis of these reverse transients may be a promising area of investigation in the future. Implementing such a search requires a level of automated calibration, imaging, and source extraction that is not currently available at the VLA. In my upcoming postdoc (a Jansky Fellowship at the NRAO), I intend on adapting my transient pipeline to work with general observations, and adding it as a standard task in the VLA calibration pipeline. With the permission of PIs, this type of transient detection will be run on all subsequent 3 GHz observations. Any discoveries will acknowledge the PI and will be sent to a database for further analysis by the community.

Idea (2) is a similar concept, where observations taken at any radio frequency can be used to check for late-time counterparts to transients found in the rapidly expanding archives of optical and high-energy transients. This will require some careful consideration of false alarm probabilities, since LSST in particular will fill the entire sky with potential transient counterparts. However, I think it is likely that this issue will be surmountable, particularly with the inclusion of loose priors from theoretical expectations (e.g., on the reasonable luminosity of radio counterparts) and well-localized radio observations. Much like idea (1), this type of follow-up can also be implemented in the VLA calibration pipeline using the same source extraction, and artifact rejection techniques that I developed for VLASS.

Finally, looking to the slightly farther future, both the DSA 2000 and the ngVLA will be great boons for radio transient detection. The DSA 2000 will be an especially powerful detection instrument, conducting a uniform multi-epoch, all-sky survey at a sensitivity that is $\sim$2 orders of magnitude deeper than VLASS. Techniques for the direct detection of transients will be important for maximizing the scientific impact of this instrument, though there will be some additional challenges since the DSA 2000 will routinely detect quiescent emission from e.g., star formation and previous epochs of AGN activity and many transients will appear as variable sources. The challenges posed by detecting quiescent emission should also be surmountable with image subtraction techniques or careful modeling. The DSA 2000 will also provide some of its own contextual information in the form of sub-band SEDs and detections of the 21cm line for the hosts of extragalactic transients (in some cases providing redshifts without having to resort to optical follow-up).

Likewise, the ngVLA will provide its own contextual clues in the form of its

milliarcsecond-scale angular resolution and wide bandwidth receivers. The high angular resolution will make it an ideal instrument for serendipitous follow-up of multiwavelength transients. Simultaneously, the wide bandwidth receivers will allow for the routine characterization of the radio spectra of any detected transients, a process that in the present day requires proposing for, observing, and carefully reducing follow-up radio data. With these instruments and techniques, the prospects for future growth in the rate and quality of slow radio transient detection continues to be bright.

BIBLIOGRAPHY

Abdurro'uf et al. (Apr. 2022). "The Seventeenth Data Release of the Sloan Digital Sky Surveys: Complete Release of MaNGA, MaStar, and APOGEE-2 Data". In: *ApJS* 259.2, 35, p. 35. DOI: 10.3847/1538-4365/ac4414. arXiv: 2112.02026 [astro-ph.GA].

Aguado, D. S. et al. (Feb. 2019). "The Fifteenth Data Release of the Sloan Digital Sky Surveys: First Release of MaNGA-derived Quantities, Data Visualization Tools, and Stellar Library". In: *ApJS* 240.2, 23, p. 23. DOI: 10.3847/1538-4365/aaf651. arXiv: 1812.02759 [astro-ph.IM].

Alexander, K. D., E. Berger, et al. (Mar. 2016). "Discovery of an Outflow from Radio Observations of the Tidal Disruption Event ASASSN-14li". In: *ApJL* 819.2, L25, p. L25. DOI: 10.3847/2041-8205/819/2/L25. arXiv: 1510.01226 [astro-ph.HE].

Alexander, K. D., M. H. Wieringa, et al. (Mar. 2017). "Radio Observations of the Tidal Disruption Event XMMSL1 J0740-85". In: *ApJ* 837.2, 153, p. 153. DOI: 10.3847/1538-4357/aa6192. arXiv: 1610.03861 [astro-ph.HE].

Alexander, Kate D. et al. (June 2020). "Radio Properties of Tidal Disruption Events". In: *SSRv* 216.5, 81, p. 81. DOI: 10.1007/s11214-020-00702-w. arXiv: 2006.01159 [astro-ph.HE].

Aller, H. D. and S. P. Reynolds (June 1985). "The decrease with time of the radio flux of the Crab nebula." In: *ApJL* 293, pp. L73–L75. DOI: 10.1086/184494.

Anderson, G. E. et al. (Apr. 2017). "The peculiar mass-loss history of SN 2014C as revealed through AMI radio observations". In: *MNRAS* 466.3, pp. 3648–3662. DOI: 10.1093/mnras/stw3310. arXiv: 1612.06059 [astro-ph.HE].

Anderson, M. M. et al. (Oct. 2019). "Caltech-NRAO Stripe 82 Survey (CNSS) Paper III: The First Radio-Discovered Tidal Disruption Event, CNSS J0019+00". In: *arXiv e-prints*, arXiv:1910.11912, arXiv:1910.11912. arXiv: 1910.11912 [astro-ph.HE].

– (Nov. 2020). "Caltech-NRAO Stripe 82 Survey (CNSS). III. The First Radio-discovered Tidal Disruption Event, CNSS J0019+00". In: *ApJ* 903.2, 116, p. 116. DOI: 10.3847/1538-4357/abb94b. arXiv: 1910.11912 [astro-ph.HE].

Asada, Keiichi and Masanori Nakamura (Feb. 2012). "The Structure of the M87 Jet: A Transition from Parabolic to Conical Streamlines". In: *ApJL* 745.2, L28, p. L28. DOI: 10.1088/2041-8205/745/2/L28. arXiv: 1110.1793 [astro-ph.HE].

Asplund, Martin et al. (Sept. 2009). "The Chemical Composition of the Sun". In: *ARA&A* 47.1, pp. 481–522. DOI: 10.1146/annurev.astro.46.060407.145222. arXiv: 0909.0948 [astro-ph.SR].

Astropy Collaboration, A. M. Price-Whelan, et al. (Sept. 2018). "The Astropy Project: Building an Open-science Project and Status of the v2.0 Core Package". In: *AJ* 156.3, 123, p. 123. DOI: 10.3847/1538-3881/aabc4f. arXiv: 1801.02634 [astro-ph.IM].

Astropy Collaboration, Thomas P. Robitaille, et al. (Oct. 2013). "Astropy: A community Python package for astronomy". In: *A&A* 558, A33, A33. DOI: 10.1051/0004-6361/201322068. arXiv: 1307.6212 [astro-ph.IM].

Atoyan, A. M. (June 1999). "Radio spectrum of the Crab nebula as an evidence for fast initial spin of its pulsar". In: *A&A* 346, pp. L49–L52. arXiv: astro-ph/9905204 [astro-ph].

Atoyan, A. M. and F. A. Aharonian (Jan. 1996). "On the mechanisms of gamma radiation in the Crab Nebula". In: *MNRAS* 278.2, pp. 525–541. DOI: 10.1093/mnras/278.2.525.

Baade, W. and F. Zwicky (May 1934). "On Super-novae". In: *Proceedings of the National Academy of Science* 20.5, pp. 254–259. DOI: 10.1073/pnas.20.5.254.

Baars, J. W. M. et al. (Oct. 1977). "Reprint of 1977A&A....61...99B. The absolute spectrum of Cas A; an accurate flux density scale and a set of secondary calibrators." In: *A&A* 500, pp. 135–142.

Baldwin, J. A., M. M. Phillips, and R. Terlevich (Feb. 1981a). "Classification parameters for the emission-line spectra of extragalactic objects." In: *PASP* 93, pp. 5–19. DOI: 10.1086/130766.

– (Feb. 1981b). "Classification parameters for the emission-line spectra of extragalactic objects." In: *PASP* 93, pp. 5–19. DOI: 10.1086/130766.

Barbarino, C. et al. (Oct. 2020). "Type Ic supernovae from the (intermediate) Palomar Transient Factory". In: *arXiv e-prints*, arXiv:2010.08392, arXiv:2010.08392. arXiv: 2010.08392 [astro-ph.SR].

Barniol Duran, Rodolfo, Ehud Nakar, and Tsvi Piran (July 2013). "Radius Constraints and Minimal Equipartition Energy of Relativistically Moving Synchrotron Sources". In: *ApJ* 772.1, 78, p. 78. DOI: 10.1088/0004-637X/772/1/78. arXiv: 1301.6759 [astro-ph.HE].

Bassa, C. G. et al. (July 2017). "FRB 121102 Is Coincident with a Star-forming Region in Its Host Galaxy". In: *ApJL* 843.1, L8, p. L8. DOI: 10.3847/2041-8213/aa7a0c. arXiv: 1705.07698 [astro-ph.HE].

Becker, R. H., R. L. White, and D. J. Helfand (Sept. 1995). "The FIRST Survey: Faint Images of the Radio Sky at Twenty Centimeters". In: *ApJ* 450, p. 559. DOI: 10.1086/176166.

Begelman, M. C., C. F. McKee, and G. A. Shields (Aug. 1983). "Compton heated winds and coronae above accretion disks. I. Dynamics." In: *ApJ* 271, pp. 70–88. DOI: 10.1086/161178.

Bellm, E. (Jan. 2014). "The Zwicky Transient Facility". In: *The Third Hot-wiring the Transient Universe Workshop*. Ed. by P. R. Wozniak et al., pp. 27–33. arXiv: 1410.8185 [astro-ph.IM].

Bellovary, Jillian M. et al. (Jan. 2019). "Multimessenger signatures of massive black holes in dwarf galaxies". In: *MNRAS* 482.3, pp. 2913–2923. DOI: 10.1093/mnras/sty2842. arXiv: 1806.00471 [astro-ph.GA].

Beloborodov, Andrei M. (July 2017). "A Flaring Magnetar in FRB 121102?" In: *ApJL* 843.2, L26, p. L26. DOI: 10.3847/2041-8213/aa78f3. arXiv: 1702.08644 [astro-ph.HE].

Beloborodov, Andrei M. and Xinyu Li (Dec. 2016). "Magnetar Heating". In: *ApJ* 833.2, 261, p. 261. DOI: 10.3847/1538-4357/833/2/261. arXiv: 1605.09077 [astro-ph.HE].

Beniamini, Paz et al. (July 2019). "Formation rates and evolution histories of magnetars". In: *MNRAS* 487.1, pp. 1426–1438. DOI: 10.1093/mnras/stz1391. arXiv: 1903.06718 [astro-ph.HE].

Bennett, C. L. et al. (Oct. 2014). "The 1% Concordance Hubble Constant". In: *ApJ* 794.2, 135, p. 135. DOI: 10.1088/0004-637X/794/2/135. arXiv: 1406.1718 [astro-ph.CO].

Bera, Apurba and Jayaram N. Chengalur (Nov. 2019). "Super-giant pulses from the Crab pulsar: energy distribution and occurrence rate". In: *MNRAS* 490.1, pp. L12–L16. DOI: 10.1093/mnrasl/slz140. arXiv: 1909.13812 [astro-ph.HE].

Bernardini, M. G. et al. (Mar. 2012). "The X-ray light curve of gamma-ray bursts: clues to the central engine". In: *A&A* 539, A3, A3. DOI: 10.1051/0004-6361/201117895. arXiv: 1112.1058 [astro-ph.HE].

Bietenholz, M. F., N. Bartel, et al. (Feb. 2021). "The Radio Luminosity-risetime Function of Core-collapse Supernovae". In: *ApJ* 908.1, 75, p. 75. DOI: 10.3847/1538-4357/abccd9. arXiv: 2011.11737 [astro-ph.HE].

Bietenholz, M. F., D. A. Frail, and J. J. Hester (Oct. 2001). "The Crab Nebula's Moving Wisps in Radio". In: *ApJ* 560.1, pp. 254–260. DOI: 10.1086/322244. arXiv: astro-ph/0106339 [astro-ph].

Bilinski, Christopher et al. (Mar. 2018). "SN2012ab: a peculiar Type IIn supernova with aspherical circumstellar material". In: *MNRAS* 475.1, pp. 1104–1120. DOI: 10.1093/mnras/stx3214. arXiv: 1712.03370 [astro-ph.SR].

Blandford, R. D. and A. Königl (Aug. 1979). "Relativistic jets as compact radio sources." In: *ApJ* 232, pp. 34–48. DOI: 10.1086/157262.

Blandford, R. D. and R. L. Znajek (May 1977). "Electromagnetic extraction of energy from Kerr black holes." In: *MNRAS* 179, pp. 433–456. DOI: 10.1093/mnras/179.3.433.

Blandford, Roger and David Eichler (Oct. 1987). "Particle acceleration at astrophysical shocks: A theory of cosmic ray origin". In: *PhR* 154.1, pp. 1–75. DOI: 10.1016/0370-1573(87)90134-7.

Blondin, Stéphane and John L. Tonry (July 2011). *SNID: Supernova Identification*. Astrophysics Source Code Library, record ascl:1107.001. ascl: 1107.001.

Blum, Robert D. et al. (June 2016). "The DECam Legacy Survey". In: *American Astronomical Society Meeting Abstracts #228*. Vol. 228. American Astronomical Society Meeting Abstracts, 317.01, p. 317.01.

Bochenek, C. D. et al. (Nov. 2020). "A fast radio burst associated with a Galactic magnetar". In: *Nature* 587.7832, pp. 59–62. DOI: 10.1038/s41586-020-2872-x. arXiv: 2005.10828 [astro-ph.HE].

Bochenek, Christopher D., Vikram Ravi, and Dillon Dong (Feb. 2021). "Localized Fast Radio Bursts Are Consistent with Magnetar Progenitors Formed in Core-collapse Supernovae". In: *ApJL* 907.2, L31, p. L31. DOI: 10.3847/2041-8213/abd634. arXiv: 2009.13030 [astro-ph.HE].

Boller, Th. et al. (Apr. 2016). "Second ROSAT all-sky survey (2RXS) source catalogue". In: *A&A* 588, A103, A103. DOI: 10.1051/0004-6361/201525648. arXiv: 1609.09244 [astro-ph.HE].

Bonnerot, Clément and Wenbin Lu (June 2020). "Simulating disc formation in tidal disruption events". In: *MNRAS* 495.1, pp. 1374–1391. DOI: 10.1093/mnras/staa1246. arXiv: 1906.05865 [astro-ph.HE].

Boquien, M. (Jan. 2020). "CIGALE: a python Code Investigating GALaxy Emission". In: *American Astronomical Society Meeting Abstracts #235*. Vol. 235. American Astronomical Society Meeting Abstracts, 228.01, p. 228.01.

Bradley, T. R. et al. (Nov. 2006). "A composite H ii region luminosity function in Hα of unprecedented statistical weight". In: *A&A* 459.1, pp. L13–L16. DOI: 10.1051/0004-6361:20066151. arXiv: astro-ph/0609607 [astro-ph].

Bühler, R. and R. Blandford (June 2014). "The surprising Crab pulsar and its nebula: a review". In: *Reports on Progress in Physics* 77.6, 066901, p. 066901. DOI: 10.1088/0034-4885/77/6/066901. arXiv: 1309.7046 [astro-ph.HE].

Burbidge, G. R. and E. Margaret Burbidge (Jan. 1957). "The Sources of Radio Emission in NGC 5128 and NGC 1316." In: *ApJ* 125, p. 1. DOI: 10.1086/146279.

Calzetti, Daniela et al. (Apr. 2000). "The Dust Content and Opacity of Actively Star-forming Galaxies". In: *ApJ* 533.2, pp. 682–695. DOI: 10.1086/308692. arXiv: astro-ph/9911459 [astro-ph].

Campana, S. (July 2009). "Linking Burst-Only X-Ray Binary Sources to Faint X-Ray Transients". In: *ApJ* 699.2, pp. 1144–1152. DOI: 10.1088/0004-637X/699/2/1144. arXiv: 0905.0607 [astro-ph.HE].

Campana, S. et al. (Aug. 2006). "The association of GRB 060218 with a supernova and the evolution of the shock wave". In: *Nature* 442.7106, pp. 1008–1010. DOI: 10.1038/nature04892. arXiv: astro-ph/0603279 [astro-ph].

Cann, Jenna M. et al. (Jan. 2019). "The Limitations of Optical Spectroscopic Diagnostics in Identifying Active Galactic Nuclei in the Low-mass Regime". In: *ApJL* 870.1, L2, p. L2. DOI: 10.3847/2041-8213/aaf88d. arXiv: 1812.06170 [astro-ph.GA].

Cappellari, Michele and Eric Emsellem (Feb. 2004). "Parametric Recovery of Line-of-Sight Velocity Distributions from Absorption-Line Spectra of Galaxies via Penalized Likelihood". In: *PASP* 116.816, pp. 138–147. DOI: 10.1086/381875. arXiv: astro-ph/0312201 [astro-ph].

Cavagnolo, K. W. et al. (Sept. 2010). "A Relationship Between AGN Jet Power and Radio Power". In: *ApJ* 720.2, pp. 1066–1072. DOI: 10.1088/0004-637X/720/2/1066. arXiv: 1006.5699 [astro-ph.CO].

Cendes, Y. et al. (Oct. 2021). "Radio Observations of an Ordinary Outflow from the Tidal Disruption Event AT2019dsg". In: *ApJ* 919.2, 127, p. 127. DOI: 10.3847/1538-4357/ac110a. arXiv: 2103.06299 [astro-ph.HE].

Cendes, Yvette et al. (June 2022). "A Mildly Relativistic Outflow Launched Two Years after Disruption in the Tidal Disruption Event AT2018hyz". In: *arXiv e-prints*, arXiv:2206.14297, arXiv:2206.14297. arXiv: 2206.14297 [astro-ph.HE].

Chambers, K. C. et al. (Dec. 2016). "The Pan-STARRS1 Surveys". In: *arXiv e-prints*, arXiv:1612.05560, arXiv:1612.05560. arXiv: 1612.05560 [astro-ph.IM].

Chan, Chi-Ho et al. (Aug. 2019). "Tidal Disruption Events in Active Galactic Nuclei". In: *ApJ* 881.2, 113, p. 113. DOI: 10.3847/1538-4357/ab2b40. arXiv: 1904.12261 [astro-ph.HE].

Chandra, Poonam, Roger A. Chevalier, Nikolai Chugai, Claes Fransson, et al. (Sept. 2015). "X-Ray and Radio Emission from Type IIn Supernova SN 2010jl". In: *ApJ* 810.1, 32, p. 32. DOI: 10.1088/0004-637X/810/1/32. arXiv: 1507.06059 [astro-ph.HE].

Chandra, Poonam, Roger A. Chevalier, Nikolai Chugai, Dan Milisavljevic, et al. (Oct. 2020). "Supernova Interaction with a Dense Detached Shell in SN 2001em". In: *ApJ* 902.1, 55, p. 55. DOI: 10.3847/1538-4357/abb460. arXiv: 2008.13724 [astro-ph.HE].

Chatterjee, S. et al. (Jan. 2017). "A direct localization of a fast radio burst and its host". In: *Nature* 541.7635, pp. 58–61. DOI: 10.1038/nature20797. arXiv: 1701.01098 [astro-ph.HE].

Chen, Ge, Vikram Ravi, and Gregg W. Hallinan (Jan. 2022). "A comprehensive observational study of the FRB 121102 persistent radio source". In: *arXiv e-prints*, arXiv:2201.00999, arXiv:2201.00999. arXiv: 2201.00999 [astro-ph.HE].

Chevalier, Roger A. (May 1998). "Synchrotron Self-Absorption in Radio Supernovae". In: *ApJ* 499.2, pp. 810–819. DOI: 10.1086/305676.

– (Jan. 2004). "Pulsar wind nebulae: theoretical aspects and observational constraints". In: *Advances in Space Research* 33.4, pp. 456–460. DOI: 10.1016/j.asr.2003.04.018. arXiv: astro-ph/0301370 [astro-ph].

– (June 2012). "Common Envelope Evolution Leading to Supernovae with Dense Interaction". In: *ApJL* 752.1, L2, p. L2. DOI: 10.1088/2041-8205/752/1/L2. arXiv: 1204.3300 [astro-ph.HE].

Chevalier, Roger A. and Claes Fransson (Aug. 1992). "Pulsar Nebulae in Supernovae". In: *ApJ* 395, p. 540. DOI: 10.1086/171674.

Chevalier, Roger A. and Edison P. Liang (Sept. 1989). "The Interaction of Supernovae with Circumstellar Bubbles". In: *ApJ* 344, p. 332. DOI: 10.1086/167802.

CHIME/FRB Collaboration et al. (Nov. 2020). "A bright millisecond-duration radio burst from a Galactic magnetar". In: *Nature* 587.7832, pp. 54–58. DOI: 10.1038/s41586-020-2863-y. arXiv: 2005.10324 [astro-ph.HE].

Chiti, Anirudh et al. (Dec. 2016). "Transient Events in Archival Very Large Array Observations of the Galactic Center". In: *ApJ* 833.1, 11, p. 11. DOI: 10.3847/0004-637X/833/1/11. arXiv: 1610.00403 [astro-ph.HE].

Chomiuk, Laura et al. (Apr. 2016). "A Deep Search for Prompt Radio Emission from Thermonuclear Supernovae with the Very Large Array". In: *ApJ* 821.2, 119, p. 119. DOI: 10.3847/0004-637X/821/2/119. arXiv: 1510.07662 [astro-ph.HE].

Chugai, Nikolai N. and Roger A. Chevalier (Apr. 2006). "Late Emission from the Type Ib/c SN 2001em: Overtaking the Hydrogen Envelope". In: *ApJ* 641.2, pp. 1051–1059. DOI: 10.1086/500539. arXiv: astro-ph/0510362 [astro-ph].

Comisso, Luca, Emanuele Sobacchi, and Lorenzo Sironi (June 2020). "Hard Synchrotron Spectra from Magnetically Dominated Plasma Turbulence". In: *ApJL* 895.2, L40, p. L40. DOI: 10.3847/2041-8213/ab93dc. arXiv: 2004.07315 [astro-ph.HE].

Condon, J. J., W. D. Cotton, and J. J. Broderick (Aug. 2002). "Radio Sources and Star Formation in the Local Universe". In: *AJ* 124.2, pp. 675–689. DOI: 10.1086/341650.

Condon, J. J., W. D. Cotton, E. W. Greisen, et al. (May 1998). "The NRAO VLA Sky Survey". In: *AJ* 115.5, pp. 1693–1716. DOI: 10.1086/300337.

Condon, James J. and Scott M. Ransom (2016a). *Essential Radio Astronomy*.

– (2016b). *Essential Radio Astronomy*. Princeton University Press.

Contopoulos, J. and R. V. E. Lovelace (July 1994). "Magnetically Driven Jets and Winds: Exact Solutions". In: *ApJ* 429, p. 139. DOI: 10.1086/174307.

Cook, David O. et al. (July 2019). "Census of the Local Universe (CLU) Narrowband Survey. I. Galaxy Catalogs from Preliminary Fields". In: *ApJ* 880.1, 7, p. 7. DOI: 10.3847/1538-4357/ab2131. arXiv: 1710.05016 [astro-ph.GA].

Corbel, S. et al. (Apr. 2012). "A giant radio flare from Cygnus X-3 with associated γ-ray emission". In: *MNRAS* 421.4, pp. 2947–2955. DOI: 10.1111/j.1365-2966.2012.20517.x. arXiv: 1201.3356 [astro-ph.HE].

Cordes, J. M. and T. J. W. Lazio (July 2002). "NE2001.I. A New Model for the Galactic Distribution of Free Electrons and its Fluctuations". In: *arXiv e-prints*, astro-ph/0207156, astro–ph/0207156. arXiv: astro-ph/0207156 [astro-ph].

Cordes, J. M., I. Wasserman, et al. (July 2021). "Empirical Assessment of Aperiodic and Periodic Radio Bursts from Young Precessing Magnetars". In: *arXiv e-prints*, arXiv:2107.12874, arXiv:2107.12874. arXiv: 2107.12874 [astro-ph.HE].

Cordes, James M. and Shami Chatterjee (Aug. 2019). "Fast Radio Bursts: An Extragalactic Enigma". In: *ARA&A* 57, pp. 417–465. DOI: 10.1146/annurev-astro-091918-104501. arXiv: 1906.05878 [astro-ph.HE].

Corsi, A., A. Gal-Yam, et al. (Oct. 2016). "Radio Observations of a Sample of Broad-line Type IC Supernovae Discovered by PTF/IPTF: A Search for Relativistic Explosions". In: *ApJ* 830.1, 42, p. 42. DOI: 10.3847/0004-637X/830/1/42. arXiv: 1512.01303 [astro-ph.HE].

Corsi, A., E. O. Ofek, et al. (Feb. 2014). "A Multi-wavelength Investigation of the Radio-loud Supernova PTF11qcj and its Circumstellar Environment". In: *ApJ* 782.1, 42, p. 42. DOI: 10.1088/0004-637X/782/1/42. arXiv: 1307.2366 [astro-ph.HE].

Davis, Timothy A. et al. (Aug. 2020). "Revealing the intermediate-mass black hole at the heart of the dwarf galaxy NGC 404 with sub-parsec resolution ALMA observations". In: *MNRAS* 496.4, pp. 4061–4078. DOI: 10.1093/mnras/staa1567. arXiv: 2007.05536 [astro-ph.GA].

Dawson, Kyle S. et al. (Jan. 2013). "The Baryon Oscillation Spectroscopic Survey of SDSS-III". In: *AJ* 145.1, 10, p. 10. DOI: 10.1088/0004-6256/145/1/10. arXiv: 1208.0022 [astro-ph.CO].

De, Kishalay et al. (Dec. 2020). "The Zwicky Transient Facility Census of the Local Universe. I. Systematic Search for Calcium-rich Gap Transients Reveals Three Related Spectroscopic Subclasses". In: *ApJ* 905.1, 58, p. 58. DOI: 10.3847/1538-4357/abb45c. arXiv: 2004.09029 [astro-ph.HE].

De Cia, Annalisa et al. (June 2018). "Light Curves of Hydrogen-poor Superluminous Supernovae from the Palomar Transient Factory". In: *ApJ* 860.2, 100, p. 100. DOI: 10.3847/1538-4357/aab9b6. arXiv: 1708.01623 [astro-ph.HE].

de la Fuente, Eduardo et al. (Feb. 2020). "Ultracompact H II regions with extended emission: the complete view". In: *MNRAS* 492.1, pp. 895–914. DOI: 10.1093/mnras/stz3482. arXiv: 1912.08958 [astro-ph.GA].

DeMarchi, Lindsay et al. (Oct. 2022). "Radio Analysis of SN2004C Reveals an Unusual CSM Density Profile as a Harbinger of Core Collapse". In: *ApJ* 938.1, 84, p. 84. DOI: 10.3847/1538-4357/ac8c26.

DESI Collaboration et al. (Oct. 2016). "The DESI Experiment Part I: Science,Targeting, and Survey Design". In: *arXiv e-prints*, arXiv:1611.00036, arXiv:1611.00036. arXiv: 1611.00036 [astro-ph.IM].

Domınguez, A. et al. (Feb. 2013). "Dust Extinction from Balmer Decrements of Star-forming Galaxies at 0.75 <= z <= 1.5 with Hubble Space Telescope/Wide-Field-Camera 3 Spectroscopy from the WFC3 Infrared Spectroscopic Parallel Survey". In: *ApJ* 763.2, 145, p. 145. DOI: 10.1088/0004-637X/763/2/145. arXiv: 1206.1867 [astro-ph.CO].

Dong, D. Z. et al. (Sept. 2021). "A transient radio source consistent with a merger-triggered core collapse supernova". In: *Science* 373.6559, pp. 1125–1129. DOI: 10.1126/science.abg6037. arXiv: 2109.01752 [astro-ph.HE].

Dong, Dillon and Gregg Hallinan (June 2022). "A Flat-Spectrum Radio Transient at 122 Mpc consistent with an Emerging Pulsar Wind Nebula". In: *arXiv e-prints*, arXiv:2206.11911, arXiv:2206.11911. arXiv: 2206.11911 [astro-ph.HE].

Donley, J. L. et al. (Sept. 2002). "Large-Amplitude X-Ray Outbursts from Galactic Nuclei: A Systematic Survey using ROSAT Archival Data". In: *AJ* 124.3, pp. 1308–1321. DOI: 10.1086/342280. arXiv: astro-ph/0206291 [astro-ph].

Dopita, M. A. et al. (Oct. 2000). "A Theoretical Recalibration of the Extragalactic H II Region Sequence". In: *ApJ* 542.1, pp. 224–234. DOI: 10.1086/309538.

Doré, Olivier et al. (Dec. 2014). "Cosmology with the SPHEREX All-Sky Spectral Survey". In: *arXiv e-prints*, arXiv:1412.4872, arXiv:1412.4872. arXiv: 1412.4872 [astro-ph.CO].

Draine, Bruce T. (2011). *Physics of the Interstellar and Intergalactic Medium*. Princeton University Press.

Drlica-Wagner, A. et al. (Apr. 2020). "Milky Way Satellite Census. I. The Observational Selection Function for Milky Way Satellites in DES Y3 and Pan-STARRS DR1". In: *ApJ* 893.1, 47, p. 47. DOI: 10.3847/1538-4357/ab7eb9. arXiv: 1912.03302 [astro-ph.GA].

Duffell, Paul C. and Anna Y. Q. Ho (Sept. 2020). "How Dense of a Circumstellar Medium Is Sufficient to Choke a Jet?" In: *ApJ* 900.2, 193, p. 193. DOI: 10.3847/1538-4357/aba90a.

Eftekhari, T., E. Berger, B. Margalit, P. K. Blanchard, et al. (May 2019). "A Radio Source Coincident with the Superluminous Supernova PTF10hgi: Evidence for a Central Engine and an Analog of the Repeating FRB 121102?" In: *ApJL* 876.1, L10, p. L10. DOI: 10.3847/2041-8213/ab18a5. arXiv: 1901.10479 [astro-ph.HE].

Eftekhari, T., E. Berger, B. Margalit, B. D. Metzger, et al. (June 2020). "Wandering Massive Black Holes or Analogs of the First Repeating Fast Radio Burst?" In: *ApJ* 895.2, 98, p. 98. DOI: 10.3847/1538-4357/ab9015. arXiv: 2001.02688 [astro-ph.HE].

Eftekhari, T., E. Berger, B. A. Zauderer, et al. (Feb. 2018). "Radio Monitoring of the Tidal Disruption Event Swift J164449.3+573451. III. Late-time Jet Energetics and a Deviation from Equipartition". In: *ApJ* 854.2, 86, p. 86. DOI: 10.3847/1538-4357/aaa8e0. arXiv: 1710.07289 [astro-ph.HE].

Egron, Elise et al. (Jan. 2021). "Investigating the Mini and Giant Radio Flare Episodes of Cygnus X-3". In: *ApJ* 906.1, 10, p. 10. DOI: 10.3847/1538-4357/abc5b1. arXiv: 2010.15002 [astro-ph.HE].

Elmegreen, Bruce G. (Oct. 2007). "On the Rapid Collapse and Evolution of Molecular Clouds". In: *ApJ* 668.2, pp. 1064–1082. DOI: 10.1086/521327. arXiv: 0707.2252 [astro-ph].

Fanaroff, B. L. and J. M. Riley (May 1974). "The morphology of extragalactic radio sources of high and low luminosity". In: *MNRAS* 167, 31P–36P. DOI: 10.1093/mnras/167.1.31P.

Fender, R. P., T. M. Belloni, and E. Gallo (Dec. 2004). "Towards a unified model for black hole X-ray binary jets". In: *MNRAS* 355.4, pp. 1105–1118. DOI: 10.1111/j.1365-2966.2004.08384.x. arXiv: astro-ph/0409360 [astro-ph].

Fender, R. P., J. Homan, and T. M. Belloni (July 2009). "Jets from black hole X-ray binaries: testing, refining and extending empirical models for the coupling to X-rays". In: *MNRAS* 396.3, pp. 1370–1382. DOI: 10.1111/j.1365-2966.2009.14841.x. arXiv: 0903.5166 [astro-ph.HE].

Fender, R. P., G. G. Pooley, et al. (Mar. 2000). "The very flat radio-millimetre spectrum of Cygnus X-1". In: *MNRAS* 312.4, pp. 853–858. DOI: 10.1046/j.1365-8711.2000.03219.x. arXiv: astro-ph/9910184 [astro-ph].

Feroz, F., M. P. Hobson, and M. Bridges (Oct. 2009). "MULTINEST: an efficient and robust Bayesian inference tool for cosmology and particle physics". In: *MNRAS* 398.4, pp. 1601–1614. DOI: 10.1111/j.1365-2966.2009.14548.x. arXiv: 0809.3437 [astro-ph].

Fleishman, G. D. and M. F. Bietenholz (Apr. 2007). "Diffusive synchrotron radiation from pulsar wind nebulae". In: *MNRAS* 376.2, pp. 625–633. DOI: 10.1111/j.1365-2966.2007.11450.x. arXiv: astro-ph/0702105 [astro-ph].

Fleishman, Gregory D. (Feb. 2006). "Diffusive Synchrotron Radiation from Relativistic Shocks in Gamma-Ray Burst Sources". In: *ApJ* 638.1, pp. 348–353. DOI: 10.1086/498732. arXiv: astro-ph/0502245 [astro-ph].

Flesch, Eric Wim (May 2021). "The Million Quasars (Milliquas) v7.2 Catalogue, now with VLASS associations. The inclusion of SDSS-DR16Q quasars is detailed". In: *arXiv e-prints*, arXiv:2105.12985, arXiv:2105.12985. arXiv: 2105.12985 [astro-ph.GA].

Fong, W. and E. Berger (Oct. 2013). "The Locations of Short Gamma-Ray Bursts as Evidence for Compact Object Binary Progenitors". In: *ApJ* 776.1, 18, p. 18. DOI: 10.1088/0004-637X/776/1/18. arXiv: 1307.0819 [astro-ph.HE].

Foreman-Mackey, D. et al. (Mar. 2013). "emcee: The MCMC Hammer". In: *PASP* 125, p. 306. DOI: 10.1086/670067. arXiv: 1202.3665 [astro-ph.IM].

Frail, D. A., S. R. Kulkarni, E. O. Ofek, et al. (Mar. 2012). "A Revised View of the Transient Radio Sky". In: *ApJ* 747.1, 70, p. 70. DOI: 10.1088/0004-637X/747/1/70. arXiv: 1111.0007 [astro-ph.HE].

Frail, D. A., S. R. Kulkarni, R. Sari, et al. (Nov. 2001). "Beaming in Gamma-Ray Bursts: Evidence for a Standard Energy Reservoir". In: *ApJL* 562.1, pp. L55–L58. DOI: 10.1086/338119. arXiv: astro-ph/0102282 [astro-ph].

Frail, D. A. and B. R. Scharringhausen (May 1997). "A Radio Survey for Pulsar Wind Nebulae". In: *ApJ* 480.1, pp. 364–370. DOI: 10.1086/303943.

Frail, D. A., E. Waxman, and S. R. Kulkarni (July 2000). "A 450 Day Light Curve of the Radio Afterglow of GRB 970508: Fireball Calorimetry". In: *ApJ* 537.1, pp. 191–204. DOI: 10.1086/309024. arXiv: astro-ph/9910319 [astro-ph].

Frank, J. and M. J. Rees (Sept. 1976). "Effects of massive black holes on dense stellar systems." In: *MNRAS* 176, pp. 633–647. DOI: 10.1093/mnras/176.3.633.

Fransson, Claes et al. (Dec. 2014). "High-density Circumstellar Interaction in the Luminous Type IIn SN 2010jl: The First 1100 Days". In: *ApJ* 797.2, 118, p. 118. DOI: 10.1088/0004-637X/797/2/118. arXiv: 1312.6617 [astro-ph.HE].

Fruchter, A. S. et al. (May 2006). "Long γ-ray bursts and core-collapse supernovae have different environments". In: *Nature* 441.7092, pp. 463–468. DOI: 10.1038/nature04787. arXiv: astro-ph/0603537 [astro-ph].

Gaensler, B. M. et al. (Oct. 2000). "Limits on radio emission from pulsar wind nebulae". In: *MNRAS* 318.1, pp. 58–66. DOI: 10.1046/j.1365-8711.2000.03626.x. arXiv: astro-ph/0004273 [astro-ph].

Gaensler, Bryan M. and Patrick O. Slane (Sept. 2006). "The Evolution and Structure of Pulsar Wind Nebulae". In: *ARA&A* 44.1, pp. 17–47. DOI: 10.1146/annurev.astro.44.051905.092528. arXiv: astro-ph/0601081 [astro-ph].

Gal-Yam, Avishay (Aug. 2019). "The Most Luminous Supernovae". In: *ARA&A* 57, pp. 305–333. DOI: 10.1146/annurev-astro-081817-051819. arXiv: 1812.01428 [astro-ph.HE].

Gal-Yam, Avishay et al. (Dec. 2011). "PTF weekly SN discovery report, December 8, 2011". In: *The Astronomer's Telegram* 3798, p. 1.

Galloway, Duncan K. and Laurens Keek (Jan. 2021). "Thermonuclear X-ray Bursts". In: *Astrophysics and Space Science Library*. Ed. by Tomaso M. Belloni, Mariano Méndez, and Chengmin Zhang. Vol. 461. Astrophysics and Space Science Library, pp. 209–262. DOI: 10.1007/978-3-662-62110-3_5. arXiv: 1712.06227 [astro-ph.HE].

Gavriil, F. P. et al. (Mar. 2008). "Magnetar-Like Emission from the Young Pulsar in Kes 75". In: *Science* 319.5871, p. 1802. DOI: 10.1126/science.1153465. arXiv: 0802.1704 [astro-ph].

Gehrels, N. (Apr. 1986). "Confidence Limits for Small Numbers of Events in Astrophysical Data". In: *ApJ* 303, p. 336. DOI: 10.1086/164079.

Ghirlanda, G. et al. (Sept. 2015). "Are short Gamma Ray Bursts similar to long ones?" In: *Journal of High Energy Astrophysics* 7, pp. 81–89. DOI: 10.1016/j.jheap.2015.04.002.

Goldreich, Peter and William H. Julian (Aug. 1969). "Pulsar Electrodynamics". In: *ApJ* 157, p. 869. DOI: 10.1086/150119.

Gordon, Yjan A., Michelle M. Boyce, Christopher P. O'Dea, Lawrence Rudnick, Heinz Andernach, Adrian N. Vantyghem, Stefi A. Baum, Jean-Paul Bui, and Mathew Dionyssiou (Oct. 2020). "A Catalog of Very Large Array Sky Survey Epoch 1 Quick Look Components, Sources, and Host Identifications". In: *Research Notes of the American Astronomical Society* 4.10, 175, p. 175. DOI: 10.3847/2515-5172/abbe23.

Gordon, Yjan A., Michelle M. Boyce, Christopher P. O'Dea, Lawrence Rudnick, Heinz Andernach, Adrian N. Vantyghem, Stefi A. Baum, Jean-Paul Bui, Mathew Dionyssiou, et al. (Aug. 2021). "A Quick Look at the 3 GHz Radio Sky. I. Source Statistics from the Very Large Array Sky Survey". In: *ApJS* 255.2, 30, p. 30. DOI: 10.3847/1538-4365/ac05c0. arXiv: 2102.11753 [astro-ph.GA].

Granot, Jonathan and Re'em Sari (Apr. 2002). "The Shape of Spectral Breaks in Gamma-Ray Burst Afterglows". In: *ApJ* 568.2, pp. 820–829. DOI: 10.1086/338966. arXiv: astro-ph/0108027 [astro-ph].

Granot, Jonathan and Alexander J. van der Horst (Feb. 2014). "Gamma-Ray Burst Jets and their Radio Observations". In: *PASA* 31, e008, e008. DOI: 10.1017/pasa.2013.44.

Green, D. A. (Aug. 2019). "A revised catalogue of 294 Galactic supernova remnants". In: *Journal of Astrophysics and Astronomy* 40.4, 36, p. 36. DOI: 10.1007/s12036-019-9601-6. arXiv: 1907.02638 [astro-ph.GA].

Greene, Jenny E., Jay Strader, and Luis C. Ho (Aug. 2020). "Intermediate-Mass Black Holes". In: *ARA&A* 58, pp. 257–312. DOI: 10.1146/annurev-astro-032620-021835. arXiv: 1911.09678 [astro-ph.GA].

Guillochon, James et al. (Jan. 2017). "An Open Catalog for Supernova Data". In: *ApJ* 835.1, 64, p. 64. DOI: 10.3847/1538-4357/835/1/64. arXiv: 1605.01054 [astro-ph.SR].

Guth, Alan H. (Jan. 1981). "Inflationary universe: A possible solution to the horizon and flatness problems". In: *PhRvD* 23.2, pp. 347–356. DOI: 10.1103/PhysRevD.23.347.

Hallinan, G. et al. (Dec. 2017). "A radio counterpart to a neutron star merger". In: *Science* 358.6370, pp. 1579–1583. DOI: 10.1126/science.aap9855. arXiv: 1710.05435 [astro-ph.HE].

Hallinan, Gregg et al. (Sept. 2019). "The DSA-2000 — A Radio Survey Camera". In: *Bulletin of the American Astronomical Society*. Vol. 51, 255, p. 255. arXiv: 1907.07648 [astro-ph.IM].

Heng, Kevin (Mar. 2010). "Balmer-Dominated Shocks: A Concise Review". In: *PASA* 27.1, pp. 23–44. DOI: 10.1071/AS09057. arXiv: 0908.4080 [astro-ph.GA].

Hicken, Malcolm et al. (Nov. 2017). "Type II Supernova Light Curves and Spectra from the CfA". In: *ApJS* 233.1, 6, p. 6. DOI: 10.3847/1538-4365/aa8ef4. arXiv: 1706.01030 [astro-ph.HE].

Higson, Edward et al. (2019). "Dynamic nested sampling: an improved algorithm for parameter estimation and evidence calculation". In: *Statistics and Computing* 29.5, pp. 891–913. DOI: 10.1007/s11222-018-9844-0. URL: https://doi.org/10.1007/s11222-018-9844-0.

Hjellming, R. M. and K. J. Johnston (May 1988). "Radio Emission from Conical Jets Associated with X-Ray Binaries". In: *ApJ* 328, p. 600. DOI: 10.1086/166318.

Ho, Anna Y. Q., Daniel A. Perley, et al. (May 2020). "The Koala: A Fast Blue Optical Transient with Luminous Radio Emission from a Starburst Dwarf Galaxy at z = 0.27". In: *ApJ* 895.1, 49, p. 49. DOI: 10.3847/1538-4357/ab8bcf. arXiv: 2003.01222 [astro-ph.HE].

Ho, Anna Y. Q., E. Sterl Phinney, et al. (Jan. 2019). "AT2018cow: A Luminous Millimeter Transient". In: *ApJ* 871.1, 73, p. 73. DOI: 10.3847/1538-4357/aaf473. arXiv: 1810.10880 [astro-ph.HE].

Horesh, A., S. B. Cenko, and I. Arcavi (Jan. 2021). "Delayed radio flares from a tidal disruption event". In: *Nature Astronomy* 5, pp. 491–497. DOI: 10.1038/s41550-021-01300-8. arXiv: 2102.11290 [astro-ph.HE].

Hughes, V. A. and A. Woodsworth (Mar. 1972). "Radio Flare on β Persei". In: *Nature Physical Science* 236.64, pp. 42–43. DOI: 10.1038/physci236042a0.

Hyman, Scott D., T. Joseph W. Lazio, Namir E. Kassim, and Ashlee L. Bartleson (Mar. 2002). "Low-Frequency Radio Transients in the Galactic Center". In: *AJ* 123.3, pp. 1497–1501. DOI: 10.1086/338905. arXiv: astro-ph/0110151 [astro-ph].

Hyman, Scott D., T. Joseph W. Lazio, Namir E. Kassim, Paul S. Ray, et al. (Mar. 2005). "A powerful bursting radio source towards the Galactic Centre". In: *Nature* 434.7029, pp. 50–52. DOI: 10.1038/nature03400. arXiv: astro-ph/0503052 [astro-ph].

Hyman, Scott D., Rudy Wijnands, et al. (May 2009). "GCRT J1742-3001: A New Radio Transient Toward the Galactic Center". In: *ApJ* 696.1, pp. 280–286. DOI: 10.1088/0004-637X/696/1/280. arXiv: 0811.1972 [astro-ph].

Igoshev, Andrei P. et al. (May 2022). "Initial periods and magnetic fields of neutron stars". In: *arXiv e-prints*, arXiv:2205.06823, arXiv:2205.06823. arXiv: 2205.06823 [astro-ph.HE].

in't Zand, J. J. M. et al. (Jan. 2019). "Searching for the most powerful thermonuclear X-ray bursts with the Neil Gehrels Swift Observatory". In: *A&A* 621, A53, A53. DOI: 10.1051/0004-6361/201834270. arXiv: 1811.06486 [astro-ph.HE].

Ishibashi, W. and T. J. -L. Courvoisier (Sept. 2009). "X-ray variability time scales in active galactic nuclei". In: *A&A* 504.1, pp. 61–66. DOI: 10.1051/0004-6361/200911958. arXiv: 0905.4842 [astro-ph.CO].

Ivanova, N. et al. (Feb. 2013). "Common envelope evolution: where we stand and how we can move forward". In: *A&A Rv* 21, 59, p. 59. DOI: 10.1007/s00159-013-0059-2. arXiv: 1209.4302 [astro-ph.HE].

Ivezić, Ž. et al. (Mar. 2019). "LSST: From Science Drivers to Reference Design and Anticipated Data Products". In: *ApJ* 873, 111, p. 111. DOI: 10.3847/1538-4357/ab042c. arXiv: 0805.2366.

Izotov, Y. I. et al. (Mar. 2006). "The chemical composition of metal-poor emission-line galaxies in the Data Release 3 of the Sloan Digital Sky Survey". In: *A&A* 448.3, pp. 955–970. DOI: 10.1051/0004-6361:20053763. arXiv: astro-ph/0511644 [astro-ph].

Jermyn, Adam S. et al. (Apr. 2022). "Effects of an Immortal Stellar Population in AGN Disks". In: *ApJ* 929.2, 133, p. 133. DOI: 10.3847/1538-4357/ac5d40. arXiv: 2203.06187 [astro-ph.GA].

Jetsu, Lauri and Sebastien Porceddu (Dec. 2015). "Shifting Milestones of Natural Sciences: The Ancient Egyptian Discovery of Algol's Period Confirmed". In: *PLoS ONE* 10, p. 44140. DOI: 10.1371/journal.pone.0144140. arXiv: 1601.06990 [astro-ph.SR].

Jones, Frank C. and Donald C. Ellison (Dec. 1991). "The plasma physics of shock acceleration". In: *SSRv* 58.1, pp. 259–346. DOI: 10.1007/BF01206003.

Josephy, A. et al. (Sept. 2019). "CHIME/FRB Detection of the Original Repeating Fast Radio Burst Source FRB 121102". In: *ApJL* 882.2, L18, p. L18. DOI: 10.3847/2041-8213/ab2c00. arXiv: 1906.11305 [astro-ph.HE].

Kagan, Daniel, Ehud Nakar, and Tsvi Piran (May 2018). "Physics of the saturation of particle acceleration in relativistic magnetic reconnection". In: *MNRAS* 476.3, pp. 3902–3912. DOI: 10.1093/mnras/sty452. arXiv: 1711.08701 [astro-ph.HE].

Kameno, Seiji et al. (Jan. 2003). "Free-Free Absorption and the Unified Scheme". In: *PASA* 20.1, pp. 213–221. DOI: 10.1071/AS03037. arXiv: astro-ph/0302256 [astro-ph].

Kasen, Daniel and Lars Bildsten (July 2010). "Supernova Light Curves Powered by Young Magnetars". In: *ApJ* 717.1, pp. 245–249. DOI: 10.1088/0004-637X/717/1/245. arXiv: 0911.0680 [astro-ph.HE].

Kaspi, Victoria M. and Andrei M. Beloborodov (Aug. 2017). "Magnetars". In: *ARA&A* 55.1, pp. 261–301. DOI: 10.1146/annurev-astro-081915-023329. arXiv: 1703.00068 [astro-ph.HE].

Kaspi, Victoria M., Mallory S. E. Roberts, and Alice K. Harding (2006). "Isolated neutron stars". In: *Compact stellar X-ray sources*. Vol. 39, pp. 279–339.

Kellermann, K. I. and I. I. K. Pauliny-Toth (Jan. 1981). "Compact radio sources". In: *ARA&A* 19, pp. 373–410. DOI: 10.1146/annurev.aa.19.090181.002105.

Kennicutt, Robert C. and Neal J. Evans (Sept. 2012). "Star Formation in the Milky Way and Nearby Galaxies". In: *ARA&A* 50, pp. 531–608. DOI: 10.1146/annurev-astro-081811-125610. arXiv: 1204.3552 [astro-ph.GA].

Kewley, L. J. et al. (July 2001). "Theoretical Modeling of Starburst Galaxies". In: *ApJ* 556.1, pp. 121–140. DOI: 10.1086/321545. arXiv: astro-ph/0106324 [astro-ph].

Kewley, Lisa J., Michael A. Dopita, et al. (Sept. 2013). "Theoretical Evolution of Optical Strong Lines across Cosmic Time". In: *ApJ* 774.2, 100, p. 100. DOI: 10.1088/0004-637X/774/2/100. arXiv: 1307.0508 [astro-ph.CO].

Kewley, Lisa J. and Sara L. Ellison (July 2008). "Metallicity Calibrations and the Mass-Metallicity Relation for Star-forming Galaxies". In: *ApJ* 681.2, pp. 1183–1204. DOI: 10.1086/587500. arXiv: 0801.1849 [astro-ph].

Kewley, Lisa J., David C. Nicholls, et al. (July 2019). "Theoretical ISM Pressure and Electron Density Diagnostics for Local and High-redshift Galaxies". In: *ApJ* 880.1, 16, p. 16. DOI: 10.3847/1538-4357/ab16ed. arXiv: 1908.05504 [astro-ph.GA].

Kirsten, F. et al. (Feb. 2022). "A repeating fast radio burst source in a globular cluster". In: *Nature* 602.7898, pp. 585–589. DOI: 10.1038/s41586-021-04354-w. arXiv: 2105.11445 [astro-ph.HE].

Kiryati, N., Y. Eldar, and A. M. Bruckstein (Jan. 1991). "A probabilistic Hough transform". In: *Pattern Recognition* 24.4, pp. 303–316. DOI: 10.1016/0031-3203(91)90073-E.

Klencki, Jakub et al. (June 2020). "Massive donors in interacting binaries: effect of metallicity". In: *A&A* 638, A55, A55. DOI: 10.1051/0004-6361/202037694. arXiv: 2004.00628 [astro-ph.SR].

Kochanek, C. S. et al. (Oct. 2017). "The All-Sky Automated Survey for Supernovae (ASAS-SN) Light Curve Server v1.0". In: *PASP* 129.980, p. 104502. DOI: 10.1088/1538-3873/aa80d9. arXiv: 1706.07060 [astro-ph.SR].

Kolmogorov, A. (Jan. 1941). "The Local Structure of Turbulence in Incompressible Viscous Fluid for Very Large Reynolds' Numbers". In: *Akademiia Nauk SSSR Doklady* 30, pp. 301–305.

Kormendy, John and Jr. Kennicutt Robert C. (Sept. 2004). "Secular Evolution and the Formation of Pseudobulges in Disk Galaxies". In: *ARA&A* 42.1, pp. 603–683. DOI: 10.1146/annurev.astro.42.053102.134024. arXiv: astro-ph/0407343 [astro-ph].

Kou, F. F. and H. Tong (June 2015). "Rotational evolution of the Crab pulsar in the wind braking model". In: *MNRAS* 450.2, pp. 1990–1998. DOI: 10.1093/mnras/stv734. arXiv: 1501.01534 [astro-ph.HE].

Kulkarni, S. R., D. A. Frail, et al. (Oct. 1998). "Radio emission from the unusual supernova 1998bw and its association with the γ-ray burst of 25 April 1998". In: *Nature* 395.6703, pp. 663–669. DOI: 10.1038/27139.

Kulkarni, S. R., D. A. Perley, and A. A. Miller (June 2018). "The Redshift Completeness of Local Galaxy Catalogs". In: *ApJ* 860.1, 22, p. 22. DOI: 10.3847/1538-4357/aabf85. arXiv: 1710.04223 [astro-ph.GA].

Kumar, Pawan and Bing Zhang (Feb. 2015). "The physics of gamma-ray bursts & relativistic jets". In: *PhR* 561, pp. 1–109. DOI: 10.1016/j.physrep.2014.09.008. arXiv: 1410.0679 [astro-ph.HE].

Lacy, M. et al. (Mar. 2020). "The Karl G. Jansky Very Large Array Sky Survey (VLASS). Science Case and Survey Design". In: *PASP* 132.1009, 035001, p. 035001. DOI: 10.1088/1538-3873/ab63eb. arXiv: 1907.01981 [astro-ph.IM].

Lang, Dustin (Dec. 2020). "A hybrid Fourier–Real Gaussian Mixture method for fast galaxy–PSF convolution". In: *arXiv e-prints*, arXiv:2012.15797, arXiv:2012.15797. arXiv: 2012.15797 [astro-ph.IM].

Langer, N. (Sept. 2012). "Presupernova Evolution of Massive Single and Binary Stars". In: *ARA&A* 50, pp. 107–164. DOI: 10.1146/annurev-astro-081811-125534. arXiv: 1206.5443 [astro-ph.SR].

Law, C. J. et al. (Oct. 2018). "Discovery of the Luminous, Decades-long, Extragalactic Radio Transient FIRST J141918.9+394036". In: *ApJL* 866.2, L22, p. L22. DOI: 10.3847/2041-8213/aae5f3. arXiv: 1808.08964 [astro-ph.HE].

Law, Casey J., Liam Connor, and Kshitij Aggarwal (Mar. 2022). "On the Fast Radio Burst and Persistent Radio Source Populations". In: *ApJ* 927.1, 55, p. 55. DOI: 10.3847/1538-4357/ac4c42. arXiv: 2110.15323 [astro-ph.HE].

Law, Nicholas M. et al. (Dec. 2009). "The Palomar Transient Factory: System Overview, Performance, and First Results". In: *PASP* 121.886, p. 1395. DOI: 10.1086/648598. arXiv: 0906.5350 [astro-ph.IM].

Leitherer, Claus et al. (July 1999). "Starburst99: Synthesis Models for Galaxies with Active Star Formation". In: *ApJS* 123.1, pp. 3–40. DOI: 10.1086/313233. arXiv: astro-ph/9902334 [astro-ph].

Li, Zhi-Yun and Roger A. Chevalier (Dec. 1999). "Radio Supernova SN 1998bw and Its Relation to GRB 980425". In: *ApJ* 526.2, pp. 716–726. DOI: 10.1086/308031. arXiv: astro-ph/9903483 [astro-ph].

Lien, Amy et al. (Sept. 2016). "The Third Swift Burst Alert Telescope Gamma-Ray Burst Catalog". In: *ApJ* 829.1, 7, p. 7. DOI: 10.3847/0004-637X/829/1/7. arXiv: 1606.01956 [astro-ph.HE].

Linden, S. T. et al. (June 2020). "The Star Formation in Radio Survey: 3-33 GHz Imaging of Nearby Galaxy Nuclei and Extranuclear Star-forming Regions". In: *ApJS* 248.2, 25, p. 25. DOI: 10.3847/1538-4365/ab8a4d. arXiv: 2004.10230 [astro-ph.GA].

Liodakis, I. et al. (June 2017). "Bimodal radio variability in OVRO-40 m-monitored blazars". In: *MNRAS* 467.4, pp. 4565–4576. DOI: 10.1093/mnras/stx432. arXiv: 1702.05493 [astro-ph.HE].

Lister, Matthew L. (Nov. 2001). "Relativistic Beaming and Flux Variability in Active Galactic Nuclei". In: *ApJ* 561.2, pp. 676–683. DOI: 10.1086/323528. arXiv: astro-ph/0107532 [astro-ph].

Lourie, Nathan P. et al. (Dec. 2020). "The wide-field infrared transient explorer (WINTER)". In: *Society of Photo-Optical Instrumentation Engineers (SPIE) Conference Series*. Vol. 11447. Society of Photo-Optical Instrumentation Engineers (SPIE) Conference Series, 114479K, 114479K. DOI: 10.1117/12.2561210. arXiv: 2102.01109 [astro-ph.IM].

Lu, Wenbin and Clément Bonnerot (Feb. 2020). "Self-intersection of the fallback stream in tidal disruption events". In: *MNRAS* 492.1, pp. 686–707. DOI: 10.1093/mnras/stz3405. arXiv: 1904.12018 [astro-ph.HE].

Lyne, A. G., R. S. Pritchard, and F. Graham Smith (Dec. 1993). "23 years of Crab pulsar rotational history." In: *MNRAS* 265, pp. 1003–1012. DOI: 10.1093/mnras/265.4.1003.

Lyutikov, Maxim et al. (Oct. 2019). "Interpreting Crab Nebula's synchrotron spectrum: two acceleration mechanisms". In: *MNRAS* 489.2, pp. 2403–2416. DOI: 10.1093/mnras/stz2023. arXiv: 1811.01767 [astro-ph.HE].

Macıas-Pérez, J. F. et al. (Mar. 2010). "Global Spectral Energy Distribution of the Crab Nebula in the Prospect of the Planck Satellite Polarization Calibration". In: *ApJ* 711.1, pp. 417–423. DOI: 10.1088/0004-637X/711/1/417. arXiv: 0802.0412 [astro-ph].

MacLeod, Morgan, Eve C. Ostriker, and James M. Stone (Dec. 2018). "Bound Outflows, Unbound Ejecta, and the Shaping of Bipolar Remnants during Stellar Coalescence". In: *ApJ* 868.2, 136, p. 136. DOI: 10.3847/1538-4357/aae9eb. arXiv: 1808.05950 [astro-ph.SR].

Magnier, Eugene A. et al. (Nov. 2020). "Pan-STARRS Pixel Analysis: Source Detection and Characterization". In: *ApJS* 251.1, 5, p. 5. DOI: 10.3847/1538-4365/abb82c. arXiv: 1612.05244 [astro-ph.IM].

Manchester, R. N., B. M. Gaensler, et al. (Jan. 2002). "Evolution of the Radio Remnant of SN 1987A: 1990-2001". In: *PASA* 19.2, pp. 207–221. DOI: 10.1071/AS01042. arXiv: astro-ph/0110693 [astro-ph].

Manchester, R. N., G. B. Hobbs, et al. (Apr. 2005). "The Australia Telescope National Facility Pulsar Catalogue". In: *AJ* 129.4, pp. 1993–2006. DOI: 10.1086/428488. arXiv: astro-ph/0412641 [astro-ph].

Maraston, C. and G. Strömbäck (Dec. 2011). "Stellar population models at high spectral resolution". In: *MNRAS* 418.4, pp. 2785–2811. DOI: 10.1111/j.1365-2966.2011.19738.x. arXiv: 1109.0543 [astro-ph.CO].

Margalit, Ben and Brian D. Metzger (Nov. 2018). "A Concordance Picture of FRB 121102 as a Flaring Magnetar Embedded in a Magnetized Ion-Electron Wind Nebula". In: *ApJL* 868.1, L4, p. L4. DOI: 10.3847/2041-8213/aaedad. arXiv: 1808.09969 [astro-ph.HE].

Margutti, R., A. Kamble, et al. (Feb. 2017). "Ejection of the Massive Hydrogen-rich Envelope Timed with the Collapse of the Stripped SN 2014C". In: *ApJ* 835.2, 140, p. 140. DOI: 10.3847/1538-4357/835/2/140. arXiv: 1601.06806 [astro-ph.HE].

Margutti, R., B. D. Metzger, et al. (Feb. 2019). "An Embedded X-Ray Source Shines through the Aspherical AT 2018cow: Revealing the Inner Workings of the Most Luminous Fast-evolving Optical Transients". In: *ApJ* 872.1, 18, p. 18. DOI: 10.3847/1538-4357/aafa01. arXiv: 1810.10720 [astro-ph.HE].

Martinez, L. et al. (Apr. 2022). "Type II supernovae from the Carnegie Supernova Project-I. II. Physical parameter distributions from hydrodynamical modelling". In: *A&A* 660, A41, A41. DOI: 10.1051/0004-6361/202142076. arXiv: 2111.06529 [astro-ph.SR].

Matsumoto, Tatsuya, Ehud Nakar, and Tsvi Piran (June 2019). "Generalized compactness limit from an arbitrary viewing angle". In: *MNRAS* 486.2, pp. 1563–1573. DOI: 10.1093/mnras/stz923. arXiv: 1903.06712 [astro-ph.HE].

Mattila, S. et al. (Aug. 2018). "A dust-enshrouded tidal disruption event with a resolved radio jet in a galaxy merger". In: *Science* 361.6401, pp. 482–485. DOI: 10.1126/science.aao4669. arXiv: 1806.05717 [astro-ph.GA].

Mattila, Seppo et al. (July 2010). "Abundances and Density Structure of the Inner Circumstellar Ring Around SN 1987A". In: *ApJ* 717.2, pp. 1140–1156. DOI: 10.1088/0004-637X/717/2/1140. arXiv: 1002.4195 [astro-ph.SR].

McMullin, J. P. et al. (2007). "CASA Architecture and Applications". In: *Astronomical Data Analysis Software and Systems XVI*. Ed. by R. A. Shaw, F. Hill, and D. J. Bell. Vol. 376. Astronomical Society of the Pacific Conference Series, p. 127.

Meier, D. L. (Feb. 2001). "The Association of Jet Production with Geometrically Thick Accretion Flows and Black Hole Rotation". In: *ApJL* 548.1, pp. L9–L12. DOI: 10.1086/318921. arXiv: astro-ph/0010231 [astro-ph].

Metzger, Brian D., Edo Berger, and Ben Margalit (May 2017). "Millisecond Magnetar Birth Connects FRB 121102 to Superluminous Supernovae and Long-duration Gamma-Ray Bursts". In: *ApJ* 841.1, 14, p. 14. DOI: 10.3847/1538-4357/aa633d. arXiv: 1701.02370 [astro-ph.HE].

Metzger, Brian D., P. K. G. Williams, and Edo Berger (June 2015). "Extragalactic Synchrotron Transients in the Era of Wide-field Radio Surveys. I. Detection Rates and Light Curve Characteristics". In: *ApJ* 806.2, 224, p. 224. DOI: 10.1088/0004-637X/806/2/224. arXiv: 1502.01350 [astro-ph.HE].

Milisavljevic, D. et al. (Dec. 2015). "Metamorphosis of SN 2014C: Delayed Interaction between a Hydrogen Poor Core-collapse Supernova and a Nearby Circumstellar Shell". In: *ApJ* 815.2, 120, p. 120. DOI: 10.1088/0004-637X/815/2/120. arXiv: 1511.01907 [astro-ph.HE].

Milisavljevic, Dan, Robert A. Fesen, et al. (May 2012). "Late-time Optical Emission from Core-collapse Supernovae". In: *ApJ* 751.1, 25, p. 25. DOI: 10.1088/0004-637X/751/1/25. arXiv: 1203.0006 [astro-ph.HE].

Milisavljevic, Dan, Daniel J. Patnaude, et al. (Sept. 2018). "Evidence for a Pulsar Wind Nebula in the Type Ib Peculiar Supernova SN 2012au". In: *ApJL* 864.2, L36, p. L36. DOI: 10.3847/2041-8213/aadd4e. arXiv: 1809.01141 [astro-ph.HE].

Minkowski, R. (Aug. 1941). "Spectra of Supernovae". In: *PASP* 53.314, p. 224. DOI: 10.1086/125315.

Moe, Maxwell and Rosanne Di Stefano (June 2017). "Mind Your Ps and Qs: The Interrelation between Period (P) and Mass-ratio (Q) Distributions of Binary Stars". In: *ApJS* 230.2, 15, p. 15. DOI: 10.3847/1538-4365/aa6fb6. arXiv: 1606.05347 [astro-ph.SR].

Mohan, N. and D. Rafferty (Feb. 2015a). *PyBDSF: Python Blob Detection and Source Finder*. Astrophysics Source Code Library. ascl: 1502.007.

– (Feb. 2015b). *PyBDSF: Python Blob Detection and Source Finder*. Astrophysics Source Code Library. ascl: 1502.007.

Molina, Mallory, Amy E. Reines, Jenny E. Greene, et al. (Mar. 2021). "Outflows, Shocks, and Coronal Line Emission in a Radio-selected AGN in a Dwarf Galaxy". In: *ApJ* 910.1, 5, p. 5. DOI: 10.3847/1538-4357/abe120. arXiv: 2101.12217 [astro-ph.GA].

Molina, Mallory, Amy E. Reines, Colin J. Latimer, et al. (Dec. 2021). "A Sample of Massive Black Holes in Dwarf Galaxies Detected via [Fe X] Coronal Line Emission: Active Galactic Nuclei and/or Tidal Disruption Events". In: *ApJ* 922.2, 155, p. 155. DOI: 10.3847/1538-4357/ac1ffa. arXiv: 2108.09307 [astro-ph.GA].

Mooley, K. P., G. Hallinan, et al. (Feb. 2016). "The Caltech-NRAO Stripe 82 Survey (CNSS). I. The Pilot Radio Transient Survey In 50 deg^2". In: *ApJ* 818.2, 105, p. 105. DOI: 10.3847/0004-637X/818/2/105. arXiv: 1601.01693 [astro-ph.HE].

Mooley, K. P., S. T. Myers, et al. (Jan. 2019). "The Caltech-NRAO Stripe 82 Survey (CNSS). II. On-the-fly Mosaicking Methodology". In: *ApJ* 870.1, 25, p. 25. DOI: 10.3847/1538-4357/aaef7c. arXiv: 1811.08445 [astro-ph.IM].

Mooley, K. P., E. Nakar, et al. (Feb. 2018). "A mildly relativistic wide-angle outflow in the neutron-star merger event GW170817". In: *Nature* 554.7691, pp. 207–210. DOI: 10.1038/nature25452. arXiv: 1711.11573 [astro-ph.HE].

Moustakas, John et al. (Oct. 2010). "Optical Spectroscopy and Nebular Oxygen Abundances of the Spitzer/SINGS Galaxies". In: *ApJS* 190.2, pp. 233–266. DOI: 10.1088/0067-0049/190/2/233. arXiv: 1007.4547 [astro-ph.CO].

Murphy, E. J. et al. (Aug. 2011). "Calibrating Extinction-free Star Formation Rate Diagnostics with 33 GHz Free-free Emission in NGC 6946". In: *ApJ* 737.2, 67, p. 67. DOI: 10.1088/0004-637X/737/2/67. arXiv: 1105.4877 [astro-ph.CO].

Murphy, Tara, Shami Chatterjee, et al. (Feb. 2013). "VAST: An ASKAP Survey for Variables and Slow Transients". In: *PASA* 30, e006, e006. DOI: 10.1017/pasa.2012.006. arXiv: 1207.1528 [astro-ph.IM].

Murphy, Tara, David L. Kaplan, et al. (Oct. 2021). "The ASKAP Variables and Slow Transients (VAST) Pilot Survey". In: *PASA* 38, e054, e054. DOI: 10.1017/pasa.2021.44. arXiv: 2108.06039 [astro-ph.HE].

Nakar, Ehud and Re'em Sari (Mar. 2012). "Relativistic Shock Breakouts—A Variety of Gamma-Ray Flares: From Low-luminosity Gamma-Ray Bursts to Type Ia Supernovae". In: *ApJ* 747.2, 88, p. 88. DOI: 10.1088/0004-637X/747/2/88. arXiv: 1106.2556 [astro-ph.HE].

Nicholl, M. et al. (Oct. 2015). "On the diversity of superluminous supernovae: ejected mass as the dominant factor". In: *MNRAS* 452.4, pp. 3869–3893. DOI: 10.1093/mnras/stv1522. arXiv: 1503.03310 [astro-ph.SR].

Niu, C. -H. et al. (Oct. 2021). "A repeating FRB in a dense environment with a compact persistent radio source". In: *arXiv e-prints*, arXiv:2110.07418, arXiv:2110.07418. arXiv: 2110.07418 [astro-ph.HE].

Nyland, Kristina, Timothy A. Davis, et al. (Aug. 2017). "A Multi-wavelength Study of the Turbulent Central Engine of the Low-mass AGN Hosted by NGC 404". In: *ApJ* 845.1, 50, p. 50. DOI: 10.3847/1538-4357/aa7ecf. arXiv: 1707.02303 [astro-ph.GA].

Nyland, Kristina, Dillon Z. Dong, et al. (Dec. 2020). "Quasars That Have Transitioned from Radio-quiet to Radio-loud on Decadal Timescales Revealed by VLASS and FIRST". In: *ApJ* 905.1, 74, p. 74. DOI: 10.3847/1538-4357/abc341. arXiv: 2011.08872 [astro-ph.GA].

O'Dea, C. P., S. A. Baum, and C. Stanghellini (Oct. 1991). "What Are the Gigahertz Peaked-Spectrum Radio Sources?" In: *ApJ* 380, p. 66. DOI: 10.1086/170562.

Ofek, Eran O. (Sept. 2017). "A Search for FRB 121102-like Persistent Radio-luminous Sources—Candidates and Implications for the FRB Rate and Searches". In: *ApJ* 846.1, 44, p. 44. DOI: 10.3847/1538-4357/aa8310. arXiv: 1707.09044 [astro-ph.HE].

Oke, J. B. et al. (Apr. 1995). "The Keck Low-Resolution Imaging Spectrometer". In: *PASP* 107, p. 375. DOI: 10.1086/133562.

Orosz, Jerome A. et al. (Dec. 2011). "The Mass of the Black Hole in Cygnus X-1". In: *ApJ* 742.2, 84, p. 84. DOI: 10.1088/0004-637X/742/2/84. arXiv: 1106.3689 [astro-ph.HE].

Osterbrock, Donald E. and Gary J. Ferland (2006). *Astrophysics of gaseous nebulae and active galactic nuclei*. University Science Books.

Palliyaguru, Nipuni T. et al. (Feb. 2019). "The Double-peaked Radio Light Curve of Supernova PTF11qcj". In: *ApJ* 872.2, 201, p. 201. DOI: 10.3847/1538-4357/aaf64d. arXiv: 1802.09683 [astro-ph.SR].

Panagia, N., R. A. Sramek, and K. W. Weiler (Jan. 1986). "Subluminous, Radio Emitting Type I Supernovae". In: *ApJL* 300, p. L55. DOI: 10.1086/184602.

Pejcha, Ondřej et al. (Nov. 2017). "Pre-explosion Spiral Mass Loss of a Binary Star Merger". In: *ApJ* 850.1, 59, p. 59. DOI: 10.3847/1538-4357/aa95b9. arXiv: 1710.02533 [astro-ph.SR].

Pelletier, Guy et al. (July 2017). "Towards Understanding the Physics of Collisionless Relativistic Shocks. Relativistic Collisionless Shocks". In: *SSRv* 207.1-4, pp. 319–360. DOI: 10.1007/s11214-017-0364-6. arXiv: 1705.05549 [astro-ph.HE].

Pérez-González, Pablo G. et al. (July 2003). "Spatial Analysis of the Hα Emission in the Local Star-forming UCM Galaxies". In: *ApJ* 591.2, pp. 827–842. DOI: 10.1086/375364. arXiv: astro-ph/0303323 [astro-ph].

Perley, Daniel A. (Aug. 2019). "Fully Automated Reduction of Longslit Spectroscopy with the Low Resolution Imaging Spectrometer at the Keck Observatory". In: *PASP* 131.1002, p. 084503. DOI: 10.1088/1538-3873/ab215d. arXiv: 1903.07629 [astro-ph.IM].

Perley, R. A. and B. J. Butler (May 2017). "An Accurate Flux Density Scale from 50 MHz to 50 GHz". In: *ApJS* 230.1, 7, p. 7. DOI: 10.3847/1538-4365/aa6df9. arXiv: 1609.05940 [astro-ph.IM].

Perley, R. A., C. J. Chandler, et al. (Sept. 2011). "The Expanded Very Large Array: A New Telescope for New Science". In: *ApJL* 739.1, L1, p. L1. DOI: 10.1088/2041-8205/739/1/L1. arXiv: 1106.0532 [astro-ph.IM].

Perlman, Eric S. et al. (June 2017). "Compact Resolved Ejecta in the Nearest Tidal Disruption Event". In: *ApJ* 842.2, 126, p. 126. DOI: 10.3847/1538-4357/aa71b1. arXiv: 1705.01669 [astro-ph.HE].

Perlmutter, S. et al. (June 1999). "Measurements of Ω and Λ from 42 High-Redshift Supernovae". In: *ApJ* 517.2, pp. 565–586. DOI: 10.1086/307221. arXiv: astro-ph/9812133 [astro-ph].

Perna, Rosalba, Davide Lazzati, and Matteo Cantiello (Jan. 2021). "Electromagnetic Signatures of Relativistic Explosions in the Disks of Active Galactic Nuclei". In: *ApJL* 906.2, L7, p. L7. DOI: 10.3847/2041-8213/abd319. arXiv: 2011.08873 [astro-ph.HE].

Peters, Charee et al. (Feb. 2019). "Observational Constraints on Late-time Radio Rebrightening of GRB/Supernovae". In: *ApJ* 872.1, 28, p. 28. DOI: 10.3847/1538-4357/aafb3c. arXiv: 1901.01197 [astro-ph.HE].

Phinney, E. S. (Jan. 1989). "Manifestations of a Massive Black Hole in the Galactic Center". In: *The Center of the Galaxy*. Ed. by Mark Morris. Vol. 136, p. 543.

Pietka, M., R. P. Fender, and E. F. Keane (Feb. 2015). "The variability time-scales and brightness temperatures of radio flares from stars to supermassive black holes". In: *MNRAS* 446.4, pp. 3687–3696. DOI: 10.1093/mnras/stu2335. arXiv: 1411.1067 [astro-ph.HE].

Plavin, A. V. et al. (May 2019). "Significant core shift variability in parsec-scale jets of active galactic nuclei". In: *MNRAS* 485.2, pp. 1822–1842. DOI: 10.1093/mnras/stz504. arXiv: 1811.02544 [astro-ph.GA].

Predehl, P. et al. (Mar. 2021). "The eROSITA X-ray telescope on SRG". In: *A&A* 647, A1, A1. DOI: 10.1051/0004-6361/202039313. arXiv: 2010.03477 [astro-ph.HE].

Proga, Daniel, James M. Stone, and Timothy R. Kallman (Nov. 2000). "Dynamics of Line-driven Disk Winds in Active Galactic Nuclei". In: *ApJ* 543.2, pp. 686–696. DOI: 10.1086/317154. arXiv: astro-ph/0005315 [astro-ph].

Pskovskii, Iu. P. (Dec. 1977). "Light curves, color curves, and expansion velocity of type I supernovae as functions of the rate of brightness decline". In: *Soviet Ast.* 21, p. 675.

Pye, J. P. et al. (Sept. 2015). "A survey of stellar X-ray flares from the XMM-Newton serendipitous source catalogue: HIPPARCOS-Tycho cool stars". In: *A&A* 581, A28, A28. DOI: 10.1051/0004-6361/201526217. arXiv: 1506.05289 [astro-ph.SR].

Rau, A. et al. (Aug. 2005). "The 1st INTEGRAL SPI-ACS gamma-ray burst catalogue". In: *A&A* 438.3, pp. 1175–1183. DOI: 10.1051/0004-6361:20053159. arXiv: astro-ph/0504357 [astro-ph].

Ravi, Vikram et al. (Feb. 2021). "FIRST J153350.8+272729: the radio afterglow of a decades-old tidal disruption event". In: *arXiv e-prints*, arXiv:2102.05795, arXiv:2102.05795. arXiv: 2102.05795 [astro-ph.HE].

Raynaud, Raphaël et al. (Mar. 2020). "Magnetar formation through a convective dynamo in protoneutron stars". In: *Science Advances* 6.11, eaay2732. DOI: 10.1126/sciadv.aay2732. arXiv: 2003.06662 [astro-ph.HE].

Rees, Martin J. (June 1988). "Tidal disruption of stars by black holes of 10^6-10^8 solar masses in nearby galaxies". In: *Nature* 333.6173, pp. 523–528. DOI: 10.1038/333523a0.

Reines, Amy E., James J. Condon, et al. (Jan. 2020). "A New Sample of (Wandering) Massive Black Holes in Dwarf Galaxies from High-resolution Radio Observations". In: *ApJ* 888.1, 36, p. 36. DOI: 10.3847/1538-4357/ab4999.

Reines, Amy E. and Marta Volonteri (Nov. 2015). "Relations between Central Black Hole Mass and Total Galaxy Stellar Mass in the Local Universe". In: *ApJ* 813.2, 82, p. 82. DOI: 10.1088/0004-637X/813/2/82. arXiv: 1508.06274 [astro-ph.GA].

Resmi, L., J. Vink, and C. H. Ishwara-Chandra (Nov. 2021). "Implications of the lowest frequency detection of the persistent counterpart of FRB121102". In: *A&A* 655, A102, A102. DOI: 10.1051/0004-6361/202039771. arXiv: 2010.14334 [astro-ph.HE].

Reynolds, S. P. and R. A. Chevalier (Mar. 1984). "Evolution of pulsar-driven supernova remnants." In: *ApJ* 278, pp. 630–648. DOI: 10.1086/161831.

Reynolds, Stephen P., Kazimierz J. Borkowski, and Peter H. Gwynne (Apr. 2018). "Expansion and Brightness Changes in the Pulsar-wind Nebula in the Composite Supernova Remnant Kes 75". In: *ApJ* 856.2, 133, p. 133. DOI: 10.3847/1538-4357/aab3d3. arXiv: 1803.09128 [astro-ph.HE].

Richardson, Chris T. et al. (May 2016). "Interpreting the ionization sequence in star-forming galaxy emission-line spectra". In: *MNRAS* 458.1, pp. 988–1012. DOI: 10.1093/mnras/stw100. arXiv: 1601.03372 [astro-ph.GA].

Riess, Adam G. et al. (Sept. 1998). "Observational Evidence from Supernovae for an Accelerating Universe and a Cosmological Constant". In: *AJ* 116.3, pp. 1009–1038. DOI: 10.1086/300499. arXiv: astro-ph/9805201 [astro-ph].

Rust, B. W. (Jan. 1974). "The Use of Supernovae Light Curves for Testing the Expansion Hypothesis and Other Cosmological Relations." PhD thesis. Oak Ridge National Laboratory, Tennessee.

Rybicki, George B. and Alan P. Lightman (1986). *Radiative Processes in Astrophysics*.

Ryder, Stuart et al. (Oct. 1993). "SN 1978K: an Extraordinary Supernova in the Nearby Galaxy NGC 1313". In: *ApJ* 416, p. 167. DOI: 10.1086/173223.

Sądowski, Aleksander and Ramesh Narayan (Mar. 2016). "Three-dimensional simulations of supercritical black hole accretion discs - luminosities, photon trapping and variability". In: *MNRAS* 456.4, pp. 3929–3947. DOI: 10.1093/mnras/stv2941. arXiv: 1509.03168 [astro-ph.HE].

Saikia, Payaswini et al. (Dec. 2019). "Lorentz Factors of Compact Jets in Black Hole X-Ray Binaries". In: *ApJ* 887.1, 21, p. 21. DOI: 10.3847/1538-4357/ab4a09. arXiv: 1910.01151 [astro-ph.HE].

Salas, P. et al. (Jan. 2013). "SN 2007bg: the complex circumstellar medium around one of the most radio-luminous broad-lined Type Ic supernovae". In: *MNRAS* 428.2, pp. 1207–1217. DOI: 10.1093/mnras/sts104. arXiv: 1208.3455 [astro-ph.HE].

Salim, Samir, Médéric Boquien, and Janice C. Lee (May 2018). "Dust Attenuation Curves in the Local Universe: Demographics and New Laws for Star-forming Galaxies and High-redshift Analogs". In: *ApJ* 859.1, 11, p. 11. DOI: 10.3847/1538-4357/aabf3c. arXiv: 1804.05850 [astro-ph.GA].

Salim, Samir, Janice C. Lee, et al. (Nov. 2016). "GALEX-SDSS-WISE Legacy Catalog (GSWLC): Star Formation Rates, Stellar Masses, and Dust Attenuations of 700,000 Low-redshift Galaxies". In: *ApJS* 227.1, 2, p. 2. DOI: 10.3847/0067-0049/227/1/2. arXiv: 1610.00712 [astro-ph.GA].

Salpeter, Edwin E. (Jan. 1955). "The Luminosity Function and Stellar Evolution." In: *ApJ* 121, p. 161. DOI: 10.1086/145971.

Sana, H. et al. (July 2012). "Binary Interaction Dominates the Evolution of Massive Stars". In: *Science* 337.6093, p. 444. DOI: 10.1126/science.1223344. arXiv: 1207.6397 [astro-ph.SR].

Sarbadhicary, Sumit K. et al. (Jan. 2017). "Supernova remnants in the Local Group - I. A model for the radio luminosity function and visibility times of supernova remnants". In: *MNRAS* 464.2, pp. 2326–2340. DOI: 10.1093/mnras/stw2566. arXiv: 1605.04923 [astro-ph.HE].

Sarzi, Marc et al. (Mar. 2006). "The SAURON project - V. Integral-field emission-line kinematics of 48 elliptical and lenticular galaxies". In: *MNRAS* 366.4, pp. 1151–1200. DOI: 10.1111/j.1365-2966.2005.09839.x. arXiv: astro-ph/0511307 [astro-ph].

Schlickeiser, R. and E. Fuerst (July 1989). "The origin of flat radio spectra in shell-type supernova remnants". In: *A&A* 219.1-2, pp. 192–194.

Schrøder, Sophie Lund et al. (Mar. 2020). "Explosions Driven by the Coalescence of a Compact Object with the Core of a Massive-star Companion inside a Common Envelope: Circumstellar Properties, Light Curves, and Population Statistics". In: *ApJ* 892.1, 13, p. 13. DOI: 10.3847/1538-4357/ab7014. arXiv: 1906.04189 [astro-ph.HE].

Schwab, F. R. (July 1984). "Relaxing the isoplanatism assumption in self-calibration; applications to low-frequency radio interferometry". In: *AJ* 89, pp. 1076–1081. DOI: 10.1086/113605.

Scott, M. A. and A. C. S. Readhead (Sept. 1977). "The low-frequency structure of powerful radio sources and limits to departures from equipartition." In: *MNRAS* 180, pp. 539–550. DOI: 10.1093/mnras/180.4.539.

Serino, Motoko et al. (Oct. 2014a). "MAXI observations of gamma-ray bursts". In: *PASJ* 66.5, 87, p. 87. DOI: 10.1093/pasj/psu063. arXiv: 1406.3912 [astro-ph.HE].

– (Oct. 2014b). "MAXI observations of gamma-ray bursts". In: *PASJ* 66.5, 87, p. 87. DOI: 10.1093/pasj/psu063. arXiv: 1406.3912 [astro-ph.HE].

Sfaradi, Itai et al. (July 2022). "A Late-time Radio Flare Following a Possible Transition in Accretion State in the Tidal Disruption Event AT 2019azh". In: *ApJ* 933.2, 176, p. 176. DOI: 10.3847/1538-4357/ac74bc. arXiv: 2202.00026 [astro-ph.HE].

Shappee, B. J. et al. (June 2014). "The Man behind the Curtain: X-Rays Drive the UV through NIR Variability in the 2013 Active Galactic Nucleus Outburst in NGC 2617". In: *ApJ* 788.1, 48, p. 48. DOI: 10.1088/0004-637X/788/1/48. arXiv: 1310.2241 [astro-ph.HE].

Shimwell, T. W. et al. (Feb. 2017). "The LOFAR Two-metre Sky Survey. I. Survey description and preliminary data release". In: *A&A* 598, A104, A104. DOI: 10.1051/0004-6361/201629313. arXiv: 1611.02700 [astro-ph.IM].

Sironi, Lorenzo and Anatoly Spitkovsky (Nov. 2011). "Acceleration of Particles at the Termination Shock of a Relativistic Striped Wind". In: *ApJ* 741.1, 39, p. 39. DOI: 10.1088/0004-637X/741/1/39. arXiv: 1107.0977 [astro-ph.HE].

Sivakoff, Gregory R., Craig L. Sarazin, and Andrés Jordán (May 2005). "Luminous X-Ray Flares from Low-Mass X-Ray Binary Candidates in the Early-Type Galaxy NGC 4697". In: *ApJL* 624.1, pp. L17–L20. DOI: 10.1086/430374. arXiv: astro-ph/0503195 [astro-ph].

Skilling, John (Nov. 2004). "Nested Sampling". In: *Bayesian Inference and Maximum Entropy Methods in Science and Engineering: 24th International Workshop on Bayesian Inference and Maximum Entropy Methods in Science and Engineering*. Ed. by Rainer Fischer, Roland Preuss, and Udo Von Toussaint. Vol. 735. American Institute of Physics Conference Series, pp. 395–405. DOI: 10.1063/1.1835238.

– (2006). "Nested sampling for general Bayesian computation". In: *Bayesian Analysis* 1.4, pp. 833–859. DOI: 10.1214/06-BA127. URL: https://doi.org/10.1214/06-BA127.

Smith, Nathan (Aug. 2014). "Mass Loss: Its Effect on the Evolution and Fate of High-Mass Stars". In: *ARA&A* 52, pp. 487–528. DOI: 10.1146/annurev-astro-081913-040025. arXiv: 1402.1237 [astro-ph.SR].

Soderberg, A. M., E. Berger, et al. (May 2008). "An extremely luminous X-ray outburst at the birth of a supernova". In: *Nature* 453.7194, pp. 469–474. DOI: 10.1038/nature06997. arXiv: 0802.1712 [astro-ph].

Soderberg, A. M., S. Chakraborti, et al. (Jan. 2010). "A relativistic type Ibc supernova without a detected γ-ray burst". In: *Nature* 463.7280, pp. 513–515. DOI: 10.1038/nature08714. arXiv: 0908.2817 [astro-ph.HE].

Soderberg, A. M., S. R. Kulkarni, et al. (Aug. 2006). "Relativistic ejecta from X-ray flash XRF 060218 and the rate of cosmic explosions". In: *Nature* 442.7106, pp. 1014–1017. DOI: 10.1038/nature05087. arXiv: astro-ph/0604389 [astro-ph].

Soker, Noam (Nov. 2017). "Energizing the last phase of common-envelope removal". In: *MNRAS* 471.4, pp. 4839–4843. DOI: 10.1093/mnras/stx1978. arXiv: 1706.03720 [astro-ph.SR].

Soker, Noam, Aldana Grichener, and Avishai Gilkis (Apr. 2019). "Diversity of common envelope jets supernovae and the fast transient AT2018cow". In: *MNRAS* 484.4, pp. 4972–4979. DOI: 10.1093/mnras/stz364. arXiv: 1811.11106 [astro-ph.HE].

Somalwar, Jean J., Vikram Ravi, Dillon Dong, et al. (Aug. 2021). "The nascent milliquasar VT J154843.06+220812.6: tidal disruption event or extreme accretion-state change?" In: *arXiv e-prints*, arXiv:2108.12431, arXiv:2108.12431. arXiv: 2108.12431 [astro-ph.HE].

Somalwar, Jean J., Vikram Ravi, Dillon Z. Dong, et al. (July 2022). "A candidate relativistic tidal disruption event at 340 Mpc". In: *arXiv e-prints*, arXiv:2207.02873, arXiv:2207.02873. arXiv: 2207.02873 [astro-ph.HE].

Speagle, Joshua S. (Apr. 2020). "DYNESTY: a dynamic nested sampling package for estimating Bayesian posteriors and evidences". In: *MNRAS* 493.3, pp. 3132–3158. DOI: 10.1093/mnras/staa278. arXiv: 1904.02180 [astro-ph.IM].

Sridhar, Navin and Brian D. Metzger (June 2022). "Radio Nebul\from Hyper-Accreting X-ray Binaries as Common Envelope Precursors and Persistent Counterparts of Fast Radio Bursts". In: *arXiv e-prints*, arXiv:2206.10486, arXiv:2206.10486. arXiv: 2206.10486 [astro-ph.HE].

Staelin, David H. and III Reifenstein Edward C. (Dec. 1968). "Pulsating Radio Sources near the Crab Nebula". In: *Science* 162.3861, pp. 1481–1483. DOI: 10.1126/science.162.3861.1481.

Stappers, B. W. et al. (June 2011). "Observing pulsars and fast transients with LOFAR". In: *A&A* 530, A80, A80. DOI: 10.1051/0004-6361/201116681. arXiv: 1104.1577 [astro-ph.IM].

Stein, Robert et al. (Feb. 2021). "A tidal disruption event coincident with a high-energy neutrino". In: *Nature Astronomy* 5, pp. 510–518. DOI: 10.1038/s41550-020-01295-8. arXiv: 2005.05340 [astro-ph.HE].

Stritzinger, Maximilian and Takashi Moriya (Jan. 2018). "Workshop 8: Supernovae". In: *arXiv e-prints*, arXiv:1801.06643, arXiv:1801.06643. arXiv: 1801.06643 [astro-ph.HE].

Stroh, Michael C. et al. (Dec. 2021). "Luminous Late-time Radio Emission from Supernovae Detected by the Karl G. Jansky Very Large Array Sky Survey (VLASS)". In: *ApJL* 923.2, L24, p. L24. DOI: 10.3847/2041-8213/ac375e. arXiv: 2106.09737 [astro-ph.HE].

Sugizaki, Mutsumi et al. (Nov. 2011). "In-Orbit Performance of MAXI Gas Slit Camera (GSC) on ISS". In: *PASJ* 63, S635–S644. DOI: 10.1093/pasj/63.sp3.S635. arXiv: 1102.0891 [astro-ph.IM].

Sun, Ning-Chen, Justyn R. Maund, and Paul A. Crowther (Oct. 2020). "The changing-type SN 2014C may come from an 11-$M_{\odot}$ star stripped by binary interaction and violent eruption". In: *MNRAS* 497.4, pp. 5118–5135. DOI: 10.1093/mnras/staa2277. arXiv: 2003.09325 [astro-ph.SR].

Sutton, Andrew D., Timothy P. Roberts, and Matthew J. Middleton (Oct. 2013). "The ultraluminous state revisited: fractional variability and spectral shape as diagnostics of super-Eddington accretion". In: *MNRAS* 435.2, pp. 1758–1775. DOI: 10.1093/mnras/stt1419. arXiv: 1307.8044 [astro-ph.HE].

Taam, Ronald E. and Eric L. Sandquist (Jan. 2000). "Common Envelope Evolution of Massive Binary Stars". In: *ARA&A* 38, pp. 113–141. DOI: 10.1146/annurev.astro.38.1.113.

Tabatabaei, F. S. et al. (Apr. 2013). "A detailed study of the radio-FIR correlation in NGC 6946 with Herschel-PACS/SPIRE from KINGFISH". In: *A&A* 552, A19, A19. DOI: 10.1051/0004-6361/201220249. arXiv: 1301.6884 [astro-ph.CO].

Taddia, F., J. Sollerman, et al. (Feb. 2015). "Early-time light curves of Type Ib/c supernovae from the SDSS-II Supernova Survey". In: *A&A* 574, A60, A60. DOI: 10.1051/0004-6361/201423915. arXiv: 1408.4084 [astro-ph.HE].

Taddia, F., M. D. Stritzinger, M. Bersten, et al. (Feb. 2018). "The Carnegie Supernova Project I. Analysis of stripped-envelope supernova light curves". In: *A&A* 609, A136, A136. DOI: 10.1051/0004-6361/201730844. arXiv: 1707.07614 [astro-ph.HE].

Taddia, F., M. D. Stritzinger, J. Sollerman, et al. (July 2013). "Carnegie Supernova Project: Observations of Type IIn supernovae". In: *A&A* 555, A10, A10. DOI: 10.1051/0004-6361/201321180. arXiv: 1304.3038 [astro-ph.CO].

Taggart, Kirsty and Daniel Perley (Nov. 2019). "Core-collapse, superluminous, and gamma-ray burst supernova host galaxy populations at low redshift: the importance of dwarf and starbursting galaxies". In: *arXiv e-prints*, arXiv:1911.09112, arXiv:1911.09112. arXiv: 1911.09112 [astro-ph.HE].

Tanaka, Shuta J. and Katsuaki Asano (June 2017). "On the Radio-emitting Particles of the Crab Nebula: Stochastic Acceleration Model". In: *ApJ* 841.2, 78, p. 78. DOI: 10.3847/1538-4357/aa6f13. arXiv: 1704.06746 [astro-ph.HE].

Tauris, T. M. et al. (Sept. 2017). "Formation of Double Neutron Star Systems". In: *ApJ* 846.2, 170, p. 170. DOI: 10.3847/1538-4357/aa7e89. arXiv: 1706.09438 [astro-ph.HE].

Tavani, M. et al. (Apr. 2021). "An X-ray burst from a magnetar enlightening the mechanism of fast radio bursts". In: *Nature Astronomy* 5, pp. 401–407. DOI: 10.1038/s41550-020-01276-x. arXiv: 2005.12164 [astro-ph.HE].

Taylor, Matt et al. (Sept. 2014). "The Core Collapse Supernova Rate from the SDSS-II Supernova Survey". In: *ApJ* 792.2, 135, p. 135. DOI: 10.1088/0004-637X/792/2/135. arXiv: 1407.0999 [astro-ph.SR].

Tchekhovskoy, Alexander et al. (Jan. 2014). "Swift J1644+57 gone MAD: the case for dynamically important magnetic flux threading the black hole in a jetted tidal disruption event". In: *MNRAS* 437.3, pp. 2744–2760. DOI: 10.1093/mnras/stt2085. arXiv: 1301.1982 [astro-ph.HE].

Tendulkar, S. P. et al. (Jan. 2017). "The Host Galaxy and Redshift of the Repeating Fast Radio Burst FRB 121102". In: *ApJL* 834.2, L7, p. L7. DOI: 10.3847/2041-8213/834/2/L7. arXiv: 1701.01100 [astro-ph.HE].

Terlevich, R. and J. Melnick (June 1981). "The dynamics and chemical composition of giant extragalactic H II regions". In: *MNRAS* 195, pp. 839–851. DOI: 10.1093/mnras/195.4.839.

The CHIME/FRB Collaboration et al. (June 2021). "The First CHIME/FRB Fast Radio Burst Catalog". In: *arXiv e-prints*, arXiv:2106.04352, arXiv:2106.04352. arXiv: 2106.04352 [astro-ph.HE].

Thomas, D. et al. (May 2013). "Stellar velocity dispersions and emission line properties of SDSS-III/BOSS galaxies". In: *MNRAS* 431.2, pp. 1383–1397. DOI: 10.1093/mnras/stt261. arXiv: 1207.6115 [astro-ph.CO].

Thomas, Daniel, Claudia Maraston, and Jonas Johansson (Apr. 2011). "Flux-calibrated stellar population models of Lick absorption-line indices with variable element abundance ratios". In: *MNRAS* 412.4, pp. 2183–2198. DOI: 10.1111/j.1365-2966.2010.18049.x. arXiv: 1010.4569 [astro-ph.CO].

Uchida, D. et al. (Jan. 2014). "GRB 140814A: MAXI/GSC detection." In: *GRB Coordinates Network* 16686, p. 1.

Urry, C. Megan and Paolo Padovani (Sept. 1995). "Unified Schemes for Radio-Loud Active Galactic Nuclei". In: *PASP* 107, p. 803. DOI: 10.1086/133630. arXiv: astro-ph/9506063 [astro-ph].

van der Horst, A. J. et al. (May 2007). "GRB 030329: 3 years of radio afterglow monitoring". In: *Philosophical Transactions of the Royal Society of London Series A* 365.1854, pp. 1241–1246. DOI: 10.1098/rsta.2006.1993. arXiv: 0706.1323 [astro-ph].

van Dyk, Schuyler D., Richard A. Sramek, et al. (May 1993). "The Radio Emission from the Type IC Supernova SN 1990B". In: *ApJ* 409, p. 162. DOI: 10.1086/172652.

van Dyk, Schuyler D., Kurt W. Weiler, Richard A. Sramek, and Nino Panagia (Dec. 1993). "SN 1988Z: The Most Distant Radio Supernova". In: *ApJL* 419, p. L69. DOI: 10.1086/187139.

van Dyk, Schuyler D., Kurt W. Weiler, Richard A. Sramek, Michael P. Rupen, et al. (Sept. 1994). "SN 1993J: The Early Radio Emission and Evidence for a Changing Presupernova Mass-Loss Rate". In: *ApJL* 432, p. L115. DOI: 10.1086/187525.

van Velzen, Sjoert, Glennys R. Farrar, et al. (Nov. 2011). "Optical Discovery of Probable Stellar Tidal Disruption Flares". In: *ApJ* 741.2, 73, p. 73. DOI: 10.1088/0004-637X/741/2/73. arXiv: 1009.1627 [astro-ph.CO].

van Velzen, Sjoert, Thomas W. -S. Holoien, et al. (Oct. 2020). "Optical-Ultraviolet Tidal Disruption Events". In: *SSRv* 216.8, 124, p. 124. DOI: 10.1007/s11214-020-00753-z. arXiv: 2008.05461 [astro-ph.HE].

Vanderplas, J.T. et al. (Oct. 2012). "Introduction to astroML: Machine learning for astrophysics". In: *Conference on Intelligent Data Understanding (CIDU)*, pp. 47–54. DOI: 10.1109/CIDU.2012.6382200.

von Kienlin, A. et al. (Apr. 2020). "The Fourth Fermi-GBM Gamma-Ray Burst Catalog: A Decade of Data". In: *ApJ* 893.1, 46, p. 46. DOI: 10.3847/1538-4357/ab7a18. arXiv: 2002.11460 [astro-ph.HE].

Walker, Mark A. (Feb. 1998). "Interstellar scintillation of compact extragalactic radio sources". In: *MNRAS* 294, pp. 307–311. DOI: 10.1046/j.1365-8711.1998.01238.x.

Walker, Mark A. (Feb. 2001). "Erratum: Interstellar scintillation of compact extragalactic radio sources". In: *MNRAS* 321.1, pp. 176–176. DOI: 10.1046/j.1365-8711.2001.04104.x.

Wang, Ziteng et al. (Oct. 2021). "Discovery of ASKAP J173608.2-321635 as a Highly Polarized Transient Point Source with the Australian SKA Pathfinder". In: *ApJ* 920.1, 45, p. 45. DOI: 10.3847/1538-4357/ac2360. arXiv: 2109.00652 [astro-ph.HE].

Weiler, K. W. et al. (Feb. 1986). "Radio Supernovae". In: *ApJ* 301, p. 790. DOI: 10.1086/163944.

Weiler, Kurt W., Nino Panagia, and Richard A. Sramek (Dec. 1990). "Radio Emission from Supernovae. II. SN 1986J: A Different Kind of Type II". In: *ApJ* 364, p. 611. DOI: 10.1086/169444.

Weiler, Kurt W., Schuyler D. van Dyk, et al. (Oct. 1991). "The 10 Year Radio Light Curves for SN 1979C". In: *ApJ* 380, p. 161. DOI: 10.1086/170571.

Werner, G. R. et al. (Jan. 2016). "The Extent of Power-law Energy Spectra in Collisionless Relativistic Magnetic Reconnection in Pair Plasmas". In: *ApJL* 816.1, L8, p. L8. DOI: 10.3847/2041-8205/816/1/L8. arXiv: 1409.8262 [astro-ph.HE].

White, Richard L. et al. (Feb. 1997). "A Catalog of 1.4 GHz Radio Sources from the FIRST Survey". In: *ApJ* 475.2, pp. 479–493. DOI: 10.1086/303564.

Wiktorowicz, Grzegorz et al. (Nov. 2019). "Populations of Stellar-mass Black Holes from Binary Systems". In: *ApJ* 885.1, 1, p. 1. DOI: 10.3847/1538-4357/ab45e6. arXiv: 1907.11431 [astro-ph.HE].

Wołowska, Aleksandra et al. (June 2021). "Caltech-NRAO Stripe 82 Survey (CNSS). V. AGNs That Transitioned to Radio-loud State". In: *ApJ* 914.1, 22, p. 22. DOI: 10.3847/1538-4357/abe62d. arXiv: 2103.08422 [astro-ph.GA].

Wright, E. L. (Dec. 2006). "A Cosmology Calculator for the World Wide Web". In: *PASP* 118.850, pp. 1711–1715. DOI: 10.1086/510102. arXiv: astro-ph/0609593 [astro-ph].

Wu, Samantha and Jim Fuller (Jan. 2021). "A Diversity of Wave-driven Presupernova Outbursts". In: *ApJ* 906.1, 3, p. 3. DOI: 10.3847/1538-4357/abc87c. arXiv: 2011.05453 [astro-ph.HE].

Yalinewich, A. et al. (Aug. 2019). "Radio emission from the unbound debris of tidal disruption events". In: *MNRAS* 487.3, pp. 4083–4092. DOI: 10.1093/mnras/stz1567. arXiv: 1903.02575 [astro-ph.HE].

Yao, Yuhan et al. (Nov. 2020). "Multi-wavelength Observations of AT2019wey: a New Candidate Black Hole Low-mass X-ray Binary". In: *arXiv e-prints*, arXiv:2012.00169, arXiv:2012.00169. arXiv: 2012.00169 [astro-ph.HE].

Younes, G. et al. (June 2016). "The Wind Nebula around Magnetar Swift J1834.9-0846". In: *ApJ* 824.2, 138, p. 138. DOI: 10.3847/0004-637X/824/2/138. arXiv: 1604.06472 [astro-ph.HE].

Zauderer, B. A. et al. (Aug. 2011). "Birth of a relativistic outflow in the unusual γ-ray transient Swift J164449.3+573451". In: *Nature* 476.7361, pp. 425–428. DOI: 10.1038/nature10366. arXiv: 1106.3568 [astro-ph.HE].

Zhang, Fabao et al. (Oct. 2022). "Transient Radio Emission from Low-redshift Galaxies at z < 0.3 Revealed by the VLASS and FIRST Surveys". In: *ApJ* 938.1, 43, p. 43. DOI: 10.3847/1538-4357/ac8a9a. arXiv: 2208.08308 [astro-ph.GA].